

Liquid Vapor Phase Transitions: Modeling, Riemann Solvers and Computation

Von der Fakultät für Mathematik und Physik der Universität Stuttgart
zur Erlangung der Würde eines Doktors der
Naturwissenschaften (Dr. rer. nat.) genehmigte Abhandlung

Vorgelegt von

Christoph Zeiler

aus Sigmaringen

Hauptberichter:

Prof. Dr. Christian Rohde

Mitberichter:

Prof. Dr. Christophe Chalons

Prof. Dr. Claus-Dieter Munz

Tag der mündlichen Prüfung: 18. Dezember 2015

Institut für Angewandte Analysis und Numerische Simulation, Universität Stuttgart

2015

D 93

Abstract

The numerical approximation of liquid vapor flows within the compressible regime is a challenging task because complex physical effects at the phase interfaces govern the global flow behavior. We develop a sharp interface approach which treats the phase boundary like a shock wave discontinuity and takes capillarity effects into account. The approach relies on the solution of Riemann problems across the interface that separates the liquid and the vapor phase. The Riemann solution accounts for the relevant physics by enforcing appropriate jump conditions at the phase boundary. A wide variety of interface effects can be handled in a thermodynamically consistent way. This includes surface tension, as well as, mass and energy transfer by phase transition. Moreover, the local normal speed of the interface, which is needed to calculate the time evolution of the phase boundary, is given by the Riemann solution.

The focus of this work is the development of isothermal and non-isothermal two-phase Riemann solvers for the sharp interface approach. To verify the solvers with respect to numerical and thermodynamic requirements, one-dimensional and radially symmetric problems are studied. Furthermore, the Riemann solvers and the sharp interface approach are successfully validated against shock tube experiments of real fluids (alkanes).

Zusammenfassung

Die numerische Approximation von Zweiphasenströmungen (flüssig/Dampf) in kompressiblen Medien ist eine Herausforderung, da komplexe physikalische Effekte an der Phasengrenze das globale Strömungsverhalten bestimmen. Wir entwickeln einen Sharp-Interface Ansatz, der Phasengrenzen als Schockwellen-Unstetigkeiten behandelt und Kapillareffekte berücksichtigt. Der Ansatz beruht auf der Lösung von Riemann-Problemen an der Grenzfläche zwischen Flüssigkeit und Dampf. Die Riemann-Lösung berücksichtigt relevante physikalische Effekte, indem Sprungbedingungen an der Phasengrenze vorgegeben werden. Dadurch kann eine Vielzahl an Grenzeffekten, wie Oberflächenspannung, Massen- und Energieaustausch durch Phasenübergänge, thermodynamisch konsistent gehandhabt werden. Darüber hinaus ist die lokale Geschwindigkeit in Normalenrichtung, die für die Berechnung der zeitlichen Entwicklung der Phasengrenze benötigt wird, durch die Riemann-Lösungen bestimmt.

Der Schwerpunkt dieser Arbeit liegt auf der Entwicklung von isothermen und nicht-isothermen Zweiphasen-Riemannlösern für den Sharp-Interface Ansatz. Zur Verifizierung der Löser bezüglich numerischer und thermodynamischer Anforderungen werden eindimensionale und radial symmetrische Probleme untersucht. Darüber hinaus werden die Riemannlöser und der Sharp-Interface Ansatz erfolgreich durch den Vergleich mit Stoßrohr-Experimenten mit echten Fluiden (Alkane) validiert.

Acknowledgment

This thesis was developed during my time as research associate at the *Institute for Applied Analysis and Numerical Simulation* of the *University of Stuttgart*. At this point, I want to express my gratitude for all the support I received in the past few years.

First of all, I want to thank my advisor Professor Dr. Christian Rohde for giving me the opportunity to be part of his research group and for his support. I also want to thank Professor Dr. Christophe Chalons and Professor Dr. Claus-Dieter Munz for being co-referees of my thesis. Furthermore, I thank the *German Research Foundation* (DFG) for the financial support of this project.

I want to express my gratitude to all my colleagues at the institute and all my collaborators. Special thanks go to Maria Wiebe, Dr. Stefan Fechter and Dr. Patrick Engel for applying the microsolvers in their multidimensional codes and for creating videos of the simulation results according to my specifications. Furthermore, I want to thank Dr. Jan Giesselmann for many fruitful discussions and for his help in proofreading the manuscript.

Last but not least, I want to express my gratitude to everyone who supported me during the last years, especially my family.

Stuttgart, February 2016

Christoph Zeiler

Contents

Abstract / Zusammenfassung	iii
Acknowledgment	v
Contents	vii
1 Introduction	1
2 The mathematical model	7
2.1 Geometric setting	7
2.2 Balance laws in integral form	8
2.3 Isothermal two-phase thermodynamics	10
2.4 Isothermal free boundary formulation	15
3 Front tracking with micro-scale models	19
3.1 The front tracking approach	19
3.2 Micro-scale models and microsolver interfaces	21
3.2.1 Planar two-phase Riemann problems	21
3.2.2 Micro-scale model in Eulerian coordinates	22
3.2.3 Micro-scale model in Lagrangian coordinates	24
3.3 Elementary waves and phase transitions	26
4 Microsolver for Liu's entropy criterion	31
4.1 Mixture equations of state including surface tension	31
4.2 Solving the generalized Riemann problem exactly	33
4.3 Algorithm and illustrating examples	40
4.4 Interim conclusion	43
5 Microsolver for monotone decreasing kinetic functions	45
5.1 Solving the generalized Riemann problem exactly	46
5.2 Algorithm and an illustrating example	54
6 Kinetic relations for microsolvers	57
6.1 Kinetic relations and kinetic functions	57
6.2 Illustrating examples of k -micro solutions	67
6.3 Validation with shock tube experiments	68
6.4 Interim conclusion	70

7	Relaxation microsolver for kinetic relations	73
7.1	Relaxation approximation of the Euler equations	73
7.2	Well-posedness of the \mathbb{K} -relaxation microsolver	76
7.3	Algorithm and verification	79
7.4	Interim conclusion	82
8	Bulk solver with front tracking for radially symmetric solutions	83
8.1	Moving mesh finite volume method	83
8.2	Algorithm and properties of the method	86
9	Verification and validation of the complete method	89
9.1	Experimental order of convergence	90
9.1.1	Application of the k -microsolver 1D	91
9.1.2	Application of the Liu microsolver in 1D	92
9.1.3	Application of the \mathbb{K} -relaxation microsolver in 1D	94
9.1.4	Error analysis for radially symmetric solutions	96
9.2	Global entropy release and steady state solutions	98
9.3	Condensation of bubbles	100
9.4	Validation with shock tube experiments	101
9.5	Conclusion on the isothermal methods	102
10	Non-isothermal liquid vapor flows	105
10.1	The mathematical model	106
10.1.1	Two-phase thermodynamics	106
10.1.2	Non-isothermal Euler systems and latent heat	108
10.1.3	Free boundary formulation	110
10.2	Microsolver for kinetic relations	113
10.2.1	Micro-scale model	114
10.2.2	Algorithm	115
10.2.3	\mathbb{k} -micro solutions and influence of parameters	119
10.3	Numerical and thermodynamic verification	123
10.3.1	Experimental order of convergence	123
10.3.2	Global entropy release and steady state solutions	124
10.4	Validation with shock tube experiments	127
10.4.1	Validation of \mathbb{k} -micro solutions	127
10.4.2	Validation of the complete method	130
10.5	Shock-droplet interaction	131
10.6	Conclusion on the non-isothermal method	136
11	Conclusion and outlook	137
	Bibliography	139
	Index	145

Chapter 1

Introduction

The aim of this work is the numerical computation of fully compressible flow phenomena in systems containing gas and liquid. We consider single component two-phase flows, where the gas consists of the vapor of the liquid, for example liquid water and water steam. In particular, phase transitions and surface tension are taken into account and the fluid may condensate or evaporate completely.

Liquid vapor flows appear in nature and in many applications. It is an interesting field in fluid mechanics, that is far from being completely understood. Technical applications, in which two-phase flows play an important role are, for instance, pumps that are operating close to the saturation pressure. If liquid pressure falls below a critical value, e.g. near pump vanes, then phase change occurs and vapor will be present in the system. Similar effects occur on ship propellers or in injection nozzles. Such cavitation effects may cause serious problems for operators and engineers. When the bubbles collapse, they can generate intense shock waves, which, over time, will cause damage on the propellers, turbine blades or nozzles [10], see Figure 1.1.

As another example, most power plants have large boilers to produce steam for use in turbines. In such cases, pressurized water is passed through heat pipes and it changes to steam as it moves through the pipes. The design of boilers and pipe systems requires a deep understanding of two-phase flows, heat transfer and pressure drop behavior, since

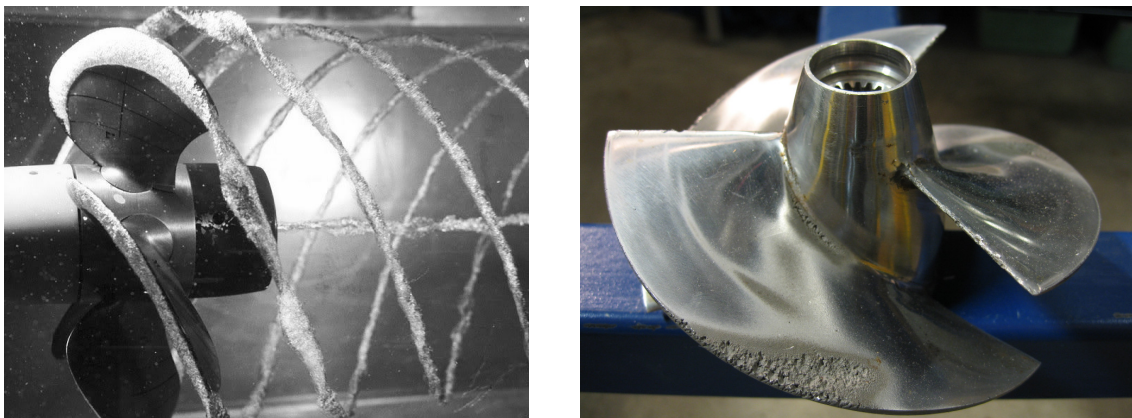


Figure 1.1: Cavitating bubbles at propeller blades [22] (left) and damage caused by cavitation on a propeller of a personal watercraft [5].

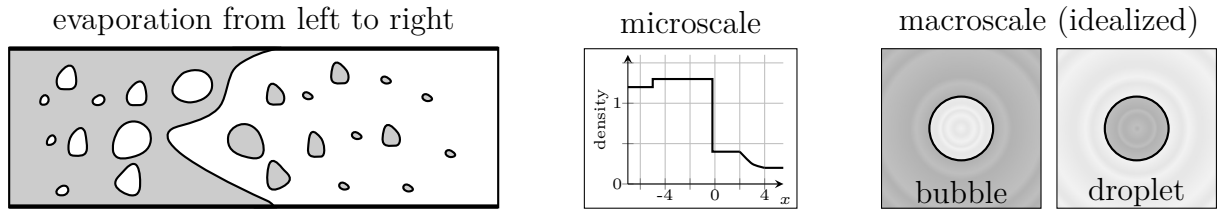


Figure 1.2: Evaporation in a pipe (left), density distribution of a typical Riemann solution (center) and idealized spherical bubble and droplet (right).

two-phase flow properties are significantly different from the single phase case. This becomes even more critical in case of nuclear power plants, where water is used to remove heat from the reactor core. Here, loss of pressure in the pipe system may lead to a *loss-of-coolant accident* [23, 53].

Two-phase flows can appear in various forms. Figure 1.2 (left) illustrates, for example, the evaporation of a liquid in a pipe from left to right. Evaporation may be caused by heating up the pipe or by pressure drop. At the left end of the pipe, vapor bubbles start nucleating in the pure liquid. The bubbles grow and merge together. More and more liquid evaporates and only droplets remain. The droplets shrink and evaporate completely until only pure vapor remains.

Considering such a fully multidimensional evaporation process is complex. In this work, we concentrate on the microscopic dynamics at phase boundaries, described by means of solutions of Riemann problems with initial states in different phases. The density distribution of such a typical Riemann solution is depicted in Figure 1.2 (center). High density values indicate the liquid phase and low density values the vapor phase. Furthermore, we study the macroscopic dynamics of idealized spherical bubbles and droplets, cf. Figure 1.2 (right). Nucleation is not considered.

We are interested in the direct numerical simulation of the dynamics of liquid vapor flows, assuming homogeneous compressible fluids. The underlying mathematical models account not only for the bulk phases' evolution, but also for the interfacial dynamics which are supposed to be driven by surface tension and mass exchange caused by evaporation and condensation.

There are two fundamentally different approaches towards interface driven dynamics, that are the diffuse interface and the sharp interface ansatz. For the first one, the interface between phases is represented as a smooth function with strong gradients across a small interfacial zone. In the interface zone some mixture states have to be defined together with a mathematical model for its time evolution. Typically, only one set of equations has to be solved in the computational domain (see e.g. [3, 66] for compressible diffuse-interface models). Here we focus on the sharp interface approach where the bulk regions are governed by an ensemble of fluid mechanical equations. The interface appears as an unknown free boundary such that state variables are discontinuous across this hypersurface. Appropriate coupling conditions across the interface have to be formulated to ensure the well-posedness and thermodynamic consistency of the overall model.

More precisely, we describe the compressible hydrodynamics of the fluid in the bulk phases by the Euler equations. The modeling of appropriate coupling conditions is quite delicate. In the isothermal case it is well established that the coupling conditions should

consist of mass conservation, a dynamic version of the Young-Laplace law for momentum balance, and an extended entropy condition. This could be a kinetic relation [49, 67], the entropy criterion of Liu [40, 55] or another extended entropy principle [21]. Kinetic relations pose a condition on the interfacial entropy production. It is clear that entropy increases in time but the correct rate of growth is an open question. Thus, it is generally unknown, which additional condition holds in nature.

Conservation laws and one of the mentioned extended entropy conditions have also to hold in the non-isothermal case, where we neglect viscosity and heat conduction such that the fluid is described by the Euler equations. But, in addition, the release of latent heat at the interface has to be modeled by an algebraic term, since it turns out that the two-phase Euler model is thermodynamically inconsistent in the temperature dependent case. Note that the non-isothermal Euler model is not an extension of the isothermal one. From a thermodynamic point of view these are completely different models. In the isothermal case it is assumed that the heat flux balances out any thermal difference instantaneously. One may think of an infinite heat flux. In the non-isothermal model heat conduction is neglected, that means heat flux is set to zero.

Analysis of Riemann problems for two-phase flows has been a very active field of research in the last decade (see [47] for a general theory and [35, 37, 40, 45, 58] for specific examples), but it is mostly restricted to either simplified thermodynamic relations or to homogeneous coupling conditions that neglect surface tension. Explicit results for arbitrary pressure relations, kinetic relations and surface tension are, even for the isothermal case, not available.

Many numerical methods have been suggested for various types of compressible multiphase flows. We mention here the classes of ghost fluid methods [31], volume-of-fluid schemes [39], or general front tracking schemes [4, 18, 64, 71]. However, these schemes are not applicable for phase change problems. In this case, the state space is made up of two distinct bulk sets, where the Euler equations are hyperbolic, and a spinodal non-physical region, where the Euler system is elliptic. While values in the spinodal region do not appear on the continuous level, they might be present in the above mentioned schemes due to some kind of averaging. To overcome this source of instability an extended front tracking method based on Riemann solvers at the interface has been introduced [24, 58]. The use of two-phase Riemann solvers prevents values in the spinodal region.

The objective of this work is the development and validation of such Riemann solvers for front tracking schemes. This incorporates, in particular, also the verification of the interface model with respect to thermodynamic requirements. We call the aforementioned two-phase Riemann solvers *microsolvers* to emphasize that they take the microscopic dynamics at phase boundaries into account. The *complete method* consists of a front tracking scheme combined with a microsolver.

The work addresses two cases: Chapter 2 to Chapter 9 are concerned with isothermal flows, while Chapter 10 studies the non-isothermal case. All chapters, that contribute to verification or validation issues, are closed with a section for (interim) conclusions.

The outline of this work is as follows. In Chapter 2, we present the continuous mathematical model as a free boundary value problem in arbitrary spatial dimension. Adequate models for isothermal and non-isothermal microsolvers are based on the fundamental balance laws described in Section 2.2. Chapter 3 introduces the general concept of a

front tracking scheme, that meets our requirements. The scheme applies microsolvers to compute local properties of the interface like local speeds and adjacent bulk states.

The microsolvers obey different entropy principles. In Chapter 4, it is the entropy criterion of Liu. The solver of Chapter 5 is conceived for monotone decreasing kinetic functions. In Chapter 6, we have a closer look at kinetic relations and we prove necessary and sufficient conditions for the existence of monotone decreasing kinetic functions. Furthermore, a kinetic function, that resembles the entropy criterion of Liu, is stated and we compare the microsolvers with shock tube experiments for validation. Chapter 7 introduces an approximate microsolver that is applicable to more general kinetic relations.

We present, in Chapter 8, a conservative method for radially symmetric solutions. This scheme is used as a test environment to study the proposed microsolvers under the presence of surface tension. We conclude the isothermal part with numerical results in Chapter 9. This chapter verifies the complete method numerically and with respect to thermodynamic consistency. Furthermore, we compare the complete methods with shock tube experiments for validation and we show examples for the dynamics of spherical droplets and bubbles.

Chapter 10 presents the mathematical model for the non-isothermal case. We state a constitutive condition for latent heat and it follows the construction of the corresponding microsolvers. The chapter provides the verification and validation of the complete method and a two-dimensional application to physically realistic droplet dynamics. Final conclusions and outlook are given in Chapter 11.

The major results of this work are:

Thermodynamically consistent microsolvers for front tracking schemes including surface tension. The mathematical two-phase models have the form of free boundary problems. Such problems are particularly challenging for the numerical discretization. We present with Algorithm 3.1 a novel way to incorporate capillary forces in front tracking schemes. While curvature is measured on a macro-scale, surface tension is exclusively handled with microsolvers. Here it appears as an inhomogeneity in the Rankine-Hugoniot condition at the phase boundary.

The complete methods are successfully verified with respect to the following thermodynamic requirements.

- Saturation states are preserved.
- Total entropy increases in time until the thermodynamic equilibrium is reached.

Note that equilibrium solutions depend on surface tension, such that this is also a validation test for the surface tension treatment.

For the first demand it suffices to verify the microsolvers. If they predict correct steady state solutions, so does the complete scheme. The entropy production property of the numerical solution is analyzed in Section 9.2 for isothermal flows and in Subsection 10.3.2 for non-isothermal flows.

Shock tube experiment validated microsolvers and front tracking scheme. The microsolvers and the complete methods are validated against real world experiments with great correspondence. Shock tube experiments provide data of evaporation front speeds. We compare this data with the numerical solutions in Section 6.3, Section 9.4 for the isothermal case and in Section 10.4 for the non-isothermal case.

Note that this requires the application of equations of state for real fluids, what is challenging for the numerics, because of highly different density ratios and the stiff liquid pressure. Our sharp interface approach relies merely on basic assumptions for equations of state and even external thermodynamic libraries can be used.

It is generally unknown, which extended entropy principle holds in nature. We review the shock tube experiments under the assumption that the process obeys a kinetic relation. It turns out that the associated kinetic function is, in particular, non-decreasing. However, in state of the art analysis of two-phase Riemann problems, it is generally assumed that kinetic functions are monotone decreasing [13, 19, 47, 48, 49], such that the classical theory does not apply here.

Some results have already been published or submitted for publication. The microsolver proposed in Chapter 4 is published in

- F. Jaegle, C. Rohde, and C. Zeiler. “A multiscale method for compressible liquid-vapor flow with surface tension”. *ESAIM: Proceedings* 38 (2012), pp. 387–408.

The approximate microsolvors of Chapter 7 and the front tracking scheme of Chapter 8 are published in

- C. Rohde and C. Zeiler. “A relaxation Riemann solver for compressible two-phase flow with phase transition and surface tension”. *Applied Numerical Mathematics* 95 (2015), pp. 267–279.

The non-isothermal model and the microsolvors of Chapter 10 are submitted.

- S. Fechter, C.-D. Munz, C. Rohde, and C. Zeiler. “A sharp interface method for compressible liquid-vapor flow with phase transition and surface tension”. Submitted to *Journal of Computational Physics*.

Chapter 2

The mathematical model

The compressible hydrodynamics in the bulk phases is governed for the inviscid case by the Euler equations. The two-phase modeling is much more challenging because possible curvature and phase transition effects induce a complex transfer of mass, momentum and energy through the interface. In the sharp interface approach, the flow equations in each bulk region are coupled by appropriate trace conditions.

We introduce in Section 2.1 the geometric setting and the notation, that is used in the sequel. In continuum mechanics, fluid motion is described by balance laws. Section 2.2 gives an overview of the balance laws for mass, momentum, total energy and total entropy. The first two sections are independent of the question if the flow is isothermal or not.

Section 2.3 introduces the thermodynamic framework for the isothermal model. Definition 2.2 provides equations of state and specifies the notation of phases used in the isothermal part of this work. Equilibrium conditions are introduced for fluids at rest with coexisting liquid and vapor phase under the presence of capillary forces. The isothermal mathematical model in Section 2.4 is finally a special case of the balance laws of Section 2.2, closed with equations of state from Definition 2.2.

2.1 Geometric setting

Consider a domain, that is filled with a fluid in its vapor and its liquid phase, as illustrated in Figure 2.1. A precise notion of phases will be given in Section 2.3. So far it is only important that there are domains where the fluid displays different properties and a thin layer called *phase boundary* that separates the domains. Indeed, such a layer has a certain thickness, below the critical temperature in the order of a few molecule diameters. That is some orders of magnitudes smaller than volume sizes which we want to consider in this work. The evolution of the phase boundary is considered on scales much larger than the width of the transition layer. As the basic modeling approach we assume from now on that the phase boundary has zero thickness.

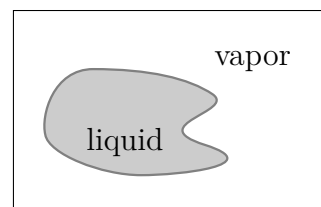
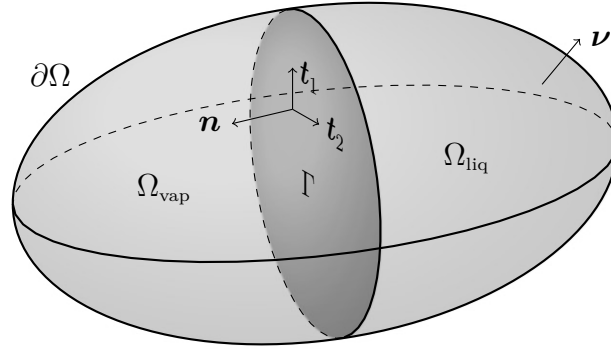


Figure 2.1: Domain and fluid phases.

Figure 2.2: Material volume for $d = 3$.

More precisely, let for any $t \in [0, \theta]$, $\theta > 0$ an arbitrary open subset $\Omega(t) \subset \mathbb{R}^d$, with $d = \{1, 2, 3\}$ and sufficiently smooth boundary, be occupied by the fluid under consideration. The set $\Omega(t)$ is considered as a material volume of the fluid at time t , that has the property that there is no mass flux through its boundary $\partial\Omega(t)$. That means the boundary of the material volume moves with the fluid velocity. Assume further that $\Omega(t)$ is partitioned into the union of two open sets $\Omega_{\text{vap}}(t)$, $\Omega_{\text{liq}}(t)$, which contain the fluid in the vapor and the liquid phase, and a sufficiently smooth hypersurface $\Gamma(t)$ – **the sharp interface** –, that separates the two spatial bulk sets.

Figure 2.2 shows the two bulk volumes $\Omega_{\text{vap}}(t)$, $\Omega_{\text{liq}}(t)$ and the sharp phase boundary $\Gamma(t)$. The normal vector of the material boundary $\partial\Omega(t)$ is denoted with $\boldsymbol{\nu} \in \mathbb{S}^{d-1}$ and points outwards. For $\boldsymbol{\gamma} \in \Gamma(t)$, we denote the speed of $\Gamma(t)$ in the normal direction $\boldsymbol{n} = \boldsymbol{n}(\boldsymbol{\gamma}, t) \in \mathbb{S}^{d-1}$ by $s = s(\boldsymbol{\gamma}, t) \in \mathbb{R}$. The direction of the normal vector is always chosen such that \boldsymbol{n} points into the vapor domain $\Omega_{\text{vap}}(t)$. The complete set of vectors tangential to \boldsymbol{n} is denoted by $\boldsymbol{t}_1, \dots, \boldsymbol{t}_{d-1} \in \mathbb{S}^{d-1}$.

Let a second representation of the sharp interface at time t be given by the level set $\{\boldsymbol{x} \in \Omega \mid \varphi(\boldsymbol{x}, t) = 0\}$ for a function $\varphi \in \mathcal{C}^2(\Omega)$. Assume that $\{\boldsymbol{x} \in \Omega \mid \varphi(\boldsymbol{x}, t) < 0\} = \Omega_{\text{liq}}(t)$ and $\{\boldsymbol{x} \in \Omega \mid \varphi(\boldsymbol{x}, t) > 0\} = \Omega_{\text{vap}}(t)$. Normal vector and the **mean curvature** are then related to φ by

$$\boldsymbol{n} = \frac{\text{grad } \varphi}{|\text{grad } \varphi|}, \quad \kappa = -\text{div } \boldsymbol{n}. \quad (2.1)$$

In the following, we consider the projection of \boldsymbol{n} and κ to $\Gamma(t)$, thus normal vector and mean curvature are functions of $(\boldsymbol{\gamma}, t)$.

Remark 2.1 (Sign of the curvature).

Consider a spherical bubble ($\Omega_{\text{vap}} = B_r(\mathbf{0})$) and a spherical droplet ($\Omega_{\text{liq}} = B_r(\mathbf{0})$), where $B_r(\mathbf{0})$ is the unit ball of radius $r > 0$ and center in the origin.

The definition of \boldsymbol{n} and κ implies that the bubble has the mean curvature $\kappa = 1/r$, while the droplet has the mean curvature $\kappa = -1/r$.

2.2 Balance laws in integral form

We consider an inviscid, heat conducting fluid, that consists of a single substance and we neglect any kind of sources, like gravity, radiation or supply of entropy. The sharp

interface has no mass and is permeable for heat and matter flow. Furthermore, the sharp interface is exclusively equipped with surface tension. The subsequent list of conservation laws assumes the geometric setting of Section 2.1 and is taken from [43]. The balance equation for entropy is from [60].

Conservation of mass. Mass is neither created nor destroyed and fluxes through $\partial\Omega(t)$ are excluded, thus the volume integral over the (mass) **density** $\varrho = \varrho(\mathbf{x}, t) > 0$ with $\mathbf{x} \in \Omega_{\text{liq}}(t) \cup \Omega_{\text{vap}}(t)$ and $t \in [0, \theta]$ is conserved. For the time derivative holds

$$\frac{d}{dt} \int_{\Omega_{\text{liq}}(t) \cup \Omega_{\text{vap}}(t)} \varrho \, d v = 0, \quad (2.2)$$

where $d v$ denotes a material volume element in space.

Conservation of momentum. According to Newtons law, the change in the total momentum equals the total force acting on the material volume. The total momentum is the volume integral over the **momentum** given as the product $\varrho \mathbf{v}$, where $\mathbf{v} = \mathbf{v}(\mathbf{x}, t) \in \mathbb{R}^d$ is the **fluid velocity** in $\mathbf{x} \in \Omega_{\text{liq}}(t) \cup \Omega_{\text{vap}}(t)$, $t \in [0, \theta]$.

The fluid is inviscid, such that only **pressure** $p = p(\mathbf{x}, t) \in \mathbb{R}$ acts on the material surface and **surface tension** $(d-1) \zeta^* \kappa$ acts on the interface. Although the surface tension coefficient $\zeta^* \geq 0$ depends, in particular, on temperature, we will assume that ζ^* is constant. Note that the star superscript is used for material constants.

This leads to the equation

$$\frac{d}{dt} \int_{\Omega_{\text{liq}} \cup \Omega_{\text{vap}}} \varrho \mathbf{v} \, d v = \int_{\partial\Omega_{\text{liq}} \cup \partial\Omega_{\text{vap}} \setminus \Gamma} -p \boldsymbol{\nu} \, d a + \int_{\Gamma} (d-1) \zeta^* \kappa \mathbf{n} \, d a. \quad (2.3)$$

Note that we skipped the time dependency of the integration domains and that $d a$ denotes an area element of the material surface or the interface.

Conservation of energy. The **total energy** is given by the volume integral

$$\int_{\Omega_{\text{liq}} \cup \Omega_{\text{vap}}} \varrho \left(\varepsilon + \frac{1}{2} |\mathbf{v}|^2 \right) \, d v,$$

where $\varepsilon = \varepsilon(\mathbf{x}, t) \in \mathbb{R}$ denotes the **specific internal energy** and $\frac{1}{2} |\mathbf{v}|^2$ is the **specific kinetic energy**.

The first law of thermodynamics states that the total energy is conserved. That means the change in total energy equals the power of external forces acting on the material surface and on the interface, and the **heat flux** $\mathbf{q} = \mathbf{q}(\mathbf{x}, t) \in \mathbb{R}^d$ entering the volume through the material surface

$$\begin{aligned} \frac{d}{dt} \int_{\Omega_{\text{liq}} \cup \Omega_{\text{vap}}} \varrho \left(\varepsilon + \frac{1}{2} |\mathbf{v}|^2 \right) \, d v = & \int_{\partial\Omega_{\text{liq}} \cup \partial\Omega_{\text{vap}} \setminus \Gamma} \mathbf{q} \cdot \boldsymbol{\nu} - p \mathbf{v} \cdot \boldsymbol{\nu} \, d a \\ & + \int_{\Gamma} (d-1) \zeta^* \kappa s \, d a. \end{aligned} \quad (2.4)$$

Here, pressure, surface tension and heat flux contribute to the total energy. Recall that s is the speed of Γ in normal direction.

Balance of entropy. In general, the entropy is not conserved. The second law of thermodynamics states that the amount of **total entropy** $\int_{\Omega_{\text{liq}} \cup \Omega_{\text{vap}}} \varrho \eta \, dv$ increases with progressing time, where $\eta = \eta(\mathbf{x}, t) \in \mathbb{R}$ denotes the **specific entropy**. We introduce the function $\eta_{\Omega} = \eta_{\Omega}(\mathbf{x}, t) \geq 0$ to account for **local entropy production in the bulk** and $\eta_{\Gamma} = \eta_{\Gamma}(\boldsymbol{\gamma}, t) \geq 0$, $\boldsymbol{\gamma} \in \Gamma(t)$, $t \in [0, \theta]$, to account for **local entropy production on the phase boundary**. This allows formulating the balance equation

$$\frac{d}{dt} \int_{\Omega_{\text{liq}} \cup \Omega_{\text{vap}}} \varrho \eta \, dv = \int_{\partial\Omega_{\text{liq}} \cup \partial\Omega_{\text{vap}} \setminus \Gamma} \boldsymbol{\varphi} \cdot \boldsymbol{\nu} \, da + \int_{\Omega_{\text{liq}} \cup \Omega_{\text{vap}}} \eta_{\Omega} \, dv + \int_{\Gamma} \eta_{\Gamma} \, da. \quad (2.5)$$

Here the **entropy flux** is denoted by $\boldsymbol{\varphi} = \boldsymbol{\varphi}(\mathbf{x}, t) \in \mathbb{R}^d$.

Note that considering temperature dependent surface tension coefficients would require additional surface gradient terms in (2.3) and (2.4), cf. [43, 60]. The main part of this work addresses isothermal flows where constant ζ^* does not constitute a restriction. For the more general case, including multi-component fluids and interfacial mass, we refer to [60].

2.3 Isothermal two-phase thermodynamics

This section introduces functions, that relate one thermodynamic quantity to the other ones under isothermal conditions. Such a function for the pressure will explain the notation of phases. Furthermore, basic thermodynamic properties and relations shall be reviewed in this section. We refer to standard textbooks like [38, 59].

A thermodynamic process that takes place at constant temperature is called **isothermal**. It is assumed that heat flow balances thermal differences without any delay, such that the system remains in global thermal equilibrium. We assume that the **temperature** is constant or more precisely

$$T(\mathbf{x}, t) = T_{\text{ref}} \text{ for all } t \in [0, \theta], \mathbf{x} \in \Omega(t) \text{ and } T_{\text{ref}} > 0. \quad (2.6)$$

Functions, that relate a thermodynamic quantity like the pressure to the other ones, are called **equations of state**. The definition below introduces the thermodynamic framework for the isothermal context. It defines, in particular, equations of state and phases with respect to the specific volume, whereby the **specific volume** $\tau > 0$ is the reciprocal of the density.

Definition 2.2 (Isothermal equations of state).

Let the numbers $\tau_{\text{liq}}^{\min}, \tau_{\text{liq}}^{\max}, \tau_{\text{vap}}^{\min}, \tau_{\text{vap}}^{\max}, \zeta^{\min}, \zeta^{\max} \in \mathbb{R}$ with $0 < \tau_{\text{liq}}^{\min} < \tau_{\text{liq}}^{\max} < \tau_{\text{vap}}^{\min}, \zeta^{\min} < 0 < \zeta^{\max}$ and functions

$$p \in \mathcal{C}^2(\mathcal{A}_{\text{liq}} \cup \mathcal{A}_{\text{vap}}, \mathbb{R}), \quad \psi, \mu \in \mathcal{C}^3(\mathcal{A}_{\text{liq}} \cup \mathcal{A}_{\text{vap}}, \mathbb{R})$$

be given. The intervals $\mathcal{A}_{\text{liq}} = (\tau_{\text{liq}}^{\min}, \tau_{\text{liq}}^{\max})$ and $\mathcal{A}_{\text{vap}} = (\tau_{\text{vap}}^{\min}, \infty)$ define the **liquid phase** and the **vapor phase** and $\mathcal{A} := \mathcal{A}_{\text{liq}} \cup \mathcal{A}_{\text{vap}}$ is called **admissible set of specific volume values**.

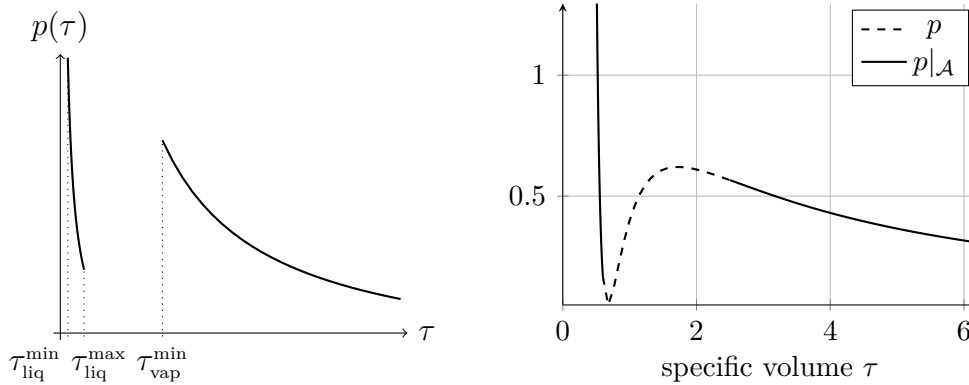


Figure 2.3: Left: prototypical example of a pressure function that fulfills Definition 2.2. Right: van der Waals pressure of Example 2.4 and the restriction to \mathcal{A} such that the conditions of Definition 2.2 are fulfilled.

The functions p , ψ , μ are called **pressure**, **specific Helmholtz free energy** and **specific Gibbs free energy**, respectively, if they satisfy

$$p(\tau) = -\psi'(\tau) \text{ and } \mu(\tau) = \psi(\tau) + p(\tau)\tau \quad (2.7)$$

and for any $\zeta \in \mathcal{Z} := (\zeta^{\min}, \zeta^{\max})$ the conditions

$$p' < 0 \text{ in } \mathcal{A}, \quad (2.8)$$

$$p'' > 0 \text{ in } \mathcal{A}, \quad (2.9)$$

$$\exists \tau_{\text{liq}}^{\text{sat}}(\zeta) \in \mathcal{A}_{\text{liq}}, \tau_{\text{vap}}^{\text{sat}}(\zeta) \in \mathcal{A}_{\text{vap}} : \begin{cases} p(\tau_{\text{vap}}^{\text{sat}}) - p(\tau_{\text{liq}}^{\text{sat}}) = \zeta, \\ \mu(\tau_{\text{vap}}^{\text{sat}}) - \mu(\tau_{\text{liq}}^{\text{sat}}) = 0, \end{cases} \quad (2.10)$$

$$p(\tau) \rightarrow \infty \text{ for } \tau \rightarrow \tau_{\text{liq}}^{\min}, \quad (2.11)$$

$$\forall \tau_{\text{liq}} \in \mathcal{A}_{\text{liq}}, \tau_{\text{vap}} \in \mathcal{A}_{\text{vap}} : p'(\tau_{\text{liq}}) < p'(\tau_{\text{vap}}), \quad (2.12)$$

$$\lim_{R \rightarrow \infty} \int_{\tau_{\text{vap}}^{\min}}^R c(\tau) d\tau = \infty \text{ with } c(\tau) := \sqrt{-p'(\tau)} \quad (2.13)$$

hold. The **sound speed** is given as $\tau c(\tau)$.

Note that p is monotone decreasing and convex in both phases, see Figure 2.3 (left) for some illustration. The interval $[\tau_{\text{liq}}^{\max}, \tau_{\text{vap}}^{\min}]$ is excluded from our studies. The number ζ is linked to surface tension and hypothesis (2.10) ensures that there is a **pair of saturation states** $(\tau_{\text{liq}}^{\text{sat}}(\zeta), \tau_{\text{vap}}^{\text{sat}}(\zeta)) \in \mathcal{A}_{\text{liq}} \times \mathcal{A}_{\text{vap}}$. These states are attained in the thermodynamic equilibrium, see Definition 2.5 below. The limitation of ζ to the interval $\mathcal{Z} = (\zeta^{\min}, \zeta^{\max})$ will be clarified in Remark 2.7 below.

Hypotheses (2.9), (2.11) and (2.12) limit the amount of different wave configurations of the solution to Riemann problems. In (2.11) it is assumed that there is a minimal molecular distance, where the liquid cannot be compressed further and (2.12) is natural, since the sound speed in the liquid phase of a fluid is usually much higher than in the vapor phase. Hypothesis (2.13) excludes the case of vacuum which is out of our interests.

A consequence of the hypotheses is the following lemma. It states that phase boundaries move slower than sound in the liquid phase. That means in terms of the pressure function,

that the slope of p in $\tau_{\text{liq}} \in \mathcal{A}_{\text{liq}}$ is steeper as the slope of the chord from $(\tau_{\text{liq}}, p(\tau_{\text{liq}}) + \zeta)$ to $(\tau_{\text{vap}}, p(\tau_{\text{vap}}))$, for any $\tau_{\text{vap}} \in \mathcal{A}_{\text{vap}}$.

Lemma 2.3 (Sound in the liquid travels faster than phase boundaries).

Let the pressure function $p : \mathcal{A}_{\text{liq}} \cup \mathcal{A}_{\text{vap}} \rightarrow \mathbb{R}$ of Definition 2.2 be given.

For all $\tau_{\text{liq}} \in \mathcal{A}_{\text{liq}}$ and $\tau_{\text{vap}} \in \mathcal{A}_{\text{vap}}$ it holds, that

$$p'(\tau_{\text{liq}}) < \frac{p(\tau_{\text{vap}}) - p(\tau_{\text{liq}}) - \zeta}{\tau_{\text{vap}} - \tau_{\text{liq}}}.$$

Proof. Consider first the case $\tau_{\text{liq}} = \tau_{\text{liq}}^{\text{sat}}$. Define

$$f(\tau) := p'(\tau_{\text{liq}}^{\text{max}})(\tau - \tau_{\text{liq}}^{\text{max}}) + p(\tau_{\text{liq}}^{\text{max}}) + \zeta - p(\tau).$$

Due to (2.8) and (2.10) $f(\tau_{\text{vap}}^{\text{min}}) < 0$ holds, and due to (2.12) $f'(\tau_{\text{vap}}^{\text{min}}) < 0$. With (2.9) it follows

$$\begin{aligned} p(\tau_{\text{vap}}) &> p(\tau_{\text{liq}}^{\text{max}}) + \zeta + p'(\tau_{\text{liq}}^{\text{max}})(\tau_{\text{vap}} - \tau_{\text{liq}}^{\text{max}}) \\ &= p(\tau_{\text{liq}}^{\text{max}}) + \zeta + p'(\tau_{\text{liq}}^{\text{max}})(\tau_{\text{liq}} - \tau_{\text{liq}}^{\text{max}}) + p'(\tau_{\text{liq}}^{\text{max}})(\tau_{\text{vap}} - \tau_{\text{liq}}) \\ &> p(\tau_{\text{liq}}) + \zeta + p'(\tau_{\text{liq}})(\tau_{\text{vap}} - \tau_{\text{liq}}) \end{aligned}$$

□

Equations of state have to be determined, e.g. by experimental measurements. However, for a simple model fluid, that may occur in a liquid and a vapor phase, we consider the following explicit form of an equation of state.

Example 2.4 (Van der Waals equation of state).

The *van der Waals equations of state* are given by the pressure function

$$p(\tau) = \frac{RT_{\text{ref}}}{\tau - \tau_{\text{liq}}^{\text{min}}} - \frac{a}{\tau^2}, \quad (2.14)$$

with positive constants $a, \tau_{\text{liq}}^{\text{min}}, R$ for $\tau > \tau_{\text{liq}}^{\text{min}}$ and corresponding specific Helmholtz and Gibbs free energy functions according to (2.7). Figure 2.4 shows the graph of p at different temperatures. The function is monotone decreasing above the **critical temperature** $T_c = 8a/(27R\tau_{\text{liq}}^{\text{min}})$. Below the critical temperature there are two decreasing parts which determine the phases. The increasing part in between is called **elliptic** or **spinodal region**. This region refers to **unstable thermodynamic states** and the sound speed, i.e. function c in (2.13), is not defined there.

The van der Waals equations of state are defined for all $\tau \in (\tau_{\text{liq}}^{\text{min}}, \infty)$. They fulfill the conditions of Definition 2.2 for temperature values below T_c . One has basically to constrain the admissible set \mathcal{A} to the convex parts of p , see Figure 2.3 (right) for an illustration. Thus, the spinodal region is a subset of the interval $[\tau_{\text{liq}}^{\text{max}}, \tau_{\text{vap}}^{\text{min}}]$, that is excluded from in Definition 2.2.

The parameters for the graphs in Figure 2.3, Figure 2.4 and Figure 2.5 are given by

$$a = 3, \quad \tau_{\text{liq}}^{\text{min}} = \frac{1}{3}, \quad R = \frac{8}{3} \quad \text{and} \quad T_{\text{ref}} = 0.85. \quad (2.15)$$

For this numbers, the critical temperature is $T_c = 1$.

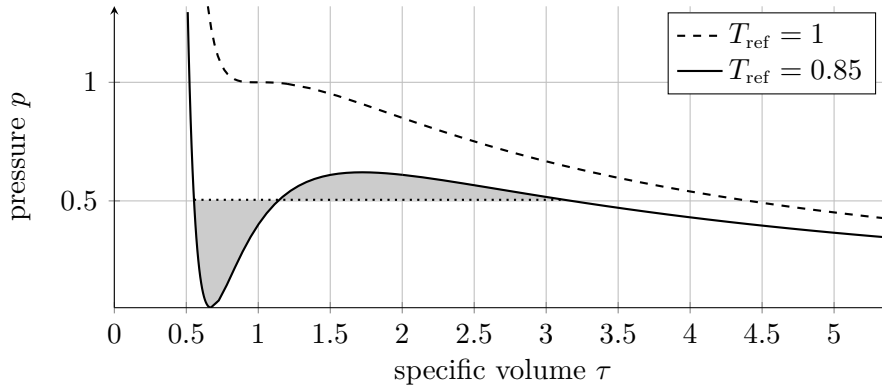


Figure 2.4: Van der Waals pressure (2.14) with parameters in (2.15) at the critical temperature $T_c = 1$ and below that temperature. The gray area refers to the Maxwell construction (2.19).

A particular solution of the balance laws of Section 2.2 is given by the global thermodynamic equilibrium. For that solution, fluid and phase boundary are at rest and thermodynamic quantities satisfy the conditions of the definition below. Furthermore, we distinguish between local and global equilibrium. The definition refers to the temperature dependent case, in order to complete the list of equilibrium conditions.

Definition 2.5 (Thermodynamic equilibrium).

Consider a point $\gamma \in \Gamma(t)$ on the sharp interface at time $t \in [0, \theta]$ and denote the trace values for temperature, pressure and specific Gibbs free energy with $T_{\text{liq/vap}}, p_{\text{liq/vap}}, \mu_{\text{liq/vap}}$. Denote the mean curvature (2.1) in that point with $\kappa = \kappa(\gamma, t) \in \mathbb{R}$ and the surface tension coefficient with $\zeta^* \geq 0$. The interface point γ is at time t in **local thermodynamic equilibrium**, if and only if

$$T_{\text{liq}} = T_{\text{vap}}, \quad p_{\text{vap}} - p_{\text{liq}} = (d-1)\zeta^* \kappa \quad \text{and} \quad \mu_{\text{liq}} = \mu_{\text{vap}} \quad (2.16)$$

holds.

The system at time t is said to be **globally in thermodynamic equilibrium** if and only if all thermodynamic quantities are constant in the bulk phases and (2.16) holds. The surface tension term is abbreviated with

$$\zeta := (d-1)\zeta^* \kappa \quad (2.17)$$

in systems with constant curvature everywhere on Γ .

The conditions can be interpreted as follows. Thermal differences between the phases are compensated by the heat flux, what leads to the first condition, the **thermal equilibrium**. Note that (2.6) is nothing but the assumption that the fluid is globally in thermal equilibrium. The second condition refers to a balance of mechanical forces and is therefore called **mechanical equilibrium**.

The first two conditions are valid also for material boundaries separating different substances, since temperature and mechanical forces can be balanced without matter flow. The third condition in (2.16) states that the phases are in equilibrium with respect to matter flow. The more general form of this condition, called **chemical equilibrium**, states that the chemical potential is equal in both phases. However, for single component

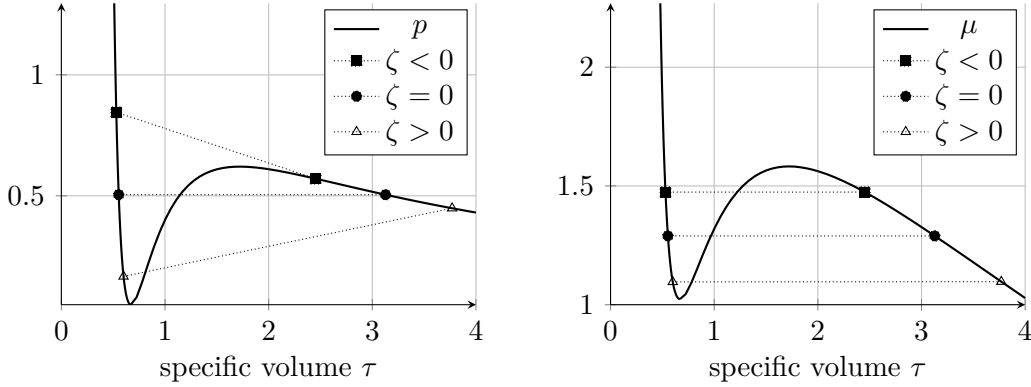


Figure 2.5: Van der Waals pressure (left) and Gibbs free energy (right). Pair of saturation states for a droplet ($\zeta < 0$), the planar case ($\zeta = 0$) and a bubble ($\zeta > 0$).

substances the chemical potential reduces to the Gibbs free energy. When the latter condition holds, no chemical reactions (excluded anyway) and no transitions between the phases take place.

Neglecting capillary forces ($\zeta^* = 0$) one finds the conditions of Definition 2.5 in [38]. The condition for mechanical equilibrium with surface tension is known as **Young-Laplace law**, cf. [23, 46].

Example 2.6 (Maxwell construction for the van der Waals equations of state).

Figure 2.4 provides a geometric interpretation of (2.16) for the van der Waals Example 2.4 with $\zeta^* = 0$. The condition for mechanical equilibrium reads

$$p(\tau_{\text{liq}}) = p(\tau_{\text{vap}}) =: p^{\text{sat}}, \quad (2.18)$$

where $\tau_{\text{liq}} \in \mathcal{A}_{\text{liq}}$ and $\tau_{\text{vap}} \in \mathcal{A}_{\text{vap}}$ and the condition for chemical equilibrium gives

$$\begin{aligned} 0 &= \mu(\tau_{\text{vap}}) - \mu(\tau_{\text{liq}}) = \psi(\tau_{\text{vap}}) - \psi(\tau_{\text{liq}}) + \tau_{\text{vap}} p(\tau_{\text{vap}}) - \tau_{\text{liq}} p(\tau_{\text{liq}}) \\ &= - \int_{\tau_{\text{liq}}}^{\tau_{\text{vap}}} p(\tau) \, d\tau + \tau_{\text{vap}} p(\tau_{\text{vap}}) - \tau_{\text{liq}} p(\tau_{\text{liq}}). \end{aligned} \quad (2.19)$$

Note that p in (2.14) is defined for all $\tau > \tau_{\text{liq}}^{\text{min}}$. Equation (2.19) states, that the signed area (gray shaded in Figure 2.4) between the chord joining $(\tau_{\text{liq}}, p(\tau_{\text{liq}}))$ to $(\tau_{\text{vap}}, p(\tau_{\text{vap}}))$ and the graph of $p|_{[\tau_{\text{liq}}, \tau_{\text{vap}}]}$ is zero. The solution of (2.18) and (2.19) is given by the pair of saturation states $\tau_{\text{liq}}^{\text{sat}}(0)$, $\tau_{\text{vap}}^{\text{sat}}(0)$.

A modification of p , where the pressure function between the saturation states is replaced by the constant saturation pressure p^{sat} (dotted line in Figure 2.4) is called **Maxwell construction** or **equal area rule**, cf. [38, 59]. The constant line portion of the modified pressure then corresponds to coexisting liquid vapor phases or **mixture states**. Such a modified equation of state is used in Chapter 4, however without the intention to introduce mixture states.

If capillary forces are regarded, then the pair of saturation states is determined by (2.10). Note that they depend on the surface tension term (2.17). Figure 2.5 shows equations of state and saturation states for a spherical droplet, the planar case and a

spherical bubble. Due to the definition of the mean curvature (2.1) the surface tension term $\zeta = (d-1)\zeta^*\kappa$ for droplets is negative. Apparently, the saturated specific volume values $\tau_{\text{liq}}^{\text{sat}}(\zeta)$ and $\tau_{\text{vap}}^{\text{sat}}(\zeta)$ are monotone increasing in terms of ζ and there are values of ζ where no solution of (2.10) exists. Furthermore, equations of state are usually fitted to measurements made without surface tension. That means, in particular, that for decreasing bubble or droplet radii the equation of state loses validity.

Remark 2.7 (Equations of state and surface tension).

Pairs of saturation states exist, provided that the absolute value of ζ is small enough. This applies to all equations of state considered in this work and Definition 2.2 is therefore restricted to a moderate amount of surface tension, i.e. $\zeta \in \mathcal{Z}$, in the sense that (2.10) has a solution.

Generally, vapor fluids attain pressure values below the saturation pressure and liquid fluids attain values above that pressure. But this is not always the case. Assume that a pair of saturation states $\tau_{\text{liq}}^{\text{sat}}, \tau_{\text{vap}}^{\text{sat}}$ is given. A liquid, that is expanded below the saturation pressure $p(\tau_{\text{liq}}^{\text{sat}})$ without phase transition is called metastable or superheated liquid. The same holds for the vapor: if it is compressed beyond the saturation pressure $p(\tau_{\text{vap}}^{\text{sat}})$ without phase transition, it is called metastable or supercooled vapor. The labels superheated and supercooled stem from the fact, that metastable states can be achieved also by heating up or cooling down the fluid.

A metastable liquid or vapor attains states in the *metastable region* $(\tau_{\text{liq}}^{\text{sat}}, \tau_{\text{liq}}^{\text{max}}) \cup (\tau_{\text{vap}}^{\text{min}}, \tau_{\text{vap}}^{\text{sat}})$. On the other hand, we call a state or region *stable* if it is not metastable. Note that we do not consider states in the spinodal region. This is excluded by Definition 2.2.

The van der Waals pressure (2.14) is composed for a model fluid consisting of particles with a non-zero volume and pairwise attractive inter-particle forces. Although parameters for (2.14) are available for many substances, they fit very poorly with measured data, in particular for $T \ll T_c$. Nowadays accurate thermodynamic properties are obtained from derivatives of a high order polynomial representation of the Helmholtz free energy. For instance, see [72] for water or [50] for n-dodecane. Such accurate equations of state are implemented in several tools.

For the numerical examples we will either use the van der Waals equation of state of Example 2.4 or we will rely on the open source library *CoolProp* [6] to access real fluid properties.

2.4 Isothermal free boundary formulation

We derive partial differential equations and jump conditions from the balance laws of mass (2.2) and total momentum (2.3). That merely requires the application of Reynolds transport theorem and the divergence theorem (cf. [32, 43, 60]). For the sake of simplicity we fix the domain Ω in time and exclude flow across its boundary. The resulting equations in the bulk are known as the isothermal Euler equations. At the phase boundary, we find inhomogeneous Rankine-Hugoniot conditions.

Definition 2.8 (Isothermal model).

Let equations of state as in Definition 2.2 be given. The function

$$\tilde{p} : \tilde{\mathcal{A}} \rightarrow \mathbb{R}_+, \quad \tilde{p}(\varrho) := p(1/\varrho)$$

is the **pressure function with respect to the fluid density** $\varrho = 1/\tau$ and $\tilde{\mathcal{A}} := \tilde{\mathcal{A}}_{\text{vap}} \cup \tilde{\mathcal{A}}_{\text{liq}}$, $\tilde{\mathcal{A}}_{\text{liq/vap}} := \{ \varrho > 0 \mid 1/\varrho \in \mathcal{A}_{\text{liq/vap}} \}$ are the corresponding admissible sets.

For any $t \in [0, \theta]$, $\theta > 0$, assume that the fixed domain $\Omega \subset \mathbb{R}^d$, $d \in \{1, 2, 3\}$ with smooth boundary, is partitioned into the union of two open sets $\Omega_{\text{vap}}(t)$, $\Omega_{\text{liq}}(t)$, which contain the two bulk phases, and the sharp interface $\Gamma(t)$, that separates the two spatial bulk sets.

In the spatial-temporal bulk set $\{ (\mathbf{x}, t) \in \mathbb{R}^d \times (0, \theta) \mid \mathbf{x} \in \Omega_{\text{vap}}(t) \cup \Omega_{\text{liq}}(t) \}$ the dynamics of the fluid are governed by the system

$$\begin{aligned} \varrho_t + \operatorname{div}(\varrho \mathbf{v}) &= 0, \\ (\varrho \mathbf{v})_t + \operatorname{div}(\varrho \mathbf{v} \otimes \mathbf{v} + \tilde{p}(\varrho) \mathbf{I}) &= \mathbf{0}. \end{aligned} \quad (2.20)$$

The unknown density field is denoted by $\varrho = \varrho(\mathbf{x}, t) > 0$ and the unknown velocity field by $\mathbf{v} = \mathbf{v}(\mathbf{x}, t) = (v_1(\mathbf{x}, t), \dots, v_d(\mathbf{x}, t))^T \in \mathbb{R}^d$. The d -dimensional unit matrix is denoted with $\mathbf{I} \in \mathbb{R}^{d \times d}$. For fixed initial position of the interface $\Gamma(0)$ and given initial density function ϱ_0 with $\varrho_0|_{\Omega_{\text{liq/vap}}} \in \tilde{\mathcal{A}}_{\text{liq/vap}}$ and given velocity field \mathbf{v}_0 , assume that

$$\varrho(\mathbf{x}, 0) = \varrho_0(\mathbf{x}), \quad \mathbf{v}(\mathbf{x}, 0) = \mathbf{v}_0(\mathbf{x}) \quad \text{for } \mathbf{x} \in \Omega_{\text{vap}}(0) \cup \Omega_{\text{liq}}(0), \quad (2.21)$$

while at the boundary

$$\mathbf{v} \cdot \boldsymbol{\nu} = \mathbf{0} \quad \text{on } \partial\Omega \quad (2.22)$$

holds for the outer normal vector $\boldsymbol{\nu}$ to $\partial\Omega$.

For $\boldsymbol{\gamma} \in \Gamma(t)$ denote the speed of $\Gamma(t)$ in the normal direction $\mathbf{n} = \mathbf{n}(\boldsymbol{\gamma}, t) \in \mathbb{S}^{d-1}$ by $s = s(\boldsymbol{\gamma}, t) \in \mathbb{R}$. The vector \mathbf{n} points into Ω_{vap} . Across the smooth interface the following $d+1$ trace conditions which represent the conservation of mass and the balance of momentum in presence of capillary surface forces are posed:

$$\llbracket \varrho(\mathbf{v} \cdot \mathbf{n} - s) \rrbracket = 0, \quad (2.23)$$

$$\llbracket \varrho(\mathbf{v} \cdot \mathbf{n} - s) \mathbf{v} \cdot \mathbf{n} + \tilde{p}(\varrho) \rrbracket = (d-1) \zeta^* \kappa, \quad (2.24)$$

$$\llbracket \mathbf{v} \cdot \mathbf{t}_l \rrbracket = 0 \quad (l = 1, \dots, d-1). \quad (2.25)$$

Here $\llbracket a \rrbracket := a_{\text{vap}} - a_{\text{liq}}$ and $a_{\text{vap/liq}} := \lim_{\varepsilon \rightarrow 0, \varepsilon > 0} a(\boldsymbol{\gamma} \pm \varepsilon \mathbf{n})$ for some quantity a defined in $\Omega_{\text{vap}}(t) \cup \Omega_{\text{liq}}(t)$. The mean curvature $\kappa = \kappa(\boldsymbol{\gamma}, t) \in \mathbb{R}$ of $\Gamma(t)$ in (2.24) is given by (2.1). The constant surface tension coefficient is $\zeta^* \geq 0$, and $\mathbf{t}_1, \dots, \mathbf{t}_{d-1} \in \mathbb{S}^{d-1}$ are a complete set of tangential vectors. The **mass flux** from the liquid phase to the vapor phase is given by

$$j := \varrho_{\text{liq}}(\mathbf{v}_{\text{liq}} \cdot \mathbf{n} - s) = \varrho_{\text{vap}}(\mathbf{v}_{\text{vap}} \cdot \mathbf{n} - s). \quad (2.26)$$

Let us point out that for what follows a tilde on functions like \tilde{p} or sets like $\tilde{\mathcal{A}}_{\text{liq}}$, $\tilde{\mathcal{A}}_{\text{vap}}$ indicates dependence on ϱ while the same symbol without tilde has to be understood to depend on τ .

The system (2.20) can be written for $\tilde{\mathbf{U}} = (\varrho, \varrho v_1, \dots, \varrho v_d)^T$ in the conservation form

$$\tilde{\mathbf{U}}_t + \mathbf{f}^1(\tilde{\mathbf{U}})_{x_1} + \dots + \mathbf{f}^d(\tilde{\mathbf{U}})_{x_d} = \mathbf{0},$$

with appropriately defined fluxes $\mathbf{f}^1, \dots, \mathbf{f}^d$. For $\tilde{\mathbf{U}} \in \tilde{\mathcal{A}}_{\text{vap}} \cup \tilde{\mathcal{A}}_{\text{liq}} \times \mathbb{R}^d$ and $\boldsymbol{\omega} \in \mathbb{S}^{d-1}$ the eigenvalues of the Jacobian of the $\boldsymbol{\omega}$ -directional flux $\omega_1 \mathbf{f}^1(\tilde{\mathbf{U}}) + \dots + \omega_d \mathbf{f}^d(\tilde{\mathbf{U}})$ are then given by

$$\begin{aligned}\tilde{\lambda}_1(\tilde{\mathbf{U}}; \boldsymbol{\omega}) &= \mathbf{v} \cdot \boldsymbol{\omega} - \sqrt{\tilde{p}'(\varrho)} = \mathbf{v} \cdot \boldsymbol{\omega} - \tau c(\tau), \\ \tilde{\lambda}_2(\tilde{\mathbf{U}}; \boldsymbol{\omega}) &= \dots = \lambda_d(\tilde{\mathbf{U}}; \boldsymbol{\omega}) = \mathbf{v} \cdot \boldsymbol{\omega}, \\ \tilde{\lambda}_{d+1}(\tilde{\mathbf{U}}; \boldsymbol{\omega}) &= \mathbf{v} \cdot \boldsymbol{\omega} + \sqrt{\tilde{p}'(\varrho)} = \mathbf{v} \cdot \boldsymbol{\omega} + \tau c(\tau).\end{aligned}\tag{2.27}$$

Example 2.9 (Isothermal model with van der Waals pressure).

The pressure function of Example 2.4 is composed of two decreasing parts and one increasing part in between. The sound speed in the increasing part becomes imaginary. Thus, the isothermal model of Definition 2.8, equipped with that equation of state, is not a hyperbolic system of partial differential equations. It is said to be of *mixed hyperbolic-elliptic type*, see [47].

Recall that $\tau c(\tau) = \sqrt{\tilde{p}'(\varrho)}$ is the speed of sound with c in (2.13). As a consequence of Definition 2.2, $\tilde{\mathbf{U}} \in (\tilde{\mathcal{A}}_{\text{liq}} \cup \tilde{\mathcal{A}}_{\text{vap}}) \times \mathbb{R}^d$ is a necessary (and in fact sufficient) criterion for (2.20) to be hyperbolic. We search for functions $\tilde{\mathbf{U}} = \tilde{\mathbf{U}}(\mathbf{x}, t)$ which are weak solutions with $\varrho(\mathbf{x}, t) \in \tilde{\mathcal{A}}_{\text{liq/vap}}$ for almost all $(\mathbf{x}, t) \in \Omega_{\text{liq/vap}}(t) \times [0, \theta]$ and satisfy an entropy condition.

The appropriate mathematical entropy condition is derived from the balance law for energy (2.4) and entropy (2.5) using $\boldsymbol{\varphi} T = \mathbf{q}$. The condition is a consequence of the thermodynamic entropy principle (see [60, Section 1.3.2]) and is often tacitly adopted [23, 43, 70]. We multiply (2.5) with the constant temperature T_{ref} and subtract the result from (2.4). With the thermodynamic relation $\psi = \varepsilon - T \eta$ we find the balance law

$$\begin{aligned}\frac{d}{dt} \int_{\Omega_{\text{liq}} \cup \Omega_{\text{vap}}} \varrho \left(\psi + \frac{1}{2} |\mathbf{v}|^2 \right) dv &= \int_{\partial \Omega_{\text{liq}} \cup \partial \Omega_{\text{vap}} \setminus \Gamma} -p \mathbf{v} \cdot \boldsymbol{\nu} da \\ &+ \int_{\Gamma} (d-1) \zeta^* \kappa s da - \int_{\Omega_{\text{liq}} \cup \Omega_{\text{vap}}} T_{\text{ref}} \eta_{\Omega} dv - \int_{\Gamma} T_{\text{ref}} \eta_{\Gamma} da\end{aligned}\tag{2.28}$$

for any domain Ω . Let us introduce

$$E(\varrho, \mathbf{m}) := \varrho \psi(\varrho^{-1}) + \frac{|\mathbf{m}|^2}{2\varrho}, \quad \text{with} \quad \mathbf{m} = \varrho \mathbf{v}$$

and recall that η_{Ω} and η_{Γ} are in general unknown, but not negative. Applying Reynolds transport theorem and the divergence theorem lead to

$$(E(\varrho, \mathbf{m}))_t + \text{div}((E(\varrho, \mathbf{m}) + \tilde{p}(\varrho)) \mathbf{v}) \leq 0\tag{2.29}$$

in the bulk phases and

$$-s [[E(\varrho, \mathbf{m}) - (d-1) \zeta^* \kappa]] + [(E(\varrho, \mathbf{m}) + \tilde{p}(\varrho)) \mathbf{v} \cdot \mathbf{n}] \leq 0\tag{2.30}$$

at the interface. It is straightforward to check that E is convex for $(\varrho, \mathbf{m}) \in (\tilde{\mathcal{A}}_{\text{liq}} \cup \tilde{\mathcal{A}}_{\text{vap}}) \times \mathbb{R}^d$ and thus it is a *mathematical entropy* for (2.20), cf. [20]. We search for weak solutions,

that satisfy (2.29) in the distributional sense in the single bulk regions and (2.30) at the interface. We call weak solutions of that type *entropy solutions*.

Entropy inequality (2.30) takes the surface tension into account. Capillary forces are neglected in the bulk phases and (entropy admissible) shock waves in the bulk satisfy (2.30) with $\zeta^* = 0$.

Remark 2.10 (Lack of well-posedness of mixed hyperbolic-elliptic problems).

The free boundary value problem is non-standard due to the non-homogeneous Rankine-Hugoniot condition. Moreover and more fundamentally, a well-posed solution can only be expected if a stronger entropy condition is enforced. Inequalities (2.29) and (2.30) are not sufficient in order to single out a unique entropy solution. As in mixed hyperbolic-elliptic problems, the reason is the non-convexity (globally) of the pressure function, see [1, 47, 70].

Although formally the elliptic region is removed from (2.20) by the specification of the equations of state (see Definition 2.2), we say that the model is of mixed hyperbolic-elliptic type, since the same difficulties arise. In Chapter 4, we overcome the lack of well-posedness with an extended Lax shock criterion. Chapter 5 states an algebraic condition that also leads to unique entropy solutions. This algebraic condition is related to a constitutive condition for η_Γ . In Chapter 6, we discuss such constitutive conditions.

Chapter 3

Front tracking with micro-scale models

The isothermal model of Definition 2.8 has the form of a free boundary problem. Free boundary problems are particularly challenging for the numerical discretization. We present here a novel approach for its efficient multidimensional numerical simulation. The first section introduces a front tracking method in order to guarantee, that the phase boundary remains sharp. The main topic of this section is the coupling of the equations in the bulk phases with Riemann problems at the interface.

The Riemann problems have initial states in different phases and are specified in Section 3.2. Furthermore, mappings are introduced, that serve as interfaces for solvers to Riemann problems. We will, in particular, refer to such mappings as microsolvers. Self-similar solutions of the two-phase Riemann problems are composed of shock and rarefaction waves. These waves are introduced in Section 3.3.

3.1 The front tracking approach

The Euler equations in the bulk phases are considered as the *macro-scale model*. To solve the macro-scale model we propose to use common CFD¹ solvers like finite volume or discontinuous Galerkin schemes. In the following we call numerical schemes for the macro-scale model *bulk solvers*. The effect of the trace conditions (2.23) and in particular the Young-Laplace equation (2.24) enters via a kind of *micro-scale model* which will be a generalized Riemann problem with non-homogeneous jump conditions.

For the curvature-free case and using a completely different mass transfer via the interface this approach has been introduced in [24, 28, 58]. It relies on ghost fluid ideas tracking back to [31].

Including surface energy necessitates two features to be incorporated in the numerical scheme: the first is the evaluation of the local curvature of the interface, the second is the application of the surface force on the flow. In the literature, a common way to do the latter is to replace the surface force by a distribution of a volume source term, e.g. the continuum surface force method of Brackbill and Kothe [9]. In the present study, the

¹Computational fluid dynamics

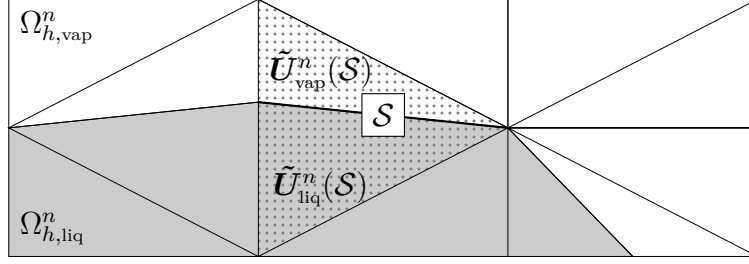


Figure 3.1: Mesh configuration and discrete solution associated with face $\mathcal{S} \in \Gamma_h^n$.

effect of surface tension is entirely handled on the micro-scale (see Section 3.2). This way, the surface tension force is exerted on the macro-scale through the fluxes at the phase boundary. Inversely, it is necessary to provide the micro-scale with information on the mean curvature.

We describe the basic elements of the front tracking scheme, based on a finite volume method for convenience. Assume that a triangulation for Ω with mesh size parameter $h > 0$ is given. For the n -th discrete time step $t = t^n \in (0, T)$ let us denote by Γ_h^n an approximation of $\Gamma(t^n)$ that will be referred to as the **computational interface**. In the sample case it is supposed to consist of a family of mesh faces such that it separates uniquely two sets of elements $\Omega_{h,vap}^n, \Omega_{h,liq}^n \subset \Omega$. As in the continuous setting these sets are disjoint, associated with the discrete bulk phases, and supposed to satisfy $\bar{\Omega} = \bar{\Omega}_{h,vap}^n \cup \bar{\Omega}_{h,liq}^n$, see Figure 3.1 for illustration. For each element in $\Omega_{h,vap}^n$ ($\Omega_{h,liq}^n$) the discrete solution \tilde{U}_{vap}^n (\tilde{U}_{liq}^n) is given by a constant state vector such that the density component is in the vapor phase (liquid phase). We summarize our algorithm to advance to the next time level as follows.

Algorithm 3.1 (Concept of the front tracking scheme).

Step 1: curvature reconstruction. For each face $\mathcal{S} \in \Gamma_h^n$ an approximate local mean curvature value $\kappa_h(\mathcal{S})$ is computed.

Step 2: micro-scale solution. For the numerical flux computation associated with some face $\mathcal{S} \in \Gamma_h^n$ (see Step 3 below) a Riemann problem is solved. The initial states of the Riemann problem are provided by values of the approximate solution $\tilde{U}_{liq}^n(\mathcal{S})$ in the associated element in $\Omega_{h,liq}^n$ and $\tilde{U}_{vap}^n(\mathcal{S})$ in the associated element in $\Omega_{h,vap}^n$, cf. Figure 3.1. The Riemann solver takes into account the local curvature $\kappa_h(\mathcal{S})$ from Step 1. The Riemann solution contains a phase boundary connecting two states $\tilde{U}_{liq}(\mathcal{S}) \in \tilde{\mathcal{A}}_{liq}^d \times \mathbb{R}^d$, $\tilde{U}_{vap}(\mathcal{S}) \in \tilde{\mathcal{A}}_{vap}^d \times \mathbb{R}^d$ and is moving with local speed $s(\mathcal{S})$.

Step 3: macro-scale solution. An explicit (finite volume) scheme is used to advance the density and velocity field in $\Omega_{h,vap}^n$ and $\Omega_{h,liq}^n$ to the next time level t^{n+1} . For the numerical flux evaluation at the intersection of $\Omega_{h,vap}^n$ ($\Omega_{h,liq}^n$) and Γ_h^n the state $\tilde{U}_{vap}(\mathcal{S})$ ($\tilde{U}_{liq}(\mathcal{S})$) from Step 2 is used. The time step is controlled by a CFL-like condition.

Step 4: interface tracking. The local normal front speeds $s(\mathcal{S})$ calculated in Step 2 for any face $\mathcal{S} \in \Gamma_h^n$ is used to advance Γ_h^n to Γ_h^{n+1} . The new position of the computational interface Γ_h^{n+1} determines new sets $\Omega_{h,vap}^{n+1}$ and $\Omega_{h,liq}^{n+1}$ and the bulk flow field is extrapolated to the new geometry.

The key ingredient of the approach are Riemann solvers for initial states in different phases (Step 2). Solvers of that type – *microsolvers* – and the corresponding *micro solutions* will be introduced in Chapter 4, Chapter 5 and Chapter 7. The underlying micro-scale models are derived in the next subsection.

Step 1 and Step 4 are related to the transport of the interface and the transfer of information between scales. These tasks are challenging, especially for the case of two or three-dimensional flows. For instance an additional level set equations has to be solved to track the interface in Step 4, cf. [64]. The discrete curvature κ_h in Step 1 is then obtained from level-set function via (2.1).

Remark 3.2 (Classification of the front tracking scheme).

Let us mention that the front tracking concept provides a versatile approach, since any kind of microsolver can be applied in Step 2. Also, phase field models or even molecular dynamic models can be used to compute the dynamics of the phase boundary in Step 2. In this context, Algorithm 3.1 can be naturally interpreted as a heterogeneous multiscale method in the spirit of e.g. [74]. The labels micro-scale and macro-scale stem from this point of view. On the other hand, using Riemann problems in Step 2 to determine the numerical fluxes between the grid cells, Algorithm 3.1 belongs to the class of Godunov-type schemes (on moving meshes).

We introduce in Chapter 8 a moving mesh finite volume method for radially symmetric solutions in order to study the approach. In this way it is possible to take into account capillarity effects without requiring a complex computation of the curvature. A successful multidimensional application is shown in Section 10.5.

Note that Algorithm 3.1 is not limited to isothermal flows, Chapter 10 introduces microsolvers for the full Euler system. Furthermore, the front tracking concept is expandable to higher order schemes. Then, the Riemann solver must be activated for several integration points on the faces and for several Runge-Kutta steps used to achieve the same order in time. For discontinuous Galerkin variants of our approach we refer to [27, 29, 30, 40].

3.2 Micro-scale models and microsolver interfaces

The section is organized as follows. In Subsection 3.2.1, we will transfer the discrete macro-scale data of the front tracking scheme to initial data of a planar two-phase Riemann problem. Then, a one-dimensional version of the Riemann problem specifies the micro-scale model in Subsection 3.2.2. In order to determine self-similar solutions of the micro-scale model it will be convenient to use Lagrangian coordinates. Subsection 3.2.3 introduces the corresponding micro-scale model.

3.2.1 Planar two-phase Riemann problems

Algorithm 3.1 provides for any time step t^n and any face \mathcal{S} of the computational interface states as input data for a (formally) planar Riemann problem. In Step 2 these states are $\tilde{\mathbf{U}}_{\text{Liq}}^n(\mathcal{S}) \in \tilde{\mathcal{A}}_{\text{liq}} \times \mathbb{R}^d$, $\tilde{\mathbf{U}}_{\text{vap}}^n(\mathcal{S}) \in \tilde{\mathcal{A}}_{\text{vap}} \times \mathbb{R}^d$ and an associated (constant) curvature value $\kappa_h(\mathcal{S}) \in \mathbb{R}$ from Step 1. Let furthermore the normal $\mathbf{n} \in \mathbb{S}^{d-1}$, a full set of tangential

vectors $\mathbf{t}_1, \dots, \mathbf{t}_{d-1} \in \mathbb{S}^{d-1}$ and the center (or a quadrature point) $\boldsymbol{\gamma}$ of the face \mathcal{S} be given. The normal direction is such that the liquid is always on the left hand side and the vapor on the right hand side.

Aforementioned numbers are the input arguments for the microsolver. In particular, the constant states $(\varrho_L, \mathbf{v}_L)^\top := \tilde{\mathbf{U}}_{\text{liq}}^n(\mathcal{S})$ and $(\varrho_R, \mathbf{v}_R)^\top := \tilde{\mathbf{U}}_{\text{vap}}^n(\mathcal{S})$ are employed for the initial datum. The microsolver gives back a phase boundary wave (i.e., states $\tilde{\mathbf{U}}_{\text{liq}} \in \mathcal{A}_{\text{liq}} \times \mathbb{R}^d$, $\tilde{\mathbf{U}}_{\text{vap}} \in \mathcal{A}_{\text{vap}} \times \mathbb{R}^d$ and speed $s \in \mathbb{R}$) that appears uniquely in the solution of the Riemann problem.

The Riemann problem under consideration is then

$$\begin{pmatrix} \varrho \\ \varrho v \\ \varrho \mathbf{u} \end{pmatrix}_t + \begin{pmatrix} \varrho v \\ \varrho v^2 + \tilde{p}(\varrho) \\ \varrho v \mathbf{u} \end{pmatrix}_x = \begin{pmatrix} 0 \\ 0 \\ \mathbf{0} \end{pmatrix},$$

for $x := (\mathbf{x} - \boldsymbol{\gamma}) \cdot \mathbf{n}$, $v := \mathbf{v} \cdot \mathbf{n}$ and $\mathbf{u} := (\mathbf{v} \cdot \mathbf{t}_1, \dots, \mathbf{v} \cdot \mathbf{t}_{d-1})^\top$ combined with the interface conditions (2.23), (2.24) and (2.25). It is subject to the initial condition

$$\begin{pmatrix} \varrho \\ v \\ \mathbf{u} \end{pmatrix}(x, 0) = \begin{cases} \left(\varrho_L, \mathbf{v}_L \cdot \mathbf{n}, \mathbf{v}_L \cdot \mathbf{t}_1, \dots, \mathbf{v}_L \cdot \mathbf{t}_{d-1} \right)^\top & \text{for } x \leq 0, \\ \left(\varrho_R, \mathbf{v}_R \cdot \mathbf{n}, \mathbf{v}_R \cdot \mathbf{t}_1, \dots, \mathbf{v}_R \cdot \mathbf{t}_{d-1} \right)^\top & \text{for } x > 0. \end{cases} \quad (3.1)$$

The corresponding solution for a single phase Riemann problem consists of at most $d + 1$ waves: a rarefaction or shock wave followed by a contact discontinuity of multiplicity $d - 1$ and again a rarefaction or shock wave. The waves are separated by constant states. Exact Riemann solvers of this type can be found in, for instance, [32].

With initial states in different phases, we expect in addition a phase boundary. So we seek for self-similar functions that match the following structure: one standard elementary wave (admissible shock wave, rarefaction wave or attached rarefaction-shock wave) in the liquid phase starting from the left state in (3.1), an intermediate phase boundary and intermediate contact discontinuities, and one standard elementary wave in the vapor phase connecting to the right state. Due to the non-convex shape of the pressure function the phase boundary appears naturally as an additional discontinuous wave in the solution of the Riemann problem, see [57].

There are three intermediate states, either connected by the phase boundary or a contact wave. Due to the linear degenerate field $\lambda_2 = \dots = \lambda_d = v$ in (2.27) only tangential velocities are discontinuous across the multiple contact wave. Figure 3.2 illustrates that fact for one possible configuration of bulk waves. The phase boundary connects adjacent states $(\varrho_{\text{liq}}, v_{\text{liq}}, \mathbf{u}_R)$ and $(\varrho_{\text{vap}}, v_{\text{vap}}, \mathbf{u}_R)$. The order of the waves may change but it suffices to consider a one-dimensional situation instead of the planar one, since values of the tangential velocities are a priori known.

3.2.2 Micro-scale model in Eulerian coordinates

We have seen in the last subsection, that density and normal momentum are decoupled and can be reduced to the one-dimensional problem. In the next chapters we will introduce exact and approximate solutions for that reduced system. From the technical viewpoint the upshot of these chapters will be mappings called microsolvors which map the initial

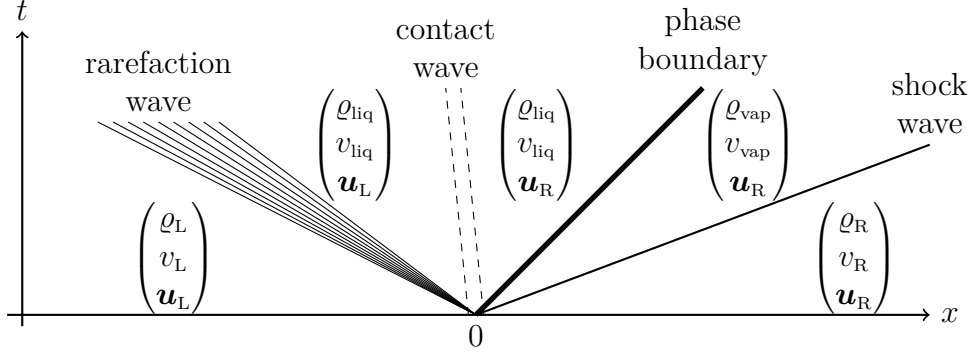


Figure 3.2: Typical wave structure for the two-phase Riemann solution.

conditions and a constant surface tension term $\zeta := (d-1)\zeta^* \kappa_h \in \mathcal{Z}$ to the states at the phase boundary of the solution.

Definition 3.3 (Micro-scale model and microsolver in Eulerian coordinates).

Let $\gamma = \gamma(t) \in \mathbb{R}$ be the position of the phase boundary at time $t \in [0, \theta]$ and $s(t) = \gamma_t(t) \in \mathbb{R}$ be the speed of γ . The bulk set is given by $\{(x, t) \in \mathbb{R} \times (0, \theta) \mid x \neq \gamma(t)\}$. The density and velocity fields $\varrho = \varrho(x, t) > 0$ and $v = v(x, t) \in \mathbb{R}$ satisfy

$$\begin{aligned} \begin{pmatrix} \varrho \\ \varrho v \end{pmatrix}_t + \begin{pmatrix} \varrho v \\ \varrho v^2 + \tilde{p}(\varrho) \end{pmatrix}_x = \begin{pmatrix} 0 \\ 0 \end{pmatrix}, \quad \begin{aligned} \llbracket \varrho(v-s) \rrbracket &= 0, \\ \llbracket \varrho(v-s)v + \tilde{p}(\varrho) \rrbracket &= \zeta \end{aligned} \end{aligned} \quad (3.2)$$

in the bulk set and at the phase boundary, respectively, and for the constant surface tension term $\zeta \in \mathcal{Z}$. System (3.2) is subject to the initial condition

$$\begin{pmatrix} \varrho \\ v \end{pmatrix}(x, 0) = \begin{cases} \begin{pmatrix} \varrho_L, v_L \end{pmatrix}^\top & \text{for } x \leq 0, \\ \begin{pmatrix} \varrho_R, v_R \end{pmatrix}^\top & \text{for } x > 0. \end{cases} \quad (3.3)$$

The *microsolver* is a mapping of type

$$\tilde{\mathcal{M}} : \begin{cases} \tilde{\mathcal{A}}_{\text{liq}} \times \mathbb{R} \times \tilde{\mathcal{A}}_{\text{vap}} \times \mathbb{R} \times \mathcal{Z} & \rightarrow \tilde{\mathcal{A}}_{\text{liq}} \times \mathbb{R} \times \tilde{\mathcal{A}}_{\text{vap}} \times \mathbb{R} \times \mathbb{R} \\ (\varrho_L, v_L, \varrho_R, v_R, \zeta) & \mapsto (\varrho_{\text{liq}}, v_{\text{liq}}, \varrho_{\text{vap}}, v_{\text{vap}}, s), \end{cases} \quad (3.4)$$

which maps the initial conditions (3.3) and the surface tension term ζ to the trace values

$$\begin{pmatrix} \varrho_{\text{liq}} \\ v_{\text{liq}} \end{pmatrix} = \lim_{\substack{x/t \rightarrow s \\ x/t < s}} \begin{pmatrix} \varrho \\ v \end{pmatrix}(x/t, 1), \quad \begin{pmatrix} \varrho_{\text{vap}} \\ v_{\text{vap}} \end{pmatrix} = \lim_{\substack{x/t \rightarrow s \\ x/t > s}} \begin{pmatrix} \varrho \\ v \end{pmatrix}(x/t, 1)$$

of a self-similar solution to (3.2) with exactly one phase boundary and its speed.

Note that the linear degenerate field dropped out (cf. Figure 3.3 and Figure 3.2), since the eigenvalues of the Jacobian of the flux $(\varrho v, \varrho v^2 + \tilde{p}(\varrho))^\top$ are $v \mp \sqrt{\tilde{p}'(\varrho)}$.

Definition 3.4 (Entropy solution of the micro-scale model in Eulerian coordinates).

Let $\varrho = \varrho(x, t) > 0$, $v = v(x, t) \in \mathbb{R}$ be a weak solution of the micro-scale model in Definition 3.3 for some given surface tension term $\zeta \in \mathcal{Z}$.

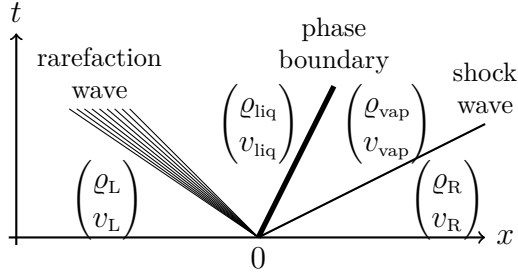


Figure 3.3: Typical wave structure for the two-phase Riemann solution for $d = 1$ with three waves. It consists of a rarefaction wave followed by the phase boundary, and a shock wave.

The solution is called **entropy solution** if it satisfies (2.29) for $d = 1$ in the distributional sense in the bulk set and

$$-s \llbracket E(\varrho, m) - \zeta \rrbracket + \llbracket (E(\varrho, m) + \tilde{p}(\varrho)) v \rrbracket \leq 0 \quad (3.5)$$

at the interface, with $E(\varrho, m) = \varrho \psi(\varrho^{-1}) + \frac{m^2}{2\varrho}$ and $m = \varrho v$.

The trace states \tilde{U}_{liq}^n , \tilde{U}_{vap}^n for Step 3 in Algorithm 3.1 are given via the initial conditions (3.1) and the solution of the microsolver $\tilde{\mathcal{M}}(\varrho_L^n, \mathbf{v}_L^n \cdot \mathbf{n}, \varrho_R^n, \mathbf{v}_R^n \cdot \mathbf{n}, (d-1)\zeta^* \kappa_h) = (\varrho_{\text{liq}}, v_{\text{liq}}, \varrho_{\text{vap}}, v_{\text{vap}}, s)$ as

$$\tilde{U}_{\text{liq}}^n = \begin{cases} \varrho_{\text{liq}} \left(1, v_{\text{liq}}, \mathbf{v}_L^n \cdot \mathbf{t}_1, \dots, \mathbf{v}_L^n \cdot \mathbf{t}_{d-1} \right)^\top & \text{for } j \leq 0, \\ \varrho_{\text{liq}} \left(1, v_{\text{liq}}, \mathbf{v}_R^n \cdot \mathbf{t}_1, \dots, \mathbf{v}_R^n \cdot \mathbf{t}_{d-1} \right)^\top & \text{for } j > 0, \end{cases}$$

$$\tilde{U}_{\text{vap}}^n = \begin{cases} \varrho_{\text{vap}} \left(1, v_{\text{vap}}, \mathbf{v}_L^n \cdot \mathbf{t}_1, \dots, \mathbf{v}_L^n \cdot \mathbf{t}_{d-1} \right)^\top & \text{for } j \leq 0, \\ \varrho_{\text{vap}} \left(1, v_{\text{vap}}, \mathbf{v}_R^n \cdot \mathbf{t}_1, \dots, \mathbf{v}_R^n \cdot \mathbf{t}_{d-1} \right)^\top & \text{for } j > 0, \end{cases}$$

where j is the mass flux (2.26). Note that $j > 0$ refers to the wave order depicted in Figure 3.2, while $j \leq 0$ refers to the situation, where the phase boundary propagates slower than the contact wave.

3.2.3 Micro-scale model in Lagrangian coordinates

It will be convenient to compute the solution of the micro-scale model using Lagrangian coordinates, naming Lagrangian coordinates by (ξ, t) .

Definition 3.5 (Micro-scale model and microsolver in Lagrangian coordinates).
The specific volume and velocity fields $\tau = \tau(\xi, t) > 0$ and $v = v(\xi, t) \in \mathbb{R}$ satisfy

$$\begin{pmatrix} \tau \\ v \end{pmatrix}_t + \begin{pmatrix} -v \\ p(\tau) \end{pmatrix}_\xi = \begin{pmatrix} 0 \\ 0 \end{pmatrix} \quad (3.6)$$

in the bulk set. Here $p = p(\tau)$ is the pressure of Definition 2.2. Let $\mathbf{s}(t)$ be the speed of the phase boundary in Lagrangian coordinates and $\zeta \in \mathcal{Z}$ the constant surface tension term. Across the interface following trace conditions are

$$\mathbf{s} \llbracket \tau \rrbracket + \llbracket v \rrbracket = 0, \quad -\mathbf{s} \llbracket v \rrbracket + \llbracket p(\tau) \rrbracket = \zeta. \quad (3.7)$$

System (3.6) is subject to the initial condition

$$\begin{pmatrix} \tau \\ v \end{pmatrix}(\xi, 0) = \begin{cases} (\tau_L, v_L)^\top & \text{for } \xi \leq 0, \\ (\tau_R, v_R)^\top & \text{for } \xi > 0. \end{cases} \quad (3.8)$$

The **microsolver** is a mapping of type

$$\mathcal{M} : \begin{cases} \mathcal{A}_{\text{liq}} \times \mathbb{R} \times \mathcal{A}_{\text{vap}} \times \mathbb{R} \times \mathcal{Z} & \rightarrow \mathcal{A}_{\text{liq}} \times \mathbb{R} \times \mathcal{A}_{\text{vap}} \times \mathbb{R} \times \mathbb{R} \\ (\tau_L, v_L, \tau_R, v_R, \zeta) & \mapsto (\tau_{\text{liq}}, v_{\text{liq}}, \tau_{\text{vap}}, v_{\text{vap}}, \mathfrak{s}) \end{cases} \quad (3.9)$$

which maps the initial conditions (3.8) and the surface tension term ζ to the interface states of a self-similar solution of (3.6) with exactly one phase boundary satisfying (3.7) and its speed.

A proof for the transformation from the isothermal Euler system to the p-system (3.6) can be found in [32, Section 1. Definitions and examples]. Note that we call both (3.9) and (3.4) microsolver. It will be clear from the context which one is meant. Furthermore, we use different symbols.

System (3.6) can be written for $\mathbf{U} = (\tau, v)^\top$ in conservation form $\mathbf{U}_t + \mathbf{f}(\mathbf{U})_x = 0$ with $\mathbf{f} = (-v, p(\tau))^\top$. The eigenvalues of \mathbf{f} are

$$\lambda_1(\tau) = -c(\tau), \quad \lambda_2(\tau) = c(\tau). \quad (3.10)$$

Using Lagrangian coordinates, we refer to $c = c(\tau)$ as the **sound speed**. The Eulerian speed of the phase boundary transforms with

$$\mathfrak{s} = \varrho_{\text{liq}}(s - v_{\text{liq}}) = \varrho_{\text{vap}}(s - v_{\text{vap}})$$

to the Lagrangian speed. That corresponds to the mass flux (2.26) in Eulerian coordinates since $\mathfrak{s} = -j$. For further use, we transform also entropy inequality (3.5) to Lagrangian coordinates. We find $-\mathfrak{s} [\psi(\tau) + v^2/2] + [p(\tau)v] - s\zeta \leq 0$ or with (3.7)

$$-\mathfrak{s} ([\psi(\tau)] + [\tau] \{p(\tau)\} + \zeta \{\tau\}) \leq 0, \quad (3.11)$$

where $\{\tau\} := \frac{1}{2}(\tau_{\text{vap}} + \tau_{\text{liq}})$.

Definition 3.6 (Entropy solution of the micro-scale model in Lagrangian coordinates). *Let $\tau = \tau(\xi, t) > 0$, $v = v(\xi, t) \in \mathbb{R}$ be a weak solution of the micro-scale model in Definition 3.5 for some given surface tension term $\zeta \in \mathcal{Z}$.*

*The solution is called **entropy solution** if it satisfies $(\psi(\tau) + \frac{1}{2}v^2)_t + (p(\tau)v)_\xi \leq 0$ in the distributional sense in the bulk set and (3.11) at the interface.*

Note that we use one symbol ϱ for density in Lagrangian coordinates (ξ, t) , and in Eulerian coordinates (\mathbf{x}, t) , (x, t) . The same holds for specific volume and fluid velocity. This misuse of notation will not lead to ambiguity, since the following chapter will either refer to the micro-scale model in Eulerian coordinates or in Lagrangian coordinates. Furthermore, the microsolver (3.4) resp. (3.9) maps only constant numbers, independent of the underlying coordinate system. For state vectors we introduced both variants, $\tilde{\mathbf{U}} : (\mathbf{x}, t) \mapsto (\varrho, \mathbf{m})^\top$ for Eulerian coordinates in \mathbb{R}^d and $\mathbf{U} : (\xi, t) \mapsto (\tau, v)^\top$ for Lagrangian coordinates in one spatial dimension.

We close the subsection with a special solution of the micro-scale models: a traveling wave solution without mass transfer between the phases ($j = 0$). The solution in Lagrangian coordinates is static, since $\mathfrak{s} = j = 0$.

Lemma 3.7 (Thermodynamic equilibrium solution).

Consider the pair of saturation states $\tau_{\text{liq}}^{\text{sat}}, \tau_{\text{vap}}^{\text{sat}}$ as in Definition 2.2 for a fixed $\zeta \in \mathcal{Z}$ and initial conditions $\tau_{\text{L}} = \tau_{\text{liq}}^{\text{sat}}, \tau_{\text{R}} = \tau_{\text{vap}}^{\text{sat}}$ and $v_{\text{L}} = v_{\text{R}} = \hat{v}$ for arbitrary $\hat{v} \in \mathbb{R}$. Then

- $\mathcal{M}(\tau_{\text{liq}}^{\text{sat}}, \hat{v}, \tau_{\text{vap}}^{\text{sat}}, \hat{v}, \zeta) = (\tau_{\text{liq}}^{\text{sat}}, \hat{v}, \tau_{\text{vap}}^{\text{sat}}, \hat{v}, 0)$ holds and

$$\begin{pmatrix} \tau \\ v \end{pmatrix}(\xi, t) = \begin{cases} \left(\tau_{\text{liq}}^{\text{sat}}, \hat{v} \right)^{\top} & \text{for } \xi \leq 0, \\ \left(\tau_{\text{vap}}^{\text{sat}}, \hat{v} \right)^{\top} & \text{for } \xi > 0 \end{cases} \quad (3.12)$$

is an entropy solution as in Definition 3.6.

- $\tilde{\mathcal{M}}(\varrho_{\text{liq}}^{\text{sat}}, \hat{v}, \varrho_{\text{vap}}^{\text{sat}}, \hat{v}, \zeta) = (\varrho_{\text{liq}}^{\text{sat}}, \hat{v}, \varrho_{\text{vap}}^{\text{sat}}, \hat{v}, \hat{s})$ holds with $\hat{s} = \hat{v}$, $\varrho_{\text{liq}}^{\text{sat}} = 1/\tau_{\text{liq}}^{\text{sat}}$, $\varrho_{\text{vap}}^{\text{sat}} = 1/\tau_{\text{vap}}^{\text{sat}}$ and

$$\begin{pmatrix} \varrho \\ \varrho v \end{pmatrix}(x, t) = \begin{cases} \varrho_{\text{liq}}^{\text{sat}}(1, \hat{v})^{\top} & \text{for } x \leq \hat{s}t, \\ \varrho_{\text{vap}}^{\text{sat}}(1, \hat{v})^{\top} & \text{for } x > \hat{s}t \end{cases} \quad (3.13)$$

is an entropy solution as in Definition 3.4.

We call (3.12) and (3.13) **thermodynamic equilibrium solution**.

Proof. Obviously (3.12) satisfies (3.7) with $\mathfrak{s} = 0$ and (3.11) holds with an equal sign. Function (3.13) is just the transformation to Eulerian coordinates. \square

3.3 Elementary waves and phase transitions

We look for self-similar solutions of the two-phase Riemann problems, that consist of multiple waves separated by constant states. These waves are shock and rarefaction waves in the bulk phases as well as shock waves connecting states in different phases, called phase transitions. We distinguish subsonic, sonic and supersonic phase transitions. Our particular attention is focused on subsonic phase transitions. Here the entropy inequalities (2.29) and (2.30) are not sufficient to single out a unique solution. Chapter 4 and Chapter 6 will provide additional conditions. But let us first summarize all waves the solution may consist of. All formula refer to the micro-scale model in Lagrangian coordinates (Definition 3.5) and we refer to standard textbooks like [32, 51].

Rarefaction wave. A left state $\mathbf{U}_1 = (\tau_1, v_1)^{\top} \in \mathcal{A} \times \mathbb{R}$ and a right state $\mathbf{U}_r = (\tau_r, v_r)^{\top} \in \mathcal{A} \times \mathbb{R}$ of the same phase can be connected by a ***rarefaction wave*** ($i = 1, 2$) if

$$\mathbf{U}(\xi, t) = \begin{cases} \mathbf{U}_1 & \text{for } \xi < \lambda_i(\tau_1)t, \\ \bar{\mathbf{U}}(\xi/t) & \text{for } \lambda_i(\tau_1)t < \xi < \lambda_i(\tau_r)t, \\ \mathbf{U}_r & \text{for } \xi > \lambda_i(\tau_r)t > 0 \end{cases}$$

is a classical solution of system (3.6) for some function $\bar{\mathbf{U}} : \mathbb{R} \rightarrow \mathcal{A} \times \mathbb{R}$ (not further needed) and $\lambda_{1/2}$ in (3.10).

For the velocity of a 1-rarefaction holds $v_r = v_1 + R(\tau_1, \tau_r)$ and for a 2-rarefaction $v_r = v_1 - R(\tau_1, \tau_r)$ with

$$R(\tau_1, \tau_r) := \int_{\tau_1}^{\tau_r} \sqrt{-p'(\tau)} \, d\tau.$$

Due to (2.9) the 1-rarefaction wave fulfills $\tau_1 < \tau_r$ and the 2-rarefaction wave fulfills $\tau_1 > \tau_r$.

Discontinuous wave. A left state $\mathbf{U}_1 = (\tau_1, v_1)^\top \in \mathcal{A} \times \mathbb{R}$ and a right state $\mathbf{U}_r = (\tau_r, v_r)^\top \in \mathcal{A} \times \mathbb{R}$ can be connected by a **discontinuous wave** of speed $\mathfrak{s} \in \mathbb{R}$ if

$$\mathbf{U}(\xi, t) = \begin{cases} \mathbf{U}_1 & \text{for } \xi - \mathfrak{s}t \leq 0, \\ \mathbf{U}_r & \text{for } \xi - \mathfrak{s}t > 0 \end{cases} \quad (3.14)$$

is a weak solution of the micro-scale model in Definition 3.5.

Lax shock wave. A discontinuous wave of speed $\mathfrak{s} \in \mathbb{R}$ is called ***i*-Lax shock** if the **Lax entropy criterion**

$$\lambda_i(\tau_1) > \mathfrak{s} > \lambda_i(\tau_r) \quad (3.15)$$

holds.

We will use the term shock wave only for waves in the bulk, that means for τ_1 and τ_r in the same phase, and we consider only Lax shock waves. For bulk shock waves in the p-system (3.6) it is known that the Lax entropy criterion is equivalent to the entropy condition (3.11) with $\zeta \equiv 0$, since here the pressure is convex, see [32, Section I.7].

Due to the Rankine-Hugoniot conditions the propagation speeds for a *i*-Lax shock satisfy

$$\mathfrak{s}_1(\tau_1, \tau_r) = -\sqrt{-\frac{p(\tau_r) - p(\tau_1)}{\tau_r - \tau_1}}, \quad \mathfrak{s}_2(\tau_1, \tau_r) = \sqrt{-\frac{p(\tau_r) - p(\tau_1)}{\tau_r - \tau_1}}.$$

The pressure function of Definition 2.2 is such that the Lax entropy criterion is satisfied for 1-shock waves if $\tau_1 > \tau_r$ and for 2-shock wave if $\tau_1 < \tau_r$. A 1-Lax shock is illustrated in Figure 3.4 (left).

In case of a 1-shock wave there holds $v_r = v_1 + S(\tau_1, \tau_r)$ and in case of a 2-shock wave $v_r = v_1 - S(\tau_1, \tau_r)$, respectively with

$$S(\tau_1, \tau_r) = \text{sign}(\tau_r - \tau_1) \sqrt{-(\tau_r - \tau_1) (p(\tau_r) - p(\tau_1))}.$$

Elementary wave. For abbreviation let us introduce elementary waves. We combine a *i*-Lax shock with a *i*-rarefaction wave to a ***i*-elementary wave**. For its velocity holds

$$v_r = \begin{cases} v_1 + G(\tau_1, \tau_r) & \text{if } i = 1, \\ v_1 - G(\tau_1, \tau_r) & \text{if } i = 2 \end{cases} \quad \text{for} \quad G(\tau_1, \tau_r) = \begin{cases} R(\tau_1, \tau_r) & \text{if } i = 1 \text{ and } \tau_1 < \tau_r, \\ S(\tau_1, \tau_r) & \text{if } i = 1 \text{ and } \tau_1 > \tau_r, \\ R(\tau_1, \tau_r) & \text{if } i = 2 \text{ and } \tau_1 > \tau_r, \\ S(\tau_1, \tau_r) & \text{if } i = 2 \text{ and } \tau_1 < \tau_r. \end{cases}$$

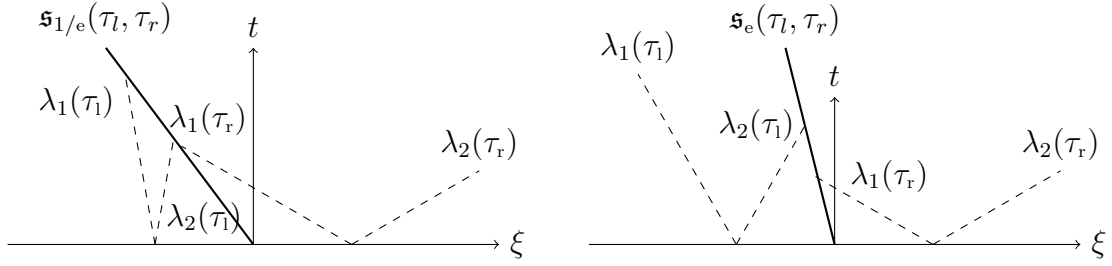


Figure 3.4: 1-Lax shock or supersonic evaporation wave (left) and subsonic evaporation wave (right). The dashed lines refer to characteristic curves $\xi = \lambda_i(\tau) t$, $i = 1, 2$.

As E already stands for the mathematical entropy, we use the letter G , thinking of a generalized wave.

Phase transition. A discontinuous wave (3.14), that connects a left state \mathbf{U}_l and a right state \mathbf{U}_r in different phases, and that satisfies the entropy condition (3.11) is called **phase transition**.

It follows from (3.7) that phase transitions propagate with speed

$$\mathfrak{s}_e(\tau_l, \tau_r) = -\sqrt{\frac{\zeta - p(\tau_r) + p(\tau_l)}{\tau_r - \tau_l}} \quad \text{or} \quad \mathfrak{s}_c(\tau_l, \tau_r) = +\sqrt{\frac{\zeta - p(\tau_r) + p(\tau_l)}{\tau_r - \tau_l}}. \quad (3.16)$$

The subscript e stands for evaporation and c for condensation. Indeed, for $\mathbf{U}_l = (\tau_l, v_l)^\top \in \mathcal{A}_{\text{liq}} \times \mathbb{R}$ and $\mathbf{U}_r = (\tau_r, v_r)^\top \in \mathcal{A}_{\text{vap}} \times \mathbb{R}$, a phase transition with negative speed is always an **evaporation wave** and a phase transition with positive speed is always a **condensation wave**. Note that the static thermodynamic equilibrium solution (3.12) is also called transition wave, although $\mathfrak{s} = j = 0$.

Furthermore, there holds for evaporation waves $v_r = v_l + P(\tau_l, \tau_r)$ and for condensation waves $v_r = v_l - P(\tau_l, \tau_r)$ with

$$P(\tau_l, \tau_r) = \text{sign}(\tau_r - \tau_l) \sqrt{(\tau_r - \tau_l) (\zeta - p(\tau_r) + p(\tau_l))}.$$

Moreover, we distinguish between phase transition and phase boundary. The first one refers to the here described wave, while the latter one refers to the set Γ .

Subsonic transition. An evaporation wave (condensation wave) is called **subsonic** if there holds

$$|\mathfrak{s}_e(\tau_l, \tau_r)| < c(\tau_l), c(\tau_r) \quad (|\mathfrak{s}_c(\tau_l, \tau_r)| < c(\tau_l), c(\tau_r)). \quad (3.17)$$

Due to $\tau_l \in \mathcal{A}_{\text{liq}}$ and Lemma 2.3 $|\mathfrak{s}_e(\tau_l, \tau_r)| < c(\tau_l)$ and $|\mathfrak{s}_c(\tau_l, \tau_r)| < c(\tau_l)$ are always satisfied. A subsonic evaporation wave is illustrated in Figure 3.4 (right).

Discontinuous waves, that satisfy (3.17), are also known as undercompressive shock waves, cf. [47]. Note that these waves violate the Lax entropy condition. An example of such a wave is the thermodynamic equilibrium solution of Lemma 3.7.

Sonic and supersonic transition. An evaporation wave (condensation wave) is called *supersonic* if

$$|\mathfrak{s}_e(\tau_l, \tau_r)| > c(\tau_r) \quad (|\mathfrak{s}_c(\tau_l, \tau_r)| > c(\tau_r)) \quad (3.18)$$

holds. Transition waves are called *sonic* or *characteristic* if (3.18) holds with an equal sign. A supersonic evaporation wave is illustrated in Figure 3.4 (left).

Note that these waves fulfill the Lax condition (3.15) due to (3.10).

Stable and metastable transition. We call a transition wave *metastable* if at least one of the trace states lies in the metastable region $(\tau_{\text{liq}}^{\text{sat}}, \tau_{\text{vap}}^{\text{sat}}) \cap \mathcal{A}$. Otherwise, the phase transition is called *stable*.

Note that the functions R , S , G and P are monotone decreasing with respect to the first argument and monotone increasing with respect to the second argument. This will become necessary in order to determine unique micro solutions in Chapter 4 and Chapter 5. Furthermore, we use the notation that the first argument refers to the left state and the second argument refers to the right state.

Chapter 4

Microsolver for Liu's entropy criterion

Two-phase Riemann problems involve multiple solutions due to the non-convex shape of the pressure functions for real fluids, cf. Remark 2.10. Thus, an additional selection criterion is required. We consider in this chapter the entropy condition of Liu [55], that is sufficient to solve the micro-scale model of Definition 3.5 uniquely for monotone pressure laws. However, the pressure function of Definition 2.2 is not monotone.

Godlewski and Seguin consider in [33] the micro-scale model of Definition 3.5 without capillary forces. They substitute the non-monotone pressure function by a non-increasing pressure isotherm using the Maxwell construction, cf. Example 2.6. Müller and Voß follow in [62] a similar concept for the full Euler system. In both cases the Liu criterion provides an appropriate selection criterion to enforce the unique solvability.

We will generalize this concept towards the surface tension dependent situation and thereby restate condition (3.7) into a classical homogeneous Rankine-Hugoniot condition with a new (non-increasing) and globally defined pressure function. We apply therefore in Section 4.1 a modification similar to the Maxwell construction. The entropy criterion and the solution of the problem are presented in Section 4.2.

Due to the pressure modification, there are initial states such that the Liu solution is not a weak solution of the original micro-scale model of Definition 3.5. Hence, we consider the corresponding microsolver in Section 4.3 as an approximate solver. This shortcoming is discussed in the final section.

The approach has been published in [40]. An application of this microsolver in a two-dimensional bulk solver can be found in the PhD thesis of Patrick Engel [26, Chapter 7].

4.1 Mixture equations of state including surface tension

The Maxwell construction replaces metastable and spinodal regions of a pressure function below the critical temperature by a constant line, see Example 2.6. This concept is generalized for the pair of saturation states $\tau_{\text{liq}}^{\text{sat}}$ and $\tau_{\text{vap}}^{\text{sat}}$ of Definition 2.2. Remember that $\tau_{\text{liq}}^{\text{sat}}$ and $\tau_{\text{vap}}^{\text{sat}}$ depend on the surface tension term ζ , where ζ is a fixed constant in the

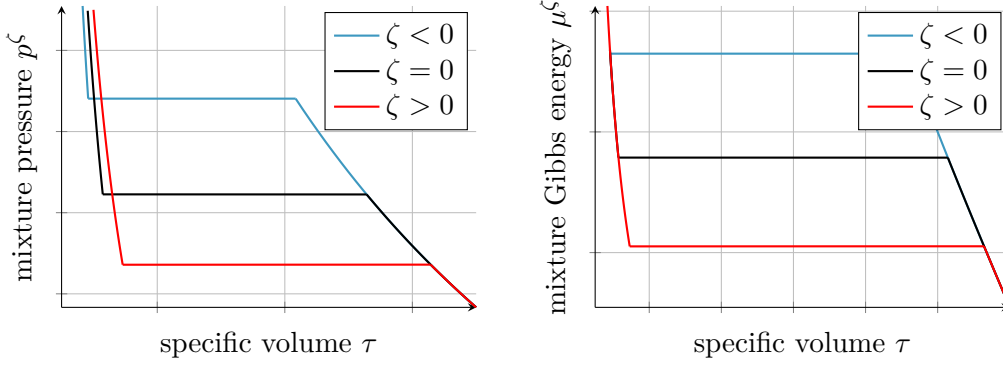


Figure 4.1: Surface tension dependent mixture pressure (left) and Gibbs free energy (right).

micro-scale models.

Definition 4.1 (Mixture equations of state).

Let the functions $p, \mu : \mathcal{A}_{\text{liq}} \cup \mathcal{A}_{\text{vap}} \rightarrow \mathbb{R}$ for pressure and specific Gibbs free energy and the pair of saturation states $\tau_{\text{liq}}^{\text{sat}} \in \mathcal{A}_{\text{liq}}$, $\tau_{\text{vap}}^{\text{sat}} \in \mathcal{A}_{\text{vap}}$ for a constant surface tension term $\zeta \in \mathcal{Z}$ as in Definition 2.2 be given.

The **mixture pressure function** is given by

$$p^\zeta(\tau) := \begin{cases} p(\tau) + \zeta & \text{for } \tau \in (\tau_{\text{liq}}^{\text{min}}, \tau_{\text{liq}}^{\text{sat}}], \\ p(\tau_{\text{vap}}^{\text{sat}}) & \text{for } \tau \in (\tau_{\text{liq}}^{\text{sat}}, \tau_{\text{vap}}^{\text{sat}}], \\ p(\tau) & \text{for } \tau \in (\tau_{\text{vap}}^{\text{sat}}, \infty), \end{cases} \quad (4.1)$$

and the associated **specific mixture Gibbs free energy function** is

$$\mu^\zeta(\tau) := \begin{cases} \mu(\tau) & \text{for } \tau \in (\tau_{\text{liq}}^{\text{min}}, \tau_{\text{liq}}^{\text{sat}}], \\ \mu(\tau_{\text{vap}}^{\text{sat}}) & \text{for } \tau \in (\tau_{\text{liq}}^{\text{sat}}, \tau_{\text{vap}}^{\text{sat}}], \\ \mu(\tau) & \text{for } \tau \in (\tau_{\text{vap}}^{\text{sat}}, \infty). \end{cases}$$

Both p^ζ and μ^ζ depend on the constant surface tension, that is emphasized by the superscript ζ . The new pressure function is monotone and globally defined, see Figure 4.1 for illustration. The original equation of state is shown in Figure 2.5.

The associated **specific mixture Helmholtz free energy** $\psi^\zeta := \mu^\zeta - p^\zeta \tau$ using (2.7) is the convex envelope of the function

$$\tau \mapsto \begin{cases} \psi(\tau) - \zeta \tau & \text{for } \tau \in \mathcal{A}_{\text{liq}}, \\ \psi(\tau) & \text{for } \tau \in \mathcal{A}_{\text{vap}}. \end{cases}$$

Remark 4.2 (Modifying the vapor branch).

With our construction procedure, one obtains a surface tension dependent pressure function (4.1) with the constant curvature term in the liquid branch. Since the solution of the micro-scale models will depend only on derivatives of p^ζ , one can alternatively modify the vapor branch without altering the final solution.

Remark 4.3 (Mixture states and phases).

The label *mixture* stems from the fact that the strait line portion from $\tau_{\text{liq}}^{\text{sat}}$ to $\tau_{\text{vap}}^{\text{sat}}$ usually refers to mixture states. We however see the mixture equations as approximate equations of state. Furthermore, we keep the sets $\mathcal{A}_{\text{liq}} = (\tau_{\text{liq}}^{\text{min}}, \tau_{\text{liq}}^{\text{max}})$, $\mathcal{A}_{\text{vap}} = (\tau_{\text{vap}}^{\text{min}}, \infty)$ and $\mathcal{A} = \mathcal{A}_{\text{liq}} \cup \mathcal{A}_{\text{vap}}$ of Definition 2.2 to distinguish phases.

4.2 Solving the generalized Riemann problem exactly

The pressure function of Definition 4.1 satisfies the hypotheses in [33], due to Lemma 2.3, such that all statements apply here. We therefore skip the proofs in this section and refer to the original paper. Nevertheless, construction details are given here since they are necessary to state the algorithm of the corresponding microsolver and to compare the solution with the approach in Chapter 5. First, we restate the generalized Riemann problem of Definition 3.5.

Definition 4.4 (Liu micro solution for mixture pressure laws).

A self-similar weak solution $\mathbf{U}(\xi, t) = (\tau, v)^\top \in \mathcal{A} \times \mathbb{R}$ of

$$\begin{pmatrix} \tau \\ v \end{pmatrix}_t + \begin{pmatrix} -v \\ p^\zeta(\tau) \end{pmatrix}_\xi = \begin{pmatrix} 0 \\ 0 \end{pmatrix} \quad \text{with} \quad \mathbf{U}(\xi, 0) = \begin{cases} \mathbf{U}_L = (\tau_L, v_L)^\top & : \xi \leq 0, \\ \mathbf{U}_R = (\tau_R, v_R)^\top & : \xi > 0 \end{cases} \quad (4.2)$$

and $\tau_L \in \mathcal{A}_{\text{liq}}$, $\tau_R \in \mathcal{A}_{\text{vap}}$, $v_L, v_R \in \mathbb{R}$ is a **Liu micro solution** if and only if all discontinuous waves satisfy the entropy condition of Liu in Definition 4.6 below. Here p^ζ is the mixture pressure function of Definition 4.1.

Note that (4.2) is now a weakly hyperbolic system. Indeed, the two eigenvalues of the Jacobian matrix of the flux $(-v, p^\zeta(\tau))^\top$ are

$$\lambda_{1/2}^\zeta(\tau) = \mp c^\zeta(\tau) \quad \text{with} \quad c^\zeta = c^\zeta(\tau) = \begin{cases} \sqrt{-p'(\tau)} & : \tau \in (\tau_{\text{liq}}^{\text{min}}, \tau_{\text{liq}}^{\text{sat}}] \cup [\tau_{\text{vap}}^{\text{sat}}, \infty), \\ 0 & : \tau \in (\tau_{\text{liq}}^{\text{sat}}, \tau_{\text{vap}}^{\text{min}}) \end{cases}$$

and the eigenvectors are $r_{1/2}^\zeta(\tau) = (1, \mp c^\zeta(\tau))^\top$. Thus, (4.2) is strictly hyperbolic for $\tau \notin (\tau_{\text{liq}}^{\text{sat}}, \tau_{\text{vap}}^{\text{min}})$. In case of $\tau \in (\tau_{\text{liq}}^{\text{sat}}, \tau_{\text{vap}}^{\text{min}})$ the sound speed $c^\zeta(\tau)$ becomes zero and the eigenvectors do not form a basis of \mathbb{R}^2 anymore. This loss of hyperbolicity was already pointed out in [11, 33] and the references therein.

Nevertheless, the Rankine-Hugoniot conditions for equation (4.2) coincide with the jump conditions (3.7) in case of stable phase transitions. For planar phase boundaries ($\zeta \equiv 0$), Godlewski and Seguin applied in [33] the entropy criterion of Liu (Definition 4.6 below) in order to find a unique entropy solution of the weakly hyperbolic Riemann problem (4.2). Following exactly this approach, we can select a unique solution for curved phase boundaries, i.e. the Liu micro solution of Definition 4.4.

The solution consists of rarefaction waves, discontinuous shock waves, attached waves and phase transitions. These waves are connected via intermediate states such that Liu's criterion is satisfied. In the following, we have a closer look at the solution and the entropy criterion.

The transition from p to p^ζ changes propagation speed and velocity of the waves introduced in Section 3.3. We use the superscript ζ to indicate that the functions depend on the mixture pressure function. Both, shock and phase transition waves propagate now with speed

$$\mathfrak{s}_1^\zeta(\tau_1, \tau_r) = -\sqrt{-\frac{p^\zeta(\tau_r) - p^\zeta(\tau_1)}{\tau_r - \tau_1}}, \quad \mathfrak{s}_2^\zeta(\tau_1, \tau_r) = \sqrt{-\frac{p^\zeta(\tau_r) - p^\zeta(\tau_1)}{\tau_r - \tau_1}}. \quad (4.3)$$

The velocity of a discontinuous i -wave (i -phase transition or i -shock wave) is $v_r = v_1 + P^\zeta(\tau_1, \tau_r)$ for $i = 1$ and $v_r = v_1 - P^\zeta(\tau_1, \tau_r)$ for $i = 2$, where

$$P^\zeta(\tau_1, \tau_r) = \text{sign}(\tau_r - \tau_1) \sqrt{-(\tau_r - \tau_1) (p^\zeta(\tau_r) - p^\zeta(\tau_1))}.$$

The velocity of an i -elementary wave changes to $v_r = v_1 + G^\zeta(\tau_1, \tau_r)$ for $i = 1$ and $v_r = v_1 - G^\zeta(\tau_1, \tau_r)$ for $i = 2$ with

$$G^\zeta(\tau_1, \tau_r) = \begin{cases} \int_{\tau_1}^{\tau_r} \sqrt{-p^{\zeta'}(\tau)} d\tau & \text{if } i = 1 \text{ and } \tau_1 < \tau_r \text{ or} \\ & i = 2 \text{ and } \tau_1 > \tau_r, \\ P^\zeta(\tau_1, \tau_r) & \text{else.} \end{cases}$$

Note that the definitions of Section 3.3 have changed only for metastable waves, as the following lemma shows.

Lemma 4.5 (Propagation speeds and velocities).

For $\tau_l, \tau_r \in \mathcal{A} \setminus (\tau_{\text{liq}}^{\text{sat}}, \tau_{\text{vap}}^{\text{sat}})$ in the same phase and $i = 1, 2$ there holds

$$\mathfrak{s}_i^\zeta(\tau_1, \tau_r) = \mathfrak{s}_i(\tau_1, \tau_r), \quad G^\zeta(\tau_1, \tau_r) = G(\tau_1, \tau_r), \quad \lambda_i^\zeta(\tau_1) = \lambda_i(\tau_1).$$

For $\tau_l \in (\tau_{\text{liq}}^{\text{min}}, \tau_{\text{liq}}^{\text{sat}})$, $\tau_r \in (\tau_{\text{vap}}^{\text{sat}}, \infty)$ there holds

$$\mathfrak{s}_1^\zeta(\tau_1, \tau_r) = \mathfrak{s}_e(\tau_1, \tau_r), \quad \mathfrak{s}_2^\zeta(\tau_1, \tau_r) = \mathfrak{s}_e(\tau_1, \tau_r), \quad P^\zeta(\tau_1, \tau_r) = P(\tau_1, \tau_r).$$

Proof. The pressure functions p and p^ζ coincide in the interval $\mathcal{A} \setminus (\tau_{\text{liq}}^{\text{sat}}, \tau_{\text{vap}}^{\text{sat}})$, thus also the derived functions. \square

We single out admissible discontinuous waves by applying Liu's criterion [55]. The criterion together with the Rankine-Hugoniot condition determines the solution of the generalized Riemann problem.

Definition 4.6 (Liu's entropy criterion).

Any discontinuous i -wave (i -phase transition or i -shock wave), with $i = 1, 2$, connecting a left state $(\tau_1, v_1)^\top \in \mathcal{A} \times \mathbb{R}$ and a right state $(\tau_r, v_r)^\top \in \mathcal{A} \times \mathbb{R}$ is said to fulfill **Liu's entropy criterion** if and only if

$$\mathfrak{s}_i^\zeta(\tau_1, \tau_r) \leq \mathfrak{s}_i^\zeta(\tau_1, \tau) \quad \text{for all } \tau \in [\min\{\tau_1, \tau_r\}, \max\{\tau_1, \tau_r\}] \quad (4.4)$$

and \mathfrak{s}_i^ζ in (4.3).

There is a simple geometrical representation of the entropy criterion. The lemma will help later on to determine the solution of Definition 4.4.

Lemma 4.7 (Geometrical representation of Liu's entropy criterion).

Let a left state $(\tau_1, v_1)^\top \in \mathcal{A} \times \mathbb{R}$ and a right state $(\tau_r, v_r)^\top \in \mathcal{A} \times \mathbb{R}$ be given.

- A discontinuous 1-wave with $\tau_1 \geq \tau_r$ or a discontinuous 2-wave with $\tau_1 \leq \tau_r$ fulfills Liu's entropy criterion if and only if the graph of the pressure lies below the chord from $(\tau_1, p^\zeta(\tau_1))$ to $(\tau_r, p^\zeta(\tau_r))$:

$$\alpha p^\zeta(\tau_1) + (1 - \alpha) p^\zeta(\tau_r) \geq p^\zeta(\alpha \tau_1 + (1 - \alpha) \tau_r) \quad \text{for all } \alpha \in (0, 1).$$

- A discontinuous 1-wave with $\tau_1 \leq \tau_r$ or a discontinuous 2-wave with $\tau_1 \geq \tau_r$ fulfills Liu's entropy criterion if and only if the graph of the pressure lies above the chord from $(\tau_1, p^\zeta(\tau_1))$ to $(\tau_r, p^\zeta(\tau_r))$:

$$\alpha p^\zeta(\tau_1) + (1 - \alpha) p^\zeta(\tau_r) \leq p^\zeta(\alpha \tau_1 + (1 - \alpha) \tau_r) \quad \text{for all } \alpha \in (0, 1).$$

Proof. Plugging $\tau = \alpha \tau_1 + (1 - \alpha) \tau_r$ into (4.4) one obtains above inequalities. \square

An important consequence of Liu's entropy criterion is that the entropy inequality follows. For the temperature dependent case it has been proven in [56]. Here it is a direct consequence of Lemma 4.7.

Corollary 4.8 (Entropy inequality).

Any discontinuous i -wave (i -phase transition or i -shock wave), with $i = 1, 2$, connecting a left state $(\tau_1, v_1)^\top \in \mathcal{A} \times \mathbb{R}$ and a right state $(\tau_r, v_r)^\top \in \mathcal{A} \times \mathbb{R}$ that fulfills the Liu's entropy criterion, satisfies

$$-\mathfrak{s}_i^\zeta(\tau_1, \tau_r) \left(\llbracket \psi^\zeta(\tau) \rrbracket + \llbracket \tau \rrbracket \{ p^\zeta(\tau) \} \right) \leq 0. \quad (4.5)$$

Here the notation $\llbracket \tau \rrbracket = \tau_r - \tau_1$ and $\{ \tau \} = \frac{1}{2}(\tau_1 + \tau_r)$ is used.

Note that the entropy inequality (4.5) is defined using the mixture Helmholtz free energy to account for surface tension, cf. (3.11).

Proof of Corollary 4.8. With the relation $\psi^{\zeta'} = -p$, inequality (4.5) is equivalent to $\mathfrak{s}_i^\zeta(\tau_1, \tau_r) (\llbracket \tau \rrbracket \{ p^\zeta(\tau) \} - \int_{\tau_{\text{liq}}}^{\tau_{\text{vap}}} p^\zeta(\tau) d\tau) \geq 0$. Due to Lemma 4.7, the bracket for $i = 1$ is not positive. The same holds for \mathfrak{s}_1 by definition (4.3). For $i = 2$ the same arguments apply: bracket and \mathfrak{s}_2 are both not negative. \square

We look for self-similar solutions composed of shock and rarefaction waves and exactly one phase transition. The next two lemmas determine specific points in \mathcal{A} , where the solution changes its structure. They are a direct consequence of the pressure function in Definition 2.2. A function g_s is introduced such that the pressure function has the same slope in $g_s(\tau)$ as the chord from $(\tau, p^\zeta(\tau))$ to $(g_s(\tau), p^\zeta(g_s(\tau)))$, see Figure 4.2 (left) for illustration. The second lemma introduces a value $\bar{\tau}$ such that the points $(\bar{\tau}, p^\zeta(\bar{\tau}))$, $(\tau_{\text{vap}}^{\text{sat}}, p^\zeta(\tau_{\text{vap}}^{\text{sat}}))$, $(\tau_{\text{R}}, p^\zeta(\tau_{\text{R}}))$ lie on one straight line, see Figure 4.3 (left).

Lemma 4.9 (The function g_s).

There exists a monotone function $g_s : [\tau_{\text{liq}}^{\text{sat}}, \tau_{\text{liq}}^{\text{max}}) \rightarrow (\tau_{\text{vap}}^{\text{sat}}, \infty)$, $\tau \mapsto g_s(\tau)$ such that

$$p^{\zeta'}(g_s(\tau)) = \frac{p^\zeta(g_s(\tau)) - p^\zeta(\tau)}{g_s(\tau) - \tau},$$

or equivalently $\lambda_1^\zeta(g_s(\tau)) = \mathfrak{s}_1^\zeta(\tau, g_s(\tau))$ holds.

Lemma 4.10 (The value $\bar{\tau}$).

For any $\tau_R \in (\tau_{\text{vap}}^{\text{sat}}, \infty)$, there exists $\bar{\tau} \in (\tau_{\text{liq}}^{\text{min}}, \tau_{\text{liq}}^{\text{sat}})$ such that

$$\frac{p^\zeta(\tau_R) - p^\zeta(\tau_{\text{vap}}^{\text{sat}})}{\tau_R - \tau_{\text{vap}}^{\text{sat}}} = \frac{p^\zeta(\tau_R) - p^\zeta(\bar{\tau})}{\tau_R - \bar{\tau}},$$

or equivalently $\mathfrak{s}_2^\zeta(\bar{\tau}, \tau_{\text{vap}}^{\text{sat}}) = \mathfrak{s}_2^\zeta(\tau_{\text{vap}}^{\text{sat}}, \tau_R)$ holds. In the limiting case $\tau_R = \tau_{\text{vap}}^{\text{sat}}$ set $\bar{\tau} = \tau_{\text{liq}}^{\text{min}}$.

At the specific volume value determined by g_s , the evaporation wave splits into two waves: an evaporation wave and a 2-rarefaction wave, see composed waves of type 2_L^ζ , 3_L^ζ and 5_L^ζ , 6_L^ζ in Table 4.1. The dependency of $\bar{\tau}$ on τ_R is skipped. At $\bar{\tau}$, the condensation wave of type 4_R^ζ in Table 4.2 breaks into a condensation wave and a 2-shock wave (a composed wave of type 5_R^ζ).

It is now possible to define generalized Lax curves for (4.2) such that the corresponding waves satisfy the entropy criterion of Definition 4.6. The Lax curve $v^* = v_L + \mathcal{L}_1^\zeta(\tau_L, \tau^*)$ of the first family is given by the Table 4.1. The corresponding multiple 1-wave alters its structure depending on the arguments of \mathcal{L}_1^ζ . We enumerate the different wave compositions with the symbols of the first column in the table. The subscript L indicates that the wave connects the left initial state $(\tau_L, v_L)^\top$ to an intermediate state $(\tau^*, v^*)^\top$, while the superscript ζ shall denote that the underlying pressure function is the mixture one of Definition 4.1.

The geometric interpretation of Lemma 4.7 is helpful to determine the different types of wave pattern. The convex envelope for a wave of type 2_L^ζ and a wave of type 3_L^ζ are exemplary shown in Figure 4.2. On the left hand side one finds the pressure p^ζ and convex hulls and on the right hand side the corresponding volume distribution. The pressure function in Figure 4.2 and Figure 4.3 is

$$p^\zeta(\tau) = \begin{cases} 2/\tau + 1 & : \tau \in (0, 1/2], \\ 5 & : \tau \in (1/2, 10/3], \\ 20/\tau - 1 & : \tau \in (10/3, \infty). \end{cases}$$

The main properties are summarized to a proposition. The proof can be found in [33].

Proposition 4.11 (Properties of the generalized Lax curve \mathcal{L}_1^ζ).

Let a left state $(\tau_L, v_L)^\top \in \mathcal{A}_{\text{liq}} \times \mathbb{R}$ and the map $\mathcal{L}_1^\zeta : \mathcal{A}_{\text{liq}} \times (\tau_{\text{liq}}^{\text{min}}, \tau_{\text{liq}}^{\text{sat}}] \cup [\tau_{\text{vap}}^{\text{sat}}, \infty) \rightarrow \mathbb{R}$ of Table 4.1 be given. Then the following properties hold.

(i) The map \mathcal{L}_1^ζ is continuous.

(ii) The map

$$(\tau_{\text{liq}}^{\text{min}}, \tau_{\text{liq}}^{\text{sat}}] \cup [\tau_{\text{vap}}^{\text{sat}}, \infty) \mapsto \mathbb{R}, \quad \tau^* \rightarrow v^* = v_L + \mathcal{L}_1^\zeta(\tau_L, \tau^*)$$

is differentiable and strictly monotone increasing in $(\tau_{\text{liq}}^{\text{min}}, \tau_{\text{liq}}^{\text{sat}}]$ and in $[\tau_{\text{vap}}^{\text{sat}}, \infty)$.

(iii) It holds that $\mathcal{L}_1^\zeta(\tau_L, \tau_{\text{liq}}^{\text{sat}}) = \mathcal{L}_1^\zeta(\tau_L, \tau_{\text{vap}}^{\text{sat}})$.

(iv) All propagation speeds are negative. In the composed wave of type 2_L^ζ and type 3_L^ζ , the phase transition propagates faster than the elementary wave in the liquid phase. In the wave of type 3_L^ζ and type 6_L^ζ the phase transition propagates slower than the elementary wave connecting to τ^* .

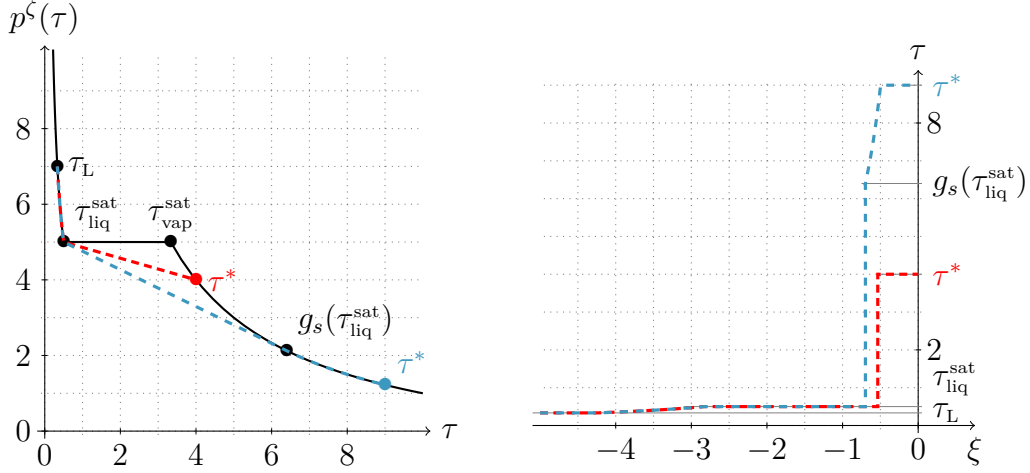


Figure 4.2: The figure on the left hand side shows the graph of the mixture pressure. The τ -values, at which the Lax curve of the first family alters its wave structure, are pinned to the pressure graph. Moreover, the convex envelope corresponding to a wave of type 2_L^ζ (red) and a wave of type 3_L^ζ (blue) are printed. The figure on the right hand side shows these waves at time $t = 1$ in the (τ, ξ) -plane.

- (v) The evaporation waves in the composed wave of type 2_L^ζ and type 3_L^ζ are subsonic, while for type 5_L^ζ and type 6_L^ζ the transition wave is supersonic and sonic.

The Lax curve $v^* = v_R + \mathcal{L}_2^\zeta(\tau^*, \tau_R)$ of the second family is given by Table 4.2. The corresponding 2-waves are enumerated with the superscript $_R$ to denote that they connect the right initial state $(\tau_R, v_R)^\top$ to an intermediate state $(\tau^*, v^*)^\top$. Concave hulls and corresponding volume distribution for a wave of type 4_R^ζ and type 5_R^ζ are exemplary plotted in Figure 4.3. The main properties are summarized to the proposition below. The proof can be found in [33].

Proposition 4.12 (Properties of the generalized Lax curve \mathcal{L}_2^ζ).

Let a right state $(\tau_R, v_R)^\top \in \mathcal{A}_{\text{vap}} \times \mathbb{R}$ and the map $\mathcal{L}_2^\zeta : (\tau_{\text{liq}}^{\min}, \tau_{\text{liq}}^{\text{sat}}] \cup [\tau_{\text{vap}}^{\text{sat}}, \infty) \times \mathcal{A}_{\text{vap}} \rightarrow \mathbb{R}$ of Table 4.2 be given. Then the following properties hold.

- (i) The map \mathcal{L}_2^ζ is continuous.

- (ii) The map

$$(\tau_{\text{liq}}^{\min}, \tau_{\text{liq}}^{\text{sat}}] \cup [\tau_{\text{vap}}^{\text{sat}}, \infty) \rightarrow \mathbb{R}, \quad \tau^* \mapsto v^* = v_R + \mathcal{L}_2^\zeta(\tau^*, \tau_R)$$

is differentiable and strictly monotone decreasing in $(\tau_{\text{liq}}^{\min}, \tau_{\text{liq}}^{\text{sat}}]$ and in $[\tau_{\text{vap}}^{\text{sat}}, \infty)$.

- (iii) It holds that $\mathcal{L}_2^\zeta(\tau_{\text{liq}}^{\text{sat}}, \tau_R) = \mathcal{L}_2^\zeta(\tau_{\text{vap}}^{\text{sat}}, \tau_R)$.

- (iv) All propagation speeds are positive. For waves of type 5_R^ζ , phase transitions propagate slower than the elementary wave in the vapor phase.

- (v) The condensation wave in the composed wave of type 5_L^ζ is subsonic. All other transition waves are supersonic.

type	τ_L	τ^*	composition	$\mathcal{L}_1^\zeta(\tau_L, \tau^*)$
1 $_L^\zeta$	$(\tau_{\text{liq}}^{\text{min}}, \tau_{\text{liq}}^{\text{sat}}]$	$(\tau_{\text{liq}}^{\text{min}}, \tau_{\text{liq}}^{\text{sat}}]$	1E	$G^\zeta(\tau_L, \tau^*)$
2 $_L^\zeta$	$(\tau_{\text{liq}}^{\text{min}}, \tau_{\text{liq}}^{\text{sat}}]$	$[\tau_{\text{vap}}^{\text{sat}}, g_s(\tau_{\text{liq}}^{\text{sat}})]$	1E-UE	$G^\zeta(\tau_L, \tau_{\text{liq}}^{\text{sat}})$ + $P^\zeta(\tau_{\text{liq}}^{\text{sat}}, \tau^*)$
3 $_L^\zeta$	$(\tau_{\text{liq}}^{\text{min}}, \tau_{\text{liq}}^{\text{sat}}]$	$(g_s(\tau_{\text{liq}}^{\text{sat}}), \infty)$	1E-UE-1R	$G^\zeta(\tau_L, \tau_{\text{liq}}^{\text{sat}})$ + $P^\zeta(\tau_{\text{liq}}^{\text{sat}}, g_s(\tau_{\text{liq}}^{\text{sat}}))$ + $G^\zeta(g_s(\tau_{\text{liq}}^{\text{sat}}), \tau^*)$
4 $_L^\zeta$	$(\tau_{\text{liq}}^{\text{sat}}, \tau_{\text{liq}}^{\text{max}})$	$(\tau_{\text{liq}}^{\text{min}}, \tau_{\text{liq}}^{\text{sat}}]$	1S	$G^\zeta(\tau_L, \tau^*)$
5 $_L^\zeta$	$(\tau_{\text{liq}}^{\text{sat}}, \tau_{\text{liq}}^{\text{max}})$	$[\tau_{\text{vap}}^{\text{sat}}, g_s(\tau_L)]$	1E	$P^\zeta(\tau_L, \tau^*)$
6 $_L^\zeta$	$(\tau_{\text{liq}}^{\text{sat}}, \tau_{\text{liq}}^{\text{max}})$	$(g_s(\tau_L), \infty)$	SE-1R	$P^\zeta(\tau_L, g_s(\tau_L))$ + $G^\zeta(g_s(\tau_L), \tau^*)$

Table 4.1: Definition of the map $\mathcal{L}_1^\zeta : \mathcal{A}_{\text{liq}} \times (\tau_{\text{liq}}^{\text{min}}, \tau_{\text{liq}}^{\text{sat}}] \cup [\tau_{\text{vap}}^{\text{sat}}, \infty) \rightarrow \mathbb{R}$, that determines the Lax curve $v^* = v_L + \mathcal{L}_1^\zeta(\tau_L, \tau^*)$ of the first family. The resulting (multiple) waves for left and right trace specific volume values τ_L and τ^* are composed of the waves given in the fourth column (from left to right): 1E stands for 1-elementary wave, 1R for 1-rarefaction wave, 1S for 1-shock wave, 1E for subsonic (undercompressive) evaporation wave, 1E for supersonic (Lax type) evaporation and SE for sonic evaporation.

type	τ^*	τ_R	composition	$\mathcal{L}_2^\zeta(\tau^*, \tau_R)$
1 $_R^\zeta$	$[\tau_{\text{vap}}^{\text{sat}}, \infty)$	$(\tau_{\text{vap}}^{\text{min}}, \tau_{\text{vap}}^{\text{sat}})$	2R-2S	$G^\zeta(\tau^*, \tau_{\text{vap}}^{\text{sat}}) + G^\zeta(\tau_{\text{vap}}^{\text{sat}} + \tau_R)$
2 $_R^\zeta$	$(\tau_{\text{liq}}^{\text{min}}, \tau_{\text{liq}}^{\text{sat}}]$	$(\tau_{\text{vap}}^{\text{min}}, \tau_{\text{vap}}^{\text{sat}})$	LC	$P^\zeta(\tau^*, \tau_R)$
3 $_R^\zeta$	$[\tau_{\text{vap}}^{\text{sat}}, \infty)$	$[\tau_{\text{vap}}^{\text{sat}}, \infty)$	2E	$G^\zeta(\tau^*, \tau_R)$
4 $_R^\zeta$	$(\tau_{\text{liq}}^{\text{min}}, \bar{\tau}]$	$[\tau_{\text{vap}}^{\text{sat}}, \infty)$	LC	$P^\zeta(\tau^*, \tau_R)$
5 $_R^\zeta$	$(\bar{\tau}, \tau_{\text{liq}}^{\text{sat}}]$	$[\tau_{\text{vap}}^{\text{sat}}, \infty)$	UC-2S	$P^\zeta(\tau^*, \tau_{\text{vap}}^{\text{sat}})$ + $G^\zeta(\tau_{\text{vap}}^{\text{sat}}, \tau_R)$

Table 4.2: Definition of the map $\mathcal{L}_2^\zeta : (\tau_{\text{liq}}^{\text{min}}, \tau_{\text{liq}}^{\text{sat}}] \cup [\tau_{\text{vap}}^{\text{sat}}, \infty) \times \mathcal{A}_{\text{vap}} \rightarrow \mathbb{R}$, that determines the Lax curve $v^* = v_R + \mathcal{L}_2^\zeta(\tau^*, \tau_R)$ of the second family. The resulting (multiple) waves for left and right trace specific volume values τ^* and τ_R are composed of the waves given in the fourth column (from left to right): 2E stands for 2-elementary wave, 2R for 2-rarefaction wave, 2S for 2-shock wave, UC for subsonic (undercompressive) condensation wave and LC for supersonic (Lax type) condensation wave.

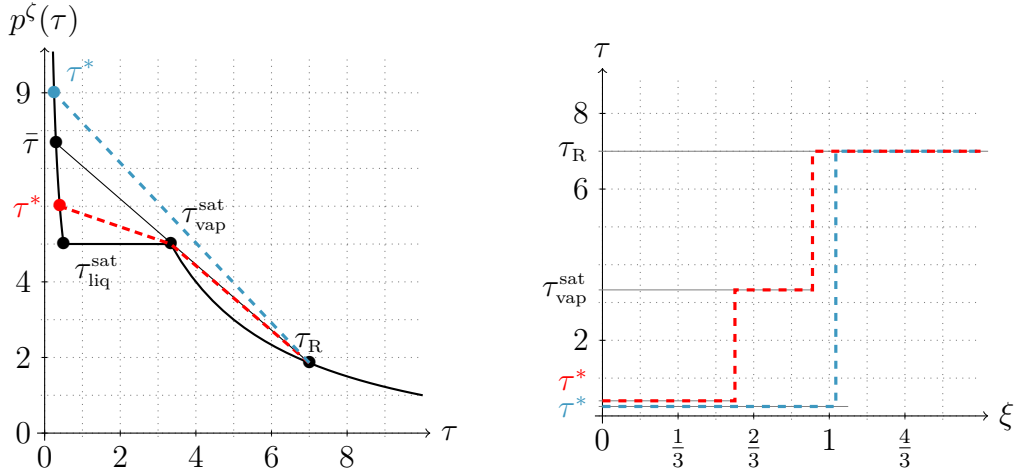


Figure 4.3: The figure on the left hand side shows the graph of of the mixture pressure. The τ -values, at which the Lax curve of the second family alters its wave structure, are pinned to the pressure graph. Moreover, the concave envelope corresponding to a wave of type 4_R^ζ (red) and a wave of type 5_R^ζ (blue) are printed. The figure on the right hand side shows these waves at time $t = 1$ in the (τ, ξ) -plane.

The following theorem is of key importance for the construction of the microsolver. It states that the Lax curves intersect each other and that there exists a unique Liu micro solution.

Theorem 4.13 (Existence and uniqueness of Liu micro solutions).

For any pair of states $(\tau_L, v_L)^\top \in \mathcal{A}_{\text{liq}} \times \mathbb{R}$ and $(\tau_R, v_R)^\top \in \mathcal{A}_{\text{vap}} \times \mathbb{R}$ the equation

$$v_L + \mathcal{L}_1^\zeta(\tau_L, \tau^*) = v_R + \mathcal{L}_2^\zeta(\tau^*, \tau_R), \quad (4.6)$$

with \mathcal{L}_1^ζ and \mathcal{L}_2^ζ in Table 4.1 and Table 4.2, respectively, has a unique intersection point in $(\tau_{\text{liq}}^{\text{min}}, \tau_{\text{liq}}^{\text{sat}}] \cup (\tau_{\text{vap}}^{\text{sat}}, \infty)$.

The model of Definition 4.4 has a unique self-similar Liu micro solution $\mathbf{U} = \mathbf{U}(\xi, t) \in \mathcal{A} \times \mathbb{R}$, that is composed of a wave connecting the left initial state with (τ^*, v^*) according to Table 4.1 and a wave connecting (τ^*, v^*) to the right initial state according to Table 4.2. Here $v^* = v_L + \mathcal{L}_1^\zeta(\tau_L, \tau^*) = v_R + \mathcal{L}_2^\zeta(\tau^*, \tau_R)$.

Let $\mathbf{U} = \mathbf{U}(\xi, t)$ and $\bar{\mathbf{U}} = \bar{\mathbf{U}}(\xi, t)$ be two self-similar Liu micro solutions for the initial states $\mathbf{U}_L \in \mathcal{A}_{\text{liq}} \times \mathbb{R}$, $\mathbf{U}_R \in \mathcal{A}_{\text{vap}} \times \mathbb{R}$ and $\bar{\mathbf{U}}_L \in \mathcal{A}_{\text{liq}} \times \mathbb{R}$, $\bar{\mathbf{U}}_R \in \mathcal{A}_{\text{vap}} \times \mathbb{R}$, respectively. Then, for any $L > 0$, there exists a constant $C > 0$ such that

$$\int_{-L}^L |\mathbf{U}(\xi, 1) - \bar{\mathbf{U}}(\xi, 1)| d\xi \leq C (|\mathbf{U}_L - \bar{\mathbf{U}}_L| + |\mathbf{U}_R - \bar{\mathbf{U}}_R|) \quad (4.7)$$

holds.

Proof. The mixture pressure function has the same properties as the pressure of Definition 2.2 for $\tau \in (\tau_{\text{liq}}^{\text{min}}, \tau_{\text{liq}}^{\text{sat}}] \cup [\tau_{\text{vap}}^{\text{sat}}, \infty)$ and Lemma 4.5 holds. Due to (2.11) and (2.13), the

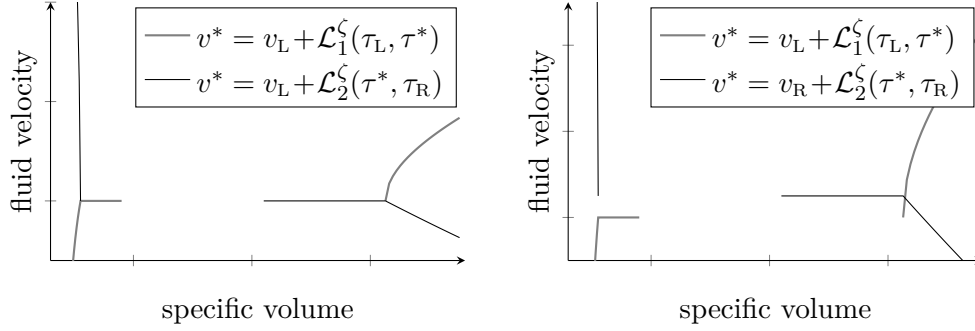


Figure 4.4: Lax curves with non-unique intersection (left) and with unique intersection point (right).

Lax curves satisfy

$$\begin{aligned} \lim_{\tau \rightarrow \tau_{\text{liq}}^{\min}} \mathcal{L}_1^z(\tau_L, \tau) &= -\infty, & \lim_{\tau \rightarrow \tau_{\text{liq}}^{\min}} \mathcal{L}_2^z(\tau, \tau_R) &= +\infty, \\ \lim_{\tau \rightarrow \infty} \mathcal{L}_1^z(\tau_L, \tau) &= +\infty, & \lim_{\tau \rightarrow \infty} \mathcal{L}_2^z(\tau, \tau_R) &= -\infty. \end{aligned}$$

Set $\Delta = \tau_{\text{vap}}^{\text{sat}} - \tau_{\text{liq}}^{\text{sat}}$. Proposition 4.11 and Proposition 4.12 ensure, that the function

$$f(\tau) = \begin{cases} v_R - v_L + \mathcal{L}_2^z(\tau, \tau_R) - \mathcal{L}_1^z(\tau_L, \tau) & \text{for } \tau \leq \tau_{\text{liq}}^{\text{sat}}, \\ v_R - v_L + \mathcal{L}_2^z(\tau - \Delta, \tau_R) - \mathcal{L}_1^z(\tau_L, \tau - \Delta) & \text{for } \tau > \tau_{\text{vap}}^{\text{sat}} \end{cases}$$

is continuous and strictly monotone decreasing from $+\infty$ to $-\infty$. Thus, $\tau^* \in (\tau_{\text{liq}}^{\min}, \infty)$ exists such that $f(\tau^*) = 0$ and τ^* resp. $\tau^* + \Delta$ is the unique solution of (4.6). For the proof of the second part we refer to [33]. \square

Note that we search for intersection points in $(\tau_{\text{liq}}^{\min}, \tau_{\text{liq}}^{\text{sat}}] \cup (\tau_{\text{vap}}^{\text{sat}}, \infty)$, while we admit metastable initial states. This makes the intersection point unique but multiple static solutions are still admitted.

Remark 4.14 (Non-uniqueness of static Liu micro solutions).

We remark that the micro-scale model for mixture pressure admits many static solutions. Since the modified pressure (4.1) is constant between the saturation states $\tau_{\text{liq}}^{\text{sat}}, \tau_{\text{vap}}^{\text{sat}}$, any solutions with initial states $\tau_L \in [\tau_{\text{liq}}^{\text{sat}}, \tau_{\text{liq}}^{\text{max}})$, $\tau_R \in (\tau_{\text{vap}}^{\min}, \tau_{\text{vap}}^{\text{sat}}]$ and $v_L = v_R \in \mathbb{R}$ are static, cf. [33]. Figure 4.4 (left) illustrates the reason: Lax curves are constant between the saturation states. The figure on the right hand side shows the case for $v_L < v_R$.

4.3 Algorithm and illustrating examples

We are now able to state the algorithm of the *Liu microsolver*, denoted by $\mathcal{M}_{\text{Liu}}^z$ resp. $\tilde{\mathcal{M}}_{\text{Liu}}^z$. The subscript $_{\text{Liu}}$ refers to the entropy condition. The superscript z indicates that this is a microsolver for the Riemann problem with mixture pressure function (Definition 4.4) and not of the original micro-scale model (Definition 3.5).

Algorithm 4.15 (Liu microsolver $\mathcal{M}_{\text{Liu}}^\zeta$).

Let the arguments $(\tau_L, v_L, \tau_R, v_R, \zeta) \in \mathcal{A}_{\text{liq}} \times \mathbb{R} \times \mathcal{A}_{\text{vap}} \times \mathbb{R} \times \mathcal{Z}$ of the microsolver map (3.9) be given.

Step 1. Determine the points in \mathcal{A} where the solution alters its structure. That are $\tau_{\text{liq/vap}}^{\text{sat}}$ due to (2.10) and $\bar{\tau}$ due to Lemma 4.10.

Step 2. Find $\tau^* \in (\tau_{\text{liq}}^{\text{min}}, \tau_{\text{liq}}^{\text{sat}}] \cup (\tau_{\text{vap}}^{\text{sat}}, \infty)$, that solves (4.6).

Step 3. Return $(\tau_{\text{liq}}, v_{\text{liq}}, \tau_{\text{vap}}, v_{\text{vap}}, \mathfrak{s})$:

- In case of $\tau^* \in (\tau_{\text{liq}}^{\text{min}}, \tau_{\text{liq}}^{\text{sat}}]$, the value τ_{liq} is the first argument of P^ζ in Table 4.1 (gray column) and τ_{vap} is the second argument. The velocities are $v_{\text{liq}} = v_L + G^\zeta(\tau_L, \tau_{\text{liq}})$ and $v_{\text{vap}} = v_{\text{liq}} + P^\zeta(\tau_{\text{liq}}, \tau_{\text{vap}})$ and the speed is $\mathfrak{s} = \mathfrak{s}_1^\zeta(\tau_{\text{liq}}, \tau_{\text{vap}})$.
- In case of $\tau^* \in (\tau_{\text{vap}}^{\text{sat}}, \infty)$, the value τ_{liq} is the first argument of P^ζ in Table 4.2 (gray column) and τ_{vap} is the second argument. The velocities are $v_{\text{vap}} = v_R - G^\zeta(\tau_{\text{vap}}, \tau_R)$ and $v_{\text{liq}} = v_{\text{vap}} - P^\zeta(\tau_{\text{liq}}, \tau_{\text{vap}})$ and the speed is $\mathfrak{s} = \mathfrak{s}_2^\zeta(\tau_{\text{liq}}, \tau_{\text{vap}})$.

Recall that Figure 4.2 and Figure 4.3 illustrate typical shapes of the first resp. second family. The final solution is a composition of both. We show further examples of Liu micro solutions.

Example 4.16 (Liu micro solution and Lax curves).

The initial states for the first example are $\mathbf{U}_L = (0.5, 0)^\top$ and $\mathbf{U}_R = (15, 2)^\top$. The Liu micro solution for $\zeta = 0$ and the mixture van der Waals pressure of Example 2.4 is shown in Figure 4.5. The micro solution is a composition of wave type 3_L^ζ and wave type 3_R^ζ in Table 4.1 and Table 4.2. The wave of type 3_L^ζ consists of a rarefaction wave, followed by an evaporation wave and an attached rarefaction wave. A wave of type 3_R^ζ is solely a shock wave.

The monotone increasing Lax curve of the first family intersects with the monotone decreasing Lax curve of the second family in the point $(\tau^*, v^*) \approx (12.65, 2.24)$. Note that the Lax curves are constant in the metastable/mixture region.

Example 4.17 (Static Liu micro solution).

The second example intends to check the basic property, that thermodynamic equilibrium solutions are preserved, cf. Lemma 3.7. The saturation states $\tau_{\text{liq}}^{\text{sat}} \approx 0.553336$, $\tau_{\text{vap}}^{\text{sat}} \approx 3.1276$ for the mixture van der Waals pressure of Example 2.4 with $\zeta = 0$ are used as initial states

$$\mathbf{U}_0(\xi) = \begin{cases} (\tau_{\text{liq}}^{\text{sat}}, 0)^\top & \text{for } \xi \leq 0, \\ (\tau_{\text{vap}}^{\text{sat}}, 0)^\top & \text{for } \xi > 0. \end{cases}$$

The red curves of Figure 4.6 show that the Liu micro solution coincides with the equilibrium solution. As expected $\mathbf{U}(\xi, t) = \mathbf{U}_0(\xi)$ for $t \geq 0$.

Example 4.18 (Influence of the surface tension term ζ).

This example uses the same initial condition as the previous one, but for the pressure p^ζ with $\zeta \neq 0$. The green curves in Figure 4.6 show that the Liu micro solution for $\zeta = -0.01$ is a composition of an evaporating wave with speed $\mathfrak{s} \approx -0.0027$ followed by a shock wave or a composition of type 5_L^ζ and type 3_R^ζ . The Liu micro solution for $\zeta = +0.01$ (the blue

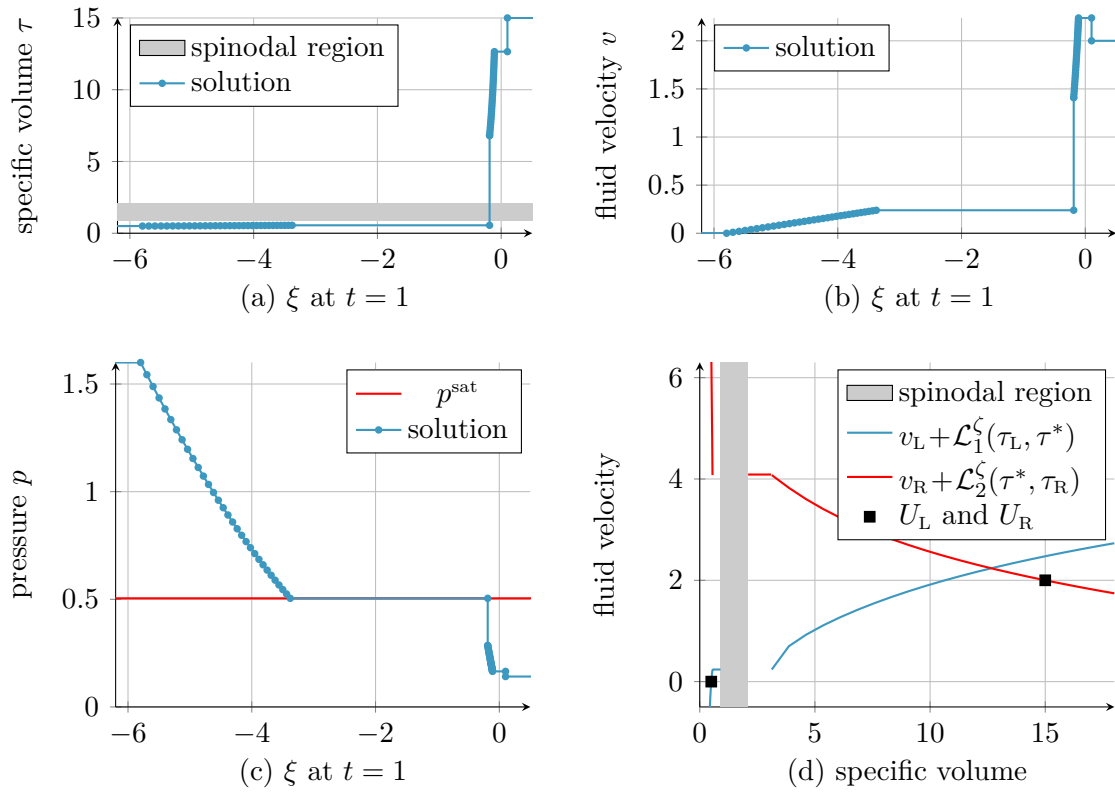


Figure 4.5: Liu micro solution of Example 4.16. The figures show (a) the specific volume, (b) the velocity and (c) the pressure over the Lagrangian space variable at time $t = 1$. The Lax curves of the first (blue) and the second (red) family are drawn in figure (d). The initial states are marked with a square.

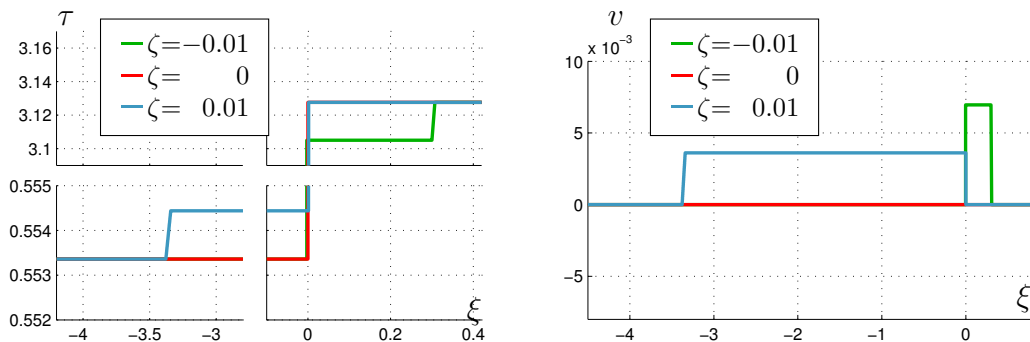


Figure 4.6: Liu micro solutions for different mixture pressure functions p^ζ due to different surface tension terms ζ . The left figure shows the specific volume and the right one the velocity as function of the Lagrangian space variable at time $t = 1$.

curve) is a composition of a rarefaction wave followed by a condensation wave with speed $\mathfrak{s} \approx 0.0014$ or a composition of type 1_L^ζ and type 2_R^ζ .

One can interpret this example as considering a spherical bubble or droplet of the same radius (cf. Remark 2.1) with the same pressure and Gibbs free energy inside and outside. In both cases, the radius decreases in order to compensate the pressure difference due to the Young-Laplace law. Note that due to that law, the pressure inside a static bubble or droplet has to be higher than outside.

4.4 Interim conclusion

We have seen, modifying the pressure (4.1) is an effective way to handle surface tension on the level of Riemann problems. In view of the application of the microsolvers for the interfacial flux computation (see Algorithm 3.1), it is reasonable to consider constant surface tension values. Recall that the curvature term is updated on every application of the microsolver.

The Liu microsolver preserves thermodynamic equilibrium solutions, cf. Example 4.17. However, it admits several static solutions, see Remark 4.14. They appear if both initial volumes are in the metastable/mixture region and if the initial velocities are equal. However, this plays a minor role since a numerical scheme, that applies the microsolver, inserts small errors to the initial velocity.

The constant line connecting the saturation points in (4.1) has a more severe effect. In the metastable region the pressure used for the Liu microsolver differs from the bulk pressure. That however means macro-scale and micro-scale model obey different entropy principles what may cause an artificial entropy increase. A concrete demonstration of such a behavior will be shown later in Example 9.8, when a bulk solver is available.

To overcome this problem one may use the mixture pressure function also in the macro-scale model. A global definition of p^ζ however requires globally constant surface tension what is in general not possible. The next chapter introduces an alternative approach to the Liu entropy which does not rely on monotone pressure functions. This will finally lead to a microsolver for the sharp interface approach with global entropy decay.

Chapter 5

Microsolver for monotone decreasing kinetic functions

In the last chapter, the Liu's criterion of Definition 4.6 was applied to single out discontinuous waves. The approach requires monotone pressure laws. However, modifying p like in Definition 4.1 leads to entropy solutions with respect to the modified pressure as discussed in Section 4.4. A different choice to determine the solution of the two-phase Riemann problem is yet another algebraic coupling condition.

Exact Riemann solvers for mixed hyperbolic-elliptic problems with kinetic functions are available since the early nineties, see in particular [47]. However, they either rely on simple kinetic functions [26, 48] or on very simple equations of state [35]. Merkle and Rohde for instance introduced in [58] linear kinetic functions for the isothermal Euler model (Definition 2.8) and van der Waals fluids. This Chapter provides microsolvers which are applicable for equations of state of real fluids (under the conditions of Definition 2.2) and any thermodynamically consistent monotone decreasing kinetic functions.

Colombo and Priuli introduced in [19] Riemann solutions for the two-phase p-system (Definition 3.5) with homogeneous Rankine-Hugoniot conditions ($\zeta \equiv 0$). The solutions are subjected to monotone decreasing kinetic functions and initial states in stable phases.

In Section 5.1, we enhance their approach for the case with surface tension and for initial data in the metastable region. Theorem 5.7 presents well-posedness results. Section 5.2 introduces the algorithm of the corresponding microsolver for a given kinetic function. Note that our implementation allows equations of state, provided by external thermodynamic libraries like [6].

In this chapter it is assumed, that kinetic functions are just given. Examples for such functions and a detailed study on their properties follow in Chapter 6. Hence, also the thermodynamic verification and validation of the new microsolvers, as well as, the interim conclusion are shifted to the end of the next chapter. In this chapter, we concentrate on the definition and technical issues of the microsolvers.

5.1 Solving the generalized Riemann problem exactly

We consider the micro-scale model in Lagrangian coordinates (Definition 3.5) and all equations of state refer to Definition 2.2. Let therefore initial states $(\tau_L, v_L)^\top$, $(\tau_R, v_R)^\top$ and a constant surface tension term be given. The required additional condition to attain unique solutions are kinetic functions. Later on subsonic phase transitions are constrained to those which are related to a kinetic function.

Definition 5.1 (Pair of monotone decreasing kinetic functions).

Let the fixed surface tension term $\zeta \in \mathcal{Z}$, corresponding equations of state from Definition 2.2, numbers $\tau_{\text{liq}}^{\text{sc}} \in (\tau_{\text{liq}}^{\text{min}}, \tau_{\text{liq}}^{\text{sat}})$, $\tau_{\text{vap}}^{\text{se}} \in (\tau_{\text{vap}}^{\text{min}}, \infty)$ and two differentiable functions

$$k_c : [\tau_{\text{liq}}^{\text{sc}}, \tau_{\text{liq}}^{\text{sat}}] \rightarrow \mathcal{A}_{\text{vap}} \quad \text{and} \quad k_e : [\tau_{\text{vap}}^{\text{sat}}, \tau_{\text{vap}}^{\text{se}}] \rightarrow \mathcal{A}_{\text{liq}}$$

be given.

We call (k_c, k_e) a **pair of monotone decreasing kinetic functions** if $k'_c \leq 0$, $k'_e \leq 0$ and the following conditions are satisfied

$$\llbracket \psi(\tau) \rrbracket + \llbracket \tau \rrbracket \{p(\tau)\} + \zeta \{\tau\} \begin{cases} \geq 0 & \text{for all } \tau_{\text{liq}} \in [\tau_{\text{liq}}^{\text{sc}}, \tau_{\text{liq}}^{\text{sat}}], \tau_{\text{vap}} = k_c(\tau_{\text{liq}}), \\ \leq 0 & \text{for all } \tau_{\text{vap}} \in [\tau_{\text{vap}}^{\text{sat}}, \tau_{\text{vap}}^{\text{se}}], \tau_{\text{liq}} = k_e(\tau_{\text{vap}}) \end{cases} \quad (5.1)$$

with $\llbracket \tau \rrbracket = \tau_{\text{vap}} - \tau_{\text{liq}}$ and $\{\tau\} = \frac{1}{2}(\tau_{\text{liq}} + \tau_{\text{vap}})$ and

$$\begin{aligned} k_c(\tau_{\text{liq}}^{\text{sat}}) &= \tau_{\text{vap}}^{\text{sat}}, & k_c(\tau_{\text{liq}}^{\text{sc}}) &= \tau_{\text{vap}}^{\text{sc}}, & \left| \mathfrak{s}_c(\tau_{\text{liq}}^{\text{sc}}, \tau_{\text{vap}}^{\text{sc}}) \right| &= c(\tau_{\text{vap}}^{\text{sc}}), \\ k_e(\tau_{\text{vap}}^{\text{sat}}) &= \tau_{\text{liq}}^{\text{sat}}, & k_e(\tau_{\text{vap}}^{\text{se}}) &= \tau_{\text{liq}}^{\text{se}}, & \left| \mathfrak{s}_e(\tau_{\text{liq}}^{\text{se}}, \tau_{\text{vap}}^{\text{se}}) \right| &= c(\tau_{\text{vap}}^{\text{se}}), & k'_e(\tau_{\text{vap}}^{\text{se}}) &= 0. \end{aligned}$$

Note that sonic condensation waves are determined by the end states $\tau_{\text{liq}}^{\text{sc}}, \tau_{\text{vap}}^{\text{sc}}$. The same holds for sonic evaporation waves with the states $\tau_{\text{vap}}^{\text{se}} = \tau_{\text{liq}}^{\text{se}}$. The superscripts ^{sc}, ^{se} stand for *sonic condensation* and *sonic evaporation*, respectively.

In this chapter, we will consider pairs of monotone decreasing kinetic functions in order to single out a unique two-phase Riemann solution. Examples of such functions will be given in Chapter 6. The subsequent chapters will also discuss the question if monotone decreasing kinetic functions occur in nature.

Definition 5.2 (Admissible phase transition).

A phase transition, that connects a left state $\mathbf{U}_l = (\tau_l, v_l)^\top \in \mathcal{A} \times \mathbb{R}$ and a right state $\mathbf{U}_r = (\tau_r, v_r)^\top \in \mathcal{A} \times \mathbb{R}$ is called **admissible phase transition** if and only if

- it is a sonic or a supersonic wave of Lax type (3.15), or
- it is a subsonic condensation wave that satisfies $k_c(\tau_{\text{liq}}) = \tau_{\text{vap}}$, or
- it is a subsonic evaporation wave that satisfies $k_e(\tau_{\text{vap}}) = \tau_{\text{liq}}$,

where k_c and k_e are a pair of monotone decreasing kinetic functions as in Definition 5.1.

type	τ_L	τ^*	composition	$\mathcal{L}_1(\tau_L, \tau^*)$		
1 _L	\mathcal{A}_{liq}	\mathcal{A}_{liq}	1E	$G(\tau_L, \tau^*)$		
2 _L	\mathcal{A}_{liq}	$[\tau_{\text{vap}}^{\text{sat}}, \tau_{\text{vap}}^{\text{se}}]$	1E-UE	$G(\tau_L, k_e(\tau^*))$	$+P(k_e(\tau^*), \tau^*)$	
3 _L	\mathcal{A}_{liq}	$(\tau_{\text{vap}}^{\text{se}}, \infty)$	1E-UE-1R	$G(\tau_L, \tau_{\text{liq}}^{\text{se}})$	$+P(\tau_{\text{liq}}^{\text{se}}, \tau_{\text{vap}}^{\text{se}})$	$+R(\tau_{\text{vap}}^{\text{se}}, \tau^*)$

Table 5.1: Definition of the map $\mathcal{L}_1 : \mathcal{A}_{\text{liq}} \times \mathcal{A}_{\text{liq}} \cup [\tau_{\text{vap}}^{\text{sat}}, \infty) \rightarrow \mathbb{R}$, that determines the Lax curve $v^* = v_L + \mathcal{L}_1(\tau_L, \tau^*)$ of the first family. The resulting (multiple) waves for left and right trace specific volume values τ_L and τ^* are composed of the waves given in the fourth column (from left to right): 1E stands for 1-elementary wave, 1R for 1-rarefaction wave, UE for subsonic (undercompressive) evaporation wave. The functions G , P and R are given in Section 3.3.

Note that with (5.1), it follows that all admissible phase transitions satisfy the entropy inequality (3.11). Furthermore, thermodynamic equilibrium solutions (cf. Lemma 3.7) are admissible subsonic phase transitions.

We seek for a self-similar entropy solutions of the micro-scale model of Definition 3.5, that contains exactly one admissible phase transition. Furthermore, we prefer solutions with subsonic phase transitions, whenever this is possible. We call such a solution ***k-micro solution***, if k_c, k_e are the corresponding pair of monotone decreasing kinetic functions.

It is possible to define generalized Lax curves for these requirements. The Lax curve $v^* = v_L + \mathcal{L}_1(\tau_L, \tau^*)$ of the first family is given by Table 5.1. The corresponding 1-wave is a composition of the waves introduced in Section 3.3. The structure changes depending on the arguments τ_L and τ^* . As in the last chapter, we enumerate the different wave patterns with the symbols of the first column in the table. The subscript _L indicates that the wave connects the left initial state $(\tau_L, v_L)^\top$ to an intermediate state $(\tau^*, v^*)^\top$.

Figure 5.1 shows a wave of type 2_L and a wave of type 3_L for the equation of state

$$p(\tau) = \begin{cases} 2/\tau + 1 & : \tau \in (0, 2/3), \\ 20/\tau - 1 & : \tau \in (3, \infty) \end{cases} \quad \text{with} \quad \tau_{\text{liq}}^{\text{sat}} = 1/2, \quad \tau_{\text{vap}}^{\text{sat}} = 10/3. \quad (5.2)$$

We summarize the main properties to a proposition.

Proposition 5.3 (Properties of the generalized Lax curve \mathcal{L}_1).

Let a left state $(\tau_L, v_L)^\top \in \mathcal{A}_{\text{liq}} \times \mathbb{R}$ and the map $\mathcal{L}_1 : \mathcal{A}_{\text{liq}} \times \mathcal{A}_{\text{liq}} \cup [\tau_{\text{vap}}^{\text{sat}}, \infty) \rightarrow \mathbb{R}$ of Table 5.1 be given. Then the following properties hold.

(i) The map \mathcal{L}_1 is continuous.

(ii) The map

$$\mathcal{A}_{\text{liq}} \cup [\tau_{\text{vap}}^{\text{sat}}, \infty) \rightarrow \mathbb{R}, \quad \tau^* \mapsto v^* = v_L + \mathcal{L}_1(\tau_L, \tau^*)$$

is differentiable and strictly monotone increasing in \mathcal{A}_{liq} and in $[\tau_{\text{vap}}^{\text{sat}}, \infty)$.

(iii) It holds that $\mathcal{L}_1(\tau_L, \tau_{\text{liq}}^{\text{sat}}) = \mathcal{L}_1(\tau_L, \tau_{\text{vap}}^{\text{sat}})$.

(iv) All propagation speeds are negative. For waves of type 2_L and type 3_L the phase transition propagates faster than the elementary wave in the liquid phase and slower than the rarefaction wave connecting to τ^* in wave type 3_L.

(v) Evaporation waves are either subsonic or sonic.

(vi) The speed of an evaporation wave is limited by the sound speed $-c(\tau_{\text{vap}}^{\text{se}})$.

Proof. (i) By definition, the map \mathcal{L}_1 is piecewise continuous. It is readily checked with Table 5.1, that also the transition from one domain of definition to another is continuous.

(ii) Note that \mathcal{L}_1 is piecewise smooth. The critical point is $\tau^* = \tau_{\text{vap}}^{\text{se}}$. A short calculation gives

$$\begin{aligned} \lim_{\tau^* \rightarrow \tau_{\text{vap}}^{\text{se}}} \frac{dS}{d\tau^*}(\tau_{\text{L}}, k_e(\tau^*)) &= 0, & \lim_{\tau^* \rightarrow \tau_{\text{vap}}^{\text{se}}} \frac{dR}{d\tau^*}(\tau_{\text{L}}, k_e(\tau^*)) &= 0 \text{ with } k'_e(\tau_{\text{vap}}^{\text{se}}) = 0, \\ \lim_{\tau^* \rightarrow \tau_{\text{vap}}^{\text{se}}} \frac{dS}{d\tau^*}(\tau_{\text{vap}}^{\text{se}}, \tau^*) &= c(\tau_{\text{vap}}^{\text{se}}), & \lim_{\tau^* \rightarrow \tau_{\text{vap}}^{\text{se}}} \frac{dR}{d\tau^*}(\tau_{\text{vap}}^{\text{se}}, \tau^*) &= c(\tau_{\text{vap}}^{\text{se}}) \text{ and} \\ \lim_{\tau^* \rightarrow \tau_{\text{vap}}^{\text{se}}} \frac{dP}{d\tau}(k_e(\tau^*), \tau^*) &= c(\tau_{\text{vap}}^{\text{se}}) & \text{with } k'_e(\tau_{\text{vap}}^{\text{se}}) = 0 \text{ and } |\mathfrak{s}_e(\tau_{\text{liq}}^{\text{sc}}, \tau_{\text{vap}}^{\text{sc}})| &= c(\tau_{\text{vap}}^{\text{sc}}) \end{aligned}$$

for the functions S , R and P , introduced in Section 3.3. Thus, the derivatives of a wave of type 2_{L} and type 3_{L} coincide in $\tau_{\text{vap}}^{\text{se}}$. The functions S and R are strictly monotone increasing with respect to the second argument. A short calculation shows that \mathcal{L}_1 is strictly monotone increasing also for a wave of type 2_{L} , since $k'_e < 0$.

(iii) The condition holds, since $P(\tau_{\text{liq}}^{\text{sat}}, \tau_{\text{vap}}^{\text{sat}}) = 0$.

(iv)-(vi) By definition, all waves of the first family have non-positive propagation speeds. The speed of the evaporation wave is between $-c(\tau_{\text{vap}}^{\text{se}})$ and 0. Due to the pressure assumptions (Definition 2.2), waves in the liquid phase propagate faster (in absolute values) than the vapor sound speed. The phase transition in wave type 3_{L} is sonic and the vapor rarefaction wave is attached. \square

The generalized Lax curve of the second family may contain a condensation wave. Condensation waves change from subsonic to supersonic or vice versa in the point $\tau_{\text{liq}}^{\text{sc}}$. The next lemmas introduce further points in \mathcal{A} where the solution changes its structure. The lemmas are a direct consequence of the pressure assumptions in Definition 2.2.

The subsequent lemmas introduce values $\hat{\tau}$, $\check{\tau}$ and a function g_s . The value $\hat{\tau}$ is such that the pressure function has the same slope in τ_{R} as the chord from $(\hat{\tau}, p(\hat{\tau}) + \zeta)$ to $(\tau_{\text{R}}, p(\tau_{\text{R}}))$, see Figure 5.2 (left) for illustration. The value $\check{\tau}$ is such that the points $(\check{\tau}, p(\check{\tau}) + \zeta)$, $(\tau_{\text{vap}}^{\text{sat}}, p(\tau_{\text{vap}}^{\text{sat}}))$, $(\tau_{\text{R}}, p(\tau_{\text{R}}))$ lie on one straight line. The function g_s is determined such that the pressure function has the same slope in $g_s(\tau)$ as the chord from $(\tau, p(\tau) + \zeta)$ to $(g_s(\tau), p(g_s(\tau)))$, see Figure 5.2 (left).

For ease of notation, we skip the dependencies on numbers that are constant in the micro-scale model of Definition 3.5, i.e. $\tau_{\text{L}} \in \mathcal{A}_{\text{liq}}$, $\tau_{\text{R}} \in \mathcal{A}_{\text{vap}}$ and $\zeta \in \mathcal{Z}$. Recall that the pressure function and saturation states depend on the constant ζ , see Definition 2.2.

Lemma 5.4 (The values $\hat{\tau}$ and $\check{\tau}$).

For a fixed $\tau_{\text{R}} \in (\tau_{\text{vap}}^{\text{min}}, \tau_{\text{vap}}^{\text{sc}}]$ there exists a unique $\hat{\tau} \in \mathcal{A}_{\text{liq}}$, such that

$$p'(\tau_{\text{R}}) = \frac{p(\tau_{\text{R}}) - p(\hat{\tau}) - \zeta}{\tau_{\text{R}} - \hat{\tau}}, \quad (5.3)$$

or equivalent $\lambda_2(\tau_{\text{R}}) = \mathfrak{s}_c(\hat{\tau}, \tau_{\text{R}})$ holds. Moreover, $\hat{\tau} \in (\tau_{\text{liq}}^{\text{min}}, \tau_{\text{liq}}^{\text{sc}}]$.

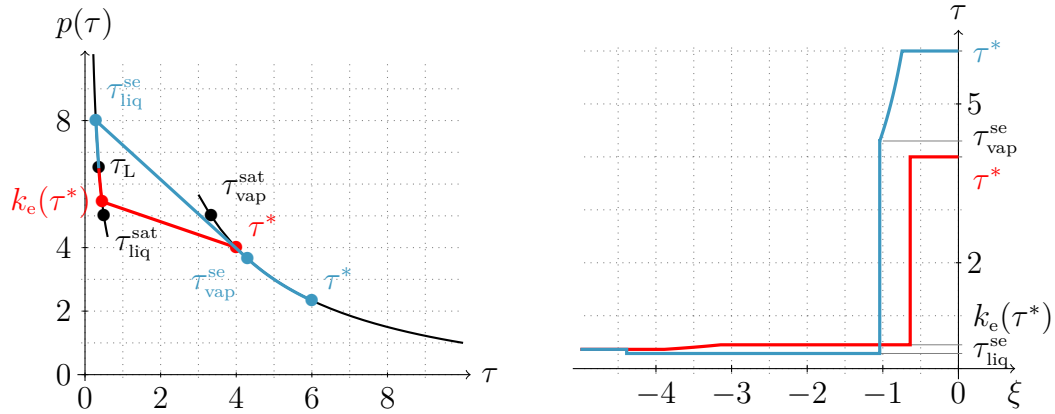


Figure 5.1: The figure on the left hand side shows the graph of (5.2). The τ -values, at which the Lax curve of the first family alters its wave structure, are pinned to the pressure graph. The red curve corresponds to wave type 2_L and the blue curve to wave type 3_L . The figure on the right hand side shows these waves at time $t = 1$ in the (τ, ξ) -plane.

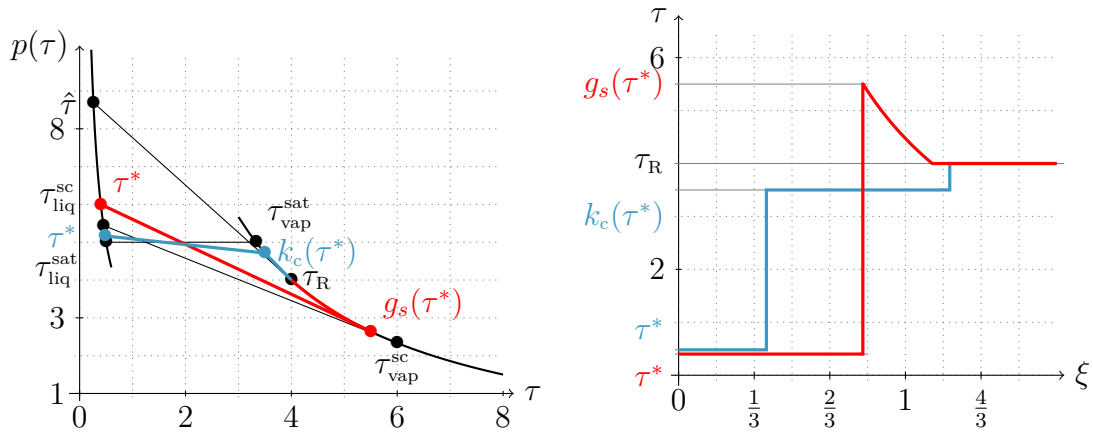


Figure 5.2: Pressure function (left) and specific volume distribution (right), like Figure 5.1. The red curve corresponds to wave type 4_R and the green curve to wave type 3_R .

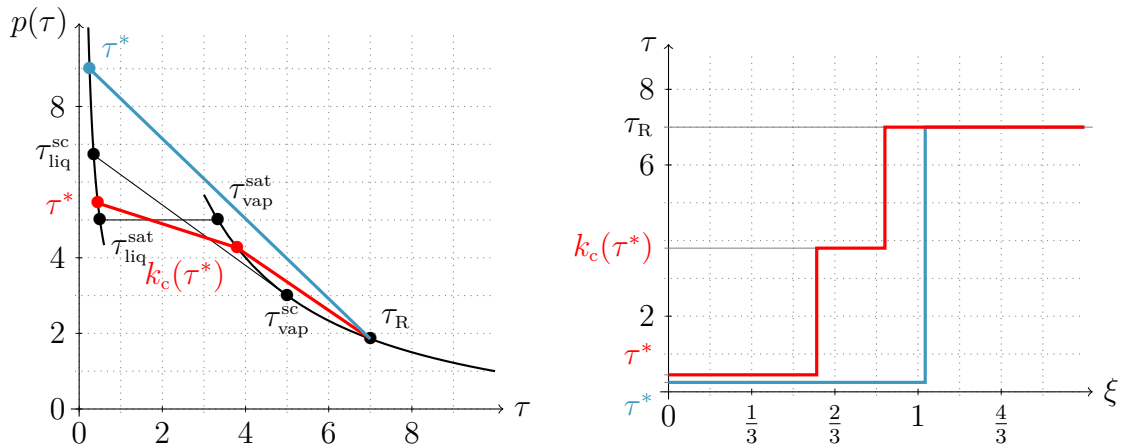


Figure 5.3: Pressure function (left) and specific volume distribution (right), like Figure 5.1. The red curve corresponds to wave type 6_R and the blue curve to wave type 5_R .

On the other hand, for fixed $\tau_R > \tau_{\text{vap}}^{\text{sc}}$, there exists a unique $\check{\tau} \in \mathcal{A}_{\text{liq}}^{\text{sc}}$, such that

$$\frac{p(k_c(\check{\tau})) - p(\check{\tau}) - \zeta}{k_c(\check{\tau}) - \check{\tau}} = \frac{p(\tau_R) - p(\check{\tau}) - \zeta}{\tau_R - \check{\tau}},$$

or equivalent $\mathfrak{s}_c(\check{\tau}, k_c(\check{\tau})) = \mathfrak{s}_2(k_c(\check{\tau}), \tau_R)$ holds. Moreover, $\check{\tau} \in (\tau_{\text{liq}}^{\text{sc}}, \tau_{\text{liq}}^{\text{sat}})$.

At the value $\hat{\tau}$, a supersonic condensation wave (see wave of type 2_R in Table 5.2) splits up into a sonic condensation wave and a 2-rarefaction wave. At the value $\check{\tau}$, a supersonic condensation wave (see wave of type 5_R) breaks into a subsonic condensation wave and a 2-shock wave.

Proof of Lemma 5.4. Define the function

$$\hat{f}(\tau; \tau_R) := p'(\tau_R) - \frac{p(\tau_R) - p(\tau) - \zeta}{\tau_R - \tau}, \quad \text{whereby} \quad \lim_{\tau \rightarrow \tau_{\text{liq}}^{\text{min}}} \hat{f}(\tau; \tau_R) = \infty$$

holds due to (2.11). By definition of the points $\tau_{\text{liq}}^{\text{sc}}, \tau_{\text{vap}}^{\text{sc}}$ we find $\hat{f}(\tau_{\text{liq}}^{\text{sc}}; \tau_R) < \hat{f}(\tau_{\text{liq}}^{\text{sc}}; \tau_{\text{vap}}^{\text{sc}}) = 0$. The function \hat{f} is continuous, thus $\hat{\tau} \in (\tau_{\text{liq}}^{\text{min}}, \tau_{\text{liq}}^{\text{sc}}]$ exists where $\hat{f}(\hat{\tau}; \tau_R) = 0$. The derivation $\hat{f}'(\tau; \tau_R) = \left(p'(\tau) - \frac{p(\tau_R) - p(\tau) - \zeta}{\tau_R - \tau} \right) / (\tau_R - \tau)$ is positive due to $\tau \in \mathcal{A}_{\text{liq}}$ and Lemma 2.3. Thus, $\hat{\tau}$ exists uniquely.

For the second part define

$$\check{f}(\tau) := \frac{p(k_c(\tau)) - p(\tau) - \zeta}{k_c(\tau) - \tau} - \frac{p(\tau_R) - p(k_c(\tau))}{\tau_R - k_c(\tau)}.$$

Note that $k_c(\tau_{\text{liq}}^{\text{sc}}) = \tau_{\text{vap}}^{\text{sc}}$ and $k_c(\tau_{\text{liq}}^{\text{sat}}) = \tau_{\text{vap}}^{\text{sat}}$. With (2.9) there holds $\check{f}(\tau_{\text{liq}}^{\text{sc}}) < 0$ and with (2.8) $\check{f}(\tau_{\text{liq}}^{\text{sat}}) > 0$. The function \check{f} is continuous such that there exists $\check{\tau} \in (\tau_{\text{liq}}^{\text{sc}}, \tau_{\text{liq}}^{\text{sat}})$ with $\check{f}(\check{\tau}) = 0$. For uniqueness, we show that \check{f} is strictly monotone increasing. From (2.12), it follows that $p'(\tau) < p'(k_c(\tau))$ for $\tau \in [\tau_{\text{liq}}^{\text{sc}}, \tau_{\text{liq}}^{\text{sat}}]$. This is applied to \check{f}' :

$$\begin{aligned} \check{f}'(\tau) &> \frac{k'_c(\tau) - 1}{k_c(\tau) - \tau} \left(p'(k_c(\tau)) - \frac{p(k_c(\tau)) - p(\tau) - \zeta}{k_c(\tau) - \tau} \right) \\ &\quad + \frac{k'_c(\tau)}{\tau_R - k_c(\tau)} \left(p'(k_c(\tau)) - \frac{p(\tau_R) - p(k_c(\tau))}{\tau_R - k_c(\tau)} \right) > 0. \end{aligned}$$

The first bracket is zero for $\tau = \tau_{\text{liq}}^{\text{sc}}$ and negative otherwise. The second bracket is negative due to (2.9). Thus, $\check{\tau}$ is uniquely determined. \square

Waves of type 3_R^ζ are composed of a sonic condensation wave and an attached 2-rarefaction wave, cf. Table 5.2. The following lemma is helpful to find the characteristic point.

Lemma 5.5 (The function g_s).

For any given $\tau_R \in (\tau_{\text{vap}}^{\text{min}}, \tau_{\text{vap}}^{\text{sc}}]$, equation (5.3) provides a unique $\hat{\tau} \in (\tau_{\text{liq}}^{\text{min}}, \tau_{\text{liq}}^{\text{sc}}]$. There exists a continuous monotone increasing function $g_s : [\hat{\tau}, \tau_{\text{liq}}^{\text{sc}}] \rightarrow [\tau_R, \tau_{\text{vap}}^{\text{sc}}]$, $\tau \mapsto g_s(\tau)$ such that

$$p'(g_s(\tau)) = \frac{p(g_s(\tau)) - p(\tau) - \zeta}{g_s(\tau) - \tau},$$

or equivalent $\lambda_2(g_s(\tau)) = \mathfrak{s}_c(g_s(\tau), \tau)$ holds.

type	τ^*	τ_R	composition	$\mathcal{L}_2(\tau^*, \tau_R)$
1 _R	\mathcal{A}_{vap}	\mathcal{A}_{vap}	2E	$+G(\tau^*, \tau_R)$
2 _R	$(\tau_{\text{liq}}^{\min}, \hat{\tau}]$	$(\tau_{\text{vap}}^{\min}, \tau_{\text{vap}}^{\text{sc}}]$	LC	$P(\tau^*, \tau_R)$
3 _R	$(\hat{\tau}, \tau_{\text{liq}}^{\text{sc}}]$	$(\tau_{\text{vap}}^{\min}, \tau_{\text{vap}}^{\text{sc}}]$	SC-2R	$P(\tau^*, g_s(\tau^*)) + R(g_s(\tau^*), \tau_R)$
4 _R	$[\tau_{\text{liq}}^{\text{sc}}, \tau_{\text{liq}}^{\text{sat}}]$	$(\tau_{\text{vap}}^{\min}, \tau_{\text{vap}}^{\text{sc}}]$	KC-2E	$P(\tau^*, k_c(\tau^*)) + G(k_c(\tau^*), \tau_R)$
5 _R	$(\tau_{\text{liq}}^{\min}, \check{\tau}]$	$(\tau_{\text{vap}}^{\text{sc}}, \infty)$	LC	$P(\tau^*, \tau_R)$
6 _R	$(\check{\tau}, \tau_{\text{liq}}^{\text{sat}}]$	$(\tau_{\text{vap}}^{\text{sc}}, \infty)$	KC-2S	$P(\tau^*, k_c(\tau^*)) + S(k_c(\tau^*), \tau_R)$

Table 5.2: Definition of the map $\mathcal{L}_2 : (\tau_{\text{liq}}^{\min}, \tau_{\text{liq}}^{\text{sat}}] \cup \mathcal{A}_{\text{vap}} \times \mathcal{A}_{\text{vap}} \rightarrow \mathbb{R}$, that determines the Lax curve $v^* = v_R + \mathcal{L}_2(\tau^*, \tau_R)$ of the second family. The resulting (multiple) waves for left and right trace specific volume values τ^* and τ_R are composed of the waves given in the fourth column (from left to right): 2E stands for 2-elementary wave, SC for sonic condensation, LC for supersonic (Lax-type) condensation and KC for stands for a condensation wave that is related to a kinetic function. The functions G , P , R and S are given in Section 3.3.

Note that the domain of definition depends on $\hat{\tau}$ and thus on τ_R . The function g_s does not depend on τ_R , however the restriction to $[\hat{\tau}, \tau_{\text{liq}}^{\text{sc}}]$ guarantees the existence of g_s .

Proof of Lemma 5.5. We apply the implicit function theorem to the function

$$F(\tau_{\text{liq}}, \tau_{\text{vap}}) := p'(\tau_{\text{vap}})(\tau_{\text{vap}} - \tau_{\text{liq}}) - p(\tau_{\text{vap}}) + p(\tau_{\text{liq}}) + \zeta.$$

With (5.3), it follows that $F(\hat{\tau}, \tau_R) = 0$. The local existence of the function g_s follows from $\partial F / \partial \tau_{\text{liq}} = -p'(\tau_{\text{vap}}) + p'(\tau_{\text{liq}}) < 0$ with (2.12). We can proceed with the latter argument until $\tau_{\text{liq}}^{\text{sc}}$ is reached, where $F(\tau_{\text{liq}}^{\text{sc}}, \tau_{\text{vap}}^{\text{sc}}) = 0$ holds.

With (2.9) it holds that $\partial F / \partial \tau_{\text{vap}} = p''(\tau_{\text{vap}})(\tau_{\text{vap}} - \tau_{\text{liq}}) > 0$. The monotonicity follows from $\frac{dF}{d\tau}(\tau, g_s(\tau)) = \partial F / \partial \tau_{\text{liq}} + \partial F / \partial \tau_{\text{vap}} g'_s(\tau) = 0$. \square

The Lax curves $v^* = v_R + \mathcal{L}_2(\tau^*, \tau_R)$ of the second family are given by Table 5.2 and the main properties are summarized to the proposition below. Examples of wave type 3_R and wave type 4_R are shown in Figure 5.2, while Figure 5.3 shows an example of waves type 5_R and wave type 6_R.

Proposition 5.6 (Properties of the generalized Lax curve \mathcal{L}_2).

Let a right state $(\tau_R, v_R)^\top \in \mathcal{A}_{\text{vap}} \times \mathbb{R}$ and the map $\mathcal{L}_2 : (\tau_{\text{liq}}^{\min}, \tau_{\text{liq}}^{\text{sat}}] \cup \mathcal{A}_{\text{vap}} \times \mathcal{A}_{\text{vap}} \rightarrow \mathbb{R}$ of Table 5.2 be given. Then the following properties hold.

(i) The map \mathcal{L}_2 is continuous.

(ii) The map

$$(\tau_{\text{liq}}^{\min}, \tau_{\text{liq}}^{\text{sat}}] \cup \mathcal{A}_{\text{vap}} \rightarrow \mathbb{R}, \quad \tau^* \mapsto v^* = v_R + \mathcal{L}_2(\tau^*, \tau_R)$$

is differentiable and strictly monotone decreasing in $(\tau_{\text{liq}}^{\min}, \tau_{\text{liq}}^{\text{sat}}]$ and in \mathcal{A}_{vap} .

(iii) It holds that $\mathcal{L}_2(\tau_{\text{liq}}^{\text{sat}}, \tau_R) = \mathcal{L}_2(\tau_{\text{vap}}^{\text{sc}}, \tau_R)$.

(iv) All propagation speeds are positive. In wave 3_R, 4_R and 6_R, the phase transition propagates slower than the elementary wave in the vapor phase.

(v) *There are subsonic sonic and supersonic condensation waves.*

Proof. (i) The map \mathcal{L}_2 is piecewise continuous and it is readily checked with Table 5.2, that also the transition from one domain of definition to another one is continuous.

(ii) Note that \mathcal{L}_2 is piecewise smooth. The critical point in the transition of wave type 2_R to wave type 3_R is $\tau^* = \hat{\tau}$, in the transition of wave type 3_R to wave type 4_R it is $\tau^* = \tau_{\text{liq}}^{\text{se}}$ and from type 5_R to type 6_R it is $\tau^* = \check{\tau}$. For later use we derive

$$\begin{aligned} \frac{dP}{d\tau}(\tau, g(\tau)) &= \frac{(g'(\tau) - 1) \mathfrak{s}_c(\tau, g(\tau))}{2} + \frac{c^2(g(\tau)) g'(\tau) - c^2(\tau)}{2 \mathfrak{s}_c(\tau, g(\tau))}, \\ \frac{dS}{d\tau}(g(\tau), \tau_R) &= -\frac{g'(\tau) \mathfrak{s}_2(g(\tau), \tau_R)}{2} - \frac{c^2(g(\tau)) g'(\tau)}{2 \mathfrak{s}_2(g(\tau), \tau_R)} \end{aligned}$$

for some smooth function g with $\tau < g(\tau) < \tau_R$, the sound speed c in (2.13) and propagation speeds in Section 3.3. Furthermore, there holds $\frac{dR}{d\tau}(g(\tau), \tau_R) = -c(g(\tau)) g'(\tau)$.

We first check the limit $\tau^* \rightarrow \hat{\tau}$ and $\tau_R \in (\tau_{\text{vap}}^{\text{min}}, \tau_{\text{vap}}^{\text{sc}}]$. Note that $g_s(\hat{\tau}) = \tau_R$ and $\mathfrak{s}_c(\hat{\tau}, \tau_R) = c(\tau_R)$ with Lemma 5.5. We use above derivative with $g = g_s$ to find

$$\begin{aligned} \lim_{\tau^* \rightarrow \hat{\tau}} \frac{dP}{d\tau^*}(\tau^*, \tau_R) &= \frac{-1}{2} \left(c(\tau_R) + \frac{c^2(\hat{\tau})}{c(\tau_R)} \right), \quad \lim_{\tau^* \rightarrow \hat{\tau}} \frac{dR}{d\tau^*}(g_s(\tau^*), \tau_R) = -g'_s(\hat{\tau}) c(\tau_R), \\ \lim_{\tau^* \rightarrow \hat{\tau}} \frac{dP}{d\tau^*}(\tau^*, g_s(\tau^*)) &= \frac{-1}{2} \left(c(\tau_R) + \frac{c^2(\hat{\tau})}{c(\tau_R)} \right) + g'_s(\hat{\tau}) c(\tau_R). \end{aligned}$$

Thus, the derivatives of a wave of type 2_R and a wave of type 3_R coincide in $\tau^* = \hat{\tau}$.

Now we check the limit $\tau^* \rightarrow \tau_{\text{liq}}^{\text{sc}}$ at $\tau_R \in (\tau_{\text{vap}}^{\text{min}}, \tau_{\text{vap}}^{\text{sc}}]$. Here, it holds $k_c(\tau_{\text{liq}}^{\text{sc}}) = g_s(\tau_{\text{liq}}^{\text{sc}}) = \tau_{\text{vap}}^{\text{sc}}$ and $\mathfrak{s}_c(\tau_{\text{liq}}^{\text{sc}}, \tau_{\text{vap}}^{\text{sc}}) = c(\tau_{\text{vap}}^{\text{sc}})$ with Definition 5.1. We find

$$\begin{aligned} \lim_{\tau^* \rightarrow \tau_{\text{liq}}^{\text{sc}}} \frac{dP}{d\tau^*}(\tau^*, k_c(\tau^*)) &= \frac{-1}{2} \left(c(\tau_{\text{vap}}^{\text{sc}}) + \frac{c^2(\tau_{\text{liq}}^{\text{sc}})}{c(\tau_{\text{vap}}^{\text{sc}})} \right) + c(\tau_{\text{vap}}^{\text{sc}}) k'_c(\tau_{\text{liq}}^{\text{sc}}), \\ \lim_{\tau^* \rightarrow \tau_{\text{liq}}^{\text{sc}}} \frac{dR}{d\tau^*}(k_c(\tau^*), \tau_R) &= \lim_{\tau^* \rightarrow \tau_{\text{liq}}^{\text{sc}}} \frac{dS}{d\tau^*}(k_c(\tau^*), \tau_R) = -c(\tau_{\text{vap}}^{\text{sc}}) k'_c(\tau_{\text{liq}}^{\text{sc}}). \end{aligned}$$

The term with k'_c cancels in wave type 4_R such that the result is independent of the function k_c . The same can be done for wave type 3_R replacing k_c by g_s . This leads to the same result and thus the derivatives coincide in $\tau^* = \tau_{\text{liq}}^{\text{sc}}$.

Finally, we have to check the limit $\tau^* \rightarrow \check{\tau}$ and $\tau_R \in (\tau_{\text{vap}}^{\text{sc}}, \infty)$. With Lemma 5.4, it holds $\mathfrak{s}_c(\check{\tau}, k_c(\check{\tau})) = \mathfrak{s}_2(k_c(\check{\tau}), \tau_R) = \mathfrak{s}_c(\check{\tau}, \tau_R)$. With above derivatives, we find that the limits from both sides (type 5_R and type 6_R) are

$$\lim_{\tau^* \rightarrow \check{\tau}} \frac{d\mathcal{L}_2}{d\tau^*}(\tau^*, \tau_R) = \frac{-1}{2} \left(\mathfrak{s}_c(\check{\tau}, \tau_R) + \frac{-c^2(\check{\tau})}{\mathfrak{s}_c(\check{\tau}, \tau_R)} \right).$$

Monotonicity: the functions G and P are strictly decreasing with respect to the first argument, thus for wave type 1_R , type 2_R and type 5_R , there is nothing to do.

Consider $\frac{d\mathcal{L}_2}{d\tau^*}(\tau^*, \tau_R)$ in case of wave type 3_R . All terms with g'_s cancel out since $\mathfrak{s}_c(\tau^*, g_s(\tau^*)) = c(g_s(\tau^*))$ holds. The remaining terms are negative such that $\mathcal{L}_2(\cdot, \tau_R)$ is a strictly decreasing function. The same holds for wave type 4_R with $k_c(\tau^*) > \tau_R$. The wave

is composed of a condensation wave and an attached 2-rarefaction wave, cf. wave type 3_R , and all terms with k'_c cancel out.

In wave type 4_R with $k_c(\tau^*) < \tau_R$ and type 6_R , the function k_c is monotonously decreasing and the term $\mathfrak{s}_c + c^2(\tau^*)/\mathfrak{s}_c$ is positive. Thus, it remains to demonstrate that

$$\mathfrak{s}_c(\tau^*, k_c(\tau^*)) + \frac{c^2(k_c(\tau^*))}{\mathfrak{s}_c(\tau^*, k_c(\tau^*))} - \mathfrak{s}_2(k_c(\tau^*), \tau_R^*) - \frac{c^2(k_c(\tau^*))}{\mathfrak{s}_2(k_c(\tau^*), \tau_R^*)} \geq 0.$$

We skip the dependencies and rearrange the inequality: $(\mathfrak{s}_2 - \mathfrak{s}_c) \left(\frac{c^2}{\mathfrak{s}_c \mathfrak{s}_2} - 1 \right) \geq 0$. This is true since the speeds in waves of type 4_R and type 6_R satisfy $c > \mathfrak{s}_2 \geq \mathfrak{s}_c$. Thus, $\mathcal{L}_2(\cdot, \tau_R)$ is a strictly decreasing function.

(iii) The condition holds due to $P(\tau_{\text{liq}}^{\text{sat}}, \tau_{\text{vap}}^{\text{sat}}) = 0$.

(iv), (v) By definition, all waves of the second family have non-negative propagation speeds. The propagation speed of sonic and subsonic condensation waves is less than the sound speed in the vapor. The (supersonic) condensation wave in waves of type 2_R propagates faster than sound. □

The solution of the micro-scale model exists as soon as the two generalized Lax curves intersect each other. As in the case of the Liu micro solution, we constrain the set of admissible intersection points to enforce uniqueness.

Theorem 5.7 (Existence and uniqueness of k -micro solutions).

Let a pair of monotone decreasing kinetic functions k_c, k_e as in Definition 5.1 be given. For any pair of states $(\tau_L, v_L)^\top \in \mathcal{A}_{\text{liq}} \times \mathbb{R}$ and $(\tau_R, v_R)^\top \in \mathcal{A}_{\text{vap}} \times \mathbb{R}$ the equation

$$v_L + \mathcal{L}_1(\tau_L, \tau^*) = v_R + \mathcal{L}_2(\tau^*, \tau_R) \quad (5.4)$$

with \mathcal{L}_1 and \mathcal{L}_2 due to Table 5.1 and Table 5.2, respectively, has a unique intersection point in $(\tau_{\text{liq}}^{\text{min}}, \tau_{\text{liq}}^{\text{sat}}] \cup (\tau_{\text{vap}}^{\text{sat}}, \infty)$.

The unique k -micro solution $\mathbf{U} = \mathbf{U}(\xi, t) \in \mathcal{A} \times \mathbb{R}$ is composed of a wave connecting the left initial state with $(\tau^*, v^*)^\top$ according to Table 5.1 and a wave connecting $(\tau^*, v^*)^\top$ to the right initial state according to Table 5.2, with $v^* = v_L + \mathcal{L}_1(\tau_L, \tau^*) = v_R + \mathcal{L}_2(\tau^*, \tau_R)$.

The k -micro solution is a self-similar entropy solution to the micro-scale model of Definition 3.5, that contains exactly one admissible phase transition in the sense of Definition 5.2. Note that the k -micro solution prefers subsonic phase transitions, whenever this is possible. For instance a single supersonic evaporation wave would be also an admissible phase transition in case of wave type 3_L . Moreover, the k -micro solution depends continuously on the initial data in the sense of (4.7). This was proven in [19] for initial data in stable phases.

Proof of Theorem 5.7. First we see that $\tau^* \notin (\tau_{\text{liq}}^{\text{sat}}, \tau_{\text{vap}}^{\text{sat}})$, such that we can exclude this interval from our consideration.

The Lax curves satisfy

$$\begin{aligned} \lim_{\tau \rightarrow \tau_{\text{liq}}^{\text{min}}} \mathcal{L}_1(\tau_L, \tau) &= -\infty & \lim_{\tau \rightarrow \tau_{\text{liq}}^{\text{min}}} \mathcal{L}_2(\tau, \tau_R) &= +\infty \\ \lim_{\tau \rightarrow \infty} \mathcal{L}_1(\tau_L, \tau) &= +\infty & \lim_{\tau \rightarrow \infty} \mathcal{L}_2(\tau, \tau_R) &= -\infty \end{aligned}$$

Set $\Delta = \tau_{\text{vap}}^{\text{sat}} - \tau_{\text{liq}}^{\text{sat}}$. Proposition 5.3 and Proposition 5.6 ensure, that the function

$$f(\tau) = \begin{cases} v_{\text{R}} - v_{\text{L}} & +\mathcal{L}_2(\tau, \tau_{\text{R}}) & -\mathcal{L}_1(\tau_{\text{L}}, \tau) & \text{for } \tau \leq \tau_{\text{liq}}^{\text{sat}} \\ v_{\text{R}} - v_{\text{L}} & +\mathcal{L}_2(\tau - \Delta, \tau_{\text{R}}) & -\mathcal{L}_1(\tau_{\text{L}}, \tau - \Delta) & \text{for } \tau > \tau_{\text{vap}}^{\text{sat}} \end{cases}$$

is continuous and strictly monotone decreasing from $+\infty$ to $-\infty$. Thus, $\tau^* \in (\tau_{\text{liq}}^{\text{min}}, \infty)$ exists such that $f(\tau^*) = 0$. If $\tau \neq \tau_{\text{liq}}^{\text{sat}}$ then τ^* resp. $\tau^* + \Delta$ is the unique solution of (5.4). If $\tau = \tau_{\text{liq}}^{\text{sat}}$, then also $\tau = \tau_{\text{vap}}^{\text{sat}}$ solves (5.4).

The existence of a unique k -micro solution follows from the unique intersection point of the Lax curves, Proposition 5.3 and Proposition 5.6. \square

5.2 Algorithm and an illustrating example

We are now able to define the k -*microsolver* due to Definition 3.5 for a properly defined pair of monotone decreasing kinetic functions k_{c} , k_{e} . Note that Step 2 requires explicit knowledge of the kinetic functions.

Algorithm 5.8 (k -microsolver \mathcal{M}_k).

Let the arguments $(\tau_{\text{L}}, v_{\text{L}}, \tau_{\text{R}}, v_{\text{R}}, \zeta) \in \mathcal{A}_{\text{liq}} \times \mathbb{R} \times \mathcal{A}_{\text{vap}} \times \mathbb{R} \times \mathcal{Z}$ of function \mathcal{M} from (3.9) be given.

Step 1. Determine the points in \mathcal{A} where the solution alters its structure. That are $\tau_{\text{liq/vap}}^{\text{sat}}$ due to (2.10), $\tau_{\text{liq/vap}}^{\text{se}}$, $\tau_{\text{liq/vap}}^{\text{sc}}$ due to Definition 5.1 and $\hat{\tau}$, $\check{\tau}$ due to Lemma 5.4.

Step 2. Find $\tau^* \in (\tau_{\text{liq}}^{\text{min}}, \tau_{\text{liq}}^{\text{sat}}] \cup (\tau_{\text{vap}}^{\text{sat}}, \infty)$, that solves (5.4).

Step 3. Return $(\tau_{\text{liq}}, v_{\text{liq}}, \tau_{\text{vap}}, v_{\text{vap}}, \mathfrak{s})$:

- In case of $\tau^* \in (\tau_{\text{liq}}^{\text{min}}, \tau_{\text{liq}}^{\text{sat}}]$, the value τ_{liq} is the first argument of P in Table 5.1 (gray column) and τ_{vap} is the second argument. The velocities are $v_{\text{liq}} = v_{\text{L}} + G(\tau_{\text{L}}, \tau_{\text{liq}})$ and $v_{\text{vap}} = v_{\text{liq}} + P(\tau_{\text{liq}}, \tau_{\text{vap}})$ and the speed is $\mathfrak{s} = \mathfrak{s}_{\text{e}}(\tau_{\text{liq}}, \tau_{\text{vap}})$.
- In case of $\tau^* \in (\tau_{\text{vap}}^{\text{sat}}, \infty)$, the value τ_{liq} is the first argument of P in Table 5.2 (gray column) and τ_{vap} is the second argument. The velocities are $v_{\text{vap}} = v_{\text{R}} - G(\tau_{\text{vap}}, \tau_{\text{R}})$ and $v_{\text{liq}} = v_{\text{vap}} - P(\tau_{\text{liq}}, \tau_{\text{vap}})$ and the speed is $\mathfrak{s} = \mathfrak{s}_{\text{c}}(\tau_{\text{liq}}, \tau_{\text{vap}})$.

Recall that Figure 5.1, Figure 5.2 and Figure 5.3 illustrate typical shapes of the first resp. second family. As proven in Theorem 5.7 the final solution is a composition of both. We close the section with an illustrating example of rather simple kinetic functions.

Example 5.9 (k -micro solution and Lax curves).

We compute the k -micro solution for the setting of Example 4.16 and the pair of monotone decreasing kinetic functions

$$k_{\text{c}}(\tau_{\text{liq}}) = \tau_{\text{vap}}^{\text{sat}}, \quad k_{\text{e}}(\tau_{\text{vap}}) = \tau_{\text{liq}}^{\text{sat}} \quad \text{for all} \quad \tau_{\text{liq}} \in [\tau_{\text{liq}}^{\text{sc}}, \tau_{\text{liq}}^{\text{sat}}], \tau_{\text{vap}} \in [\tau_{\text{vap}}^{\text{sat}}, \tau_{\text{vap}}^{\text{se}}]. \quad (5.5)$$

Figure 5.4 (left) shows the pressure distribution. The k -micro solution is a composition of a wave of type 3_{L} and type 1_{R} in Table 5.1 and Table 5.2. Waves of type 3_{L} consist of a rarefaction wave, followed by an evaporation wave and an attached rarefaction wave. A

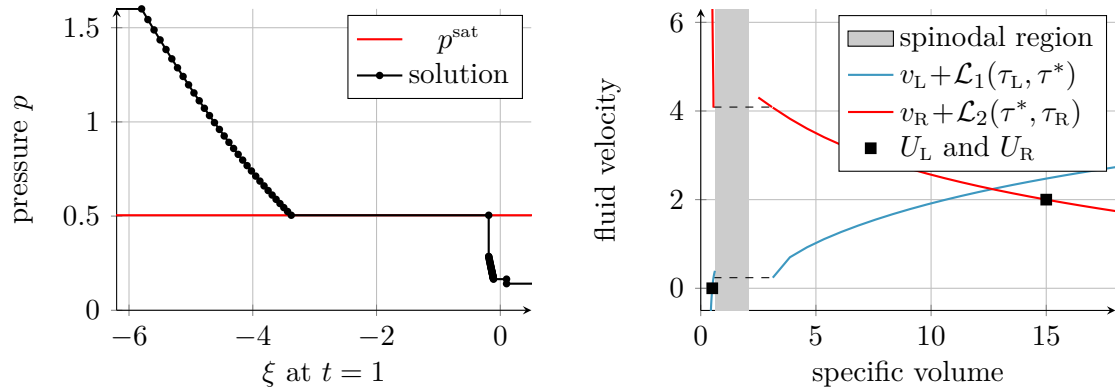


Figure 5.4: Left: pressure of the k -micro solution from Example 5.9. Right: Lax curves of the first (blue) and the second (red) family. The initial states are marked with a square.

wave of type 1_R is solely a shock wave. The figure on the right hand side shows that the monotone increasing Lax curve of the first family intersects the monotone decreasing Lax curve of the second family in the point $(\tau^*, v^*)^\top \approx (12.65, 2.24)^\top$.

Note that this is exactly the same solution as in Example 4.16 since the Lax curves differ only in the metastable region (compare Figure 4.5 and Figure 5.4). This is due to the fact that the kinetic functions was chosen in order to imitate the mixture pressure function and the entropy criterion of Chapter 4. The correlation between the k -micro solution with kinetic functions (5.5) and the Liu micro solution will be shown in Corollary 6.10.

Many kinetic functions are only implicitly available. This issue will be considered in the next chapter. The thermodynamic consistency verification of the k -microsolver and the influence of different kinetic functions on the Riemann solution are placed in Section 6.2. Furthermore, the next chapter provides in Section 6.3 a validation example via a shock tube experiment.

Chapter 6

Kinetic relations for microsolvers

Pairs of monotone decreasing kinetic functions have been introduced in the last chapter in order to determine unique k -micro solutions. The more general form of an algebraic coupling condition to overcome the lack of well-posedness of the mixed hyperbolic-elliptic problem is a kinetic relation [1, 70]. Note that we distinguish very clearly between kinetic relations, kinetic functions and, in particular, pairs of monotone decreasing kinetic functions as in Definition 5.1.

The aim of this chapter is to determine kinetic relations, that lead to pairs of monotone decreasing kinetic functions. Abeyaratne and Knowles [2] and Hantke, Dreyer and Warnecke [35] apply kinetic relations directly in order to construct Riemann solutions. However their approaches require piecewise linear pressure functions and are not applicable to the equations of state of Definition 2.2.

In the first section, Theorem 6.1 and Theorem 6.2 relate kinetic relations to kinetic functions. The theorems are then applied to examples of kinetic relations, which are known from the literature. Also some new relations are reviewed, for example, one that is related to Liu's entropy criterion.

The approach of the previous chapter is used to determine k -micro solutions for the applicable kinetic relations. We study the influence of surface tension and kinetic relations and we verify static solutions with respect to thermodynamic admissibility in Section 6.2. In Section 6.3, we validate k -micro solutions with data from a shock tube experiment. Consequences of the validation and verification examples are given in the final section. We close the chapter with interim conclusions on kinetic relations and micro solutions in Section 6.4.

6.1 Kinetic relations and kinetic functions

In the literature *kinetic relations* have been suggested (see [1, 70]), which control the entropy dissipation explicitly. In terms of a general form these are given by either

$$K = K(f, \mathfrak{s}) := f - g(\mathfrak{s}) = 0 \quad \text{or} \quad K = K(f, \mathfrak{s}) := h(f) - \mathfrak{s} = 0 \quad (6.1)$$

with continuous functions $g, h : \mathbb{R} \rightarrow \mathbb{R}$, the speed of the phase boundary \mathfrak{s} and a driving force f . Note that if g is bijective, then h is just the reciprocal. We will see examples, where this is not the case.

The speed \mathfrak{s} is given by the formulas (3.16) and the **driving force** is determined the function

$$f : \mathcal{A}_{\text{liq}} \times \mathcal{A}_{\text{vap}} \mapsto \mathbb{R}, \quad f(\tau_{\text{liq}}, \tau_{\text{vap}}) = \llbracket \psi(\tau) \rrbracket + \llbracket \tau \rrbracket \{p(\tau)\} + \zeta \{\tau\}. \quad (6.2)$$

The kinetic relation depends on the fluid, it imposes a condition on the interfacial entropy production. The relation of (6.1) to entropy consistency can be seen as follows. Multiplying (6.1) by $-\mathfrak{s}$ one obtains $-\mathfrak{s} f = -g(\mathfrak{s}) \mathfrak{s}$ respectively $-\mathfrak{s} f = -h(f) f$. This is nothing but the standard entropy jump conditions (3.11). Assuming

$$g(\mathfrak{s}) \mathfrak{s} \geq 0, \quad h(f) f \geq 0$$

ensures that the entropy is dissipated. In terms of the entropy product rate η_{Γ} in (2.5) we find $T \eta_{\Gamma} = g(\mathfrak{s}) \mathfrak{s}$.

The connection between kinetic relations and kinetic functions is given by the following theorems. We have seen in the last chapters that additional conditions are necessary only for subsonic phase transitions. The white area in Figure 6.1 illustrates admissible end states of subsonic phase transitions, i.e. the set

$$\mathcal{A}_{\text{pb}} := \left\{ (\tau_{\text{liq}}, \tau_{\text{vap}}) \in \mathcal{A}_{\text{liq}} \times \mathcal{A}_{\text{vap}} \mid p'(\tau_{\text{liq}}), p'(\tau_{\text{vap}}) \leq \frac{\llbracket p \rrbracket - \zeta}{\llbracket \tau \rrbracket}, \llbracket p \rrbracket \geq \zeta \right\}.$$

We refer in this chapter to Lagrangian coordinates and equations of state as in Definition 2.2. Note that we can switch to Eulerian coordinates replacing $\mathfrak{s} = -j$, since only jump conditions are considered here.

Theorem 6.1 (Existence and uniqueness of kinetic functions).

Let $\mathfrak{s}_c : \mathcal{A}_{\text{pb}} \rightarrow [0, \infty)$ and $\mathfrak{s}_e : \mathcal{A}_{\text{pb}} \rightarrow (-\infty, 0]$ be the propagation speed of condensation and evaporation waves, as defined in (3.16), and let a kinetic relation $K : \mathbb{R} \times \mathbb{R} \rightarrow \mathbb{R}$ be given, that is Lipschitz continuous. Assume that K fulfills $K(0, 0) = 0$ and

$$\frac{\partial K}{\partial f} \left(f(\tau_{\text{liq}}, \tau_{\text{vap}}), \mathfrak{s}_{c/e}(\tau_{\text{liq}}, \tau_{\text{vap}}) \right) - \frac{\partial K}{\partial \mathfrak{s}} \left(f(\tau_{\text{liq}}, \tau_{\text{vap}}), \mathfrak{s}_{c/e}(\tau_{\text{liq}}, \tau_{\text{vap}}) \right) \frac{1}{\llbracket \tau \rrbracket^2} \sqrt{\left| \frac{\llbracket \tau \rrbracket}{\zeta - \llbracket p \rrbracket} \right|} > 0 \quad (6.3)$$

for almost all $(\tau_{\text{liq}}, \tau_{\text{vap}}) \in \mathcal{A}_{\text{pb}}$.

Then there exist values $\tau_{\text{liq}}^{\text{sc}} \in [\tau_{\text{liq}}^{\text{min}}, \tau_{\text{liq}}^{\text{sat}})$, $\tau_{\text{vap}}^{\text{se}} \in (\tau_{\text{vap}}^{\text{sat}}, \infty]$ and two continuous functions $k_c : (\tau_{\text{liq}}^{\text{sc}}, \tau_{\text{liq}}^{\text{sat}}] \rightarrow \mathcal{A}_{\text{vap}}$ and $k_e : [\tau_{\text{vap}}^{\text{sat}}, \tau_{\text{vap}}^{\text{se}}) \rightarrow \mathcal{A}_{\text{liq}}$ with $K(f(\tau_{\text{liq}}, k_c(\tau_{\text{liq}}), \mathfrak{s}_c(\tau_{\text{liq}}, k_c(\tau_{\text{liq}}))) = 0$ and $K(f(k_e(\tau_{\text{vap}}), \tau_{\text{vap}}), \mathfrak{s}_e(k_e(\tau_{\text{vap}}), \tau_{\text{vap}})) = 0$.

We call k_c and k_e **kinetic functions**.

Note that either $\partial K / \partial f = 1$ and $\partial K / \partial \mathfrak{s} = -g'(\mathfrak{s})$ or $\partial K / \partial f = h'(f)$ and $\partial K / \partial \mathfrak{s} = -1$. Driving force and propagation speed are zero for the end states $(\tau_{\text{liq}}^{\text{sat}}, \tau_{\text{vap}}^{\text{sat}})$, such that condition $K(0, 0) = 0$ guarantees, that the saturation states are a solution of the kinetic relation. The k -microsolver of Chapter 5 requires a special type of kinetic functions. The subsequent theorem states corresponding necessary conditions for the kinetic relations.

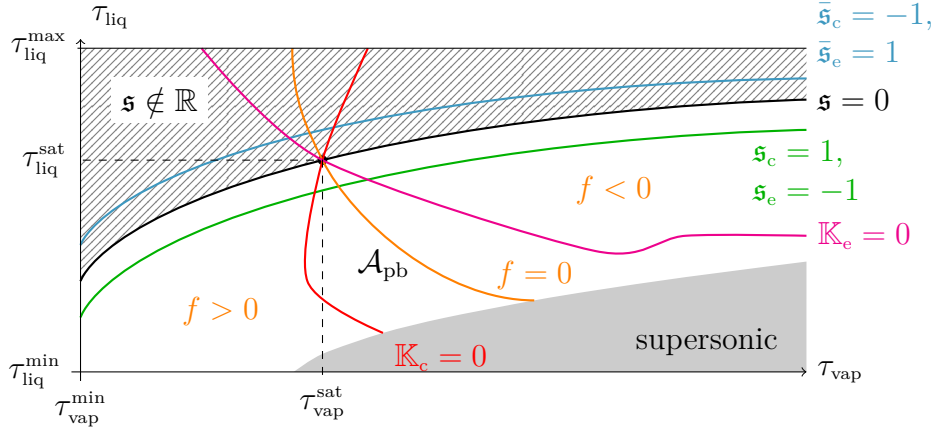


Figure 6.1: The Figure shows the set $\mathcal{A}_{\text{vap}} \times \mathcal{A}_{\text{liq}}$. The gray area corresponds to states, which lead to supersonic phase transitions. The white area refers to the set \mathcal{A}_{pb} . The shaded area corresponds to complex values of the functions \mathfrak{s}_c , \mathfrak{s}_e . The function values of the driving force is zero along the orange curve, positive on the left side of that curve and negative on the right side. The sound speed is zero along the black curve.

Theorem 6.2 (Pairs of monotone decreasing kinetic functions).

Let a kinetic relation $K : \mathbb{R} \times \mathbb{R} \rightarrow \mathbb{R}$ be given, that fulfills the conditions of Theorem 6.1. If, in addition, K is differentiable in $\mathbb{R} \times \mathbb{R} \setminus \{(0, 0)\}$ and

$$\frac{\partial K}{\partial f} \left(f(\tau_{\text{liq}}, \tau_{\text{vap}}), \mathfrak{s}_{c/e}(\tau_{\text{liq}}, \tau_{\text{vap}}) \right) + \frac{\partial K}{\partial \mathfrak{s}} \left(f(\tau_{\text{liq}}, \tau_{\text{vap}}), \mathfrak{s}_{c/e}(\tau_{\text{liq}}, \tau_{\text{vap}}) \right) \frac{1}{\llbracket \tau \rrbracket^2} \sqrt{\left| \frac{\llbracket \tau \rrbracket}{\zeta - \llbracket p \rrbracket} \right|} \geq 0 \quad (6.4)$$

holds for all $(\tau_{\text{liq}}, \tau_{\text{vap}}) \in \mathring{\mathcal{A}}_{\text{pb}}$, then a pair of monotone decreasing kinetic functions in the sense of Definition 5.1 exists uniquely.

The proof of Theorem 6.1 applies a variant of the implicit function theorem, that does not require differentiability.

Theorem 6.3 (Implicit function theorem for continuous functions).

Suppose that $F : D \subset \mathbb{R} \times \mathbb{R} \rightarrow \mathbb{R}$ is a continuous function with

$$F(a_0, b_0) = 0.$$

Assume that there exist open vicinities $A \subset \mathbb{R}$ and $B \subset \mathbb{R}$ of a_0 and b_0 , respectively, such that, for all $b \in B$, $F(\cdot, b) : A \subset \mathbb{R} \rightarrow \mathbb{R}$ is injective. Then, there for all $b \in B$, the equation

$$F(a, b) = 0$$

has a unique solution $a = H(b) \in A$, and the function $H : A \rightarrow \mathbb{R}$ is continuous.

The theorem is proven in [41] for the more general case of functions $F : D \subset \mathbb{R}^n \times \mathbb{R}^m \rightarrow \mathbb{R}^n$ with $n, m \in \mathbb{N}$.

Proof of Theorem 6.1. Let us first extend the functions \mathfrak{s}_c and \mathfrak{s}_e to the domain

$$\mathcal{A}_{\text{ext}} := \left\{ (\tau_{\text{liq}}, \tau_{\text{vap}}) \in \mathcal{A}_{\text{liq}} \times \mathcal{A}_{\text{vap}} \mid p'(\tau_{\text{liq}}), p'(\tau_{\text{vap}}) \leq \left| \frac{\llbracket p \rrbracket - \zeta}{\llbracket \tau \rrbracket} \right| \right\}.$$

Define $\bar{\mathfrak{s}}_c(\tau_{\text{liq}}, \tau_{\text{vap}}) = \text{sign}(\zeta - \llbracket p \rrbracket) \sqrt{|\zeta - \llbracket p \rrbracket| / \llbracket \tau \rrbracket}$ and $\bar{\mathfrak{s}}_e(\tau_{\text{liq}}, \tau_{\text{vap}}) = -\bar{\mathfrak{s}}_c(\tau_{\text{liq}}, \tau_{\text{vap}})$ for $(\tau_{\text{liq}}, \tau_{\text{vap}}) \in \mathcal{A}_{\text{ext}}$. Note that the pair of saturation states $(\tau_{\text{liq}}^{\text{sat}}, \tau_{\text{vap}}^{\text{sat}})$ is an inner point of the set \mathcal{A}_{ext} . In Figure 6.1, the set \mathcal{A}_{ext} is the union of the white area with the shaded area.

We will later on apply the following derivatives and monotonicity properties. One readily checks, that

$$\begin{aligned} \frac{\partial f}{\partial \tau_{\text{vap}}}(\tau_{\text{liq}}, \tau_{\text{vap}}) &= \frac{1}{2} (p'(\tau_{\text{vap}}) \llbracket \tau \rrbracket + \zeta - \llbracket p \rrbracket) < 0 \text{ in } \mathring{\mathcal{A}}_{\text{ext}}, \\ \frac{\partial f}{\partial \tau_{\text{liq}}}(\tau_{\text{liq}}, \tau_{\text{vap}}) &= \frac{1}{2} (p'(\tau_{\text{liq}}) \llbracket \tau \rrbracket + \zeta - \llbracket p \rrbracket) < 0 \text{ in } \mathcal{A}_{\text{ext}}, \\ -\frac{\partial \mathfrak{s}_c}{\partial \tau_{\text{vap}}}(\tau_{\text{liq}}, \tau_{\text{vap}}) &= \frac{\partial \mathfrak{s}_e}{\partial \tau_{\text{vap}}}(\tau_{\text{liq}}, \tau_{\text{vap}}) = \frac{1}{2 \llbracket \tau \rrbracket^2} \sqrt{\left| \frac{\llbracket \tau \rrbracket}{\zeta - \llbracket p \rrbracket} \right|} (p'(\tau_{\text{vap}}) \llbracket \tau \rrbracket + \zeta - \llbracket p \rrbracket) < 0 \text{ in } \mathring{\mathcal{A}}_{\text{ext}}, \\ \frac{\partial \mathfrak{s}_c}{\partial \tau_{\text{liq}}}(\tau_{\text{liq}}, \tau_{\text{vap}}) &= -\frac{\partial \mathfrak{s}_e}{\partial \tau_{\text{liq}}}(\tau_{\text{liq}}, \tau_{\text{vap}}) = \frac{1}{2 \llbracket \tau \rrbracket^2} \sqrt{\left| \frac{\llbracket \tau \rrbracket}{\zeta - \llbracket p \rrbracket} \right|} (p'(\tau_{\text{liq}}) \llbracket \tau \rrbracket + \zeta - \llbracket p \rrbracket) < 0 \text{ in } \mathcal{A}_{\text{ext}} \end{aligned}$$

holds. The derivatives with respect to τ_{vap} are zero in the sonic case, such that strict monotonicity holds only in the interior of the set \mathcal{A}_{ext} . The derivatives with respect to τ_{liq} are negative in the sonic point. The saturation states (2.10) satisfy $f(\tau_{\text{liq}}^{\text{sat}}, \tau_{\text{vap}}^{\text{sat}}) = 0$ and $\mathfrak{s}_{e/c}(\tau_{\text{liq}}^{\text{sat}}, \tau_{\text{vap}}^{\text{sat}}) = 0$. Furthermore, condition $K(0, 0) = 0$ ensures, that one solution is given by $(\tau_{\text{liq}}^{\text{sat}}, \tau_{\text{vap}}^{\text{sat}}) \in \mathcal{A}_{\text{ext}}$.

We start with the condensation case and define a kinetic relation in terms of specific volume values via $\mathbb{K}_c(\tau_{\text{liq}}, \tau_{\text{vap}}) = K(f(\tau_{\text{liq}}, \tau_{\text{vap}}), \bar{\mathfrak{s}}_c(\tau_{\text{liq}}, \tau_{\text{vap}}))$ for $(\tau_{\text{liq}}, \tau_{\text{vap}}) \in \mathcal{A}_{\text{ext}}$. Figure 6.1 illustrates the set $\{(\tau_{\text{liq}}, \tau_{\text{vap}}) \in \mathcal{A}_{\text{ext}} \mid \mathbb{K}_c(\tau_{\text{liq}}, \tau_{\text{vap}}) = 0\}$. With (6.3) it holds

$$\begin{aligned} \frac{d \mathbb{K}_c}{d \tau_{\text{vap}}}(\tau_{\text{liq}}, \tau_{\text{vap}}) &= \frac{\partial K}{\partial f} \frac{\partial f}{\partial \tau_{\text{vap}}} + \frac{\partial K}{\partial \mathfrak{s}} \frac{\partial \mathfrak{s}_c}{\partial \tau_{\text{vap}}} \\ &= \frac{1}{2} (p'(\tau_{\text{vap}}) \llbracket \tau \rrbracket + \zeta - \llbracket p \rrbracket) \left(\frac{\partial K}{\partial f} - \frac{\partial K}{\partial \mathfrak{s}} \frac{1}{\llbracket \tau \rrbracket^2} \sqrt{\left| \frac{\llbracket \tau \rrbracket}{\zeta - \llbracket p \rrbracket} \right|} \right) < 0 \end{aligned}$$

for almost all $(\tau_{\text{liq}}, \tau_{\text{vap}}) \in \mathring{\mathcal{A}}_{\text{ext}}$. There exist an open vicinity $B_{\text{liq}} \subset \mathcal{A}_{\text{liq}}$ of $\tau_{\text{liq}}^{\text{sat}}$ and an open vicinity $B_{\text{vap}} \subset \mathcal{A}_{\text{vap}}$ of $\tau_{\text{vap}}^{\text{sat}}$, such that the function $\mathbb{K}_c(\tau_{\text{liq}}, \cdot) : B_{\text{vap}} \rightarrow \mathbb{R}$ is strictly decreasing and injective for any $\tau_{\text{liq}} \in B_{\text{liq}}$. With Theorem 6.3, there exist a unique continuous function $k_c : B_{\text{liq}} \rightarrow B_{\text{vap}}$, such that $\mathbb{K}_c(\tau_{\text{liq}}, k_c(\tau_{\text{liq}})) = 0$ holds. For values $\tau_{\text{liq}} < \tau_{\text{liq}}^{\text{sat}}$ we can proceed with the same arguments, as long as, (6.3) holds. Finally, we restrict the domain of definition to values less or equal than $\tau_{\text{liq}}^{\text{sat}}$.

The evaporation case is very similar. For $\mathbb{K}_e(\tau_{\text{liq}}, \tau_{\text{vap}}) := K(f(\tau_{\text{liq}}, \tau_{\text{vap}}), \bar{\mathfrak{s}}_e(\tau_{\text{liq}}, \tau_{\text{vap}}))$ it

holds with (6.3)

$$\begin{aligned} \frac{d\mathbb{K}_e}{d\tau_{\text{liq}}}(\tau_{\text{liq}}, \tau_{\text{vap}}) &= \frac{\partial K}{\partial f} \frac{\partial f}{\partial \tau_{\text{liq}}} + \frac{\partial K}{\partial \mathfrak{s}} \frac{\partial \mathfrak{s}_e}{\partial \tau_{\text{liq}}} \\ &= \frac{1}{2} (p'(\tau_{\text{liq}}) \llbracket \tau \rrbracket + \zeta - \llbracket p \rrbracket) \left(\frac{\partial K}{\partial f} - \frac{\partial K}{\partial \mathfrak{s}} \frac{1}{\llbracket \tau \rrbracket^2} \sqrt{\left| \frac{\llbracket \tau \rrbracket}{\zeta - \llbracket p \rrbracket} \right|} \right) < 0 \end{aligned}$$

for almost all $(\tau_{\text{liq}}, \tau_{\text{vap}}) \in \mathcal{A}_{\text{ext}}$. The function $\mathbb{K}_e(\cdot, \tau_{\text{vap}})$ is strictly decreasing and injective in an open vicinity of the saturation states and we can apply the same arguments as above. \square

Proof of Theorem 6.2. Due to Theorem 6.1, there are continuous kinetic functions $k_c : (\tau_{\text{liq}}^{\text{sc}}, \tau_{\text{liq}}^{\text{sat}}] \rightarrow \mathcal{A}_{\text{vap}}$ and $k_e : [\tau_{\text{vap}}^{\text{sat}}, \tau_{\text{vap}}^{\text{sc}}) \rightarrow \mathcal{A}_{\text{liq}}$. The extra regularity assumption of differentiability is inherited to the kinetic functions.

We show, that k_c is a monotone decreasing function and use the functions defined in the proof of Theorem 6.1. From condition (6.4) it follows that

$$\begin{aligned} \frac{d\mathbb{K}_c}{d\tau_{\text{liq}}}(\tau_{\text{liq}}, \tau_{\text{vap}}) &= \frac{\partial K}{\partial f} \frac{\partial f}{\partial \tau_{\text{liq}}} + \frac{\partial K}{\partial \mathfrak{s}} \frac{\partial \mathfrak{s}_c}{\partial \tau_{\text{liq}}} \\ &= \frac{1}{2} (p'(\tau_{\text{liq}}) \llbracket \tau \rrbracket + \zeta - \llbracket p \rrbracket) \left(\frac{\partial K}{\partial f} + \frac{\partial K}{\partial \mathfrak{s}} \frac{1}{\llbracket \tau \rrbracket^2} \sqrt{\frac{\llbracket \tau \rrbracket}{\zeta - \llbracket p \rrbracket}} \right) \leq 0 \end{aligned}$$

for $(\tau_{\text{liq}}, \tau_{\text{vap}}) \in \mathcal{A}_{\text{pb}}$. We consider $\mathbb{K}_c(\tau, k_c(\tau)) = 0$ and derive

$$0 = \frac{d\mathbb{K}_c}{d\tau}(\tau, k_c(\tau)) = \frac{\partial \mathbb{K}_c}{\partial \tau_{\text{liq}}}(\tau, k_c(\tau)) + \frac{\partial \mathbb{K}_c}{\partial \tau_{\text{vap}}}(\tau, k_c(\tau)) k'_c(\tau).$$

The derivatives of the kinetic relation are both not positive and $\frac{\partial \mathbb{K}_c}{\partial \tau_{\text{vap}}}$ is negative except of the sonic point $\tau_{\text{vap}}^{\text{sc}}$, thus $k'_c(\tau_{\text{vap}}) \leq 0$ for all $\tau_{\text{vap}} \in [\tau_{\text{vap}}^{\text{sat}}, \tau_{\text{vap}}^{\text{sc}})$.

We proceed with the evaporation case and show that the function k_e is monotone decreasing. From (6.4) it follows that

$$\begin{aligned} \frac{d\mathbb{K}_e}{d\tau_{\text{vap}}}(\tau_{\text{liq}}, \tau_{\text{vap}}) &= \frac{\partial K}{\partial f} \frac{\partial f}{\partial \tau_{\text{vap}}} + \frac{\partial K}{\partial \mathfrak{s}} \frac{\partial \mathfrak{s}_e}{\partial \tau_{\text{vap}}} \\ &= \frac{1}{2} (p'(\tau_{\text{vap}}) \llbracket \tau \rrbracket + \zeta - \llbracket p \rrbracket) \left(\frac{\partial K}{\partial f} + \frac{\partial K}{\partial \mathfrak{s}} \frac{1}{\llbracket \tau \rrbracket^2} \sqrt{\frac{\llbracket \tau \rrbracket}{\zeta - \llbracket p \rrbracket}} \right) \leq 0 \end{aligned}$$

for $(\tau_{\text{liq}}, \tau_{\text{vap}}) \in \mathcal{A}_{\text{pb}}$. Consider $\mathbb{K}_e(k_e(\tau), \tau) = 0$ and derive

$$0 = \frac{d\mathbb{K}_e}{d\tau}(k_e(\tau), \tau) = \frac{\partial \mathbb{K}_e}{\partial \tau_{\text{liq}}}(k_e(\tau), \tau) k'_e(\tau) + \frac{\partial \mathbb{K}_e}{\partial \tau_{\text{vap}}}(k_e(\tau), \tau). \quad (6.5)$$

The term $\frac{\partial \mathbb{K}_e}{\partial \tau_{\text{liq}}}$ is negative and the term $\frac{\partial \mathbb{K}_e}{\partial \tau_{\text{vap}}}$ is not positive, thus $k'_e \leq 0$ in $(\tau_{\text{liq}}^{\text{sc}}, \tau_{\text{liq}}^{\text{sat}}]$.

It remains to show that the domain of definition can be extended up to the sonic points, with $\mathfrak{s}_c(\tau_{\text{liq}}^{\text{sc}}, k_c(\tau_{\text{liq}}^{\text{sc}})) = c(\tau_{\text{vap}}^{\text{sc}})$, $-\mathfrak{s}_e(k_e(\tau_{\text{vap}}^{\text{se}}), \tau_{\text{vap}}^{\text{se}}) = c(\tau_{\text{vap}}^{\text{se}})$ and the condition $k'_e(\tau_{\text{vap}}^{\text{se}}) = 0$. Note that the points $(\tau_{\text{liq}}^{\text{sc}}, k_c(\tau_{\text{liq}}^{\text{sc}}))$, $(k_e(\tau_{\text{vap}}^{\text{se}}), \tau_{\text{vap}}^{\text{se}})$ are the intersection points of the

no.	kinetic relation	pair of mon. dec. kinetic functions
1	$K_1(f, \mathfrak{s}) := f$	✓
2	$K_2(f, \mathfrak{s}) := f - k^* \mathfrak{s}$	✗
3	$K_3(f, \mathfrak{s}) := f - k^* \text{sign}(\mathfrak{s}) \mathfrak{s}^2$	✓ for small $k^* > 0$
4	$K_4(f, \mathfrak{s}) := f - k^* \mathfrak{s}^3$	✓ for small $k^* > 0$
5	$K_5(f, \mathfrak{s}) := \begin{cases} f + a - k^* \mathfrak{s} & : f < -a \\ -k^* \mathfrak{s} & : f \leq a \\ f - a - k^* \mathfrak{s} & : f > a \end{cases}$	✗
6	$K_6(f, \mathfrak{s}, \tau_{\text{liq}}, \tau_{\text{vap}}) := f - \text{sign}(\mathfrak{s}) \mathfrak{s}^2 \llbracket \tau \rrbracket^2$	✗
7	K_7 such that $\begin{cases} k_c(\tau_{\text{liq}}) = \tau_{\text{vap}}^{\text{sat}} & : \mathfrak{s} \geq 0 \\ k_e(\tau_{\text{vap}}) = \tau_{\text{liq}}^{\text{sat}} & : \mathfrak{s} < 0 \end{cases}$	✓
8	$K_8(f, \mathfrak{s}) := -\mathfrak{s}$	✗

Table 6.1: Different kinetic relations and existence of a corresponding pair of monotone decreasing kinetic functions due to Theorem 6.2. Parameters $k^* > 0$, $a > 0$. Kinetic relation K_6 needs more arguments and for K_7 it is simpler to state the kinetic functions directly.

kinetic functions with the boundary segment $p'(\tau_{\text{vap}}) = \frac{\llbracket p \rrbracket - \zeta}{\llbracket \tau \rrbracket}$, c.f. Figure 6.1. The kinetic functions are monotone decreasing in \mathcal{A}_{pb} . Thus, k_c and k_e intersect the boundary segment $p'(\tau_{\text{vap}}) = \frac{\llbracket p \rrbracket - \zeta}{\llbracket \tau \rrbracket}$ between the points $(\tau_{\text{liq}}^*, \tau_{\text{vap}}^{\text{sat}})$ and $(\tau_{\text{liq}}^{\text{sat}}, \tau_{\text{vap}}^*)$. The points are the intersection points with a horizontal line $\{(\tau_{\text{liq}}, \tau_{\text{vap}}) \in \mathcal{A}_{\text{pb}} \mid \tau_{\text{liq}} = \tau_{\text{liq}}^{\text{sat}}\}$ and a vertical line $\{(\tau_{\text{liq}}, \tau_{\text{vap}}) \in \mathcal{A}_{\text{pb}} \mid \tau_{\text{vap}} = \tau_{\text{vap}}^{\text{sat}}\}$ through the saturation states. The first intersection point exists due to Lemma 5.4 with $\tau_{\text{R}} = \tau_{\text{vap}}^{\text{sat}}$ and $\tau_{\text{liq}}^* = \hat{\tau}$. The second intersection point exists due to Lemma 4.9 with $\tau_{\text{vap}}^* = g_s(\tau_{\text{liq}}^{\text{sat}})$. Thus, also intersection points $(\tau_{\text{liq}}^{\text{sc}}, \tau_{\text{vap}}^{\text{sc}})$ and $(\tau_{\text{liq}}^{\text{se}}, \tau_{\text{vap}}^{\text{se}})$ exist, with $\tau_{\text{vap}}^{\text{sc}} := k_c(\tau_{\text{liq}}^{\text{sc}})$, $\tau_{\text{liq}}^{\text{se}} := k_e(\tau_{\text{vap}}^{\text{se}})$.

Finally, we find that $\frac{d k_e}{d \tau_{\text{vap}}}(\tau_{\text{liq}}^{\text{se}}, \tau_{\text{vap}}^{\text{se}}) = 0$ and $\frac{d k_c}{d \tau_{\text{liq}}}(\tau_{\text{liq}}^{\text{se}}, \tau_{\text{vap}}^{\text{se}}) > 0$ in (6.5), that means $k'_e(\tau_{\text{vap}}^{\text{se}}) = 0$. Thus, (k_c, k_e) is a pair of monotone decreasing kinetic functions. \square

Corollary 6.4 (Metastable phase transitions).

Assume a phase transition, that obeys a kinetic relation as required in Theorem 6.2. The end states of that phase transition lie in the stable phases. Thus, metastable transition waves are excluded.

Proof. Due to Theorem 6.2 there is a pair of monotone decreasing kinetic function, such that the end states $\tau_{\text{liq}} \in \mathcal{A}_{\text{liq}}$, $\tau_{\text{vap}} \in \mathcal{A}_{\text{vap}}$ satisfy $k_c(\tau_{\text{liq}}) = \tau_{\text{vap}}$ for a condensation wave and $k_e(\tau_{\text{liq}}) = \tau_{\text{vap}}$ for an evaporation wave. One pair of end states is given by the saturation states, i.e. $k_c(\tau_{\text{liq}}^{\text{sat}}) = \tau_{\text{vap}}^{\text{sat}}$ and $k_e(\tau_{\text{liq}}^{\text{sat}}) = \tau_{\text{vap}}^{\text{sat}}$. Because of the monotonicity of k_c and k_e it holds $\tau_{\text{vap}}^{\text{sat}} \leq \tau_{\text{vap}}$ for $\tau_{\text{liq}} \in [\tau_{\text{liq}}^{\text{sc}}, \tau_{\text{liq}}^{\text{sat}}]$ in the condensation case and $\tau_{\text{liq}} \leq \tau_{\text{liq}}^{\text{sat}}$ for $\tau_{\text{vap}} \in [\tau_{\text{vap}}^{\text{sat}}, \tau_{\text{vap}}^{\text{se}}]$ in the evaporation case. \square

Table 6.1 lists examples for kinetic relations. The parameter $k^* > 0$ depends on the shape of the equation of state and obviously the parameter has different physical units in K_2 – K_5 . Furthermore, there is no physical reason why evaporation waves and condensation

waves share the same value for k^* . The parameter could also depend on the sign of \mathfrak{s} in K_2 – K_5 .

Figure 6.2 shows the zero contour lines of several kinetic relations schematically. If one splits the contour lines at the saturation point into two branches, one finds the corresponding kinetic functions for evaporation $k_e = k_e(\tau_{\text{vap}})$ and condensation waves $k_c = k_c(\tau_{\text{liq}})$ respectively. One finds kinetic functions for evaporation waves to the right of the curve $K_1 = 0$ in Figure 6.2 and kinetic functions for condensation waves to the left of this curve. This is a consequence of the entropy inequality (2.30) as $f \mathfrak{s} \geq 0$ holds.

Remark 6.5 (Consequences for the k -microsolver of Chapter 5).

- Any kinetic relation, that fulfills the conditions of Theorem 6.2, is applicable to the approach of the previous chapter and the corresponding k -micro solution exists uniquely due Theorem 5.7. This holds, in particular, for K_1 , K_3 , K_4 , K_7 of Table 6.1.
- In general, there is an implicit solver needed to determine the kinetic function in Algorithm 5.8 for a given kinetic relation.
- We write *k_n -micro solution* if the solution satisfies kinetic relation K_n , with $n \in \{1, 3, 4, 7\}$. Furthermore, we write *k_n -microsolver*, \mathcal{M}_{k_n} or $\tilde{\mathcal{M}}_{k_n}$ for the associated microsolver of Algorithm 5.8 to denote the dependency on the chosen kinetic relation.

Figure 6.3 illustrates kinetic relations for an equation of state of a real fluid. To be precise the set $\{(p(\tau_{\text{vap}}), p(\tau_{\text{liq}})) \in \mathbb{R}_+^2 \mid K(\tau_{\text{liq}}, \tau_{\text{vap}}) = 0\}$ is shown. The fluid is n-dodecane at $T = 230^\circ\text{C}$ computed by the library CoolProp [6]. We proceed with a description of the respective kinetic relations of Table 6.1.

Remark 6.6 (Kinetic relations K_1 and K_2).

For kinetic relation $K_2 = f - k^* \mathfrak{s}$ we find $\partial K_2 / \partial f = 1$, $\partial K_2 / \partial \mathfrak{s} = -k^*$ such that condition (6.3) holds for any $k^* \geq 0$ but only $k^* = 0$ fulfills (6.4). The term $\sqrt{\llbracket \tau \rrbracket} / (\zeta - \llbracket p \rrbracket) = 1 / |\mathfrak{s}|$ is infinite in the saturation state ($\mathfrak{s} = 0$) and monotone decreasing in $|\mathfrak{s}|$. Due to Theorem 6.1, kinetic functions exist for any $k^* \geq 0$.

A pair of monotone decreasing kinetic functions exists only for $k^* = 0$ (kinetic relation K_1), see Theorem 6.2. A phase transition, that satisfies kinetic relation K_1 , conserves the entropy and k_e is the inverse function of k_c . From a thermodynamic point of view this can be interpreted as a reversible process.

Stability results for a linearized version of the isothermal Euler model in Definition 2.8 are available in terms of local energy estimates. For K_1 that was investigated in [7] and for K_2 in [45]. The non-linearized case is studied in [44].

Remark 6.7 (Kinetic relations K_3 and K_4).

Kinetic relations K_3 and K_4 were just chosen to satisfy the conditions of Theorem 6.2. They lead to pairs of monotone decreasing kinetic functions, for sufficiently small $k^* > 0$, and can be used for Algorithm 5.8.

Remark 6.8 (Kinetic relation K_5).

Kinetic relations like K_5 are often considered for phase transitions in solid mechanics (see [1, Section 4.4]). There, no transition takes place until the driving force f passes a certain

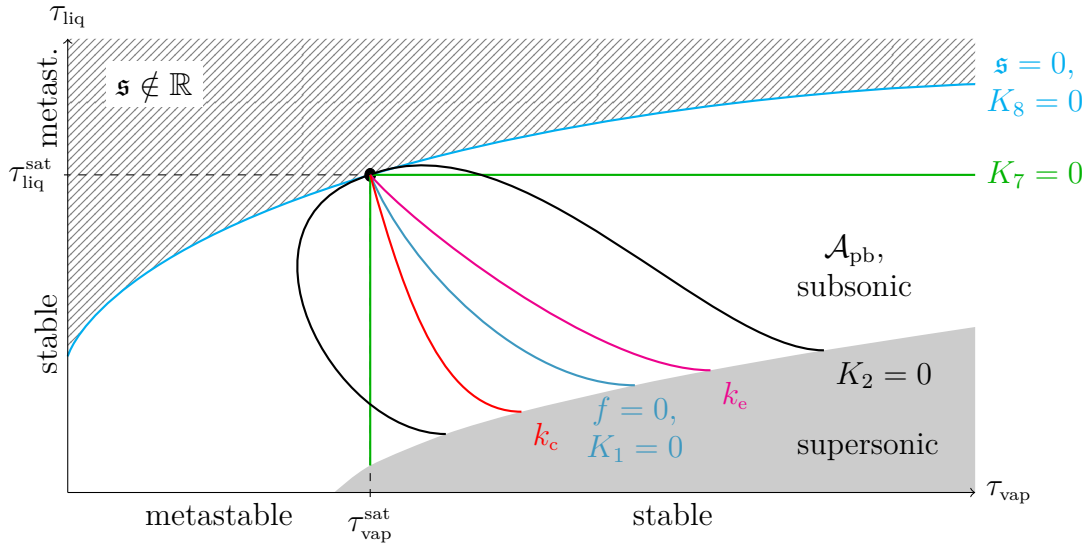


Figure 6.2: Zero contour lines of kinetic relations, i.e. $\{(\tau_{\text{liq}}, \tau_{\text{vap}}) \in \mathcal{A}_{\text{pb}} \mid K(\tau_{\text{liq}}, \tau_{\text{vap}}) = 0\}$, and an idealized pair of monotone decreasing kinetic functions, i.e. $(\tau_{\text{liq}}, k_c(\tau_{\text{liq}})) \subset \mathcal{A}_{\text{pb}}$ and $(k_e(\tau_{\text{vap}}), \tau_{\text{vap}}) \subset \mathcal{A}_{\text{pb}}$. The shaded area corresponds to complex speeds \mathfrak{s}_c , \mathfrak{s}_e and the gray area to supersonic phase transitions. The white area corresponds to the set \mathcal{A}_{pb} of subsonic phase transitions.

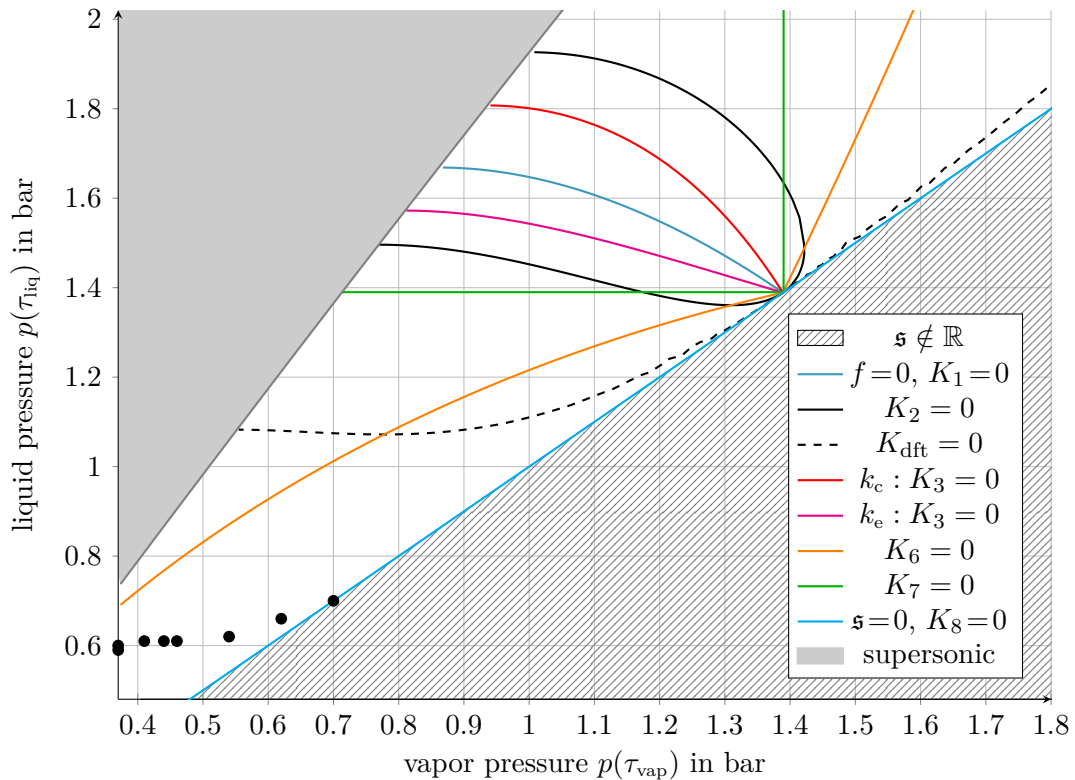


Figure 6.3: Kinetic relations for n-dodecane with respect to the pressure. Relation K_2 for $k^* = 5 \text{ m}^4/\text{kg s}$ and K_{dft} as in Example 6.13. Kinetic functions k_c and k_e result from K_3 with $k^* = 0.005 \text{ m}^6/\text{kg}^2$. The gray line marks sonic transition waves. The black dots mark measured values from the experiment in Section 6.3.

threshold $a > 0$. If the driving force f is sufficiently small, the phase boundary does not propagate. Note that this involves static phase transitions, whose end states are not the saturation states.

The conditions of Theorem 6.1 are satisfied, but for $|f| < a$ condition (6.4) is violated. Thus, the microsolver of Algorithm 5.8 is not applicable with kinetic relation K_5 . However, unique Riemann solutions can be singled out, assuming non-monotone pressure functions that are piecewise linear, see [2].

Remark 6.9 (Kinetic relation K_7 and Liu's entropy criterion).

The Liu micro solution due to Definition 4.4 implies a kinetic relation implicitly. It can be described as follows. Except of metastable transitions, all subsonic phase transitions connect to one of the saturation states. In this sense, the mixture pressure function of Definition 4.1, together with the Liu entropy criterion in Definition 4.6, determines the kinetic functions

$$\begin{aligned} k_c : [\tau_{\text{liq}}^{\text{sc}}, \tau_{\text{liq}}^{\text{sat}}] &\rightarrow \mathcal{A}_{\text{vap}}, & k_e : [\tau_{\text{vap}}^{\text{sat}}, \tau_{\text{vap}}^{\text{sc}}] &\rightarrow \mathcal{A}_{\text{liq}}, \\ \tau_{\text{liq}} &\mapsto \tau_{\text{vap}}^{\text{sat}}, & \tau_{\text{vap}} &\mapsto \tau_{\text{liq}}^{\text{sat}}. \end{aligned}$$

The corresponding kinetic relation is named K_7 in Table 6.1 and Figure 6.2. It was already applied in Example 5.9.

The kinetic functions are constant and can be seen as the limit of monotone decreasing functions, see Figure 6.2 for illustration. However, they fulfill the conditions of Definition 5.1 and can be used for the microsolver of Algorithm 5.8. The subsequent corollary compares Liu micro solutions with k_7 -micro solutions.

Corollary 6.10 (Liu micro solution and the k_7 -micro solution).

Consider Liu micro solutions as in Theorem 4.13 and k_7 -micro solution as in to Theorem 5.7. The solutions are composed of the waves given by the tables 4.1, 4.2, 5.1 and 5.2.

The waves of the following types are identical

$$\begin{aligned} \text{type } 1_L^\zeta \text{ and } 1_L, & \quad \text{type } 2_L^\zeta \text{ and } 2_L, & \quad \text{type } 3_L^\zeta \text{ and } 3_L & \quad \text{for } \tau_L \in (\tau_{\text{liq}}^{\text{min}}, \tau_{\text{liq}}^{\text{sat}}], \\ \text{type } 3_R^\zeta \text{ and } 1_R, & \quad \text{type } 4_R^\zeta \text{ and } 5_R, & \quad \text{type } 5_R^\zeta \text{ and } 6_R & \quad \text{for } \tau_R \in [\tau_{\text{liq}}^{\text{sat}}, \infty). \end{aligned}$$

The remaining wave types are different due to different pressure values in the metastable phases.

Proof of Corollary 6.10. End and intermediate states of the waves under consideration are in the stable phases, such that Lemma 4.5 holds. It remains to check the specific volume values, where the wave structure changes. For kinetic relation K_7 it holds $k_c \equiv \tau_{\text{vap}}^{\text{sat}} = \tau_{\text{vap}}^{\text{sc}}$ and $k_e \equiv \tau_{\text{liq}}^{\text{sat}} = \tau_{\text{liq}}^{\text{se}}$. The waves of the first family are equal, since $g_s(\tau_{\text{liq}}^{\text{sat}}) = \tau_{\text{vap}}^{\text{se}}$. The waves of the second family are equal, identifying $\bar{\tau}$ with $\check{\tau}$. \square

Remark 6.11 (Kinetic relation K_8).

Pushing k^* in K_2 to infinity leads to the kinetic relation $K_8(f, \mathfrak{s}) = -\mathfrak{s}$, what means that no entropy is dissipated, since $\mathfrak{s} = 0$. Theorem 6.1 can be applied but the corresponding kinetic functions are monotone increasing. Phase transitions, that obey K_8 , satisfy $\mathfrak{s} = 0$, $v_{\text{liq}} = v_{\text{vap}}$, $p(\tau_{\text{liq}}) = p(\tau_{\text{vap}})$. The kinetic functions are given by

$$k_c(\tau_{\text{liq}}) = p_{\text{vap}}^{-1}(p(\tau_{\text{liq}})) \quad \text{and} \quad k_e(\tau_{\text{vap}}) = p_{\text{liq}}^{-1}(p(\tau_{\text{vap}})), \quad (6.6)$$

where p_{liq}^{-1} is the inverse function of $p : \mathcal{A}_{\text{liq}} \rightarrow \mathbb{R}$ and p_{vap}^{-1} is the inverse of $p : \mathcal{A}_{\text{vap}} \rightarrow \mathbb{R}$.

In Eulerian coordinates $\mathfrak{s} = j = 0$ means, there is no mass flux between the phases. Such a phase transition may represent material boundaries of different immiscible substances. Riemann solvers for impermeable material boundaries can be found, e.g. in [28].

Remark 6.12 (Kinetic relation K_6).

As there is no entropy dissipation in K_1 and K_8 the kinetic relation with the highest entropy release has to be searched somewhere in between. The interfacial entropy production is given by the product $\mathfrak{s}f$, see (2.30). We may derive a kinetic relation with the highest entropy release at constant τ_{liq} or at constant τ_{vap} related to the extreme value of $f(\tau_{\text{liq}}, \tau_{\text{vap}}) \mathfrak{s}(\tau_{\text{liq}}, \tau_{\text{vap}})$. The conditions $\frac{d}{d\tau_{\text{vap}}} f \mathfrak{s}_c = 0$ and $\frac{d}{d\tau_{\text{liq}}} f \mathfrak{s}_e = 0$ lead to the relations

$$f(\tau_{\text{liq}}, \tau_{\text{vap}}) + \mathfrak{s}_c(\tau_{\text{liq}}, \tau_{\text{vap}})^2 \llbracket \tau \rrbracket^2 = 0, \quad f(\tau_{\text{liq}}, \tau_{\text{vap}}) - \mathfrak{s}_e(\tau_{\text{liq}}, \tau_{\text{vap}})^2 \llbracket \tau \rrbracket^2 = 0.$$

Kinetic relation $K_6(f, \mathfrak{s}, \tau_{\text{liq}}, \tau_{\text{vap}}) = f - \text{sign}(\mathfrak{s}) \mathfrak{s}^2 \llbracket \tau \rrbracket^2$ takes both cases into account. Figure 6.3 shows, that the corresponding kinetic functions for K_6 are monotone increasing, thus the microsolver of Algorithm 5.8 is not applicable.

Note that this kinetic relation does not correspond to the energy rate admissibility criterion in [21, 36]. There, entropy is minimized over a set of admissible Riemann solutions, while here it is minimized over a set of phase transitions with one fixed end state.

Example 6.13 (Density functional theory and kinetic relation K_2).

Density functional theory is used in [42] in order to compute resistivities for heat transfer and for mass transfer at vapor liquid interfaces. The authors assume a correlation between the interfacial mass flux and differences in the chemical potential that is similar to kinetic relation K_2 . For isothermal one-component fluids the correlation reduces to $\llbracket \mu \rrbracket = -T R j$, where $R \geq 0$ is called interfacial resistivity. That gives for (2.7), (6.2), $\zeta = 0$ and $j = -\mathfrak{s}$ the relation

$$\llbracket f \rrbracket + \{\tau\} \llbracket p \rrbracket = T R \mathfrak{s}.$$

Note that this is K_2 with $k^* = T R$ up to the term $\{\tau\} \llbracket p \rrbracket$. The missing term vanishes in the equilibrium case and it is assumed to be small for the subsequent paragraph.

One finds values of R for n-octane in [73]. We assume that the fluids octane and n-dodecane behave similar, since both are alkanes. Resistivity values of octane are now used to estimate kinetic relation K_2 for n-dodecane at 230 °C, or precisely to determine k^* . Resistivity values depend on temperature. We estimate the values with respect to the reduced temperature T/T_c . This results in the definition

$$K_{\text{dft}}(f, \mathfrak{s}) := f - \mathfrak{s} k_{\text{dft}}^* \quad \text{with} \quad k_{\text{dft}}^* = 28 \text{ m}^4/\text{kg s}. \quad (6.7)$$

Corresponding kinetic functions exist due to Theorem 6.1, but, as one can see in Figure 6.3, the functions are not monotone decreasing. Thus, Theorem 5.7 is not applicable. However, Example 6.17 shows that k_{dft} -micro solutions can nevertheless be computed.

Remark 6.14 (Micro solution for monotone increasing kinetic functions).

It is remarkable that it is possible to define monotone generalized Lax curves for kinetic relation K_8 . The corresponding kinetic functions (6.6) are monotone increasing and such

that the pressure is equal in both end states. That means the value of the Lax curve is the same as in the metastable phase. More precisely

$$\begin{aligned}\mathcal{L}_1(\tau_L, \tau_{\text{vap}}) &= \mathcal{L}_1(\tau_L, k_e(\tau_{\text{vap}})) && \text{for } \tau_{\text{vap}} \geq \tau_{\text{vap}}^{\text{sat}}, \text{ since } p(k_e(\tau_{\text{vap}})) = p(\tau_{\text{vap}}) \text{ and} \\ \mathcal{L}_2(\tau_{\text{liq}}, \tau_R) &= \mathcal{L}_2(k_c(\tau_{\text{liq}}), \tau_R) && \text{for } \tau_{\text{liq}} \leq \tau_{\text{liq}}^{\text{sat}}, \text{ since } p(k_c(\tau_{\text{liq}})) = p(\tau_{\text{liq}}).\end{aligned}$$

The domain of definition for such Lax curves is restricted since we cannot expect that the pressure function provides for any pressure value in a stable phase a corresponding metastable volume value with the same pressure. Furthermore, attached waves are excluded due to the zero propagation speed of the phase transition. However, as long as the Lax curves exist, they are monotone.

On the other hand Lax curves for K_7 are by far not constant (see Figure 5.4 (right)), that would be the crucial limit for monotonicity. We believe therefore, that considering monotone decreasing kinetic functions is too restrictive and not necessary for unique k -micro solutions.

6.2 Illustrating examples of k -micro solutions

We apply the kinetic relations to the k -microsolvers of Chapter 5. One k_7 -micro solution was already considered in Example 5.9. The first example shows, that saturation states are preserved, and we study the dependency of k -micro solutions on surface tension and different kinetic relations.

Example 6.15 (Static solutions and influence of the surface tension term ζ).

We compute the k_7 -micro solution for the initial states of Example 4.18, that are the saturation states for $\zeta = 0$ and zero velocity in both phases. As one can see in Figure 6.4, solution and initial states are identical. This is due to the fact that all kinetic relations in Theorem 6.1 fulfill $K(0, 0) = 0$ and $f(\tau_{\text{liq}}^{\text{sat}}, \tau_{\text{vap}}^{\text{sat}}) = 0$.

That changes for $\zeta \neq 0$. Figure 6.4 shows the k_7 -micro solution for $\zeta \in \{-0.01, 0, 0.0\}$. The k_7 -micro solution for $\zeta = -0.01$ is a composition of a shock wave followed by an evaporating wave with speed $\mathfrak{s} \approx -0.004$ and another shock wave respectively a composition of wave type 2_L and 1_R . On the other hand, for $\zeta = 0.01$ we find a rarefaction wave followed by a condensation wave with speed $\mathfrak{s} \approx 0.004$ and another rarefaction wave, respectively a composition of wave type 1_L and 4_R .

Note that thermodynamic equilibrium solutions (cf. Lemma 3.7) are preserved. Compared with the Liu micro solutions of Example 4.18, the phase boundary propagates faster and there occurs one more wave in the metastable region. As in Example 4.18, one can interpret the examples with surface tension as considering a spherical bubble or droplet. In both cases, the radius decreases in order to compensate the pressure difference due to the Young-Laplace law.

Example 6.16 (Influence of different kinetic relations).

This example shall illustrate the effect of different kinetic relations. We use again the van der Waals pressure of Example 2.4 and initial conditions

$$\mathbf{U}(\xi, 0) = \begin{cases} (0.57, 0)^\top & \text{for } \xi \leq 0, \\ (50, 0)^\top & \text{for } \xi > 0, \end{cases}$$

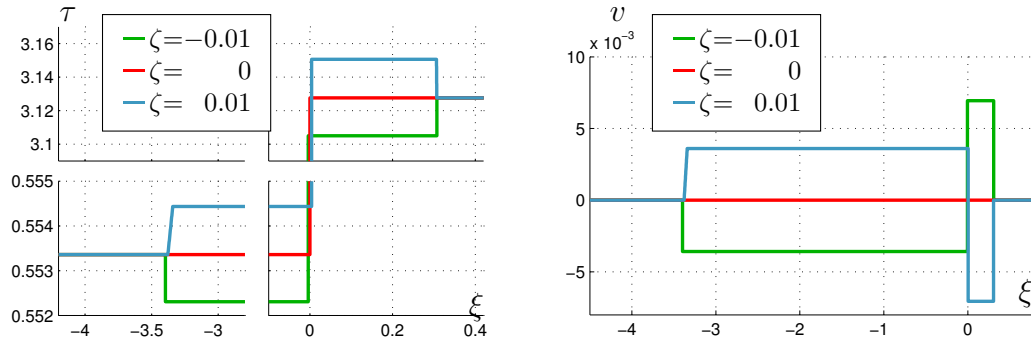


Figure 6.4: k_7 -micro solutions for different amounts of surface tensions. The left figure shows the specific volume and the right one the velocity as function of the Lagrangian space variable at time $t = 1$.

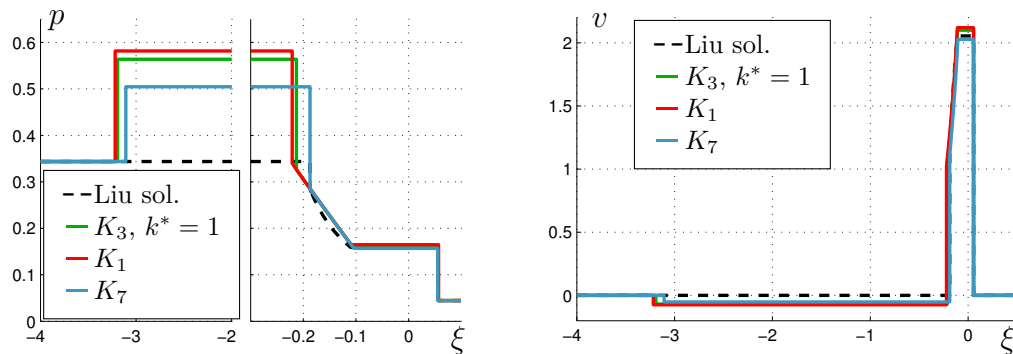


Figure 6.5: Liu micro solution (dashed line) and k -micro solution (solid lines) with different kinetic relations. The left figure shows the pressure and the right one the velocity as function of the Lagrangian space variable at time $t = 1$.

such that the liquid state is metastable. The solid lines in Figure 6.5 show the k -micro solution for $\zeta = 0$ and different kinetic relations. All k -micro solutions are composed of a shock wave followed by an evaporation wave with attached rarefaction wave and a shock wave. In terms of Table 5.1 and Table 5.2 the solution is composed of wave type 3_L and type 6_R . We see that the pressure in the liquid phase is higher for more entropy dissipation while the propagation speed gets slower.

Furthermore, the example illustrates one of the shortcomings of the Liu microsolver. The Liu micro solution is a composition of wave type 6_L^ζ and 3_R^ζ . It is plotted with a dashed line in Figure 6.5. The phase transition is a metastable transition wave, however without respecting the correct macro-scale pressure. Thus, this wave violates the Rankine-Hugoniot conditions (3.7), which are states for the original pressure function and not the mixture pressure.

6.3 Validation with shock tube experiments

We compare the numerical approaches against the shock tube experiments of Simoes-Moreira and Shepherd in [68], for the purpose of validation. In their experiments liquid n-

dodecane was relaxed into a low pressure reservoir. They observed stable evaporation fronts of high velocity. We consider here only the series of experiments at constant temperature $T = 230^\circ\text{C}$. Initially the liquid was at saturation pressure (here $p(\tau_{\text{liq}}^{\text{sat}}) = 1.37$ bar) and the vapor pressure varies between almost vacuum and the saturation pressure.

We compare the experimental data with k -micro solutions for different kinetic relations. We assume that the dissipation rate k^* in kinetic relation K_2 or K_3 depends on temperature¹, thus the *isothermal series* in [68] allows us to use the same value of k^* for all test cases.

The experiment shows stable evaporation fronts until a vapor pressure of 0.7 bar. At higher pressure there was either no evaporation process starting or they observed a train of bubbles and unstable waves. The first case corresponds to zero transition speed. In the second case no evaporation front could be determined. Our special interest lies on the test cases which led to stable evaporation fronts, in order to compare front speeds.

We provide several examples where we compare one-dimensional Riemann solutions and numerical approximations against the measured (planar) evaporation front speed. Furthermore, the authors measured the pressure near the evaporation front. Assume for a moment that the measured values are comparable to the end states at the phase boundary. This could give some hints, which is the physically correct kinetic relation. The measured pressure values (P_{bottom} and P_{exit} in [68]) are plotted into Figure 6.3 with black dots. The dots are far from what we can reach with monotone decreasing kinetic functions. A kinetic function, that is fitted to the measured values and the saturation state, would be a non-decreasing function. Note that the liquid pressure values are in the metastable region and metastable transition waves are generally excluded due to the kinetic function requirements in Definition 5.1, see Corollary 6.4. However, we assume that due to limitations in the measurement facility the measured values are not the trace states itself but at best corresponding mean values of the pressure in the respective phases. We will see in the subsequent example that K_{dft} of Example 6.13, which corresponds to non-decreasing kinetic functions, leads to consistent results.

Example 6.17 (Dodecane shock tube experiments).

This example demonstrates that Algorithm 5.8 is applicable for equations of state of real fluids and that the k -micro solutions match basic properties of the measurements. Furthermore, using K_{dft} leads to consistent results. We consider n-dodecane at $T = 230^\circ\text{C}$. Thermodynamic properties are calculated with the library CoolProp [6]. The liquid state is taken at saturation, that is $p_{\text{L}} \approx 1.39$ bar. The vapor state varies from $p_{\text{R}} = 1.37$ bar to almost vacuum. The initial velocity is zero on both sides.

Figure 6.6 shows the propagation speed in Eulerian coordinates of the evaporation wave for the kinetic relations K_1 , K_3 , K_7 and K_{dft} . The constant for K_3 is $k^* = 0.005 \text{ m}^6/\text{kg}^2$ and the corresponding kinetic functions are monotone decreasing. For K_{dft} Theorem 5.7 is not applicable, however we checked numerically that the corresponding Lax curves are monotone such that k_{dft} -micro solutions exist uniquely. The kinetic relations under consideration are shown in Figure 6.3. Note that, in Figure 6.6 the evaporation waves propagate slower if more entropy is dissipated.

We compare the solutions with the shock tube experiments. The measured front speed values are also plotted in Figure 6.6. For vapor pressure values from almost vacuum to 0.4 bar, the measured front speed values, as well as, the speed predicted by the

¹Density functional theory, cf. Example 6.13, predicts temperature dependent resistivities.

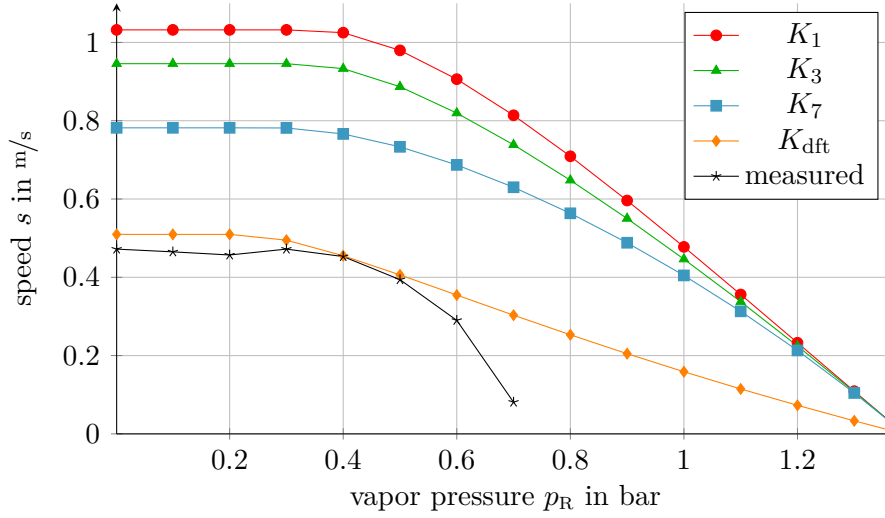


Figure 6.6: Comparison of evaporation front speeds for different initial vapor pressure values p_R . In black, the measured values from [68]. The colored lines refer to interface speeds of k -micro solutions.

k -microsolvers are constant. For lower pressure values the front speeds are decreasing.

The measured front speed is close to zero around 0.7 bar. The propagation speeds, computed via the k -microsolvers, are decreasing much slower. They reach the value $s = 0$ for $p_R = p^{\text{sat}}$. That reflects the fact that here only thermodynamic equilibrium solutions are static. A behavior, as in the experiment, would require a kinetic relation, in which the mass flux is zero until a certain threshold is passed. Such a kinetic relation is described in Remark 6.8. Recall that the authors observed unstable waves and bubbly flows for $p_R > 0.7$ bar. Such flows are not comparable with the solutions of Riemann problems.

Let us concentrate again on the range $0 \text{ bar} \leq p_R \leq 0.7 \text{ bar}$, where Simoes-Moreira and Shepherd observed stable evaporation fronts. It is remarkable that the propagation speed values of k_{dft} -micro solutions match the measured values. Note that there is no parameter that has to be tuned. The propagation speeds for the kinetic relations K_1 , K_3 and K_7 are faster than those of the experiment. The difference reduces, with rising entropy dissipation. The comparison demonstrates, that for this experiment non-decreasing kinetic functions, i.e. K_{dft} , are necessary to predict the correct propagation speed.

We have to remark that the time scale of the experiment was such that bulk waves were reflected at the boundary. Obviously this cannot be taken into account by a single Riemann problem. We will repeat the comparison with [68] in Chapter 9, when a bulk solver is available.

6.4 Interim conclusion

The chapter combined two ingredients: kinetic relations and k -microsolvers for pairs of decreasing kinetic functions. Both were carefully designed, such that they fulfill basic thermodynamic properties. This is not only the case for K_7 , which is verified in Example 6.15. It holds more general. Theorem 6.2 provides necessary conditions, such that corresponding k -micro solutions

- are uniquely determined entropy solutions and
- only thermodynamic equilibrium solutions are static.

The validation in Section 6.3 demonstrates that the k_i -microsolver, for $i = 1, 3, 7$ match basic properties of shock tube experiments. Furthermore, we found good agreements for K_{dft} of Example 6.13. However, this kinetic relation leads to non-decreasing kinetic functions and Theorem 5.7 is not applicable.

Both, the measured evaporation front speeds and the measured pressure values of the n-dodecane shock tube experiments in Section 6.3 demonstrate, that non-decreasing kinetic functions are necessary in order to match the experimental data. State of the art analysis, however, demands pairs of monotone decreasing kinetic functions such that this is an open problem.

We expect that monotonicity of kinetic functions is not a necessary condition for unique two-phase Riemann solutions. For instance, the non-decreasing kinetic functions associated with K_{dft} lead to unique solutions in Example 6.17 and applying K_8 will also lead to unique solutions, see Remark 6.14. The subsequent chapter introduces an approximate approach to apply more general kinetic relations.

Chapter 7

Relaxation microsolver for kinetic relations

Chapter 5 introduced an exact microsolver for pairs of monotone decreasing kinetic functions. Most kinetic functions are not explicitly given such that each function evaluation incorporates the solution of an implicit equation. This is rather elaborate and the implementation effort due to many possible wave structures, cf. Table 5.1 and Table 5.2, is high. Furthermore, only the subclass of monotone decreasing kinetic functions is applicable to the k -microsolver.

In [2, 35], the authors consider two-phase Riemann problems and they apply the kinetic relation directly. However, they assume piecewise linear pressure functions. The pressure function in our case is more general, merely Definition 2.2 is assumed.

This chapter introduces an approximate approach for the micro-scale model in Definition 3.3. An iterative procedure takes the kinetic relations directly into account. We consider here only the physically most relevant case of slow subsonic phase transitions. This leads to an efficient solver, since finally only one implicit equation has to be solved, per evaluation of the microsolver mapping.

We will follow the approach of Chalons, Coquel, Engel and Rohde in [12] and construct in Section 7.1 an approximate microsolver that belongs to the class of relaxation solvers. With Theorem 7.1 and Theorem 7.2 we give basic well-posedness statements for kinetic functions and kinetic relations.

We state the algorithm of the new microsolver in Section 7.3 and we analyze the quality of the relaxation approximation with respect of the exact micro solution. The results are summarized in the final section.

The relaxation approach and the analysis part have been published in [67].

7.1 Relaxation approximation of the Euler equations

We review the relaxation approach from [15] for isothermal Euler equations in the bulk. The system under consideration is given by the micro-scale model in Definition 3.3. As before, we expect that the solution of this two-phase Riemann problem consists of 3 waves,

one wave being a phase transition, see Figure 7.1 (left) for some illustration. However, for the approximate solver we restrict ourselves to subsonic phase transitions that obey a kinetic relation.

In this section we consider the problem in Eulerian coordinates. Consider the kinetic relation

$$\mathbb{K} : \mathcal{A}_{\text{liq}} \times \mathcal{A}_{\text{vap}} \times \mathbb{R} \rightarrow \mathbb{R}, \quad \mathbb{K}(\tau_{\text{liq}}, \tau_{\text{vap}}, j) = \left[\mu(\tau) + \frac{1}{2} \tau^2 j^2 \right] + g(j), \quad (7.1)$$

where μ is the specific Gibbs free energy of Definition 2.2 and $g : \mathbb{R} \rightarrow \mathbb{R}$ is a smooth function of the mass flux j , that satisfies $g(j) j \geq 0$.

Note that this is nothing else but (6.1) (left) with different arguments, since

$$\mathbb{K}(\tau_{\text{liq}}, \tau_{\text{vap}}, j) = K(f(\tau_{\text{liq}}, \tau_{\text{vap}}), -j) = f(\tau_{\text{liq}}, \tau_{\text{vap}}) + g(j). \quad (7.2)$$

We will consider only smooth kinetic relations and refer to the numbering of Table 6.1, i.e. we write \mathbb{K}_2 for $\mathbb{K}_2(\tau_{\text{liq}}, \tau_{\text{vap}}, j) = \left[\mu(\tau) + \tau^2 j^2 / 2 \right] + k^* j$ with $k^* > 0$.

We approximate the exact solution of the micro-scale model by the solution of the Riemann problem for an extended relaxation system. For purely hyperbolic systems, relaxation approximations trace back to [69]. In this case the new system contains one additional equation for an additional unknown (called π in the sequel) which substitutes the nonlinear pressure function of Definition 2.2.

The system is still nonlinear but all fields are linear degenerate which makes the solution of the Riemann problem straightforward. We first follow the idea of [69] exactly and are led to the relaxation Riemann problem

$$\mathbf{V}_t + \mathbf{G}(\mathbf{V})_x = 0 \Leftrightarrow \begin{pmatrix} \varrho \\ \varrho v \\ \varrho \pi \end{pmatrix}_t + \begin{pmatrix} \varrho v \\ \varrho v^2 + \pi \\ (\varrho \pi + a^2)v \end{pmatrix}_x = \begin{pmatrix} 0 \\ 0 \\ 0 \end{pmatrix}, \quad (7.3)$$

subject to the initial datum

$$\mathbf{V}(x, 0) = \begin{cases} \mathbf{V}_L = \varrho_L (1, v_L, \tilde{p}(\varrho_L))^\top & \text{for } x \leq 0, \\ \mathbf{V}_R = \varrho_R (1, v_R, \tilde{p}(\varrho_R))^\top & \text{for } x > 0. \end{cases} \quad (7.4)$$

The parameter $a > 0$ will be defined below. It is straightforward to see that (7.3) is hyperbolic in the convex state space $(0, (\tau_{\text{liq}}^{\min})^{-1}) \times \mathbb{R}^2$. The eigenvalues of the Jacobian of \mathbf{G} are

$$\tilde{\lambda}_1^R(\mathbf{V}) = v - \tau a, \quad \tilde{\lambda}_2^R(\mathbf{V}) = v, \quad \tilde{\lambda}_3^R(\mathbf{V}) = v + \tau a.$$

It is also readily checked that all characteristic fields of (7.3) are linear degenerate. Therefore, the weak solution of (7.3), (7.4) with $a > 0$ is uniquely determined and made up of 3 contact discontinuities. Note that a is related to the sound speed, cf. (2.27). For related work on the relaxation procedure we refer to [12, 15] and references therein.

This procedure would only provide a good approximation for one-phase problems. Because we want to solve a two-phase problem for some given kinetic relation (7.1), we will rely on a different wave fan (which in general is not a weak solution of (7.3)).

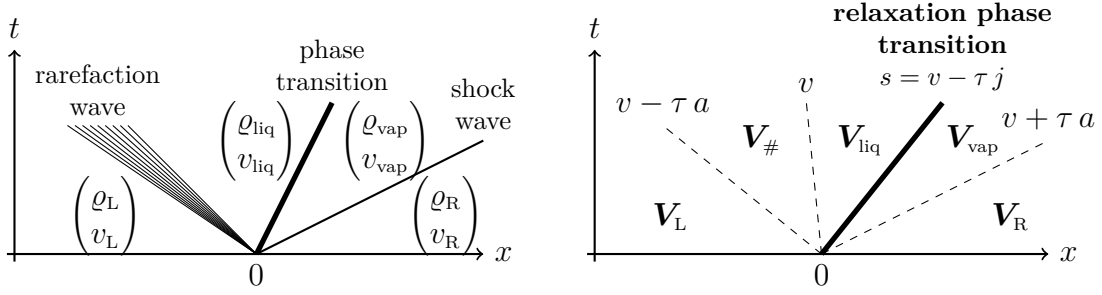


Figure 7.1: Left: typical wave structure for the two-phase Riemann solution. Right: wave fan of the relaxation approximation for some kinetic relation composed of 3 linear degenerate waves and the relaxation phase transition.

We propose to approximate the two-phase Riemann problem by adding a phase transition (see Figure 7.1 (right)). The phase transition is a discontinuous wave that is supposed to satisfy the jump conditions

$$\dot{j} [[\tau]] + [[v]] = 0, \quad \dot{j} [[v]] + [[\pi]] = \zeta, \quad \mathbb{K}(\tau_{\text{liq}}, \tau_{\text{vap}}, \dot{j}) = 0. \quad (7.5)$$

In this way, we ensure that later on the jump conditions of the original system (3.2) and the kinetic relation (7.1) are preserved for the approximation. The number $\dot{j} = \dot{j}(\mathbf{V}_L, \mathbf{V}_R)$ is an estimate for the mass flux (2.26). It is a function of the states $\mathbf{V}_L, \mathbf{V}_R$ and a priori not known exactly. We assume that this mapping satisfies

$$\dot{j} = \dot{j}(\mathbf{V}_L, \mathbf{V}_R) \in \mathcal{C}(\tilde{\mathcal{A}}_{\text{liq}} \times \mathbb{R}^2 \times \tilde{\mathcal{A}}_{\text{vap}} \times \mathbb{R}^2). \quad (7.6)$$

All other waves are kept satisfying the standard Rankine-Hugoniot conditions. Such an approach was introduced in [12] for the p -system, for simpler pressure laws and kinetic functions, and without surface tension.

Let now some \dot{j} be given and assume that \dot{j} does not vanish. W.l.o.g. we consider $\dot{j} < 0$. This implies for any $\mathbf{V} \in (0, (\tau_{\text{liq}}^{\min})^{-1}) \times \mathbb{R}^2$

$$\lambda_2^{\text{R}}(\mathbf{V}) = v < v - \tau \dot{j}.$$

The case $\dot{j} > 0$ can be treated analogously, for $\dot{j} = 0$ see Remark 7.3. Now we let $a > -\dot{j}$ and search for a function $\mathbf{V} : \mathbb{R} \times (0, T) \rightarrow (0, (\tau_{\text{liq}}^{\min})^{-1}) \times \mathbb{R}^2$ given by

$$\mathbf{V}(x, t) = \begin{pmatrix} \varrho \\ \varrho v \\ \varrho \pi \end{pmatrix} = \begin{cases} \mathbf{V}_L & \text{for } x \leq t \sigma_1, \\ \mathbf{V}_{\#} & \text{for } t \sigma_1 < x \leq t \sigma_2, \\ \mathbf{V}_{\text{liq}} & \text{for } t \sigma_2 < x \leq t \sigma_3, \\ \mathbf{V}_{\text{vap}} & \text{for } t \sigma_3 < x \leq t \sigma_4, \\ \mathbf{V}_R & \text{for } t \sigma_4 < x \end{cases} \quad (7.7)$$

with propagation speeds

$$\begin{aligned} \sigma_1 &= \tilde{\lambda}_1^{\text{R}}(\mathbf{V}_L) = \tilde{\lambda}_1^{\text{R}}(\mathbf{V}_{\#}), & \sigma_2 &= \tilde{\lambda}_2^{\text{R}}(\mathbf{V}_{\#}) = \tilde{\lambda}_2^{\text{R}}(\mathbf{V}_{\text{liq}}), \\ \sigma_3 &= v - \tau \dot{j}, & \sigma_4 &= \tilde{\lambda}_3^{\text{R}}(\mathbf{V}_{\text{vap}}) = \tilde{\lambda}_3^{\text{R}}(\mathbf{V}_R). \end{aligned}$$

$[[\mathbf{V}]] := \mathbf{V}_\# - \mathbf{V}_L$	$[[\mathbf{V}]] := \mathbf{V}_{\text{liq}} - \mathbf{V}_\#$	$[[\mathbf{V}]] := \mathbf{V}_{\text{vap}} - \mathbf{V}_{\text{liq}}$	$[[\mathbf{V}]] := \mathbf{V}_R - \mathbf{V}_{\text{vap}}$
$\sigma_1 = v - \tau a$	$\sigma_2 = v$	$\sigma_3 = v - \tau \dot{j}$	$\sigma_4 = v + \tau a$
$-a [[\tau]] + [[v]] = 0$	$[[v]] = 0$	$-\dot{j} [[\tau]] + [[v]] = 0$	$a [[\tau]] + [[v]] = 0$
$a [[v]] + [[\pi]] = 0$	$[[\pi]] = 0$	$\dot{j} [[v]] + [[\pi]] = \zeta$	$-a [[v]] + [[\pi]] = 0$
		$\mathbb{K}(\tau_{\text{liq}}, \tau_{\text{vap}}, \dot{j}) = 0$	

Table 7.1: Jump conditions for the two-phase relaxation Riemann problem. Each column stands for one wave in the representation formula (7.7).

Note that eigenvalues are constant across discontinuous waves. The states \mathbf{V}_{liq} and \mathbf{V}_{vap} are connected by a discontinuity, which we call **relaxation phase transition**. From $a > -\dot{j} > 0$ we see immediately that the ordering of the waves in (7.7) is consistent. For the case $\dot{j} > 0$ the relaxation phase transition would move slower than the contact wave associated to the eigenvalue $\tilde{\lambda}_2^R$ and the construction (7.7) has to be changed accordingly.

We summarize the conditions for the three unknown intermediate states $\mathbf{V}_\#$, \mathbf{V}_{liq} and \mathbf{V}_{vap} in (7.7) in Table 7.1. The obviously redundant relations are already skipped. Altogether we obtain 8 linear equations and one nonlinear equation for nine unknowns. Note that we use the $[[\cdot]]$ -notation not only for the (relaxation) phase transition but for all discontinuities. We call a function \mathbf{V} of from (7.7) **\mathbb{K} -relaxation approximation** if all conditions from Table 7.1 are satisfied. The solution of this algebraic problem depends on the choice of the kinetic relation and will be investigated in the next section.

The corresponding **\mathbb{K} -relaxation microsolver** – a mapping of type (3.4) – is denoted with $\tilde{\mathcal{M}}_{\mathbb{K}}^R$. The superscript R denotes that it is not an exact microsolver in the sense of Definition 3.3 but a relaxation approximation. To refer to a certain kinetic relation (i.e. \mathbb{K}_2), we write \mathbb{K}_2 -relaxation approximation, \mathbb{K}_2 -relaxation microsolver and $\tilde{\mathcal{M}}_{\mathbb{K}_2}^R$.

7.2 Well-posedness of the \mathbb{K} -relaxation microsolver

The main results of this section are Theorem 7.1 and Theorem 7.2 which give existence, uniqueness, and continuous dependence statements for monotone kinetic functions obtained by Theorem 6.2 and general kinetic relations \mathbb{K} from (7.1), respectively. Note that we impose slightly different restrictions on kinetic functions than in Definition 5.1.

Theorem 7.1 (Existence and uniqueness for decreasing kinetic functions).

Consider a smooth and strictly decreasing kinetic function $k : \mathcal{A}_{\text{liq}} \rightarrow \mathcal{A}_{\text{vap}}$ and let the arguments $(\varrho_L, v_L, \varrho_R, v_R, \zeta) \in \tilde{\mathcal{A}}_{\text{liq}} \times \mathbb{R} \times \tilde{\mathcal{A}}_{\text{vap}} \times \mathbb{R} \times \mathcal{Z}$ of the microsolver map (3.4) be given, such that $\dot{j} < 0$ holds.

Then, there exists a positive number \bar{a} , such that for all $a > \bar{a}$, there is a unique \mathbb{K}_k -relaxation approximation \mathbf{V} for the kinetic relation $\mathbb{K}_k : (\tau_{\text{liq}}, \tau_{\text{vap}}, \dot{j}) = k(\tau_{\text{liq}}) - \tau_{\text{vap}}$. In particular, \mathbf{V} satisfies $\varrho_\#, \varrho_{\text{liq}} \in \tilde{\mathcal{A}}_{\text{liq}}$ and $\varrho_{\text{vap}} \in \tilde{\mathcal{A}}_{\text{vap}}$. Furthermore, the mapping $\tilde{\mathcal{M}}_{\mathbb{K}_k}^R$ is continuous.

The theorem is given for the condensation case $\dot{j}(\mathbf{V}_L, \mathbf{V}_R) < 0$. The evaporation case is similar.

Proof of Theorem 7.1. First, we show that the system of 9 equations from Table 7.1 is uniquely solvable. Choose \bar{a} such that $\hat{j} \in (-\bar{a}, 0)$ holds, which is possible due to (7.6). Using all jump conditions except the kinetic relation, a straightforward computation shows that all unknowns can be expressed in terms of $\tau := \tau_{\text{liq}}$. In particular, we have for $a > \bar{a}$ the relation $\tau_{\text{vap}} = A^a \tau + B^a$ with

$$\begin{aligned} A^a &= A^a(\mathbf{V}_L, \mathbf{V}_R) = \frac{a \hat{j} - \hat{j}^2}{2a^2 + a \hat{j} - \hat{j}^2}, \\ B^a &= B^a(\mathbf{V}_L, \mathbf{V}_R) = \frac{\pi_R - \pi_L + a(v_R - v_L) + 2a^2 \tau_R - \zeta}{2a^2 + a \hat{j} - \hat{j}^2}. \end{aligned} \quad (7.8)$$

To conclude, we define the mapping $F_a : \mathcal{A}_{\text{liq}} \rightarrow \mathbb{R}$ by $F_a(\tau) = k^{-1}(A^a \tau + B^a)$. Recall that k is strictly decreasing and $k^{-1} : \mathcal{A}_{\text{vap}} \rightarrow \mathcal{A}_{\text{liq}}$ exists. Furthermore, we have $A^a \rightarrow 0$ and $B^a \rightarrow \tau_R \in \mathcal{A}_{\text{vap}}$ for $a \rightarrow \infty$. Thus, $A^a \tau + B^a \in \mathcal{A}_{\text{vap}}$ for all τ in the bounded set \mathcal{A}_{liq} for $a > \bar{a}$, after possibly increasing \bar{a} once more. Again, using $A^a \rightarrow 0$, we observe that F^a is contracting since k is smooth. Thus, there exists a unique solution of the equations from Table 7.1, the corresponding mapping $\tilde{\mathcal{M}}_{\mathbb{K}}^{\text{R}}$ is continuous.

There is a continuous function $\varphi = \varphi(\mathbf{V}_L, \mathbf{V}_R, a)$ with $\varphi(\mathbf{V}_L, \mathbf{V}_R, a) \rightarrow 0$ for $a \rightarrow \infty$ such that $\tau_{\#} = \tau_L + \varphi(\mathbf{V}_L, \mathbf{V}_R, a)$ holds. Then we find $\tau_{\#} \in \mathcal{A}_{\text{liq}}$ for sufficiently large \bar{a} . \square

Theorem 7.1 gives a global existence result. For kinetic relation \mathbb{K} from (7.1) we are able to show a result for initial datum close to states which produce a single phase transition as traveling wave solution. Note that we make no assumptions whether Theorem 6.1 holds for \mathbb{K} . Precisely, consider the input arguments $(\hat{\rho}_L, \hat{v}_L, \hat{\rho}_R, \hat{v}_R, \hat{\zeta}) \in \tilde{\mathcal{A}}_{\text{liq}} \times \mathbb{R} \times \tilde{\mathcal{A}}_{\text{vap}} \times \mathbb{R} \times \mathcal{Z}$ for $\tilde{\mathcal{M}}_{\mathbb{K}}^{\text{R}}$ and a number $\hat{j} < 0$, such that the conditions

$$-\hat{j}(\hat{\tau}_R - \hat{\tau}_L) + (\hat{v}_R - \hat{v}_L) = 0, \quad \hat{j}(\hat{v}_R - \hat{v}_L) + p(\hat{\tau}_R) - p(\hat{\tau}_L) = \hat{\zeta}, \quad \mathbb{K}(\hat{\tau}_L, \hat{\tau}_R, \hat{j}) = 0 \quad (7.9)$$

are satisfied. Then

$$\begin{pmatrix} \hat{\rho} \\ \hat{v} \end{pmatrix} (x, 0) = \begin{cases} (\hat{\rho}_L, \hat{v}_L)^\top & : x - \hat{s}t \leq 0, \\ (\hat{\rho}_R, \hat{v}_R)^\top & : x - \hat{s}t > 0 \end{cases} \quad (7.10)$$

is a single phase transition that solves the micro-scale model of Definition 3.3 with speed $\hat{s} = \hat{v}_L - \hat{\tau}_L \hat{j} > 0$. Due to (7.4) and (7.5) the single relaxation phase transition

$$\hat{\mathbf{V}}(x, t) = \begin{cases} \hat{\mathbf{V}}_L & := (\hat{\rho}_L, \hat{v}_L, p(\hat{\rho}_L))^\top \quad \text{for } x - \hat{s}t \leq 0, \\ \hat{\mathbf{V}}_R & := (\hat{\rho}_R, \hat{v}_R, p(\hat{\rho}_R))^\top \quad \text{for } x - \hat{s}t > 0 \end{cases} \quad (7.11)$$

is also a \mathbb{K} -relaxation approximation, when $\hat{j}(\hat{\mathbf{V}}_L, \hat{\mathbf{V}}_R) = \hat{j}$ holds. Note that densities and fluid velocities satisfy a fixed point condition in the following sense

$$\tilde{\mathcal{M}}_{\mathbb{K}}^{\text{R}}(\hat{\rho}_L, \hat{v}_L, \hat{\rho}_R, \hat{v}_R, \hat{\zeta}) = (\hat{\rho}_L, \hat{v}_L, \hat{\rho}_R, \hat{v}_R, \hat{s}).$$

Theorem 7.2 (Existence and uniqueness for kinetic relations).

Let $(\hat{\rho}_L, \hat{v}_L, \hat{\rho}_R, \hat{v}_R, \hat{\zeta}) \in \tilde{\mathcal{A}}_{\text{liq}} \times \mathbb{R} \times \tilde{\mathcal{A}}_{\text{vap}} \times \mathbb{R} \times \mathcal{Z}$ be given, such that (7.9) is satisfied for a kinetic relation \mathbb{K} . Assume that $\hat{j}(\hat{\mathbf{V}}_L, \hat{\mathbf{V}}_R) \neq 0$,

$$|\hat{j}| < \max \{ c(\hat{\tau}_L), c(\hat{\tau}_R) \} \quad \text{and} \quad \hat{j}(\hat{\mathbf{V}}_L, \hat{\mathbf{V}}_R) = \hat{j} \quad (7.12)$$

hold.

Then, there exists a number $\bar{a} > 0$ and an open set $\mathcal{W} \subset \tilde{\mathcal{A}}_{\text{liq}} \times \mathbb{R} \times \tilde{\mathcal{A}}_{\text{vap}} \times \mathbb{R} \times \mathcal{Z}$ with $(\hat{\varrho}_L, \hat{v}_L, \hat{\varrho}_R, \hat{v}_R, \hat{\zeta}) \in \mathcal{W}$, such that there exists for all $(\varrho_L, v_L, \varrho_R, v_R, \zeta) \in \mathcal{W}$ and all $a > \bar{a}$ a unique \mathbb{K} -relaxation approximation \mathbf{V} for \mathbb{K} . In particular, \mathbf{V} satisfies $\varrho_{\#}, \varrho_{\text{liq}} \in \tilde{\mathcal{A}}_{\text{liq}}$ and $\varrho_{\text{vap}} \in \tilde{\mathcal{A}}_{\text{vap}}$. Furthermore, the mapping $\tilde{\mathcal{M}}_{\mathbb{K}}^{\mathbb{R}}$ is continuous.

The first condition in (7.12) states that the single phase transition (7.10) is of subsonic type. It is included in the defining relation (3.17).

Proof of Theorem 7.2. We present the proof for the case $j(\hat{\mathbf{V}}_L, \hat{\mathbf{V}}_R) < 0$. As in the proof of Theorem 7.1, we condense the conditions in Table 7.1 to a scalar equation for τ_{vap} in terms of $\tau = \tau_{\text{liq}}$. One finds for $T_a(\tau) = T_a(\tau; \mathbf{V}_L, \mathbf{V}_R) := A^a(\mathbf{V}_L, \mathbf{V}_R)\tau + B^a(\mathbf{V}_L, \mathbf{V}_R)$ again the relation

$$\tau_{\text{vap}} = T_a(\tau_{\text{liq}}; \mathbf{V}_L, \mathbf{V}_R),$$

where A^a and B^a are defined as in (7.8). Applying the kinetic relation (7.1), we can eliminate τ_{vap} and obtain the scalar equation

$$F_a(\tau) = F_a(\tau; \mathbf{V}_L, \mathbf{V}_R) := \mathbb{K}(\tau, T_a(\tau; \mathbf{V}_L, \mathbf{V}_R), j(\mathbf{V}_L, \mathbf{V}_R)) = 0,$$

or writing out \mathbb{K}

$$\mu(T_a(\tau; \mathbf{V}_L, \mathbf{V}_R)) - \mu(\tau) + \frac{j^2}{2} (T_a(\tau; \mathbf{V}_L, \mathbf{V}_R)^2 - \tau^2) + k(j) = 0.$$

As in the proof of Theorem 7.1, we see that $F_a : \mathcal{A}_{\text{liq}} \rightarrow \mathbb{R}$ is well-defined for a sufficiently large. We know from (7.9) that $T_a(\hat{\tau}_L; \hat{\mathbf{V}}_L, \hat{\mathbf{V}}_R) = \hat{\tau}_R$, thus

$$F_a(\hat{\tau}_L; \hat{\mathbf{V}}_L, \hat{\mathbf{V}}_R) = 0 \tag{7.13}$$

holds with (7.12).

Now, recall from (2.7) that the specific Gibbs free energy satisfies $\mu'(\tau) = \tau p'(\tau)$. Then, the derivative of F_a with respect to τ is

$$\begin{aligned} F'_a(\tau) &= T_a(\tau) p'(T_a(\tau)) T'_a(\tau) - \tau p'(\tau) + j^2 (T_a(\tau) T'_a(\tau) - \tau) \\ &= \tau \left(-p'(\tau) - j^2 \right) - T_a(\tau) T'_a(\tau) \left(-p'(T_a(\tau)) - j^2 \right). \end{aligned}$$

From (7.12), we conclude $p'(\hat{\tau}_{L/R}) + \hat{j}^2 = -c^2(\hat{\tau}_{L/R}) + \hat{j}^2 < 0$. Moreover, we can choose \bar{a} such that the relation $T_a(\hat{\tau}_L; \hat{\mathbf{V}}_L, \hat{\mathbf{V}}_R) A_a(\hat{\mathbf{V}}_L, \hat{\mathbf{V}}_R) < 0$ holds for all $a > \bar{a}$, such that we get

$$F'_a(\hat{\tau}_L; \hat{\mathbf{V}}_L, \hat{\mathbf{V}}_R) > 0.$$

Then, we can deduce from (7.13) that there exists at least locally a unique \mathbb{K} -relaxation approximation \mathbf{V} for \mathbb{K} and $\tilde{\mathcal{M}}_{\mathbb{K}}^{\mathbb{R}}$ is continuous. \square

Remark 7.3 (Existence and uniqueness for vanishing mass flux estimate).

Theorem 7.2 is stated for the case that $j(\hat{\mathbf{V}}_L, \hat{\mathbf{V}}_R)$ does not vanish. The existence of a \mathbb{K} -relaxation approximation can also be proven for the zero case, provided that

$$j(\mathbf{V}_L, \mathbf{V}_R) = 0 \quad \Leftrightarrow \quad \mathbf{V}_L, \mathbf{V}_R \text{ solves (7.9) with } \hat{\mathbf{V}}_L = \mathbf{V}_L, \hat{\mathbf{V}}_R = \mathbf{V}_R \text{ and } \hat{j} = 0$$

holds. In this case, (7.7) remains well-defined, since $\mathbf{V}_{\#} = \mathbf{V}_{\text{liq}}$ holds.

7.3 Algorithm and verification

The approximate solver crucially depends on estimates \mathring{j} and $a > 0$. We provide in this section illustrating examples for specific choices of the parameters and we verify the relaxation approximations with respect to the exact solutions. Parameter $a > 0$ is linked to the sound speeds in the respective phase. In real fluids, but also for the van der Waals Example (2.4), the propagation speed in different phases differs in magnitudes. Therefore, phase depended versions

$$a_L := \alpha c(\tau_L) \quad \text{and} \quad a_R := \alpha \max \{ c(\tau_R), \mathring{j}(\mathbf{V}_L, \mathbf{V}_R) \}, \quad (7.14)$$

with $\alpha > 1$ of a are considered.

Algorithm 7.4 (\mathbb{K} -relaxation microsolver $\tilde{\mathcal{M}}_{\mathbb{K}}^R$).

Let the arguments $(\varrho_L, v_L, \varrho_R, v_R, \zeta) \in \tilde{\mathcal{A}}_{\text{liq}} \times \mathbb{R} \times \tilde{\mathcal{A}}_{\text{vap}} \times \mathbb{R} \times \mathcal{Z}$ of the microsolver map (3.4), a kinetic relation \mathbb{K} , a parameter $\alpha > 1$ and a mapping $\mathring{j} = \mathring{j}(\mathbf{V}_L, \mathbf{V}_R)$ that satisfies (7.6) be given.

Step 1. Determine the initial datum $\mathbf{V}_L, \mathbf{V}_R$ due to (7.4), the mass flux estimate \mathring{j} and a_L, a_R due to (7.14).

Step 2. If $\mathring{j} > 0$ repeat Step 1 for the arguments $(\varrho_R, -v_R, \varrho_L, -v_L, -\zeta)$.

Step 3. Solve the system defined in Table 7.1 for \mathbb{K} .

Step 4. Return $(\varrho_{\text{liq}}, v_{\text{liq}}, \varrho_{\text{vap}}, v_{\text{vap}}, s)$ or $(\varrho_{\text{vap}}, -v_{\text{vap}}, \varrho_{\text{liq}}, v_{\text{liq}}, -s)$ if Step 2 was applied.

It remains to determine the mass flux estimate (7.6). The choice should ensure, in particular, the second condition in (7.12), that is $\mathring{j}(\hat{\mathbf{V}}_L, \hat{\mathbf{V}}_R) = \hat{j}$ for the end states $\hat{\mathbf{V}}_L, \hat{\mathbf{V}}_R$ of the single relaxation phase transition (7.11). We may use one of the conditions in (7.9)

$$\begin{aligned} \mathring{j}_\tau(\mathbf{V}_L, \mathbf{V}_R) &:= \frac{v_R - v_L}{\tau_R - \tau_L}, & \mathring{j}_v(\mathbf{V}_L, \mathbf{V}_R) &:= -\frac{\pi_R - \pi_L + \zeta}{v_R - v_L}, \\ \mathring{j}_{\mathbb{K}}(\mathbf{V}_L, \mathbf{V}_R) &:= g^{-1}(-f(\tau_L, \tau_R)) \end{aligned} \quad (7.15)$$

to achieve this or a convex combination thereof. Note that we applied (7.2) for the latter one. This estimate demands that g^{-1} exists. The estimate \mathring{j}_v is undefined for $v_R = v_L$ and should therefore not be used. The estimate \mathring{j}_τ is zero for $v_R = v_L$, independent of the initial specific volume or pressure values. Thus, we rely on convex combinations of \mathring{j}_τ and $\mathring{j}_{\mathbb{K}}$.

We proceed with examples of \mathbb{K} -relaxation approximations. The first one demonstrates that the approach works well for initial states near the traveling wave solution (7.10). This was expected due to Theorem 7.2. The subsequent examples, however, show that the relaxation approximation can be very poor. We apply the van der Waals pressure of Example 2.4 and (7.14) with $\alpha = 1.2$, unless otherwise specified

Example 7.5 (Influence of the surface tension term ζ).

We compute the \mathbb{K}_2 -relaxation approximation with $k^* = 1$ for the initial conditions of Example 4.18. The initial states are the saturation states for $\zeta = 0$. The mass flux

estimate is $\mathring{j}(\mathbf{V}_L, \mathbf{V}_R) := 0.8 \mathring{j}_\tau(\mathbf{V}_L, \mathbf{V}_R) + 0.2 \mathring{j}_\mathbb{K}(\mathbf{V}_L, \mathbf{V}_R)$. The \mathbb{K}_2 -relaxation approximations are transformed to Lagrangian coordinates to compare them with the Liu micro solution of Example 4.18 and the k_3 -micro solution of Example 6.15. The micro solutions are very similar, although different kinetic relations are used.

Figure 7.2 shows the result. The initial condition constitutes a fixed point of the \mathbb{K}_2 -relaxation microsolver in case of $\zeta = 0$, thus the solution remains static. The choice (7.15) results in an evaporation wave for $\zeta = -0.01$, that propagates with speed $\mathfrak{s} \approx -0.0037$. The condensation wave for $\zeta = 0.01$ propagates with $\mathfrak{s} \approx 0.0037$. Due to the choice of a_L and a_R , bulk waves propagate faster than in case of the exact solution.

Example 7.6 (Quality of the \mathbb{K}_1 -relaxation approximation for different j).

We compare the \mathbb{K}_1 -relaxation approximation with the k_1 -micro solution. The initial condition are

$$(\tau, v)(\xi, 0) = \begin{cases} (0.5, 0.5)^\top & \text{for } \xi \leq 0, \\ (10, 0)^\top & \text{for } \xi > 0. \end{cases}$$

Figure 7.3 shows the relaxed pressure π (left) and the pressure computed from the specific volume of the solution (right). In case of the (exact) k_1 -micro solution we used $\pi(\xi, t) = p(\tau(\xi, t))$. The wave pattern of the k_1 -micro solution is composed of a rarefaction wave followed by an evaporation wave with speed $\mathfrak{s}_{\text{ex}} \approx -0.17$ and a shock wave. The \mathbb{K}_1 -relaxation approximation uses the mass flux estimate \mathring{j}_τ (blue fan in Figure 7.3) and the exact value $\mathring{j}_{\text{ex}} := -\mathfrak{s}_{\text{ex}}$ of the k_1 -micro solution (red fan in Figure 7.3). Note that $\mathring{j}_\mathbb{K}$ is not applicable since $g(j)$ is zero.

The \mathbb{K}_1 -relaxation approximation with \mathring{j}_τ predicts a condensation wave of speed $\mathfrak{s} \approx 0.05$. The relaxed pressure π , as well as, $p(\tau)$ are rather far from the exact values $p_{\text{liq}} \approx 0.55$, $p_{\text{vap}} \approx 0.45$ at the phase transition. The reason might be the poor mass flux estimate. Using \mathring{j}_{ex} , however, does not lead to a better approximation. It is even worse, using the exact mass flux leads to a solution with negative values for specific volume and pressure.

Example 7.7 (Quality of the \mathbb{K}_1 -relaxation approximation for different a).

We have seen in the last example that the \mathbb{K}_1 -relaxation approximation may lead to inadmissible states. This was the case for the mass flux estimate \mathring{j}_{ex} , here we found negative values for specific volume and pressure. According to Theorem 7.1, increasing a , or α in (7.14), leads to admissible solutions. Unfortunately that does not improve the quality of the approximation. We found, for instance, admissible solutions $(\varrho_{\text{liq}} \in \tilde{\mathcal{A}}_{\text{liq}}, \varrho_{\text{vap}} \in \tilde{\mathcal{A}}_{\text{vap}})$ for $\alpha = 3$ and $\alpha = 12$. But the specific volume and pressure values of the approximations are rather far from those of the exact solution, see Figure 7.4.

More precisely, increasing a leads to relaxation approximations, where $\mathbf{V}_{\text{liq}} \approx \mathbf{V}_L$ and $\mathbf{V}_{\text{vap}} \approx \mathbf{V}_R$ holds. This can be seen also in Table 7.1 pushing a to infinity. The solution is admissible, just like the initial states, but loses all other properties.

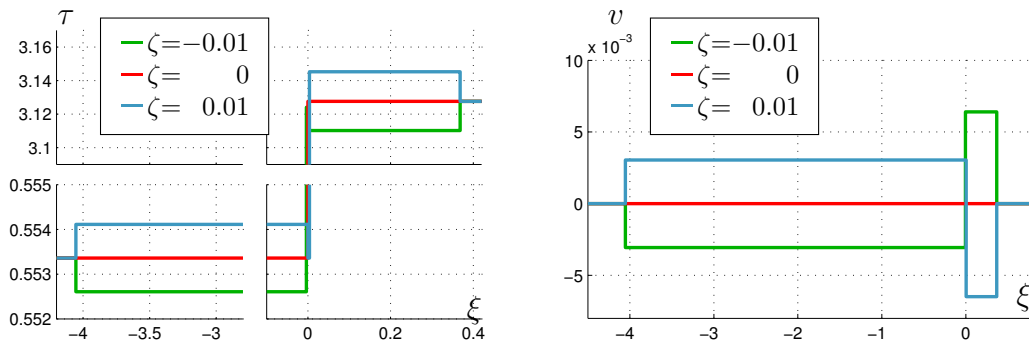


Figure 7.2: \mathbb{K}_2 -relaxation approximations for different amounts of surface tensions in Example 7.5. The left figure shows the specific volume and the right one the velocity as function of the Lagrangian space variable at time $t = 1$.

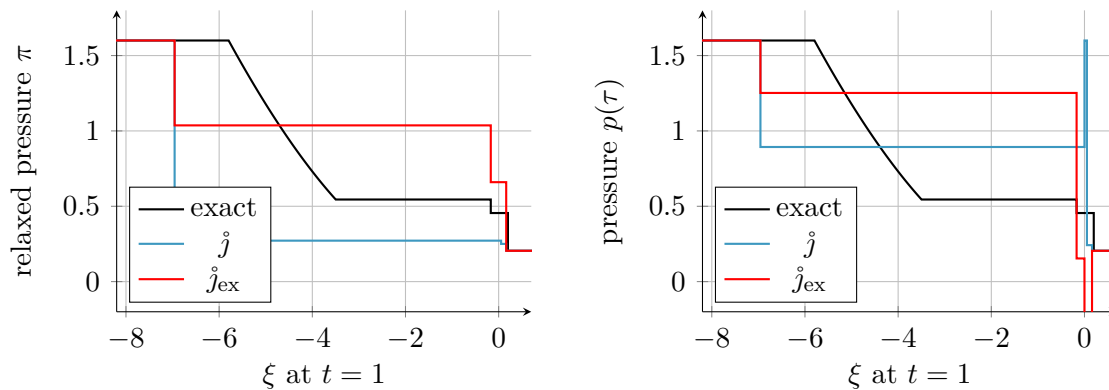


Figure 7.3: Relaxed pressure π (left) and pressure $p(\tau)$ (right), both as functions of the Lagrangian space variable at time $t = 1$. In black the k_1 -micro solution, in blue and in red \mathbb{K}_1 -relaxation approximations for different mass flux estimates in Example 7.6.

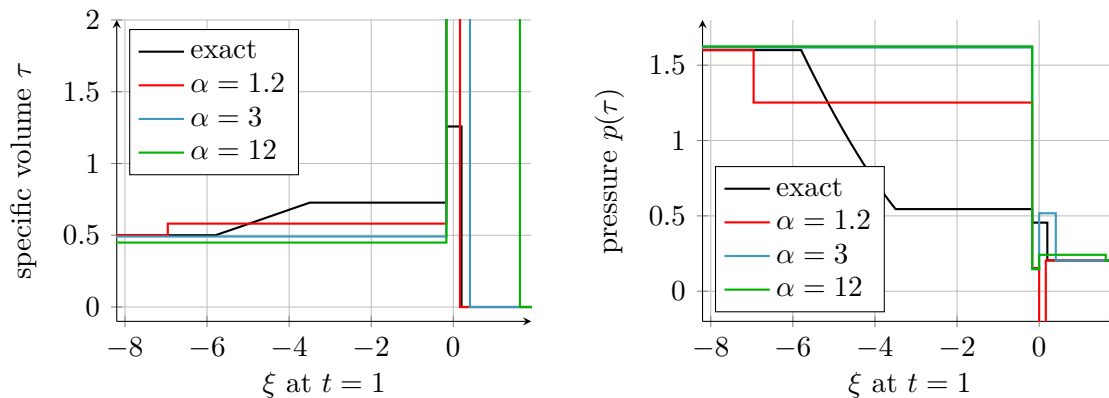


Figure 7.4: Specific volume τ (left) and pressure $p(\tau)$ (right), both as functions of the Lagrangian space variable at time $t = 1$. In black the k_1 -micro solution, in red, blue and in green \mathbb{K}_1 -relaxation approximations for different estimates of a , see Example 7.7.

7.4 Interim conclusion

The relaxation approach provides an efficient way to approximate the solution of the micro-scale model of Definition 3.3 for almost any kinetic relation. In particular the solver overcomes the shortcoming of the k -microsolver in Chapter 5, which was only for monotone decreasing kinetic functions applicable. Furthermore, the \mathbb{K} -relaxation approximation preserves thermodynamic equilibrium solutions (Example 7.5).

Unfortunately, the approximation of the \mathbb{K} -relaxation solver can be very poor. More severe, there are (tuning) parameters a and j but they are not able to improve the quality of the approximation. Theorem 7.1 and Theorem 7.2 state that increasing the parameter a leads to admissible solutions, what merely means that states are in the required phase. But, neither increasing a (cf. Example 7.7), nor improving the mass flux estimate (cf. Example 7.6) led to good results.

However, the authors in [12] observe grid convergence, combining the relaxation solver with a front tracking scheme. We will analyze the coupling of microsolver and bulk solver in Chapter 9.

Chapter 8

Bulk solver with front tracking for radially symmetric solutions

In this chapter, we present our implementation of the front tracking scheme of Algorithm 3.1. The scheme solves the free boundary value problem of Section 2.4. For other numerical methods for two-phase flow problems of mixed hyperbolic-elliptic type, we refer to [8, 14, 16, 30, 58, 75].

We will restrict ourselves to the one-dimensional case $d = 1$ and radially symmetric solutions in \mathbb{R}^d for $d > 1$. In this way it is possible to take into account curvature effects without requiring a complex computation of the curvature. Furthermore, we want to keep the scheme simple but conservative, thus it bases on a (formally) first order finite volume method with local grid adaption. The resulting method serves as a test environment for the microsolvers of the previous chapters.

The first section introduces the discrete formulation of the method and the underlying grid. Section 8.2 states the algorithm of the scheme and demonstrates that it is conservative and preserves isolated phase transitions.

The bulk solver has been published in [67], where it was combined with the \mathbb{K} -relaxation microsolver of Chapter 7.

8.1 Moving mesh finite volume method

Let us introduce first the transformed setting of the isothermal Euler system, cf. [51, Section 18.9]. For $R_{\max} > R_{\min} > 0$ let $\tilde{\mathbf{U}} = \tilde{\mathbf{U}}(\mathbf{x}, t) = (\varrho(\mathbf{x}, t), \mathbf{m}(\mathbf{x}, t)^\top)^\top$ be a radially symmetric solution of the system (2.20) in $\Omega \times [0, T)$, with $\Omega = \{\mathbf{x} \in \mathbb{R}^d \mid R_{\min} < |\mathbf{x}| < R_{\max}\}$. We assume that there is a single interface of the form $\Gamma(t) = \gamma(t) \mathbb{S}^{d-1}$ with $\gamma(t) \in (R_{\min}, R_{\max})$ for $t \in [0, T)$. Then, there is a function $\mathbf{W} = \mathbf{W}(r, t) = (\varrho(r, t), m(r, t))^\top$ with

$$\varrho(\mathbf{x}, t) = \varrho(r, t), \quad \mathbf{m}(\mathbf{x}, t) = \frac{\mathbf{x}}{r} m(r, t), \quad |\mathbf{x}| = r. \quad (8.1)$$

Note that the density is denoted with ϱ , independent of the spatial variable, while there are two versions of the momentum function $\mathbf{m} = \mathbf{m}(\mathbf{x}, t)$ and $m = m(r, t)$. The function \mathbf{W} satisfies

$$\mathbf{W}_t + \frac{1}{r^{d-1}} \left(r^{d-1} \mathbf{F}(\mathbf{W}) \right)_r = \frac{d-1}{r} \mathbf{Q}(\mathbf{W}) \quad (8.2)$$

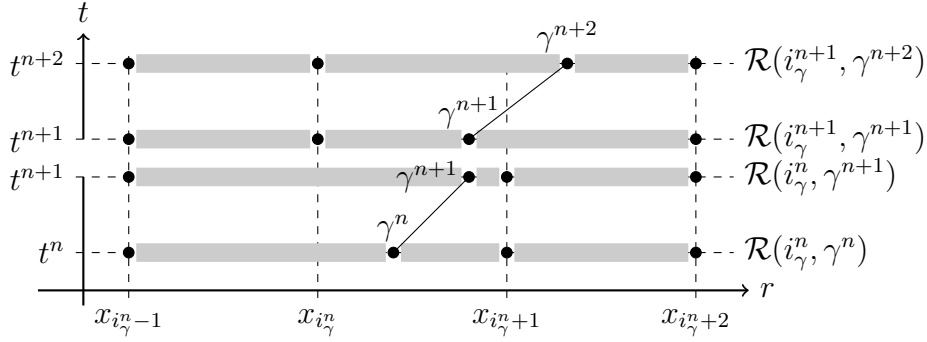


Figure 8.1: Possible mesh modification: moving mesh strategy for $t^n \rightarrow t^{n+1}$ resp. $t^{n+1} \rightarrow t^{n+2}$ and local remeshing when $i_{\gamma}^{n+1} = i_{\gamma}^n + 1$. The dots denote the actual partition obtained by applying \mathcal{R} and the gray boxes indicate the cells.

in $\{(r, t) \in (R_{\min}, R_{\max}) \times (0, T) \mid r \neq \gamma(t)\}$. In view of the isothermal model from Definition 2.8, the system (8.2) is completed with initial and boundary conditions

$$\mathbf{W}(r, 0) = \mathbf{W}_0(r) := \varrho_0(\mathbf{x}) (1, \mathbf{v}_0(\mathbf{x}) \cdot \mathbf{x})^T, \quad |\mathbf{x}| = r$$

and $m(R_{\min}, t) = m(R_{\max}, t) = 0$ for $t \in [0, T)$.

In (8.2) the functions $\mathbf{F}, \mathbf{Q} : (\tilde{\mathcal{A}}_{\text{liq}} \cup \tilde{\mathcal{A}}_{\text{vap}}) \times \mathbb{R} \rightarrow \mathbb{R}^2$ are given by

$$\mathbf{F}(\mathbf{W}) = \begin{pmatrix} m \\ \frac{m^2}{\varrho} + \tilde{p}(\varrho) \end{pmatrix}, \quad \mathbf{Q}(\mathbf{W}) = \begin{pmatrix} 0 \\ \tilde{p}(\varrho) \end{pmatrix}.$$

The bulk solver for the numerical scheme can be classified as a moving mesh finite volume scheme with explicit time stepping. For two successive time levels $t^n < t^{n+1}$, $n \in \mathbb{N}$, the associated time step is defined by $\Delta t^n = t^{n+1} - t^n$.

For the description of the moving mesh strategy, let us introduce first the points $R_{\min} = x_0 < x_1 < \dots < x_{I+1} = R_{\max}$. The numerical algorithm will determine for any $n \in \mathbb{N}$ a number $\gamma^n \in (R_{\min}, R_{\max})$, which represents the position of the discrete phase boundary at time t^n . Let

$$i_{\gamma}^n = \begin{cases} k & \text{if } |\gamma^n - x_k| < |\gamma^n - x_i| \text{ for all } i = 1, \dots, I, i \neq k, \\ i & \text{if } |\gamma^n - x_i| = |\gamma^n - x_{i+1}| \end{cases} \quad (8.3)$$

be the index of the closest point to γ^n . For the spatial discretization we introduce a time-dependent partition via the function $\mathcal{R} : \mathbb{N} \times \mathbb{R} \rightarrow \mathcal{P}(\mathbb{R})$,

$$\mathcal{R}(i_{\gamma}^n, \gamma^n) = \left\{ r_0, \dots, r_{I+1} \in [R_{\min}, R_{\max}] \mid r_i = x_i \text{ for } i \neq i_{\gamma}^n \text{ and } r_{i_{\gamma}^n} = \gamma^n \right\}.$$

Figure 8.1 shows possible realizations of \mathcal{R} .

In order to preserve the original multidimensional conservation we consider (8.2) not as a one-dimensional system, but approximate cell averages for the original spherically symmetric situation, see e.g. [54]. We follow then the classical finite volume strategy in \mathbb{R}^d and introduce multidimensional grid cells

$$K_i^n = \left\{ \mathbf{x} \in \mathbb{R}^d \mid r_i^n \leq |\mathbf{x}| \leq r_{i+1}^n \right\} \text{ for } r_i^n \in \mathcal{R}(i_{\gamma}^n, \gamma^n), \text{ and} \\ K_i^{n+1,-} = \left\{ \mathbf{x} \in \mathbb{R}^d \mid r_i^n \leq |\mathbf{x}| \leq r_{i+1}^n \right\} \text{ for } r_i^n \in \mathcal{R}(i_{\gamma}^n, \gamma^{n+1}), \quad i = 0, \dots, I,$$

with cell volume $|K_i^n| = A_d(r_{i+1}^n) - A_d(r_i^n)$ and surface measure $|\partial K_i^n| = A'_d(r_{i+1}^n) - A'_d(r_i^n)$. Here $A_d(r)$ is the volume of a d -dimensional sphere with radius $r > 0$.

Let us explain the grid notation. Within one time step Δt^n , the interface moves from γ^n to γ^{n+1} . The points are kept aligned with the interface and $\mathcal{R}(i_\gamma^n, \gamma^n)$ changes to $\mathcal{R}(i_\gamma^{n+1}, \gamma^{n+1})$. The volume of the adjacent cells may change. If the cell volume becomes small, a local remeshing is applied from $\mathcal{R}(i_\gamma^n, \gamma^n)$ to $\mathcal{R}(i_\gamma^{n+1}, \gamma^{n+1})$. Otherwise, $i_\gamma^n = i_\gamma^{n+1}$ holds and thus $K_i^{n+1,-} = K_i^{n+1,+}$. We refer again to Figure 8.1 for illustration.

Next, we consider the iterates

$$\mathbf{W}_i^n \approx \frac{1}{|K_i^n|} \int_{r_i^n}^{r_{i+1}^n} A'_d(r) \mathbf{W}(r, t^n) \, dr.$$

The family $\{\mathbf{W}_i^n \mid n \in \mathbb{N}, 0 \leq i \leq I\}$ is computed for $i = 0, \dots, I$ by

$$\begin{aligned} |K_i^{n+1,-}| \mathbf{W}_i^{n+1} &= |K_i^n| \mathbf{W}_i^n \\ &\quad - \Delta t^n \left(A'_d(r_{i+1}^n) \mathbf{F}_{i+1,-}^n - A'_d(r_i^n) \mathbf{F}_{i,+}^n - (A'_d(r_{i+1}^n) - A'_d(r_i^n)) \mathbf{Q}(\mathbf{W}_i^n) \right) \end{aligned} \quad (8.4)$$

for $n > 0$ and

$$\mathbf{W}_i^0 = \frac{1}{|K_i^0|} \int_{r_i^0}^{r_{i+1}^0} A'_d(r) \mathbf{W}_0(r) \, dr.$$

The surface measure terms A'_d in (8.4) stem from the geometric $1/r$ terms in (8.2).

It remains to fix the fluxes $\mathbf{F}_{i,-/+}^n$ in (8.4). Let $\mathbf{F}_{\text{num}} : ((\tilde{\mathcal{A}}_{\text{liq}} \cup \tilde{\mathcal{A}}_{\text{vap}}) \times \mathbb{R})^2 \rightarrow \mathbb{R}^2$ be an arbitrary numerical flux, that is consistent with \mathbf{F} , given in (8.2). Furthermore, we assume that we have a microsolver $\tilde{\mathcal{M}}$ as specified in Definition 3.3. By applying $\tilde{\mathcal{M}}$ we get (see Step 1 in Algorithm 8.2 below) two states denoted by $\mathbf{W}_{-/+}^n$ and the speed denoted by s^n from the microsolver. The fluxes for (8.4) are then given by

$$\mathbf{F}_{i,-/+}^n = \begin{cases} \mathbf{F}_{\text{num}}(\mathbf{W}_{i-1}^n, \mathbf{W}_i^n) & \text{for } i \neq i_\gamma^n, \\ \mathbf{F}(\mathbf{W}_{-/+}^n) - s^n \mathbf{W}_{-/+}^n & \text{for } i = i_\gamma^n. \end{cases} \quad (8.5)$$

For given iterates $\{\mathbf{W}_i^n \mid n \in \mathbb{N}, 0 \leq i \leq I\}$, we define the piecewise constant approximation

$$\mathbf{W}_h(r, t) = \mathbf{W}_i^n \text{ for } (r, t) \in [r_i^n, r_{i+1}^n) \times [t^n, t^{n+1}).$$

As the source term \mathbf{Q} is not stiff, one obtains the **CFL condition**

$$\Delta t^n \leq \text{CFL} \min \left\{ \frac{A'_d(r_i^n)}{|v_i^n| + \sqrt{\tilde{p}'(\varrho_i^n)}} \mid i = 0, \dots, I \right\}, \quad (8.6)$$

that constrains the maximal length of each time step. We were not faced with stability issues for $\text{CFL} \in (0, 1)$ in the numerical tests of Chapter 9. Note that A'_d might get very small for $d > 1$, thus also Δt^n . In the one-dimensional case (8.6) is the standard CFL condition, see [51] for instance.

Remark 8.1 (Classification of the Bulk solver).

We like to stress that the scheme (8.4) can be understood as a moving mesh method or alternatively as a classical finite volume method on a space-time mesh. In Figure 8.1 we display the underlying mesh structure. The use of Riemann solutions to determine the numerical fluxes between the grid cells is known as Godunov-type method. For a scalar model problem we refer to [13] and for the case $d = 1$ to [12]. The moving mesh ansatz allows us to define a conservative discretization.

8.2 Algorithm and properties of the method

We summarize the complete scheme in the subsequent algorithm which takes the form of a front tracking method with Godunov type flux computation. For ease of notation assume that the initial data is in the liquid (vapor) state for $r < \gamma^0$ ($r > \gamma^0$), which corresponds to a droplet configuration.

Algorithm 8.2 (Moving mesh method).

Let a microsolver $\tilde{\mathcal{M}}$ as in Definition 3.3, $\mathbf{W}_0^0, \dots, \mathbf{W}_I^0 \in (\tilde{\mathcal{A}}_{\text{liq}} \cup \tilde{\mathcal{A}}_{\text{vap}}) \times \mathbb{R}$ and $\gamma^0 \in (R_{\min}, R_{\max})$ be given. Find i_γ^0 via (8.3), construct $\mathcal{R}(i_\gamma^0, \gamma^0)$, and set $n = 0$, $s^0 = 0$.

While $t^n < T$ **Do**.

Step 1: interface. Solve the micro-scale model at γ^n , i.e. compute

$$(\varrho_{\text{liq}}, v_{\text{liq}}, \varrho_{\text{vap}}, v_{\text{vap}}, s^n) = \tilde{\mathcal{M}} \left(\varrho_{\text{L}}, v_{\text{L}}, \varrho_{\text{R}}, v_{\text{R}}, \frac{(d-1)\zeta^*}{\gamma^n} \right)$$

for $\mathbf{W}_-^n = \varrho_{\text{liq}}(1, v_{\text{liq}})^\top$, $\mathbf{W}_+^n = \varrho_{\text{vap}}(1, v_{\text{vap}})^\top$, $\mathbf{W}_{i_\gamma^n-1}^n = \varrho_{\text{L}}(1, v_{\text{L}})^\top$, $\mathbf{W}_{i_\gamma^n}^n = \varrho_{\text{R}}(1, v_{\text{R}})^\top$.

Step 2: time step. The time step Δt^n is chosen according to (8.6) in the bulk regions, and such that

$$2 s^n \Delta t^n < \begin{cases} (r_{i_\gamma^n-1} - \gamma^n) & \text{for } s^n \leq 0, \\ (r_{i_\gamma^n+1} - \gamma^n) & \text{for } s^n > 0 \end{cases}$$

holds. The additional constraint guarantees that $\gamma^{n+1} \in (r_{i_\gamma^n-1}^n, r_{i_\gamma^n+1}^n)$. Put $t^{n+1} = t^n + \Delta t^n$, $\gamma^{n+1} = \gamma^n + s^n \Delta t^n$.

Step 3: bulk phases. Construct the new mesh $\mathcal{R}(i_\gamma^n, \gamma^{n+1})$, compute $|K_i^{n+1,-}|$ and apply the update formula (8.4) for $i = 0, \dots, I$ to obtain $\mathbf{W}_h(\cdot, t^{n+1})$.

Step 4: projection to new mesh. Find i_γ^{n+1} according to (8.3). If $i_\gamma^{n+1} \neq i_\gamma^n$, the function $\mathbf{W}_h(\cdot, t^{n+1})$ is substituted by its L^2 -projection onto the set of piecewise constant functions defined on $\mathcal{R}(i_\gamma^{n+1}, \gamma^{n+1})$.

Step 4: advance to the next time step. $n \mapsto n + 1$

Figure 8.1 illustrates the conservative projection step from $\mathcal{R}(i_\gamma^n, \gamma^{n+1})$ to $\mathcal{R}(i_\gamma^{n+1}, \gamma^{n+1})$. The proposed Algorithm 8.2 has the following properties:

Lemma 8.3 (Mass and momentum conservation).

Algorithm 8.2 is mass conservative for $d \in \mathbb{N}$ and conserves momentum for $d = 1$.

Remark 8.4 (Momentum conservation for $d > 1$).

The momentum $m = m(r, t)$ is not conserved for $d > 1$, since m is not the correct multidimensional quantity. The multidimensional momentum $\mathbf{m} = \mathbf{m}(\mathbf{x}, t) = \frac{\mathbf{x}}{r} m(r, t)$ is always conserved, assuming radially symmetric solutions. Note that this property is independent of the discretization of the momentum balance.

Proof of Lemma 8.3. For $d = 1$ the source term in (8.2) vanishes and $\mathbf{F}_{i_\gamma, -}^n = \mathbf{F}_{i_\gamma, +}^n$ holds. The volume integral over (8.4) gives

$$\begin{aligned} \sum_{i=0}^I |K_i^{n+1, -}| \mathbf{W}_i^{n+1} &= \sum_{i=0}^I |K_i^n| \mathbf{W}_i^n - \Delta t^n \sum_{i=0}^I \left(A'_d(r_{i+1}^n) \mathbf{F}_{i+1, -}^n - A'_d(r_i^n) \mathbf{F}_{i, +}^n \right) \\ &= \sum_{i=0}^I |K_i^n| \mathbf{W}_i^n - \Delta t^n \left(A'_d(r_{I+1}^n) \mathbf{F}_{I+1, -}^n - A'_d(r_0^n) \mathbf{F}_{0, +}^n \right). \end{aligned}$$

Thus, merely inflow and outflow through the boundaries changes the total mass or momentum. With $d > 1$, the same argument holds for the first component of \mathbf{W} . \square

Lemma 8.5 (Preserving isolated phase transitions).

Assume that the interface is initially located at γ^0 , and that the numbers $\hat{\rho}_L \in \tilde{\mathcal{A}}_{\text{liq}}$, $\hat{\rho}_R \in \tilde{\mathcal{A}}_{\text{vap}}$, $\hat{v}_L, \hat{v}_R, \hat{s} \in \mathbb{R}$ satisfy

$$\tilde{\mathcal{M}} \left(\hat{\rho}_L, \hat{v}_L, \hat{\rho}_R, \hat{v}_R, \frac{(d-1)\zeta^*}{\gamma^0} \right) = (\hat{\rho}_L, \hat{v}_L, \hat{\rho}_R, \hat{v}_R, \hat{s}), \quad (8.7)$$

for the microsolver $\tilde{\mathcal{M}}$ in Step 1. Consider the Riemann problem for these states

$$\mathbf{W}(r, 0) = \begin{cases} \hat{\mathbf{W}}_L := \hat{\rho}_L (1, \hat{v}_L)^\top & \text{for } r \in (R_{\min}, \gamma^0), \\ \hat{\mathbf{W}}_R := \hat{\rho}_R (1, \hat{v}_R)^\top & \text{for } r \in [\gamma^0, R_{\max}) \end{cases}$$

and the boundary conditions $\mathbf{W}(R_{\min}, t) = \hat{\mathbf{W}}_L$, $\mathbf{W}(R_{\max}, t) = \hat{\mathbf{W}}_R$ for $t > 0$.

(i) *The solution for $d = 1$ is a single phase transition propagating with speed \hat{s} . In particular, there holds*

$$\mathbf{W}_i^n = \begin{cases} \hat{\mathbf{W}}_L & : i < i_\gamma^n, \\ \hat{\mathbf{W}}_R & : i \geq i_\gamma^n \end{cases} \quad (8.8)$$

for $n \geq 1$ and $\gamma^{n+1} = \gamma^n + \hat{s} \Delta t^n$.

(ii) *The solution for $d \geq 1$ and $\hat{v}_L = \hat{v}_R = \hat{s} = 0$ is a single static phase transition, i.e. (8.8) is valid with $i_\gamma^n = i_\gamma^0$ for all $n \geq 1$.*

Remark 8.6 (Intrinsic geometry change).

We cannot expect (8.8) in the dynamic case. This is due to the geometric terms in (8.2), which physically rise from the fact that the fluid is compressed for flows towards the domain center $r = 0$ and it spreads out for outgoing flows. Thus, constant functions are not preserved.

Proof of Lemma 8.5. (i) For $d = 1$ the source term vanishes and $\mathbf{F}_{i+1,-}^n = \mathbf{F}_{i,+}^n$ holds for $i \neq i_\gamma^n$. With (8.4) and (8.7) we obtain in the cell with index i_γ^n

$$(x_{i_\gamma^n+1} - \gamma^{n+1})\mathbf{W}_{i_\gamma^n}^{n+1} = (x_{i_\gamma^n+1} - \gamma^n)\hat{\mathbf{W}}_R - \Delta t^n \left(\mathbf{F}(\hat{\mathbf{W}}_R) - \mathbf{F}(\hat{\mathbf{W}}_R) + \hat{s} \hat{\mathbf{W}}_R \right).$$

By definition, $\gamma^{n+1} = \gamma^n + \hat{s} \Delta t^n$ such that $\mathbf{W}_{i_\gamma^n}^{n+1} = \hat{\mathbf{W}}_R$ holds. Analogously $\mathbf{W}_{i_\gamma^n-1}^{n+1} = \hat{\mathbf{W}}_L$ holds considering the cell with index $i_\gamma^n - 1$.

(ii) Let us now consider the case $d > 1$. Assume that for the n -th time step (8.8) holds with $m_i^n = 0$, $i = 0, \dots, I$. The geometric source term satisfies

$$\mathbf{Q}(\mathbf{W}_i^n) = \begin{cases} (0, \tilde{p}(\hat{\varrho}_L))^\top & \text{for } i < i_\gamma^n, \\ (0, \tilde{p}(\hat{\varrho}_R))^\top & \text{for } i \geq i_\gamma^n. \end{cases}$$

Because of Step 1 in Algorithm 8.2 and (8.7), it holds that $\mathbf{W}_{i_\gamma^n,-}^n = \hat{\mathbf{W}}_L$, $\mathbf{W}_{i_\gamma^n,+}^n = \hat{\mathbf{W}}_R$ and $s^n = \hat{s} = 0$. The numerical flux is consistent and all velocities are zero, thus $\mathbf{F}_{i,-}^n = \mathbf{F}_{i,+}^n = \mathbf{Q}(\mathbf{W}_i^n)$. The time update in (8.4) vanishes and the solution remains static, i.e. $\mathbf{W}_i^{n+1} = \mathbf{W}_i^n$ holds for $i = 0, \dots, I$. □

Remark 8.7 (Minimal bubble and droplet diameter).

The aim was to build a conservative method, originally solely for the dimensionless van der Waals gas. This purpose is completely fulfilled by the proposed algorithm. However, in Chapter 9 we apply the bulk solver for equations of state of real fluids. The sound speed differences in liquid and vapor phases are here much higher. The scheme works well but it turns out that the time step requirement (8.6) is too restrictive for bubbles or droplets of relevant diameters, i.e. diameters less than a few millimeters.

The simulation of small bubbles or droplets in real fluids necessitates a different approach. One may accumulate all geometric terms in (8.2) to the right hand side, in order to apply an implicit discretization for the source terms, cf. [51, Section 21.7.1]. Such a scheme is not conservative (except of the intrinsic momentum conservation for $d > 1$) but the CFL condition is less restrictive.

Chapter 9

Verification and validation of the complete method

With the front tracking scheme of the previous chapter at hand, we are now able to test the complete method with the proposed microsolvers. Three major issues are addressed: numerical verification in terms of grid convergence, thermodynamic verification, in particular, the global release of mathematical entropy and the validation with respect to physical experiments. We refer to the combination of front tracking scheme and k -microsolvers of Chapter 5 for the evaluation the complete method. Note that the other microsolvers are approximate solvers.

The bulk solver is combined with the Liu microsolver $\tilde{\mathcal{M}}_{\text{Liu}}^{\zeta}$ of Algorithm 4.15, the k -microsolvers $\tilde{\mathcal{M}}$ of Algorithm 5.8 and the \mathbb{K} -relaxation microsolvers $\tilde{\mathcal{M}}^{\mathbb{R}}$ of Algorithm 7.4. Pairs of decreasing kinetic functions for the k -microsolvers and kinetic relations for the \mathbb{K} -relaxation microsolvers refer to those of Chapter 6. The symbols K_i , k_i and \mathbb{K}_i are used simultaneously, as long as, the corresponding kinetic relations or functions are equivalent to each other and the subindex i refers to the number in Table 6.1.

Note that not all combinations are available, since not all kinetic relations correspond to pairs of monotone decreasing kinetic functions. Implemented are $\tilde{\mathcal{M}}_{k_1}$, $\tilde{\mathcal{M}}_{k_3}$ and $\tilde{\mathcal{M}}_{k_7}$. In addition, we implemented $\tilde{\mathcal{M}}_{k_{\text{diff}}}$ for the non-decreasing kinetic functions of Example 6.13, in order to compare with the shock tube experiment of Section 6.3. The relaxation approach provides microsolvers for more general kinetic relations. Here $\tilde{\mathcal{M}}_{\mathbb{K}_1}$, $\tilde{\mathcal{M}}_{\mathbb{K}_2}$ and $\tilde{\mathcal{M}}_{\mathbb{K}_3}$ are implemented. Remember that the Liu solution is considered as an approximate solution of the micro-scale model, since it applies a modified equation of state. In view of Corollary 6.10, we treat the Liu microsolver as an approximate microsolver for kinetic relation K_7 .

The chapter is organized as follows. The numerical verification part is performed in the first section. In case of one-dimensional Riemann problems, we can compute the exact solution. As long as the waves do not interact with the domain boundary, exact solutions are given by k -micro solutions. In that case, we can analyze if the method converges towards the exact solution. In multidimensional settings, an exact solution is not available. Here we check pure grid convergence.

The thermodynamic consistency is verified in Section 9.2. We consider the time evolution of a droplet in a closed container. The solution reaches a steady state, which is the thermodynamic equilibrium solution, and we check the dissipation of total mathematical

entropy during this process. Moreover, this is a benchmark test for the surface tension treatment, since the thermodynamic equilibrium fulfills the Young-Laplace law.

Section 9.3 compares the evolution of condensing bubbles for various fluids. It shows the impact of the chosen kinetic relation and the pressure function. Furthermore, it demonstrates that the solvers are not limited to van der Waals and n-dodecane fluids.

Section 9.4 addresses the validation of the complete method. We compare the evaporation front speed of the experiment described in Section 6.3 with the computed front speeds. Such a test was already performed in Example 6.17 for pure micro-scale solutions. Now, we validate the complete method. The last section provides concluding remarks on the numerical results of the complete method and the proposed microsolvers.

We refer to the space in Eulerian coordinates and indicate this by the tilde on the microsolver maps. For the numerical flux computation in the bulk phases, we use the local Lax-Friedrichs flux [51]. Unless otherwise specified, the time step restriction is (8.6) with CFL = 0.9. The examples apply either the dimensionless van der Waals pressure of Example 2.4 or equations of state that are provided by the thermodynamic library CoolProp [6].

9.1 Experimental order of convergence

We examine convergence rates of Algorithm 8.2 with the microsolvers $\tilde{\mathcal{M}}_{\text{Liu}}^{\zeta}$, $\tilde{\mathcal{M}}$ and $\tilde{\mathcal{M}}^{\text{R}}$. The combination of the the front tracking scheme with the k -microsolver verifies the complete method, since this is an exact solver for one-dimensional Riemann problems of the isothermal model in Definition 2.8. If this test is passed, then we proceed with the verification of the Liu solver and the \mathbb{K} -relaxation solver. Both are approximate Riemann solvers. Here, the convergence tests provide information about the quality of the approximation. Recall that the Liu solver applies a mixture pressure function. Such modified equations of state are not applicable on the macro-scale, cf. Section 4.4. Note that, we do not consider mixture states at all.

The system for radially symmetric solutions (8.2) is equipped with a kinetic relation of Table 6.1 and the initial data

$$\mathbf{W}(r, 0) = \begin{cases} \mathbf{W}_{\text{L}} & : r \in [R_{\text{min}}, \gamma^0), \\ \mathbf{W}_{\text{R}} & : r \in [\gamma^0, R_{\text{max}}]. \end{cases} \quad (9.1)$$

The states $\mathbf{W}_{\text{L}} \in \tilde{\mathcal{A}}_{\text{liq/vap}} \times \mathbb{R}$ and $\mathbf{W}_{\text{R}} \in \tilde{\mathcal{A}}_{\text{vap/liq}} \times \mathbb{R}$ are constant and in different phases. Thus, the phase boundary is initially located at γ^0 . Note that in one spatial dimension (9.1) defines a Riemann problem. The set $[R_{\text{min}}, R_{\text{max}}]$ is just an interval for any $R_{\text{min}} \in \mathbb{R}$. The domain in the multidimensional case is a disc or a ball with a hole in the center, since $R_{\text{min}} > 0$. The hole is due to the singularity of the radially symmetric system (8.2) in $r = 0$. Domain $\Omega \subset \mathbb{R}^d$ and time interval $[0, \theta]$ are chosen such that the waves originating in γ^0 do not reach the boundary. Furthermore, we use the boundary condition $\mathbf{W}(R_{\text{min}}, t) = \mathbf{W}_{\text{L}}$, $\mathbf{W}(R_{\text{max}}, t) = \mathbf{W}_{\text{R}}$ for $t \in [0, \theta]$.

With respect to a reference solution $\hat{\mathbf{W}} = (\hat{\rho}, \hat{m})^{\top}$ we compute the *relative error*

$$e_I = \int_0^{\theta} \int_{R_{\text{min}}}^{R_{\text{max}}} A_d(r) \left(\frac{|\rho_I - \hat{\rho}|}{1 + |\hat{\rho}|} + \frac{|m_I - \hat{m}|}{1 + |\hat{m}|} \right) \mathrm{d}r \mathrm{d}t,$$

	τ_L	τ_R	v_L	v_R	K	k^*	θ	structure of the solution
(a)	0.553	5.5	1.0	0.0	K_7		0.20	1S-C-2S
(b)	0.500	5.0	0.0	5.0	K_7		0.05	1R-E-1R-2R
(c)	0.557	3.0	0.0	0.0	K_7		0.10	1S-C-2R
(d)	0.553	5.5	1.0	0.0	K_3	0.2	0.20	1S-C-2S
(e)	0.530	3.0	0.1	5.0	K_3	0.2	0.10	1R-E-2R
(f)	0.557	3.0	0.0	0.0	K_3	0.2	0.10	1S-C-2R

Table 9.1: Series of initial conditions for a van der Waals fluid in one spatial dimension. The last column displays the structure of the k -micro solution. The abbreviations i S, i R stand for i -shock and i -rarefaction wave ($i = 1, 2$), E stands for evaporation wave and C for condensation wave.

where $(\varrho_I, m_I)^\top$ is the numerical solution on a grid with $I \in \mathbb{N}$ cells. It remains to specify the *reference solution*.

Convergence towards exact solutions ($d = 1$). The solution of the Riemann problem (9.1) is given by the k -micro solution after the transformation to Eulerian coordinates. Thus, the reference solution is chosen to be the k_i -micro solution for one of the accessible kinetic relations ($i \in \{1, 3, 7\}$). This framework allows us to examine convergence towards the exact solution.

Grid convergence ($d > 1$). An exact solution is not available. For simplicity and in order to visualize the wave structure let us use the same initial data (9.1). But here the reference solution is the approximation itself on a fine grid. Thus, we are merely able to examine grid convergence in the multidimensional case.

For a sequence of grids with $I_l \in \mathbb{N}$ cells and corresponding relative errors e_{I_l} we compute the *experimental order of convergence*

$$\text{eoc}_l := \frac{\ln(e_{I_{l+1}}/e_{I_l})}{\ln(I_l/I_{l+1})}. \quad (9.2)$$

Note that for Algorithm 8.2 the number I is also the number of degrees of freedom. The optimal order that can be expected in view of the first-order scheme (8.4) and solutions, that contain discontinuities is between 0.5 and 1, cf. [52].

9.1.1 Application of the k -microsolver 1D

The first subsection addresses the verification of the complete method in one spatial dimension. We apply the van der Waals pressure of Example 2.4 and a real fluid equation of state. Here we choose the fluid of the shock tube experiments in Section 6.3, i.e. is n-dodecane.

Example 9.1 (Error analysis for van der Waals equations of state).

We consider the domain is $\Omega = [0, 1]$ with initial phase boundary in $\gamma^0 = 0.5$. Table 9.1

	p_L	p_R	v_L	v_R	K	θ	γ^0	R_{\min}	R_{\max}	d
(g)	1.39 bar	0.4 bar	0	0	K_3	0.8 ms	0.7 m	0.0 m	1.0 m	1
(h)	1.39 bar	1.0 bar	0	0	K_3	0.8 ms	0.7 m	0.0 m	1.0 m	1
(i)	0.098 bar	0.13 bar	0	0	K_3	0.03 ms	0.05 m	0.033 m	0.07 m	2
(j)	0.098 bar	0.13 bar	0	0	K_3	0.03 ms	0.1 m	0.066 m	0.14 m	3

Table 9.2: Series of initial conditions for n-dodecane in d spatial dimensions. The parameter for kinetic relation K_3 is $k^* = 0.005 \text{ m}^6/\text{kg}^2$.

lists initial conditions $\mathbf{W}_L = (1, v_L)^\top / \tau_L$, $\mathbf{W}_R = (1, v_R)^\top / \tau_R$ for (9.1) in different phases for the van der Waals pressure. Furthermore, the kinetic relation under consideration, the simulation end time θ and the structure of the Riemann solution can be found in that table.

Table 9.3 shows the experimental order of convergence (9.2). The order is in the expected optimal range in view of the first-order scheme (8.4). The velocity distribution for test case (b) at the final time θ is displayed in Figure 9.1. It shows the numerical solution for a sequence of refined grids and the k_7 -micro solution over the Eulerian space variable. The solution consists of a 1-rarefaction wave, followed by an evaporation wave, an attached 1-rarefaction and a 2-rarefaction wave. The rather complicated structure of the solution is resolved very well. With decreasing grid size, \mathbf{W}_I tends to the exact solution.

From the approximation of the rarefaction waves one sees that the first order finite volume scheme is rather diffusive. The phase boundary, however, remains sharp on every grid resolution and it is located at the correct position. This demonstrates that the moving mesh algorithm resolves the phase boundary very well with the information of the k -microsolver, here $\tilde{\mathcal{M}}_{k_7}$.

Example 9.2 (Error analysis for n-dodecane equations of state).

We proceed with test cases for n-dodecane at $T = 230^\circ\text{C}$. Table 9.5 demonstrates grid convergence of optimal order for the conditions (h) and (g) detailed in Table 9.2. Here the initial densities $\varrho_L \in \tilde{\mathcal{A}}_{\text{liq}}$, $\varrho_R \in \tilde{\mathcal{A}}_{\text{vap}}$ are computed, such that the pressure values in column p_L and column p_R hold initially. Note that such conditions were already used in the n-dodecane Example 6.17.

Figure 9.2 displays the pressure distribution of test case (g) at time $t = 0.8 \text{ ms}$. The solution is a composition of a 1-shock wave, an evaporation wave, followed by a 2-shock wave. Again, the phase transition wave is tracked sharply and the bulk shock waves are approximated very well. Note that this example is more challenging as the latter one with the van der Waals fluid, since the pressure in the liquid phase is much stiffer. For instance, one finds for the initial states $p'(\tau_L) \approx -10^6 \text{ bar kg/m}^3$ in the liquid phase and $p'(\tau_R) \approx -0.65 \text{ bar kg/m}^3$ in the vapor phase.

9.1.2 Application of the Liu microsolver in 1D

We intend to verify the Liu microsolver in the framework of the one-dimensional moving mesh scheme. The solver is implemented for the van der Waals pressure.

I	Test (a) with $\tilde{\mathcal{M}}_{k_7}$		Test (b) with $\tilde{\mathcal{M}}_{k_7}$		Test (c) with $\tilde{\mathcal{M}}_{k_7}$	
	e_I	eoc	e_I	eoc	e_I	eoc
500	3.8e-04		2.9e-04		2.6e-05	
1000	2.2e-04	0.81	1.9e-04	0.64	1.9e-05	0.43
2000	1.2e-04	0.88	1.2e-04	0.68	1.3e-05	0.60
4000	6.4e-05	0.91	7.2e-05	0.71	8.6e-06	0.58
8000	3.4e-05	0.92	4.3e-05	0.74	5.6e-06	0.61

I	Test (d) with $\tilde{\mathcal{M}}_{k_3}$		Test (e) with $\tilde{\mathcal{M}}_{k_3}$		Test (f) with $\tilde{\mathcal{M}}_{k_3}$	
	e_I	eoc	e_I	eoc	e_I	eoc
500	2.8e-04		1.9e-04		2.6e-05	
1000	1.7e-04	0.76	1.3e-04	0.57	2.0e-05	0.43
2000	9.2e-05	0.84	8.5e-05	0.60	1.3e-05	0.60
4000	5.0e-05	0.89	5.5e-05	0.63	8.6e-06	0.58
8000	2.7e-05	0.91	3.5e-05	0.65	5.6e-06	0.61

Table 9.3: One-dimensional error analysis for the method with the k -microsolver and van der Waals fluid, see Example 9.1.

I	Test (a) with $\tilde{\mathcal{M}}_{\text{Liu}}^\zeta$		Test (b) with $\tilde{\mathcal{M}}_{\text{Liu}}^\zeta$		Test (c) with $\tilde{\mathcal{M}}_{\text{Liu}}^\zeta$	
	e_I	eoc	e_I	eoc	e_I	eoc
500	3.8e-04		2.9e-04		1.0e-04	
1000	2.2e-04	0.81	1.9e-04	0.64	9.7e-05	0.10
2000	1.2e-04	0.86	1.2e-04	0.68	9.2e-05	0.07
4000	6.6e-05	0.88	7.2e-05	0.71	8.9e-05	0.05
8000	3.6e-05	0.86	4.3e-05	0.74	8.7e-05	0.03

I	Test (d) with $\tilde{\mathcal{M}}_{\mathbb{K}_3}^{\text{R}}$		Test (e) with $\tilde{\mathcal{M}}_{\mathbb{K}_3}^{\text{R}}$		Test (f) with $\tilde{\mathcal{M}}_{\mathbb{K}_3}^{\text{R}}$	
	e_I	eoc	e_I	eoc	e_I	eoc
500	6.3e-04		3.9e-04		8.3e-05	
1000	4.2e-04	0.60	2.8e-04	0.49	7.4e-05	0.17
2000	2.9e-04	0.52	2.0e-04	0.47	6.6e-05	0.16
4000	2.2e-04	0.38	1.5e-04	0.45	6.1e-05	0.10
8000	1.9e-04	0.23	1.1e-04	0.41	5.8e-05	0.07

Table 9.4: One-dimensional error analysis for the method with the Liu microsolver, see Example 9.3, and the \mathbb{K}_3 -relaxation solver, see Example 9.4. Both cases apply the van der Waals equations of state.

I	Test (g) with $\tilde{\mathcal{M}}_{k_3}$		Test (h) with $\tilde{\mathcal{M}}_{k_3}$		Test (h) with $\tilde{\mathcal{M}}_{\mathbb{K}_3}^{\mathbb{R}}$	
	e_I	eoc	e_I	eoc	e_I	eoc
500	5.9e-04		8.6e-04		8.8e-04	
1000	3.7e-04	0.68	4.8e-04	0.84	6.1e-04	0.53
2000	2.2e-04	0.76	2.6e-04	0.88	4.3e-04	0.50
4000	1.2e-04	0.88	1.4e-04	0.91	3.3e-04	0.40
8000	6.2e-05	0.91	7.9e-05	0.81	2.8e-04	0.24

Table 9.5: One-dimensional error analysis for the method with the k_3 -microsolver, see Example 9.2, and the \mathbb{K}_3 -relaxation solver, see Example 9.5. Both cases apply equations of state for n-dodecane.

Example 9.3 (Error analysis applying the Liu microsolver).

We compare the numerical solution with the k_7 -micro solution on the domain $\Omega = [0, 1]$. The phase boundary is initially located at $\gamma(0) = 0.5$.

Table 9.4 shows the error values and the experimental orders of convergence for increasing grid resolution and the test cases (a)–(c) in Table 9.1. The initial values of the cases (a) and (b) are in the stable phases. Here the scheme converges with almost exactly the same error and order as observed for the k_7 -microsolver (cf. (a), (b) in Table 9.3 and Table 9.4). As might be expected, for metastable initial values (case (c)) the algorithm converges to a different solution. The error values in that case remain almost constant for decreasing grid sizes. The reason is the modification of the equation of state between the saturation states, cf. Section 4.4.

9.1.3 Application of the \mathbb{K} -relaxation microsolver in 1D

The \mathbb{K} -relaxation solver is implemented for van der Waals fluids and also for external thermodynamic libraries. Let us first fix the the reference model or more precisely the kinetic relation. For K_1 , K_3 and K_7 , we are able to compute the exact solution. On the other hand the \mathbb{K} -relaxation solvers $\tilde{\mathcal{M}}_{\mathbb{K}_1}^{\mathbb{R}}$, $\tilde{\mathcal{M}}_{\mathbb{K}_2}^{\mathbb{R}}$, $\tilde{\mathcal{M}}_{\mathbb{K}_3}^{\mathbb{R}}$ are implemented. We decided to compare solutions for K_3 . The reason is that the muss flux estimate $\dot{j}_{\mathbb{K}}$ in (7.15) exists for K_3 but not for K_1 . Thus, the reference solution is the k_3 -micro solution. In the following we use a convex combination of \dot{j}_{τ} and $\dot{j}_{\mathbb{K}_2}$, more precisely

$$\dot{j}(\mathbf{V}_L, \mathbf{V}_R) := \beta \frac{v_R - v_L}{\tau_R - \tau_L} - (1 - \beta) \operatorname{sign}(f) \sqrt{\frac{|f(\tau_L, \tau_R)|}{k^*}} \quad (9.3)$$

with $\beta = 0.8$ and the parameter $\alpha = 2$ in (7.14).

Example 9.4 (Error analysis for van der Waals equations of state).

The bulk solver combined with the \mathbb{K}_3 -relaxation microsolver is first applied to the test cases (d)–(f) in Table 9.1. The domain is $\Omega = [0, 1]$ and the interface is initially located at $\gamma(0) = 0.5$. We could not observe decreasing error norms for the time step restriction (8.6) with CFL = 0.9: the numerical solution in case (d) seemed to converge towards a different solution, initial conditions of case (e) led to negative values of specific volume and pressure and the numerical solution in case (f) was oscillatory.

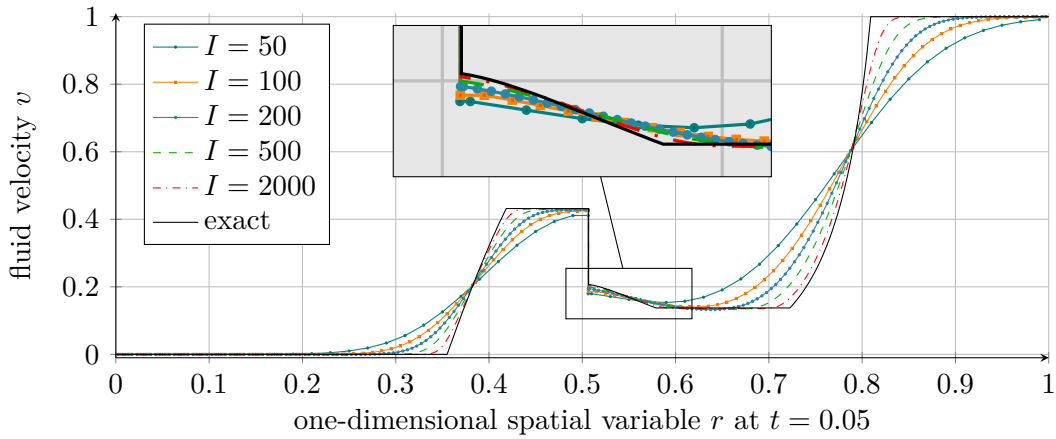


Figure 9.1: Velocity distribution for test case (b) with van der Waals fluid. In color the numerical solution with k_7 -microsolver and in black the (exact) k_7 -micro solution.

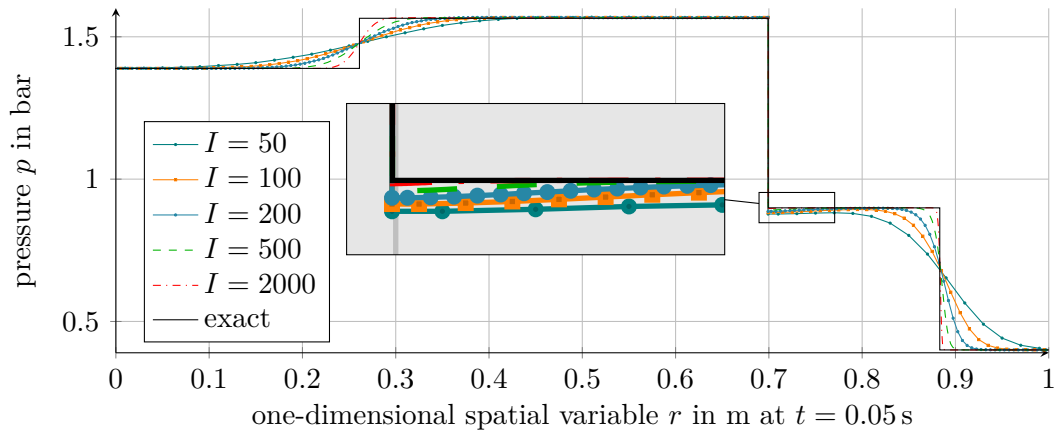


Figure 9.2: Pressure distribution for test case (g) with n-dodecane fluid. In color the numerical solution with k_3 -microsolver and in black the (exact) k_3 -micro solution.

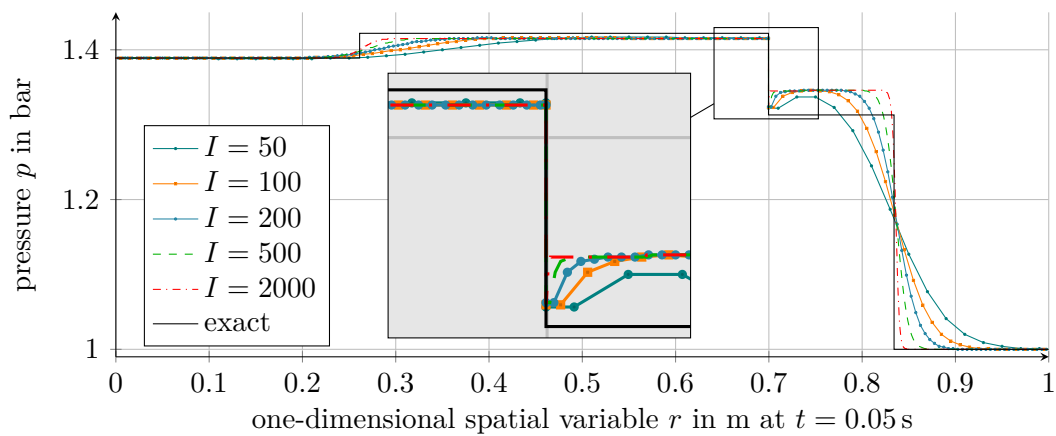


Figure 9.3: Pressure distribution for test case (h) with n-dodecane fluid. In color the numerical solution with \mathbb{K}_3 -relaxation solver and in black the (exact) k_3 -micro solution.

Table 9.4 shows the result for $\text{CFL} = 0.1$. The \mathbb{K}_3 -relaxation microsolver needs apparently more iteration steps to converge. This was already reported in [12]. However, the convergence orders are low and decreasing. In particular for case (f) the numerical solution does not converge to the k_3 -micro solution.

Example 9.5 (Error analysis for n-dodecane equations of state).

For the second example, we use the test cases of Table 9.2. The fluid under consideration is n-dodecane. The reference solution satisfies K_3 with $k^* = 0.005 \text{ m}^6/\text{kg}^2$. We tried several combinations of the estimates \hat{j} , α and CFL numbers but only test case (h) led to a stable result. Even choosing the exact mass flux of the reference solution instead of (9.3) did not improve the results. Any proper choice of the estimates for the first few iterates, failed at a later time step.

The initial conditions of test case (h) are near the equilibrium solution, here elementary waves are almost negligible and the k_3 -micro solution mainly consists of a single traveling wave. Note that this is a simple test case for the \mathbb{K}_3 -relaxation microsolver, since the solver was conceived in order to preserve isolated phase boundaries.

The error for test case (h) with $\beta = 0.8$ in (9.3), $\alpha = 2$ in (7.14) and $\text{CFL} = 0.1$ can be found in Table 9.5. Figure 9.3 displays the solution on different grids and the k_3 -micro solution. One clearly can see that the numerical solution converges, but to a different solution.

The examples demonstrate, that the $\tilde{\mathcal{M}}_{\mathbb{K}_3}^{\text{R}}$ -relaxation solver combined with the front tracking scheme does not converge to the exact solution. We observe grid convergence towards some other solution. This will be also the upshot of Example 9.7, where we compare against a highly resolved numerical solution. The relaxation microsolver in [12] was applied to a much simpler equation of state and linear kinetic functions. This might be the reason, why there the authors observed convergence towards the exact Riemann solution.

Furthermore, the $\tilde{\mathcal{M}}_{\mathbb{K}_3}^{\text{R}}$ -relaxation solver is not applicable to equations of state of real fluids. For any (non-trivial) setting, we were faced with solutions in the spinodal region or negative values of specific volumes. The reason is the shape of the pressure function. It is extreme steep in the liquid phase and the set \mathcal{A}_{liq} is extreme small compared to the spinodal region. Thus, small errors in liquid states result in huge pressure differences and values outside of the liquid or vapor phase.

We expect the same problems for the other kinetic relations. Relation K_2 is similar to K_3 and in case K_1 even a reliable mass flux estimate is missing.

9.1.4 Error analysis for radially symmetric solutions

This subsection addresses the multidimensional case. Since exact radially symmetric solutions are not available, a reference solution is computed using $I = 6400$ cells. We consider an n-dodecane bubble in liquid n-dodecane with the initial states (i) and (j) in Table 9.2. Test case (i) is considered in \mathbb{R}^2 and (j) is considered in \mathbb{R}^3 . The CFL constraint given in (8.6) depends, for $d > 1$, on the radius. The resulting time step can get very low for small values of R_{min} . This limits the size of the computational domain and thus also the diameter of bubbles or droplets. For that reason, we consider quite big bubbles, cf. Remark 8.7. The time step for $I = 6400$ and $\text{CFL} = 0.9$ was in the order of 10^{-10} s.

I	Test (i) with $\tilde{\mathcal{M}}_{k_3}$		Test (j) with $\tilde{\mathcal{M}}_{k_3}$		Test (g) with $\tilde{\mathcal{M}}_{\mathbb{K}_3}^R$	
	e_I	eoc	e_I	eoc	e_I	eoc
100	7.1e-07		4.6e-07		2.0e-07	
200	4.0e-07	0.84	2.6e-07	0.82	1.2e-07	0.71
400	2.0e-07	1.00	1.3e-07	0.97	6.9e-08	0.85
800	8.5e-08	1.23	5.8e-08	1.21	3.2e-08	1.10
1600	2.7e-08	1.65	1.8e-08	1.67	1.1e-08	1.55
3200	4.0e-09	2.77	2.3e-09	3.01	1.7e-09	2.70

Table 9.6: Multidimensional error analysis for an n-dodecane bubble at $T = 230^\circ\text{C}$. The bulk solver is combined with the k_3 -microsolver, see Example 9.6, and the \mathbb{K}_3 -relaxation solver, see Example 9.7.

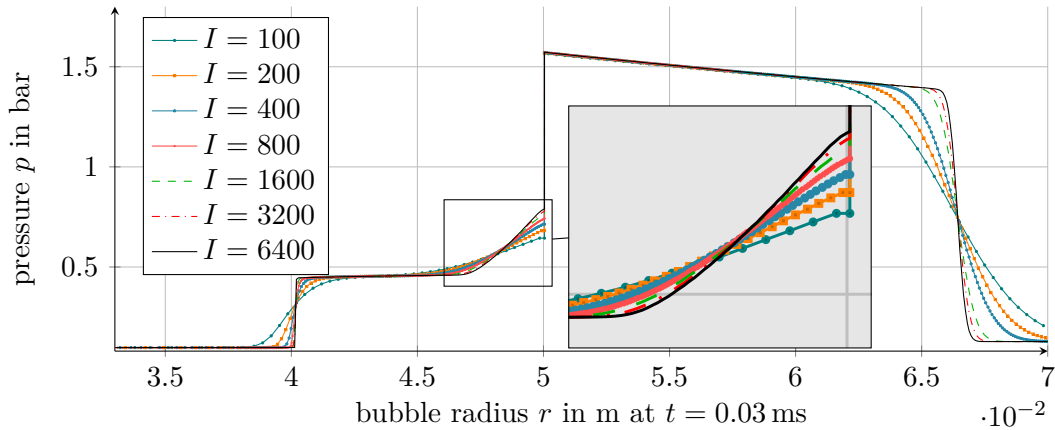


Figure 9.4: Radial symmetric two-dimensional solution. Pressure distribution of test case (i) and n-dodecane fluid. In color the numerical solution with k_3 -microsolver. The numerical solution for $I = 6400$ cells is used as reference solution for the error computation in Table 9.6.

The surface tension at $T = 230^\circ\text{C}$ is $\zeta^* = 0.0089\text{ N/m}$ (computed with [6]). Due to the chosen bubble radii, surface tension does not affect the dynamics in these examples. Note that the initial pressure values are far from the saturation pressure, here $p^{\text{sat}} \approx 1.39\text{ bar}$, and the liquid state is metastable.

Example 9.6 (Error analysis applying the k -microsolver).

Table 9.6 shows the error and the experimental order of convergence for the k_3 -microsolver in the cases (i), (j). The computed order varies between 1 and 3. Figure 9.4 displays the pressure distribution on those grids, which were used for the error analysis. This demonstrates that the numerical solution converges with increasing grid resolution towards the finest solution. Note that plateau values do not form due to the intrinsic geometry change in r , see Remark 8.6. Any fluid movement towards the center accumulates mass, while for flows in direction of the outer boundary mass is distributed over increasing volume units. Thus, the pressure between $r = 0.05$ and $r = 0.065$ is not constant.

We have already seen in Section 9.1 that for $d = 1$, the method converges to the exact solution. Here we observed grid convergence for all three test cases and real fluid equations of state. Hence, we expect that the method converges, also in the multidimensional case,

toward the exact solution.

Example 9.7 (Error analysis applying the \mathbb{K} -relaxation microsolver).

We consider the stable test case of Example 9.5 in two spatial dimensions. That means, we apply the condition of case (h) in Table 9.2 with $d = 2$. The reference solution is now the numerical solution on $I = 6400$ cells. The error and the experimental order of convergence can be found in Table 9.6.

The computed order varies between 1 and 3. This demonstrates grid convergence to the reference solution. Convergence toward a highly resolved numerical reference solution was also observed in [67]. However, we cannot expect convergence to the exact solution, cf. the one-dimensional test cases in Subsection 9.1.3.

9.2 Global entropy release and steady state solutions

A transient solution should reach its steady state $\mathbf{W}(\mathbf{x}, t) \rightarrow \mathbf{W}^\infty(\mathbf{x}) \in (\tilde{\mathcal{A}}_{\text{liq}} \cup \tilde{\mathcal{A}}_{\text{vap}}) \times \mathbb{R}$ for $t \rightarrow \infty$ and at the same time $\Gamma(t) \rightarrow \Gamma^\infty \subset \mathbb{R}^d$ and $\Omega_{\text{liq/vap}}(t) \rightarrow \Omega_{\text{liq/vap}}^\infty \subset \mathbb{R}^d$. Furthermore, the steady state should be the minimizer of the associated mathematical entropy. Reviewing the entropy balance (2.28) and the reflecting boundary condition (2.21), we find that the total entropy at time t is given by

$$\mathcal{E}(\varrho(\cdot, t), \mathbf{m}(\cdot, t)) = \int_{\Omega_{\text{liq}} \cup \Omega_{\text{vap}}} \varrho(\mathbf{x}, t) \psi \left(\frac{1}{\varrho(\mathbf{x}, t)} \right) + \frac{|\mathbf{m}(\mathbf{x}, t)|^2}{2 \varrho(\mathbf{x}, t)} \, d v + \zeta^* |\Gamma(t)|.$$

Gurtin has demonstrated in [34] that the minimum $\mathcal{E}^\infty := \min\{\mathcal{E}(\varrho^\infty, \mathbf{m}^\infty) \mid \int_\Omega \varrho^\infty \, d\mathbf{x} = \int_\Omega \varrho_0 \, d\mathbf{x}\}$ is determined by the global thermodynamic equilibrium, cf. Definition 2.5. Moreover, the minimizer corresponds to a single spherical droplet or bubble, cf. [34]. Thus, we expect that Γ^∞ is a sphere with some radius $\gamma^\infty > 0$ and

$$\varrho^\infty(\mathbf{x}) = \begin{cases} 1/\tau_{\text{liq}}^{\text{sat}} & \text{for } \mathbf{x} \in \Omega_{\text{liq}}^\infty, \\ 1/\tau_{\text{vap}}^{\text{sat}} & \text{for } \mathbf{x} \in \Omega_{\text{vap}}^\infty, \end{cases} \quad \mathbf{m}^\infty(\mathbf{x}) = \mathbf{0}.$$

Note that saturation states $\tau_{\text{liq/vap}}^{\text{sat}} = \tau_{\text{liq/vap}}^{\text{sat}}(\zeta^\infty)$ exist uniquely, since for spherical bubbles $\zeta^\infty := (d-1)\zeta^*/\gamma^\infty$ is constant, cf. Remark 2.1. The same holds for spherical droplets, with $\zeta^\infty := -(d-1)\zeta^*/\gamma^\infty$.

We consider a van der Waals fluid with $\zeta^* = 0.01$ and radially symmetric solutions in $\Omega = \{\mathbf{x} \in \mathbb{R}^2 \mid 0.005 < |\mathbf{x}| < 2\}$. The phase boundary is initially located at $\Gamma(0) = \mathbb{S}$. The saturation states of a droplet with radius 1 are $\tau_{\text{liq}}^{\text{sat}}(0.01) \approx 0.55444$, $\tau_{\text{vap}}^{\text{sat}}(0.01) \approx 3.15$. Initial condition

$$\begin{pmatrix} \varrho \\ \mathbf{v} \end{pmatrix}(\mathbf{x}, 0) = \begin{cases} (1/\tau_{\text{liq}}^{\text{sat}}, 0.05)^\top & \text{for } |\mathbf{x}| \in [0.005, 1], \\ (1/\tau_{\text{vap}}^{\text{sat}}, -0.05)^\top & \text{for } |\mathbf{x}| \in (1, 2] \end{cases}$$

and boundary condition $\mathbf{v} \cdot \boldsymbol{\nu} = 0$ at $\partial\Omega$ are such that, right from the beginning, waves are emitted and reflected from the boundary. The initial condition satisfies $\varrho(\mathbf{x}, 0) = \varrho^\infty(\mathbf{x})$,

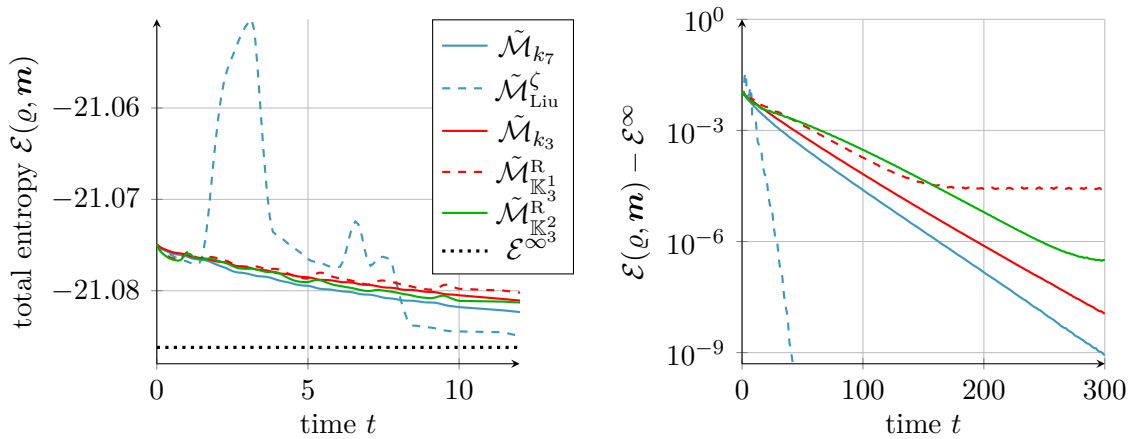


Figure 9.5: Evolution of the total mathematical entropy in time. Both figures correspond to the same legend.

such that potential energy and surface energy are initially at the global minimum, while the total kinetic energy is positive. As time passes, waves slop ahead and back within some density range around the saturation solution and with decreasing amplitudes.

The numerical results are performed with the moving mesh scheme of Chapter 8, on a grid with $I = 100$ cells, combined with the microsolvers $\tilde{\mathcal{M}}_{k_3^1}$, $\tilde{\mathcal{M}}_{\mathbb{K}_3^1}^R$, $\tilde{\mathcal{M}}_{\mathbb{K}_3^2}^R$, $\tilde{\mathcal{M}}_{k_7}$ and $\tilde{\mathcal{M}}_{\text{Liu}}^\zeta$. The parameter for K_3^1 is $k^* = 0.2$ and for K_3^2 is $k^* = 2$. The time step is restricted via (8.6) and $\text{CFL} = 0.5$. The \mathbb{K} -relaxation microsolvers require smaller CFL numbers. Here we apply $\tilde{\mathcal{M}}_{K_3^1}^R$ and $\tilde{\mathcal{M}}_{K_3^2}^R$ with $\text{CFL} = 0.01$.

Example 9.8 (Entropy release applying the Liu microsolver).

Figure 9.5 shows the evolution of the total entropy $t \rightarrow \mathcal{E}(\varrho, \mathbf{m})$ (left) and the shifted total entropy $t \mapsto \mathcal{E}(\varrho, \mathbf{m}) - \mathcal{E}^\infty$ (right) in order to use a logarithmic scale. The steady state solution is given by above saturation states. We find $\mathcal{E}^\infty \approx -21.08621$, where the contribution of the surface energy is $\zeta^* |\Gamma^\infty| = 0.02\pi$.

Observe that the Liu microsolver leads to an increase in the total entropy at the beginning of the simulation time. For $t > 8$, the entropy decays very fast compared with the solution obtained by $\tilde{\mathcal{M}}_{k_7}$. This strange behavior is due to the fact that $\tilde{\mathcal{M}}_{\text{Liu}}^\zeta$ applies a different pressure function as the bulk solver. Note that the initial states were chosen, such that the bulk solution varies around the saturation states. Thus, initial states for the microsolvers are very often in the metastable region, where the pressure functions actually are different.

Example 9.9 (Entropy release applying the \mathbb{K} -relaxation microsolver).

For the \mathbb{K}_3^1 -relaxation microsolver with $k^* = 0.2$, one observes in Figure 9.5 that the method converge to the stationary solution within a difference of 10^{-5} . For $t > 150$, the numerical solution behaves unstable and \mathcal{E} remains on a constant level. The entropy decay is not completely monotone, furthermore a CFL number of 0.01 was necessary. For $\text{CFL} = 0.5$ and $\text{CFL} = 0.1$, the final difference to the stationary solution was around 10^{-2} . Decreasing the CFL number once more (not shown in the figure) or using a higher dissipation rate, i.e. $\tilde{\mathcal{M}}_{\mathbb{K}_3^2}^R$ with $k^* = 2$, pushes the final difference below 10^{-6} .

Example 9.10 (Entropy release applying the k -microsolver).

The numerical results for the front tracking scheme combined with the k -microsolvers are convincing. Figure 9.5 shows strictly monotone decreasing values of total mathematical entropy towards the expected limit \mathcal{E}^∞ . Although surface tension is entirely handled on the micro-scale level, the method is capable to predict the global contribution of the surface energy. The decay rate for $\tilde{\mathcal{M}}_{k_7}$ is higher than for $\tilde{\mathcal{M}}_{k_2}$. Note that kinetic relation K_7 dissipates more entropy than K_2 with $k^* = 0.2$. This indicates that increasing the interfacial entropy dissipation has a damping effect.

9.3 Condensation of bubbles

We consider spherical bubbles in the domain $\Omega = \{ \boldsymbol{x} \in \mathbb{R}^2 \mid 0.5 \text{ mm} < |\boldsymbol{x}| < 20 \text{ mm} \}$ with initial and boundary conditions such that the bubbles vanish. More precisely, we compare the evolution of the phase boundary until it approaches the inner boundary. The test is performed for equations of state of the fluids n-dodecane at 230 °C, butane at 20 °C, acetone at 20 °C, water at 80 °C and different kinetic relations. The fluid n-dodecane was already used in former test cases, the other fluids are just randomly selected.

The setting is as follows. We compute the saturation pressure p^{sat} (with $\zeta = 0$) for each fluid and apply initial density values such that the vapor pressure is $0.4 p^{\text{sat}}$ and the liquid pressure is $4 p^{\text{sat}}$. The initial fluid velocity is zero and the bubble radius is $\gamma(0) = 10 \text{ mm}$. Waves at the inner boundary are reflected (2.22). At the outer boundary we apply a Dirichlet condition for the density to keep the pressure constant. The fixed pressure at the outer boundary guarantees that the bubble vanishes.

We use the moving mesh finite volume scheme with the k -microsolver for $I = 100$ cells and CFL = 0.9. The evolution of the bubble radii, see Figure 9.6, depends on the selected fluid and the kinetic relation. We do not want to classify that correlation. But, as expected, all bubbles vanish for the selected boundary condition. For higher entropy dissipation (kinetic relation K_7) the vapor liquefies faster. The difference is low for butane and n-dodecane but still visible. Once more, we see that increasing the interfacial entropy dissipation has a damping effect.

The radius is not always monotone decreasing, see the example of acetone with K_1 . At $t = 1.2 \text{ ms}$ the radius is increasing. This is an effect of the bulk dynamics, but we are wondering if it is influenced by curvature effects or the volume change towards the center. The same setting with $\zeta^* = 0$ (circles in Figure 9.6) shows that surface tension is too low to affect the evolution. The behavior in the one-dimensional setting (denoted by triangles) is different. The radius decreases monotone but slower.

Let us remark, that nucleation of bubbles is not taken into account. However, we observe waves of high amplitudes and negative pressure values in the liquid shortly after the bubbles collapsed. Negative pressure values may indicate the nucleation of a new vapor phase. The effect of surface tension was not visible in the examples, since the curvature is too low. The simulation of smaller bubbles require a different bulk solver, see Remark 8.7. The time step in this experiment was between 10^{-10} s and 10^{-9} s , independent of the fluid. However, the simulation of the water test cases took much longer, the evaluation of the associated equations of state is apparently more expensive.

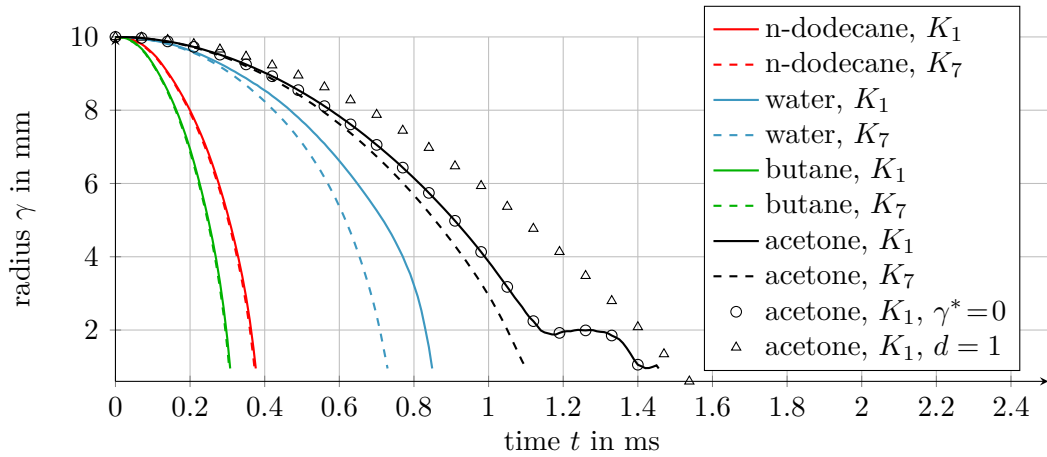


Figure 9.6: Time evolution of the radii $\gamma(t)$ of vapor bubbles in different fluids and for different kinetic relations.

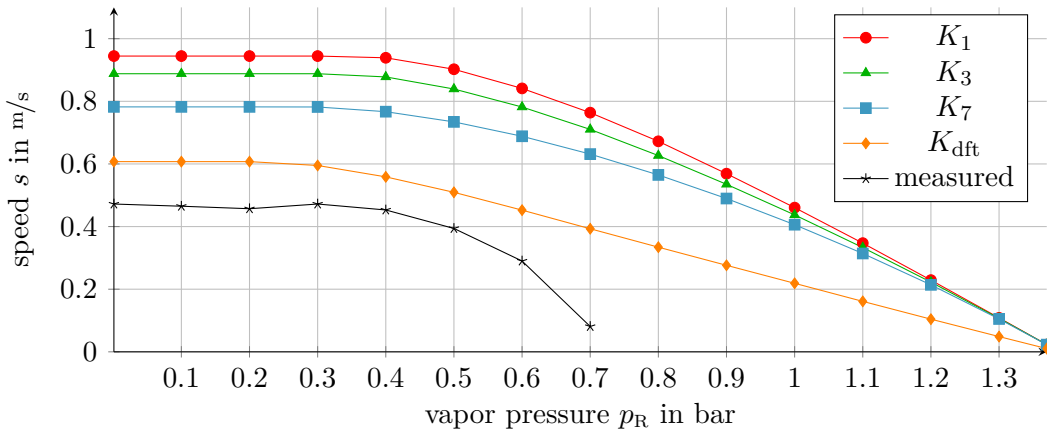


Figure 9.7: Comparison of evaporation front speeds for different initial vapor pressure values p_R . In black, the measured values from [68]. The colored lines refer to simulation results for different kinetic relations.

9.4 Validation with shock tube experiments

This section addresses the validation of the complete method with the shock tube experiment of Section 6.3. Recall that in Example 6.17, we already compared one-dimensional Riemann solutions with the measurements. The pure k_{dft} -micro solution matches the measured data and the pure k_7 -micro solution matches up to a factor of 1.6. The conclusion was, that non-decreasing kinetic functions, i.e. K_{dft} , are necessary to predict the correct evaporation wave speed. As remarked in the example, the time scale of the experiment is such that waves are reflected at the boundary. This is now taken into account with the combination of bulk solver and microsolvers, in order to examine the impact of boundary conditions.

Example 9.11 (Dodecane shock tube experiments).

We use the same initial conditions as in Example 6.17: saturated liquid on the left hand side and the vapor pressure values p_R in Figure 9.7 on the right hand side. The k -microsolvers

are combined with the moving mesh scheme on a one-dimensional domain of length 1 m. The phase boundary is initially located at the center and the simulation end time is $\theta = 0.1$ s. This is in the time range where the experiment shows steady motion [68]. At the left end of the domain we use reflecting boundary conditions (2.22). At the right boundary, where in the experimental facility the low pressure chamber was mounted, we apply the outflow condition $\mathbf{F}_{I+1,-}^n = \mathbf{F}(\mathbf{W}_I^n)$. The domain was decomposed in $I = 100$ cells and we restrict the time step with $\text{CFL} = 0.9$.

Figure 9.7 compares the propagation speed of the numerical solution (actually the arithmetic mean within the last 0.02 s) with the measured front speed of the experiment. The results are very similar to the previous ones, obtained by pure k -micro solutions (see Example 6.17). The propagation speeds for K_1 and K_3 are a bit slower but still faster than in the experiment. Modifying the numerical setting, i.e. boundary conditions, simulation time and initial position of the phase boundary, did not decrease the discrepancy decisively.

Recall that the theory for the k -microsolver is restricted to pairs of monotone decreasing kinetic functions (Theorem 5.7). The \mathbb{K} -relaxation microsolver is applicable for more general kinetic relations, e.g. K_{dft} . However, the \mathbb{K} -microsolvers are much too unstable for this setting and, furthermore, may lead to wrong solutions, see Example 9.5.

Although Theorem 5.7 is not applicable to K_{dft} , the corresponding k_{dft} -microsolver is implemented and leads to unique solutions. The propagation speeds, applying this microsolver, are faster as in Example 6.17. Higher values of entropy dissipation rate, i.e. K_2 with $k^* > k_{\text{dft}}^*$ for k_{dft}^* in (6.7), would be necessary in order to match the experimental data.

The chosen boundary conditions seem to have no significant impact. More entropy dissipation seems to have a damping effect. This was also the observation of the previous two sections and is visible in Figure 9.7. Furthermore, achieving good agreements of the simulation results with the measurements, requires non-decreasing kinetic functions.

9.5 Conclusion on the isothermal methods

We performed many numerical tests in order to examine the complete method and the approximate microsolvers. The combination of the front tracking scheme with the bulk solver and, in particular, the exact k -microsolvers enables us to pronounce statements about the quality of the complete method. The method converges to the exact one-dimensional entropy solution, even for equations of state of real fluids. The order of convergence was in the expected optimal range, see Subsection 9.1.1. In absence of multidimensional exact solutions, we could demonstrate in Example 9.6 grid convergence for radially symmetric solutions.

Furthermore, the method passed the important thermodynamic consistency verification process, as pronounced in the introduction chapter. The global entropy decays monotonously towards the thermodynamic correct steady state, as demonstrated in Example 9.10. Note that the entropy minimum depends on the surface energy. Thus, regarding curvature effects exclusively in the (formally one-dimensional) k -microsolver is a successful way to take capillary forces into account.

The highest level of qualification processes is the validation against real world measurements. The close match with the shock tube experiments proves the reliability of the

numerical method. We found qualitatively the same results for the complete method in Example 9.11 as for the pure Riemann solution in Example 6.17. Temperature differences may also affect the dynamics of the shock tube experiments, this is taken into account by the following chapter.

The Liu microsolver is an exact Riemann solver but for a different pressure law. The results are the same as for the k_7 -microsolver, as long as, the initial state are in the stable phases. However, this is rarely the case and may lead to a sharp increase of total mathematical entropy as in Example 9.8. The combination of Liu microsolver and bulk solver leads to uniquely determined stationary solutions, that coincide with the thermodynamic equilibrium solution. This was already suspected in Section 4.4. An important by-product, analyzing the Liu micro solution, was kinetic relation K_7 and the final upshot is to use the k_7 -microsolver rather than the Liu microsolver. As a consequent, the solver inherits all above described positive properties of the (exact) k -microsolvers.

The picture for the \mathbb{K} -relaxation solvers is not uniform. We saw grid convergence but not towards the correct solution, see Example 9.4, Example 9.5 and Example 9.7. The global entropy decay is almost monotone but Example 9.9 shows stability issues and the thermodynamic equilibrium solution was not reached in all cases. Even more disadvantageous is that the \mathbb{K} -relaxation solvers is not applicable to equations of state of reals fluids. The combination of \mathbb{K} -relaxation solvers and bulk solver leads constantly to premature aborts, due to density values in the metastable region or in the wrong phase.

Chapter 10

Non-isothermal liquid vapor flows

We consider in this chapter the non-isothermal case. As before, the interface position appears as an unknown free boundary such that state variables are discontinuous across this manifold of codimension one. Appropriate jump conditions couple the states of the bulk regions at the interface and have to be formulated to ensure the well-posedness and thermodynamic consistency of the overall model.

More precisely, for the compressible hydrodynamics in the bulk phases we neglect viscosity and heat conductivity such that the fluid is described by the Euler equations with the conservative unknowns being density, momentum, and total energy. The modeling of appropriate coupling conditions is quite delicate. In the isothermal case it is well established that the coupling conditions should consist of mass conservation, a dynamic version of the Young-Laplace law for momentum balance, and an additional entropy relation, see Chapter 2. These conditions have also to be valid in the considered temperature dependent case. However, since there is no mechanism for heat conduction, the release of latent heat has to be modeled in a different way. We suggest to use an algebraic term.

Müller and Voß [62], Hattori [37] and Chen and Hattori [17] consider Riemann problems without latent heat. We will see in Lemma 10.6 that this leads to thermodynamically inconsistent static solutions below the critical temperature. In contrast, our model permits thermodynamically consistent static solutions, see Lemma 10.10.

We present in this chapter an exact solution of the Riemann problem with initial data from different phases, which takes latent heat and surface tension into account. Section 10.1 describes the full mathematical model as a free boundary value problem in arbitrary spatial dimensions. Also, shortcomings of the inviscid two-phase Euler model and the phenomena of latent heat are discussed. We consider the physically most relevant case of slow subsonic phase boundaries and add a kinetic relation to the classical coupling conditions (conservation of mass, dynamic Young-Laplace law, energy balance). As a local interface model we obtain a planar Riemann problem, independent of the original spatial dimension. We present a constructive algorithm in Section 10.2 to obtain a self-similar solution of the Riemann problem, see Theorem 10.13. We conclude with numerical sections for verification (Section 10.3), validation with shock tube experiments (Section 10.4), as well as, an application to physically realistic multidimensional droplet dynamics (Section 10.5).

The latter application is taken from the joint publication [30]. In that publication, also the model and the algorithm of the microsolver are published.

10.1 The mathematical model

The temperature in the thermodynamic process under consideration varies in time and space, while, on the other hand, heat flux is neglected. This differs from the isothermal model in Section 2.4, where temperature differences were assumed to be balanced out by sufficiently strong heat fluxes. Furthermore, the energy balance law is not negligible anymore. The equations of state depend on two thermodynamic quantities, i.e. density and temperature. Also, phases, regions and sets for saturation states are extended by an additional degree of freedom.

The thermodynamic framework for this chapter is fixed in Subsection 10.1.1. In Subsection 10.1.2, we consider again the balance laws in integral form of Section 2.2. It turns out that ignoring heat fluxes leads to wrong steady state solutions. Furthermore, the subsection explains the correlation between heat flux through the phase boundary and latent heat. We state a mathematical model that resolves this problem by an interfacial source term for latent heat in Subsection 10.1.3.

10.1.1 Two-phase thermodynamics

Let us consider a fluid in *local thermodynamic equilibrium* what (in the bulk) means that the thermodynamic state of the fluid is determined by any two thermodynamic variables [38]. We will employ in this chapter a different notation as in the previous ones. For ease of notation, the same symbol for the corresponding *equations of state* is used, even if they depend on different arguments. For instance, we use

$$p = p(\varrho, \varepsilon) = p(\tau, \eta) = p(\tau, T), \quad \varepsilon = \varepsilon(\tau, \eta) = \varepsilon(\tau, T),$$

where ϱ , $\tau = 1/\varrho$, p , ε , η , T , are the density, specific volume, pressure, specific internal energy, specific entropy and temperature, respectively. For a given *specific internal energy* function $\varepsilon = \varepsilon(\tau, \eta)$ one obtains the *pressure* and the *temperature* as

$$p(\tau, \eta) = -\varepsilon_\tau(\tau, \eta), \quad T(\tau, \eta) = \varepsilon_\eta(\tau, \eta). \quad (10.1)$$

The *specific Helmholtz free energy* ψ and the *specific Gibbs free energy* μ are related by

$$\psi(\tau, \eta) = \varepsilon(\tau, \eta) - \eta T(\tau, \eta), \quad \mu(\tau, \eta) = \psi(\tau, \eta) + \tau p(\tau, \eta). \quad (10.2)$$

We consider fluids below the *critical point* such that (neglecting solid configurations) only liquid and vapor states exist. To characterize these bulk states, we assume that two disjoint open connected sets $\mathcal{A}_{\text{liq}} \subset \mathbb{R}_+ \times \mathbb{R}$ and $\mathcal{A}_{\text{vap}} \subset \mathbb{R}_+ \times \mathbb{R}$ are given such that the smooth function

$$\varepsilon : \begin{cases} \mathcal{A}_{\text{liq}} \cup \mathcal{A}_{\text{vap}} & \rightarrow \mathbb{R}, \\ (\tau, \eta) & \mapsto \varepsilon(\tau, \eta) \end{cases} \quad \text{is strictly convex.} \quad (10.3)$$

The sets $\mathcal{A}_{\text{liq/vap}}$ define the liquid and the vapor phase. As a consequence we obtain a positive real valued function for *speed of sound* c in both phases, because we have

$$c(\tau, \eta) := \tau \sqrt{-p_\tau(\tau, \eta)} = \tau \sqrt{\varepsilon_{\tau\tau}(\tau, \eta)} > 0 \quad \text{for} \quad (\tau, \eta) \in \mathcal{A}_{\text{liq}} \cup \mathcal{A}_{\text{vap}}. \quad (10.4)$$

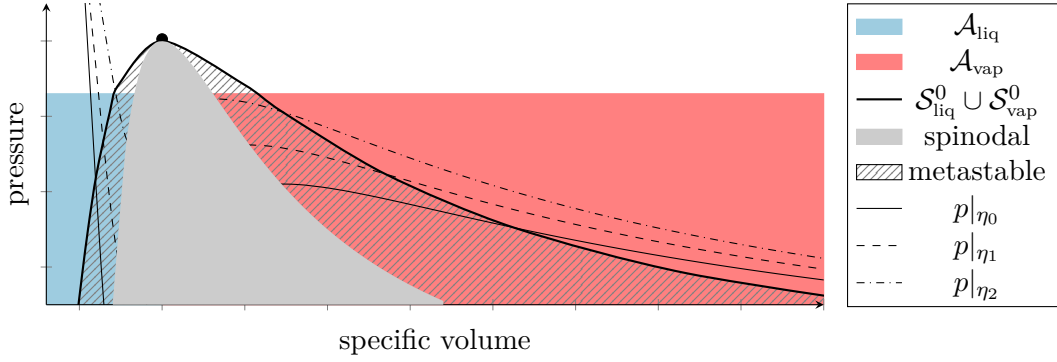


Figure 10.1: Phase diagram: colored areas for liquid and vapor phases, thin lines for isentropes $\tau \rightarrow p(\tau, \eta)$ at constant specific entropy values $\eta_0 < \eta_1 < \eta_2$ and the thick line for the image of the saturation curves for $\zeta = 0$. The bullet marks the critical point.

To illustrate the set-up, Figure 10.1 shows the so called *isentropes*: $\tau \mapsto p(\tau, \eta)$ at constant values of η . Note, in particular, that the isentropes are monotone decreasing in each phase. The area between \mathcal{A}_{liq} , \mathcal{A}_{vap} is called elliptic or *spinodal region*. Thermodynamic states in this region are unstable and the region is excluded.

We require that saturation curves exist below the critical temperature for any constant surface tension term $\zeta := (d-1)\zeta^* \kappa$ in some predefined range.

Definition 10.1 (Saturation states and curves).

Let a constant $\zeta \in \mathcal{Z} := (\zeta^{\min}, \zeta^{\max})$ with $\zeta^{\min} < 0 < \zeta^{\max}$, the set

$$\mathcal{S}_{liq}^{\zeta} = \left\{ (\tau_{liq}^{\text{sat}}, \eta_{liq}^{\text{sat}}) \in \mathcal{A}_{liq} \mid \exists (\tau_{vap}^{\text{sat}}, \eta_{vap}^{\text{sat}}) \in \mathcal{A}_{vap} \text{ such that (10.5) holds} \right\}$$

and the analog set $\mathcal{S}_{vap}^{\zeta} \subset \mathcal{A}_{vap}$ be given. A pair of states $((\tau_{liq}^{\text{sat}}, \eta_{liq}^{\text{sat}}), (\tau_{vap}^{\text{sat}}, \eta_{vap}^{\text{sat}})) \in \mathcal{A}_{liq} \times \mathcal{A}_{vap}$ with

$$\begin{aligned} T(\tau_{liq}^{\text{sat}}, \eta_{liq}^{\text{sat}}) &= T(\tau_{vap}^{\text{sat}}, \eta_{vap}^{\text{sat}}), & \mu(\tau_{liq}^{\text{sat}}, \eta_{liq}^{\text{sat}}) &= \mu(\tau_{vap}^{\text{sat}}, \eta_{vap}^{\text{sat}}), \\ p(\tau_{liq}^{\text{sat}}, \eta_{liq}^{\text{sat}}) - p(\tau_{vap}^{\text{sat}}, \eta_{vap}^{\text{sat}}) &= \zeta \end{aligned} \quad (10.5)$$

is called *pair of saturation states*.

Assume that the set $\mathcal{S}_{liq}^{\zeta}$ ($\mathcal{S}_{vap}^{\zeta}$) is the image of a simple curve. The curve is called *saturation liquid (vapor) curve* if parameterizations with respect to temperature, specific Gibbs free energy and liquid (vapor) pressure exist.

The area between saturation curves and spinodal region is called *metastable region*, see Figure 10.1.

Recall that the interface is in *local thermodynamic equilibrium* if (10.5) holds, cf. Definition 2.5. As in the isothermal case, the pair of saturation states depends on surface tension.

We assume that the saturation curves are given and that $\tau_{liq}^{\text{sat}} < \tau_{vap}^{\text{sat}}$, $\eta_{liq}^{\text{sat}} < \eta_{vap}^{\text{sat}}$ holds for any pair of saturation states. Let furthermore the functions $\tau_{liq/vap}^{\text{sat}} = \tau_{liq/vap}^{\text{sat}}(\alpha)$, $\eta_{liq/vap}^{\text{sat}} = \eta_{liq/vap}^{\text{sat}}(\alpha)$, $T^{\text{sat}} = T^{\text{sat}}(\alpha)$, $p_{liq/vap}^{\text{sat}} = p_{liq/vap}^{\text{sat}}(\alpha)$, with $\alpha \in \{T, \mu, p_{liq}, p_{vap}\}$, be the (saturated) volume, entropy, temperature, Gibbs free energy and pressure, respectively, evaluated on the saturation curve. This dependency on the constant ζ is skipped for brevity.

Remark 10.2 (Equations of state for real fluids).

Equations of state for real fluids can be rather complicated [57]. We assume, for the construction of the non-isothermal microsolver, that we can find sets \mathcal{A}_{liq} and \mathcal{A}_{vap} such that above assumptions hold. This implies in particular, that temperature and pressure values are below the critical point, as one can see in Figure 10.1. Riemann problems for more complex equations of state are considered in [62].

10.1.2 Non-isothermal Euler systems and latent heat

Remember that the bulk domains are separated by the sharp interface. This sharp interface is a priori unknown and has to be determined. The following system is derived from the balance laws of Section 2.2. We apply Reynolds transport theorem and the divergence theorem (cf. [32, 43, 60]).

Definition 10.3 (Two-phase Euler Fourier system).

Assume the geometric setting of Section 2.1 and the notation of Section 2.2. The dynamics of the fluid in the bulk are governed by the system

$$\begin{aligned} \varrho_t + \operatorname{div}(\varrho \mathbf{v}) &= 0, & (\varrho e)_t + \operatorname{div}((\varrho e + p) \mathbf{v} + \mathbf{q}) &= 0, \\ (\varrho \mathbf{v})_t + \operatorname{div}(\varrho \mathbf{v} \otimes \mathbf{v} + p \mathbf{I}) &= \mathbf{0}, & (\varrho \eta)_t + \operatorname{div}((\varrho \eta) \mathbf{v} + \boldsymbol{\varphi}) &= \eta_\Omega. \end{aligned}$$

The **specific total energy** $e = e(\mathbf{x}, t) \in \mathbb{R}$ is related to the specific internal energy via $e = \varepsilon + \frac{1}{2} |\mathbf{v}|^2$. At the phase boundary the following trace conditions hold

$$\begin{aligned} \llbracket \varrho (\mathbf{v} \cdot \mathbf{n} - s) \rrbracket &= 0, \\ \llbracket \varrho (\mathbf{v} \cdot \mathbf{n} - s) \mathbf{v} \cdot \mathbf{n} + p \rrbracket &= (d-1) \zeta^* \kappa, \\ \llbracket \varrho (\mathbf{v} \cdot \mathbf{n} - s) \mathbf{v} \cdot \mathbf{t}_l \rrbracket &= 0 \text{ for } l = 1, \dots, d-1, \\ \llbracket \varrho (\mathbf{v} \cdot \mathbf{n} - s) e + p \mathbf{v} \cdot \mathbf{n} + \mathbf{q} \cdot \mathbf{n} \rrbracket &= s (d-1) \zeta^* \kappa, \\ \llbracket \varrho (\mathbf{v} \cdot \mathbf{n} - s) \eta + \boldsymbol{\varphi} \cdot \mathbf{n} \rrbracket &= \eta_\Gamma. \end{aligned}$$

The trace conditions represent the conservation of mass, momentum and total energy in presence of capillary surface forces and heat flux. Note that the **mass flux** from the liquid phase to the vapor phase is again given by

$$j := \varrho_{\text{liq}} (\mathbf{v}_{\text{liq}} \cdot \mathbf{n} - s) = \varrho_{\text{vap}} (\mathbf{v}_{\text{vap}} \cdot \mathbf{n} - s). \quad (10.6)$$

Positive values of j correspond to evaporation waves and negative values to condensation waves.

A simple assumption for the heat flux is Fourier's law

$$\mathbf{q} = -\alpha \operatorname{grad} T, \quad \alpha > 0, \quad (10.7)$$

cf. [60]. However, this assumption introduces an additional derivative and the system is not hyperbolic anymore. On the other hand, neglecting heat flux (and entropy flux $\boldsymbol{\varphi}$) leads to thermodynamically inconsistent static solutions, see Lemma 10.6 below. For further refereeing we give a short definition of the system without heat flux.

Definition 10.4 (Two-phase Euler system).

The system of Definition 10.3 with $\mathbf{q} \equiv 0$ and $\boldsymbol{\varphi} \equiv \mathbf{0}$ is called **two-phase Euler system**.

The subsequent two lemmas show the thermodynamic inconsistency of the two-phase Euler system. The demonstration bases on the assumption, that in $\mathcal{A}_{\text{liq}} \cup \mathcal{A}_{\text{vap}}$, at most, three thermodynamic quantities are in equilibrium. Along the saturation curve $\eta_{\text{liq}}^{\text{sat}} < \eta_{\text{vap}}^{\text{sat}}$ holds. If pressure, Gibbs free energy and entropy are continuous at the interface, then $[[T]] \neq 0$.

Lemma 10.5 (The two-phase Euler system prevents condensation).

Consider the system of Definition 10.4. A phase transition with end states, such that $\eta_{\text{liq}} < \eta_{\text{vap}}$ holds, is not a condensation wave.

Proof. Note that $[[\eta]] > 0$ holds along the saturation curve and in a vicinity thereof. The mass flux j is determined by (10.6) and the entropy balance reads $j [[\eta]] = \eta_{\Gamma}$, with $\eta_{\Gamma} \geq 0$. Thus, $j \geq 0$ and the phase transition is not a condensation wave. \square

Lemma 10.6 (Static solutions are not in thermodynamic equilibrium).

Consider the system of Definition 10.4 equipped with a kinetic relation $\eta_{\Gamma} = b(j) j$, where $b : \mathbb{R} \rightarrow \mathbb{R}$ is a continuous function with $b(0) = 0$.

Then, static solutions of the two-phase Euler system are not in global thermodynamic equilibrium (Definition 2.5). In particular, for $j \rightarrow 0$, the jump conditions at the interface become

$$[[p]] = \zeta, \quad [[\eta]] = 0, \quad [[\mu + T \eta]] = 0. \quad (10.8)$$

The argument for the inconsistency is as follows: assume one of the equilibrium conditions in Definition 2.5, e.g. $[[\mu]] = 0$. Then, $[[T]] \neq 0$ since at most three quantities are in equilibrium.

Proof of Lemma 10.6. We rewrite the balance equations for normal momentum, energy and entropy in terms of the mass flux j

$$j [[v]] + [[p]] = \zeta, \quad j [[e + p v]] = s \zeta, \quad j [[\eta]] = b(j) j,$$

where $v := \mathbf{v} \cdot \mathbf{n}$. The term $s \zeta$ in the energy balance can be eliminated with help of the momentum balance. Furthermore, we apply the thermodynamic identity $\varepsilon = \mu - \tau p + T \eta$ from (10.2) and we cancel the mass flux in the energy and in the entropy balance. Thus, it holds

$$j [[v]] + [[p]] = \zeta, \quad [[\mu + T \eta + \frac{1}{2} \tau^2 j^2]] = 0, \quad [[\eta]] = b(j).$$

In the limit $j \rightarrow 0$ we find (10.8). \square

Ngan and Truskinovsky study in [63] the influence of latent heat on phase transitions in solids. They consider a model, that is essentially the Euler Fourier system with extra terms for viscosity and capillary. They find the jump conditions (10.8) in the limit $\alpha \rightarrow 0$, where α is the coefficient for heat conductivity in (10.7). In [63], the conditions (10.8) are called *adiabatic analogs to the Maxwell conditions*.

Remark 10.7 (Latent heat).

The inconsistencies, shown in Lemma 10.5 and Lemma 10.6, stem from the fact that heat flux is neglect, but the equations of state take latent heat into account, i.e. the function L in (10.9) is not zero.

The **latent heat** of transition at temperature $T_{\text{ref}} > 0$ is given by

$$L(T_{\text{ref}}) := T_{\text{ref}} \left(\eta_{\text{vap}}^{\text{sat}}(T_{\text{ref}}) - \eta_{\text{liq}}^{\text{sat}}(T_{\text{ref}}) \right), \quad (10.9)$$

where $\eta_{\text{vap}}^{\text{sat}}(T_{\text{ref}})$, $\eta_{\text{liq}}^{\text{sat}}(T_{\text{ref}})$ are as in Definition 10.1, cf. [25, 38, 57, 61]. Note that Definition 10.1 implies, that $L(T_{\text{ref}}) > 0$. Latent heat accounts for the release and the absorption of thermal energy during the phase transition, as we will see in the following.

Consider now the heat conducting case of Definition 10.3 with $\mathbf{q} = T \boldsymbol{\varphi}$. An isothermal phase transitions at temperature $T_{\text{ref}} = T_{\text{liq}} = T_{\text{vap}}$ satisfies

$$j \llbracket \eta \rrbracket + \left\llbracket \frac{\mathbf{q} \cdot \mathbf{n}}{T_{\text{ref}}} \right\rrbracket = \eta_{\Gamma}. \quad (10.10)$$

One obtains a correlation between heat flux and latent heat considering (10.10) at global thermodynamic equilibrium, cf. Definition 2.5. If a transition takes place reversibly, or η_{Γ} is negligible, then we find the equation

$$\llbracket \mathbf{q} \cdot \mathbf{n} \rrbracket = -j T_{\text{ref}} \left(\eta_{\text{vap}}^{\text{sat}}(T_{\text{ref}}) - \eta_{\text{liq}}^{\text{sat}}(T_{\text{ref}}) \right). \quad (10.11)$$

Note that the latent heat appears on the right hand side. The equation can be interpreted as follows. In evaporation processes ($j > 0$), heat inflow is higher than its outflow, thus the phase boundary liberates thermal energy. In the condensation case ($j < 0$) the opposite happens, thermal energy is absorbed at the phase boundary. The thermal energy in the first case is also known as heat of evaporation and in the second case as heat of condensation. In order to state a proper two-phase model we will assume that equation (10.11) also holds in the non-equilibrium case.

10.1.3 Free boundary formulation

Definition 10.8 below states a temperature dependent two-phase model that is hyperbolic in the bulk phases and that accounts for latent heat. It bases on the two-phase Euler Fourier model and the following assumptions.

- There is no heat flow ($\mathbf{q} \equiv 0$), nor entropy flow ($\boldsymbol{\varphi} \equiv 0$) in the bulk.
- At the interface $\llbracket \mathbf{q} \cdot \mathbf{n} \rrbracket / j = -L(T_{\text{ref}})$ and $\llbracket \mathbf{q} \cdot \mathbf{n} \rrbracket = T_{\text{ref}} \llbracket \boldsymbol{\varphi} \cdot \mathbf{n} \rrbracket$ holds for some reference temperature $T_{\text{ref}} > 0$.
- There is no slip at the phase boundary.

Definition 10.8 (Non-isothermal model).

For any $t \in [0, \theta]$, $\theta > 0$, assume that the domain $\Omega \subset \mathbb{R}^d$, $d \in \{1, 2, 3\}$ with smooth boundary, is partitioned into the union of two open sets $\Omega_{\text{vap}}(t)$, $\Omega_{\text{liq}}(t)$, which contain the two bulk phases, and the sharp interface $\Gamma(t)$, that separates the two spatial bulk sets.

In the spatial-temporal bulk set $\{(\mathbf{x}, t) \in \mathbb{R}^d \times (0, \theta) \mid \mathbf{x} \in \Omega_{\text{vap}}(t) \cup \Omega_{\text{liq}}(t)\}$ the dynamics of the fluid are governed by the system

$$\begin{aligned} \varrho_t + \text{div}(\varrho \mathbf{v}) &= 0, \\ (\varrho \mathbf{v})_t + \text{div}(\varrho \mathbf{v} \otimes \mathbf{v} + p \mathbf{I}) &= \mathbf{0}, \\ (\varrho e)_t + \text{div}((\varrho e + p) \mathbf{v}) &= 0. \end{aligned} \quad (10.12)$$

The unknowns are density $\varrho = \varrho(\mathbf{x}, t) > 0$, velocity $\mathbf{v} = \mathbf{v}(\mathbf{x}, t) = (v_1(\mathbf{x}, t), \dots, v_d(\mathbf{x}, t))^\top \in \mathbb{R}^d$ and the specific total energy $e = e(\mathbf{x}, t) \in \mathbb{R}$ which is related to the specific internal energy via $e = \varepsilon + \frac{1}{2}|\mathbf{v}|^2$. The system (10.12) is closed by an equation of state that relates the pressure p to the other variables. Finally, $\mathbf{I} \in \mathbb{R}^{d \times d}$ is the d -dimensional unit matrix.

For fixed initial position of the interface $\Gamma(0)$ and given initial density ϱ_0 , velocity field \mathbf{v}_0 and total energy e_0 assume that

$$\left. \begin{aligned} \varrho(\mathbf{x}, 0) &= \varrho_0(\mathbf{x}), \\ \mathbf{v}(\mathbf{x}, 0) &= \mathbf{v}_0(\mathbf{x}), \\ e(\mathbf{x}, 0) &= e_0(\mathbf{x}) \end{aligned} \right\} \quad \text{for } \mathbf{x} \in \Omega_{\text{vap}}(0) \cup \Omega_{\text{liq}}(0).$$

Furthermore, the vector $\varrho_0(\mathbf{x})(1, \mathbf{v}_0(\mathbf{x}), e_0(\mathbf{x}))$ belongs to the set of admissible unknowns

$$\mathcal{U}_{\text{liq/vap}} := \left\{ (\varrho, \varrho \mathbf{v}, \varrho e) \mid \exists \eta : e = \varepsilon(\varrho, \eta) + \frac{1}{2}|\mathbf{v}|^2, \left(\frac{1}{\varrho}, \eta\right) \in \mathcal{A}_{\text{liq/vap}} \right\}$$

for any $\mathbf{x} \in \Omega_{\text{vap}}(0) \cup \Omega_{\text{liq}}(0)$. At the boundary

$$\mathbf{v} \cdot \boldsymbol{\nu} = \mathbf{0} \quad \text{on } \partial\Omega, \quad (10.13)$$

is assumed, where $\boldsymbol{\nu}$ is the outer normal to $\partial\Omega$.

Let $T_{\text{ref}} > 0$ be given. For $\boldsymbol{\gamma} \in \Gamma(t)$ denote the speed of $\Gamma(t)$ in the normal direction $\mathbf{n} = \mathbf{n}(\boldsymbol{\gamma}, t) \in \mathbb{S}^{d-1}$ by $s = s(\boldsymbol{\gamma}, t) \in \mathbb{R}$. The vector \mathbf{n} points into Ω_{vap} and $\kappa = \kappa(\boldsymbol{\gamma}, t) \in \mathbb{R}$ denotes the mean curvature (2.1). Across the smooth interface the following $d + 2$ trace conditions are posed

$$\llbracket \varrho(\mathbf{v} \cdot \mathbf{n} - s) \rrbracket = 0, \quad (10.14)$$

$$\llbracket \varrho(\mathbf{v} \cdot \mathbf{n} - s) \mathbf{v} \cdot \mathbf{n} + p \rrbracket = (d - 1) \zeta^* \kappa, \quad (10.15)$$

$$\llbracket \mathbf{v} \cdot \mathbf{t}_l \rrbracket = 0 \quad \text{for } l = 1, \dots, d - 1, \quad (10.16)$$

$$\llbracket \mu + T \eta + \frac{1}{2}(\mathbf{v} \cdot \mathbf{n} - s)^2 \rrbracket = L(T_{\text{ref}}). \quad (10.17)$$

Here $\llbracket a \rrbracket := a_{\text{vap}} - a_{\text{liq}}$ and $a_{\text{vap/liq}} := \lim_{\varepsilon \rightarrow 0, \varepsilon > 0} a(\boldsymbol{\gamma} \pm \varepsilon \mathbf{n})$ for some quantity a defined in $\Omega_{\text{vap}}(t) \cup \Omega_{\text{liq}}(t)$. The constant surface tension coefficient is $\zeta^* \geq 0$, and $\mathbf{t}_1, \dots, \mathbf{t}_{d-1} \in \mathbb{S}^{d-1}$ are a complete set of vectors tangential to $\Gamma(t)$. Equations of state relate the specific Gibbs free energy μ , the temperature T and the specific entropy η to the other unknowns. The latent heat $L = L(T_{\text{ref}})$ in (10.17) is given by (10.9).

The trace conditions (10.14)–(10.17) represent the conservation of mass, the balance of momentum and total energy in presence of capillary surface forces, latent heat and the no slip condition.

Remark 10.9 (Choice of the reference temperature T_{ref}).

The latent heat L in (10.17) is measured at the temperature T_{ref} which has to be defined, for instance corresponding to some ambient system temperature $T_{\text{ref}} = T_\infty$. If it is reasonable to consider an ambient system pressure p_∞ one may apply the saturated specific entropy with respect to p_∞ : $L = T_{\text{ref}}^{\text{sat}}(p_\infty) \llbracket \eta^{\text{sat}}(p_\infty) \rrbracket$. Another possibility is to use a convex combination of the trace temperatures T_{liq} and T_{vap} . We will see in Lemma 10.10 below, that it is advantageous if $T_{\text{liq}} = T_{\text{vap}}$ implies $T_{\text{ref}} = T_{\text{vap}}$.

The system (10.12) can be written for $\mathbf{U} = (\varrho, \varrho v_1, \dots, \varrho v_d, \varrho e)^\top$ in the conservation form

$$\mathbf{U}_t + \mathbf{f}^1(\mathbf{U})_{x_1} + \dots + \mathbf{f}^d(\mathbf{U})_{x_d} = \mathbf{0},$$

with appropriately defined fluxes $\mathbf{f}^1, \dots, \mathbf{f}^d$. For $\mathbf{U} \in \mathcal{U}_{\text{liq}} \cup \mathcal{U}_{\text{vap}}$ and $\boldsymbol{\omega} \in \mathbb{S}^{d-1}$ the eigenvalues of the Jacobian of the $\boldsymbol{\omega}$ -directional flux $\omega_1 \mathbf{f}^1(\mathbf{U}) + \dots + \omega_d \mathbf{f}^d(\mathbf{U})$ are then given by

$$\begin{aligned} \lambda_1(\mathbf{U}; \boldsymbol{\omega}) &= \mathbf{v} \cdot \boldsymbol{\omega} - c, \\ \lambda_2(\mathbf{U}; \boldsymbol{\omega}) &= \dots = \lambda_{d+1}(\mathbf{U}; \boldsymbol{\omega}) = \mathbf{v} \cdot \boldsymbol{\omega}, \\ \lambda_{d+2}(\mathbf{U}; \boldsymbol{\omega}) &= \mathbf{v} \cdot \boldsymbol{\omega} + c, \end{aligned}$$

with c defined in (10.4).

As a consequence $\mathbf{U} \in \mathcal{U}_{\text{liq}} \cup \mathcal{U}_{\text{vap}}$ is a necessary (and in fact sufficient) criterion for (10.12) to be hyperbolic. As in the isothermal case, we search for entropy solutions. **Entropy solutions** are functions $\mathbf{U} = \mathbf{U}(\mathbf{x}, t)$, which are weak solutions of the model in Definition 10.8 with $\mathbf{U} \in \mathcal{U}_{\text{liq/vap}}$ for almost all $(\mathbf{x}, t) \in \Omega_{\text{liq/vap}}(t) \times [0, \theta]$ and satisfy the entropy condition

$$(-\varrho \eta)_t + \operatorname{div}(-\varrho \eta \mathbf{v}) \leq 0$$

in the distributional sense in the single bulk regions and

$$j \llbracket \eta \rrbracket T_{\text{ref}} - j L(T_{\text{ref}}) \geq 0$$

at the interface.

The entropy conditions are derived from the Euler Fourier model of Definition 10.3 applying above model assumptions for heat and entropy flux and $\eta_\Omega \geq 0$, $\eta_\Gamma \geq 0$. Using (10.3) one readily checks that $-\varrho \eta$ is convex in terms of $(\varrho, \varrho \mathbf{v}, \varrho e)$ for states in the bulk sets and thus, it is a **mathematical entropy** for (10.12) (see [33, Chapter II]).

In this chapter we are interested only in interfaces that are non-characteristic and subsonic phase transitions. For a **subsonic phase transition** the adjacent states $\mathbf{U}_{\text{vap/liq}}$ satisfy

$$\lambda_1(\mathbf{U}_{\text{liq}}; \boldsymbol{\omega}) < s < \lambda_{d+2}(\mathbf{U}_{\text{liq}}; \boldsymbol{\omega}) \quad \text{and} \quad \lambda_1(\mathbf{U}_{\text{vap}}; \boldsymbol{\omega}) < s < \lambda_{d+2}(\mathbf{U}_{\text{vap}}; \boldsymbol{\omega}). \quad (10.18)$$

With (10.6) and the assumption that the sound speed in the liquid phase propagates much faster than in the vapor phase, it suffices to check $|j| < \varrho_{\text{vap}} c(\tau_{\text{vap}}, \eta_{\text{vap}})$.

For the isothermal case it is known (see e.g. [1, 70]) that well-posedness of the free boundary value problem requires an additional condition. The same holds for (10.12) with van der Waals fluids, see [49]. We assume that this is also necessary for more general equations of state fulfilling (10.1).

The **kinetic relation** imposes a condition on the interfacial entropy production. That is in Eulerian coordinates $T_{\text{ref}} \eta_\Gamma = g(j) j$ with g of (6.1). We subtract T_{ref} times the entropy balance from the energy balance and apply above model assumptions. The kinetic relation then reads

$$\mathbb{k}(\mathbf{U}_{\text{liq}}, \mathbf{U}_{\text{vap}}, j) := \llbracket \mu + \frac{1}{2} \tau^2 j^2 \rrbracket + \llbracket T \eta \rrbracket - T_{\text{ref}} \llbracket \eta \rrbracket + g(j) = 0. \quad (10.19)$$

In the following, we consider only kinetic relations of the type (10.19). A specific solution, with subsonic (static) phase transitions, is given by the following lemma.

Lemma 10.10 (Static solutions of the non-isothermal model).

Let $\Omega_{\text{liq}} = B_1(\mathbf{0}) \subset \mathbb{R}^d$ and $\Omega_{\text{vap}} = [-2, 2]^d \setminus \bar{B}_1(\mathbf{0}) \subset \mathbb{R}^d$, for $d \in \{1, 2, 3\}$, a surface tension coefficient $\zeta^* \geq 0$ and a pair of saturation states $(\tau_{\text{liq}}^{\text{sat}}, \eta_{\text{liq}}^{\text{sat}}) \in \mathcal{A}_{\text{liq}}$, $(\tau_{\text{vap}}^{\text{sat}}, \eta_{\text{vap}}^{\text{sat}}) \in \mathcal{A}_{\text{vap}}$ for $\zeta = (d-1)\zeta^*$ at temperature $T_{\text{ref}} > 0$ be given. Here, $B_1(\mathbf{0})$ denotes the d -dimensional unit ball with center in the origin. Furthermore, let the initial states

$$\mathbf{U}_0(\mathbf{x}) = \begin{cases} (1, \mathbf{0}, \varepsilon(\tau_{\text{liq}}, \eta_{\text{liq}}))^{\top} / \tau_{\text{liq}} & \text{for } \mathbf{x} \in \Omega_{\text{liq}}, \\ (1, \mathbf{0}, \varepsilon(\tau_{\text{vap}}, \eta_{\text{vap}}))^{\top} / \tau_{\text{vap}} & \text{for } \mathbf{x} \in \Omega_{\text{vap}}, \end{cases}$$

for some $(\tau_{\text{liq}}, \eta_{\text{liq}}) \in \mathcal{A}_{\text{liq}}$, $(\tau_{\text{vap}}, \eta_{\text{vap}}) \in \mathcal{A}_{\text{vap}}$ be given and consider the non-isothermal model of Definition 10.8, equipped with the kinetic relation in (10.19).

Then, the function $\mathbf{U}(\mathbf{x}, t) = \mathbf{U}_0(\mathbf{x})$ solves the non-isothermal model for $t > 0$ if and only if $\tau_{\text{liq}/\text{vap}}$, $\eta_{\text{liq}/\text{vap}}$ and corresponding $p_{\text{liq}/\text{vap}}$, $\mu_{\text{liq}/\text{vap}}$, $T_{\text{liq}/\text{vap}}$ satisfy

$$[[p]] = \zeta, \quad [[\mu + T\eta]] = T_{\text{ref}}(\eta_{\text{vap}}^{\text{sat}} - \eta_{\text{liq}}^{\text{sat}}), \quad \text{and} \quad [[\mu + T\eta]] = T_{\text{ref}} [[\eta]].$$

Proof. The function $\mathbf{U}_0(\mathbf{x})$ is constant in the bulk and boundary conditions are satisfied. Thus, we have to check merely the jump conditions. The mass flux across the phase boundary is zero, due to the vanishing velocity field. If we set $j = 0$ in the jump conditions (10.14)–(10.17) and the kinetic relation, we find above jump condition. \square

Note that static solutions are not unique. For instance solutions with $T_{\text{liq}} \neq T_{\text{vap}}$ are possible. However, and in contrast to Lemma 10.5 and Lemma 10.6, one particular static solution is the thermodynamic equilibrium due to Definition 2.5.

Proposition 10.11 (Global thermodynamic equilibrium solution).

One particular static solutions of the non-isothermal model is given by $\mathbf{U}(\mathbf{x}, t) = \mathbf{U}_0(\mathbf{x})$, with $\mathbf{U}_0(\mathbf{x})$ of Lemma 10.10, and

$$[[p]] = \zeta, \quad [[\mu]] = 0 \quad \text{and} \quad T_{\text{liq}} = T_{\text{vap}} = T_{\text{ref}}. \quad (10.20)$$

The solution is called **thermodynamic equilibrium solution**.

Proof. The jump conditions (10.20) are just a special case of the jump conditions of Lemma 10.10. Note that $\eta_{\text{liq}} = \eta_{\text{liq}}^{\text{sat}}(T_{\text{ref}})$ and $\eta_{\text{vap}} = \eta_{\text{vap}}^{\text{sat}}(T_{\text{ref}})$, since (10.5) holds. \square

10.2 Microsolver for kinetic relations

We present in this section an approach to solve Riemann problems for the non-isothermal model of Definition 10.8. Exact Riemann solvers of that type can be found in [17, 62]. However, they do not cover general equations of state or general kinetic relation (10.19) nor surface tension. Furthermore, they consider the two-phase Euler system (with homogeneous Rankine-Hugoniot conditions), that suffers from thermodynamically inconsistent static solutions, see Lemma 10.6.

The section is organized as follows. The first subsection introduces the micro-model and explains the structure of the solution. Similar to the relaxation approach of Chapter 7, we rely on specific wave configurations, i.e. attached waves and supersonic phase transitions are excluded. Based on this configuration, Algorithm 10.12 defines a target function in

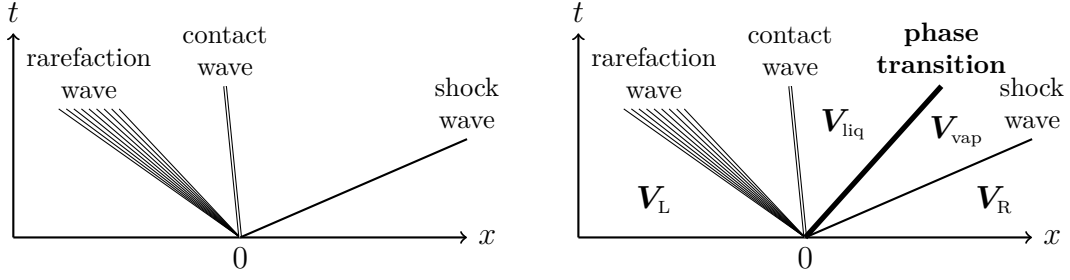


Figure 10.2: Left: typical wave structure for the single phase Riemann solution with $d + 2$ waves. It consists of a rarefaction wave followed by a contact wave of multiplicity d and a shock wave. Right: typical wave structure for the two-phase Riemann solution with $d + 3$ waves. The additional wave is the subsonic phase transition.

Section 10.2.2, whose root is the solution of the micro-scale model. This provides a very flexible method, that is applicable to general kinetic relations. Algorithm 10.15 applies the target function in order to determine the micro solution.

The micro-model depends on the constant surface tension term and reference temperature, as well as on the chosen kinetic relation. The last subsection shows their influence on the Riemann solution.

10.2.1 Micro-scale model

We follow the same approach as in Chapter 3. The front tracking scheme of Algorithm 3.1 provides for any point of the computational interface γ states as input data for the Riemann solver. These states are $\mathbf{U}_L \in \mathcal{U}_{\text{liq}}$, $\mathbf{U}_R \in \mathcal{U}_{\text{vap}}$, an orthonormal system $\mathbf{n}, \mathbf{t}_1, \dots, \mathbf{t}_{d-1} \in \mathbb{S}^{d-1}$, and an associated (constant) curvature value $\kappa \in \mathbb{R}$. The surface tension term is again abbreviated with $\zeta := (d-1)\zeta^*\kappa$ and held constant for a single micro-scale problem. With the Riemann solver, we determine interfacial bulk states $\mathbf{U}_{\text{liq}} \in \mathcal{U}_{\text{liq}}$, $\mathbf{U}_{\text{vap}} \in \mathcal{U}_{\text{vap}}$ which result from the local interaction of the input data based on a chosen kinetic relation \mathbb{k} and on the reference temperature T_{ref} for the latent heat. From the technical point of view the upshot of this section will be mappings of type

$$\tilde{M} : \begin{cases} \mathcal{U}_{\text{liq}} \times \mathcal{U}_{\text{vap}} \times (\mathbb{S}^{d-1})^d \times \mathcal{Z} & \rightarrow \mathcal{U}_{\text{liq}} \times \mathcal{U}_{\text{vap}} \times \mathbb{R} \\ (\mathbf{U}_L, \mathbf{U}_R, \mathbf{n}, \mathbf{t}_1, \dots, \mathbf{t}_{d-1}, \zeta) & \mapsto (\mathbf{U}_{\text{liq}}, \mathbf{U}_{\text{vap}}, s). \end{cases} \quad (10.21)$$

The *non-isothermal micro-scale model* under consideration is now

$$\begin{pmatrix} \varrho \\ \varrho v \\ \varrho \mathbf{u} \\ \varrho e \end{pmatrix}_t + \begin{pmatrix} \varrho v \\ \varrho v^2 + p \\ \varrho \mathbf{u} v \\ (\varrho e + p)v \end{pmatrix}_x = \begin{pmatrix} 0 \\ 0 \\ \mathbf{0} \\ 0 \end{pmatrix},$$

for $x := (\mathbf{x} - \gamma) \cdot \mathbf{n}$, $v := \mathbf{v} \cdot \mathbf{n}$ and $\mathbf{u} := (\mathbf{v} \cdot \mathbf{t}_1, \dots, \mathbf{v} \cdot \mathbf{t}_{d-1})^\top$. To simplify the subsequent algorithms, we introduce the state vector $\mathbf{V} := (\tau, v, \mathbf{u}, T)^\top$. The model is subject to the Riemann initial condition

$$\mathbf{V}(x, 0) = \begin{cases} \mathbf{V}_L = (\tau_L, \mathbf{v}_L \cdot \mathbf{n}, \mathbf{v}_L \cdot \mathbf{t}_1, \dots, \mathbf{v}_L \cdot \mathbf{t}_{d-1}, T_L)^\top & \text{for } x \leq 0, \\ \mathbf{V}_R = (\tau_R, \mathbf{v}_R \cdot \mathbf{n}, \mathbf{v}_R \cdot \mathbf{t}_1, \dots, \mathbf{v}_R \cdot \mathbf{t}_{d-1}, T_R)^\top & \text{for } x > 0. \end{cases} \quad (10.22)$$

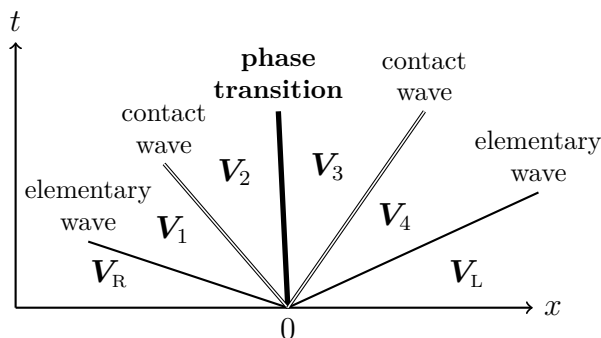


Figure 10.3: Wave fan as it is assumed in Algorithm 10.12. Depending on the wave configuration, either the left contact wave vanishes ($V_1 = V_2$), or the right contact wave vanishes ($V_3 = V_4$).

Entropy solutions of the purely hyperbolic system consist of $d + 2$ waves: two shock or rarefaction waves associated to the eigenvalues λ_1 and λ_{d+2} and contact waves of multiplicity d , as it is shown exemplary in Figure 10.2 (left). Because we want to solve a two-phase problem, we will rely on a different wave fan. We propose to solve the problem by adding a phase transition with adjacent states $\mathbf{V}_{\text{liq}}, \mathbf{V}_{\text{vap}}$ (see Figure 10.2 right). The phase transition is a discontinuous wave that is supposed to be subsonic (10.18) and to satisfy the jump conditions (10.14)–(10.17) and the kinetic relation (10.19). In this way we preserve the jump conditions at least for fixed mean curvature values $\kappa \in \mathbb{R}$. All other waves are kept satisfying the standard Rankine-Hugoniot conditions and Riemann invariants.

We call a self-similar entropy solution of the Riemann problem (10.22) a \mathbb{k} -*micro solution* if it is composed of, at most, four waves: left and right elementary wave, a contact wave and the subsonic phase transition that satisfies the kinetic relation \mathbb{k} .

10.2.2 Algorithm

The \mathbb{k} -micro solution consists of $d + 3$ waves, one wave being a subsonic phase transition with adjacent states $\mathbf{V}_{\text{liq}}, \mathbf{V}_{\text{vap}}$. Algorithm 10.12 provides the exact solution of the non-isothermal micro-scale model as the root of an implicit function, in the following called target function. The target function is solved with an iterative scheme in Algorithm 10.15.

The phase transition is subsonic but might be faster or slower than the contact wave. Thus, the phase of the state between phase transition and contact wave is not known in advance. Any iterative scheme, that relies on one fan configuration will fail if the phase of the middle state changes, since ratios of specific volume values and entropy values are very different in the liquid and the vapor. Furthermore, approximate states may belong to the spinodal region, where the equation of state cannot be evaluated. For that reason, we rely on a wave fan with two contact waves, see Figure 10.3. One contact wave is nonphysical and will be eliminated during the root finding process.

The unknowns of the target function are chosen to be the specific volume and temperature, because we will later on use thermodynamic libraries that compute all other quantities in terms of (τ, T) . Shock, rarefaction and contact waves are computed as in [33, Chapter II].

Algorithm 10.12 (Evaluation of the target function $F_{L,R}$).

Let a function $g = g(j)$, that completes the kinetic relation \mathbb{k} in (10.19), and

$$\mathbf{V}_L, \mathbf{V}_R \in \mathbb{R}^{d+1} \text{ from (10.22), } \zeta \in \mathbb{R} \text{ and } T_{\text{ref}} > 0$$

be given as constant input parameters. Furthermore, let the arguments τ_i, T_i for $i = 1, \dots, 4$ be given.

The following steps determine the **target function**

$$F_{L,R} : \mathbb{R}_+^8 \rightarrow \mathbb{R}^8, \quad (\tau_1, T_1, \tau_2, T_2, \tau_3, T_3, \tau_4, T_4) \mapsto (r_1, r_2, \dots, r_8).$$

The algorithm returns r_1, r_2, \dots, r_8 and, in addition, an error flag, states

$$\mathbf{V}_i = (\tau_i, v_i, \mathbf{u}_i, T_i)^\top \in \mathbb{R}^{d+1} \text{ for } i = 1, \dots, 4, \quad \text{and} \quad s \in \mathbb{R}.$$

Step 1. Evaluate pressures, specific entropies, inner and Gibbs free energies

$$p_i := p(\tau_i, T_i), \quad \eta_i := \eta(\tau_i, T_i), \quad \varepsilon_i := \varepsilon(\tau_i, T_i), \quad \mu_i := \mu(\tau_i, T_i)$$

for $i = L, R, 1, \dots, 4$ and assign tangential velocities

$$\mathbf{u}_1 := \mathbf{u}_2 := \mathbf{u}_L \quad \text{and} \quad \mathbf{u}_3 := \mathbf{u}_4 := \mathbf{u}_R.$$

Abort if $(\tau_1, \eta_1), (\tau_2, \eta_2) \notin \mathcal{A}_{\text{liq}}$ or $(\tau_3, \eta_3), (\tau_4, \eta_4) \notin \mathcal{A}_{\text{vap}}$ and return the error flag.

Step 2. The left elementary wave determines v_1 and r_1 .

If $p_L > p_1$, the left wave is a rarefaction wave, set

$$r_1 := \eta_1 - \eta_L, \quad v_1 := v_L + \int_{\tau_L}^{\tau_1} -\sqrt{-p_\tau(\tau, \eta_L)} \, d\tau.$$

If $p_L \leq p_1$, the left wave is a shock wave, set

$$r_1 := \varepsilon_1 - \varepsilon_L + \frac{1}{2}(p_L + p_1)(\tau_1 - \tau_L), \quad v_1 := v_L - \sqrt{|(p_L - p_1)(\tau_1 - \tau_L)|}.$$

Step 3. The right elementary wave determines v_4 and r_2 .

If $p_4 < p_R$, the right wave is a rarefaction wave, set

$$r_2 := \eta_R - \eta_4, \quad v_4 := v_R - \int_{\tau_R}^{\tau_4} -\sqrt{-p_\tau(\tau, \eta_R)} \, d\tau.$$

If $p_4 \geq p_R$, the right wave is a shock wave, set

$$r_2 := \varepsilon_R - \varepsilon_4 + \frac{1}{2}(p_4 + p_R)(\tau_R - \tau_4), \quad v_4 := v_R + \sqrt{|(p_4 - p_R)(\tau_R - \tau_4)|}.$$

Step 4. The contact waves determine (normal) fluid velocity and pressure in the adjacent states. Assign

$$r_3 := p_2 - p_1, \quad r_4 := p_4 - p_3, \quad v_2 := v_1, \quad v_3 := v_4.$$

Step 5. The mass flux through the phase boundary and its speed are

$$j := \frac{v_3 - v_2}{\tau_3 - \tau_2}, \quad s := v_2 - j \tau_2 = v_3 - j \tau_3.$$

Step 6. The left contact wave propagates with speed v_3 , the phase transition with s and the right contact wave with speed v_4 . The wave fan configuration is therefore known and the additional contact wave can be rejected, set

$$r_5 := \begin{cases} T_4 - T_3 & : j < 0, \\ (T_2 - T_1)(T_4 - T_3) & : j = 0, \\ T_2 - T_1 & : j > 0. \end{cases}$$

Step 7. The phase transition connects \mathbf{V}_2 and \mathbf{V}_3 , thus

$$\begin{aligned} r_6 &:= j(v_3 - v_2) + p_3 - p_2 - \zeta, \\ r_7 &:= (h_3 - h_2) + \frac{1}{2}j^2(\tau_3 - \tau_2) - L(T_{\text{ref}}), \\ r_8 &:= (h_3 - h_2) + \frac{1}{2}j^2(\tau_3 - \tau_2) - T_{\text{ref}}(\eta_3 - \eta_2) + g(j), \end{aligned}$$

with $h_i = \mu_i + T_i \eta_i$, $i = 2, 3$.

The task is now to find the root of the target function.

Theorem 10.13 (Root of $F_{L,R}$ determines the \mathbb{k} -micro solution).

Let $\mathbf{V}_L, \mathbf{V}_R \in \mathbb{R}^{d+1}$ from (10.22), $\zeta \geq 0$, $T_{\text{ref}} > 0$ and a function $g = g(j)$, that completes the kinetic relation \mathbb{k} in (10.19), be given.

A \mathbb{k} -micro solution, that is composed of the intermediate states $\mathbf{V}_1, \mathbf{V}_2, \mathbf{V}_3, \mathbf{V}_4$ as shown in Figure 10.3, exists if and only if Algorithm 10.12 returns the states $\mathbf{V}_1, \mathbf{V}_2, \mathbf{V}_3, \mathbf{V}_4$ and $r_i = 0$ for $i = 1, \dots, 8$.

Note that intermediate states of the \mathbb{k} -micro solution may vanish. This is the case, when propagation speeds coincide or states are equal. In particular, $\mathbf{V}_1 = \mathbf{V}_2$ or $\mathbf{V}_3 = \mathbf{V}_4$ holds, since only one contact wave is valid.

Proof of Theorem 10.13. Note that Algorithm 10.12 guarantees, that $\mathbf{V}_1, \mathbf{V}_2$ correspond to the liquid phases and $\mathbf{V}_3, \mathbf{V}_4$ correspond to the vapor phases. Furthermore, a \mathbb{k} -micro solution is composed of, at most, four waves: left and right elementary wave, a contact wave and the phase transition.

The condition $r_6 = r_7 = r_8 = 0$ is equivalent to the property, that the states \mathbf{V}_2 and \mathbf{V}_3 are connected by a phase transition that fulfills (10.14)–(10.17) and (10.19). Recall that the phase transition wave is subsonic (10.18).

We proceed with the case $j \leq 0$. The case $j > 0$ is similar. The condition $r_1 = 0$ is equivalent to the property, that the states \mathbf{V}_L and \mathbf{V}_1 are connected by a rarefaction wave or a Lax shock wave associated to λ_1 and that \mathbf{V}_1 and \mathbf{V}_2 are connected by a contact wave with characteristic speed λ_2 . The condition $r_2 = r_5 = 0$ is equivalent to the property, that $\mathbf{V}_3 = \mathbf{V}_4$ and $\mathbf{V}_5, \mathbf{V}_R$ are connected by a rarefaction wave or a Lax shock wave associated to λ_{d+2} .

Note that in the case $j = 0$, we find a phase transition with attached contact wave. Both waves propagate with the same speed. The solution remains the same (in distributional sense) if the left contact wave or the right one is attached. \square

Remark 10.14 (Requirements to the root-finding algorithms for $F_{L,R}$).

Note that the function $F_{L,R}$, determined by Algorithm 10.12, is not globally differentiable. Furthermore, it may happen that the actual guess leads to a state in the spinodal region or the wrong phase. This is recognized by Step 1 and an error flag is returned. We apply a damped Quasi-Newton method and reduce the step size until all states are in the correct phases.

Later on we will test two different choices of the reference temperature T_{ref} . This will either be a constant ambient temperature T_∞ or the arithmetic mean of the initial temperature values. To denote this difference, let us introduce a function $\mathring{T} = \mathring{T}(T_L, T_R) \in \mathcal{C}(\mathbb{R}_+^2)$ with the two choices

$$\mathring{T}_\infty(T_L, T_R) := T_\infty \quad \text{and} \quad \mathring{T}_{\{T\}}(T_L, T_R) := \frac{1}{2}(T_L + T_R). \quad (10.23)$$

Note that this is the same treatment as it was used for the surface tension in Algorithm 3.1 and the mass flux estimate in Algorithm 7.4. The reference temperature is fixed in the micro-scale model, but adapted on each application of the microsolver.

Algorithm 10.15 (Non-isothermal \mathbb{k} -microsolver $\tilde{M}_{\mathbb{k}}$).

Let the arguments $(\mathbf{U}_L, \mathbf{U}_R, \mathbf{n}, \mathbf{t}_1, \dots, \mathbf{t}_{d-1}, \zeta) \in \mathcal{U}_{\text{liq}} \times \mathcal{U}_{\text{vap}} \times (\mathbb{S}^{d-1})^d \times \mathcal{Z}$ of function \tilde{M} in (10.21), a function $\mathring{T} \in \mathcal{C}(\mathbb{R}_+^2)$ and a function $g = g(j)$ that completes the kinetic relation (10.19) be given.

Step 1. Compute specific volume $\tau_{L/R}$, temperature $T_{L/R}$, normal and tangential fluid velocities

$$v_{L/R} := \mathbf{v}_{L/R} \cdot \mathbf{n} \quad \text{and} \quad \mathbf{u}_{L/R} := \left(\mathbf{v}_{L/R} \cdot \mathbf{t}_1, \dots, \mathbf{v}_{L/R} \cdot \mathbf{t}_{d-1} \right)^\top$$

from the initial states $\mathbf{U}_{L/R}$.

Assign the constant parameters for Algorithm 10.12, that are the state vectors $\mathbf{V}_{L/R} = (\tau_{L/R}, v_{L/R}, \mathbf{u}_{L/R}, T_{L/R})^\top$, the reference temperature $T_{\text{ref}} := \mathring{T}(T_L, T_R)$, ζ and the function g .

Step 2. Assign an initial guess $\tau_i, T_i, i = 1, \dots, 4$, for the root-finding algorithm such that

$$\begin{aligned} (\tau_1, \eta(\tau_1, T_1)) &\in \mathcal{A}_{\text{liq}}, & (\tau_2, \eta(\tau_2, T_2)) &\in \mathcal{A}_{\text{liq}}, \\ (\tau_3, \eta(\tau_3, T_3)) &\in \mathcal{A}_{\text{vap}}, & (\tau_4, \eta(\tau_4, T_4)) &\in \mathcal{A}_{\text{vap}} \end{aligned}$$

holds.

Step 3. Compute the non-isothermal \mathbb{k} -micro solution. Solve

$$F_{L,R}(\tau_1, T_1, \tau_2, T_2, \tau_3, T_3, \tau_4, T_4) = \mathbf{0}$$

and store the return values $\mathbf{V}_1, \dots, \mathbf{V}_4$, s of Algorithm 10.12.

Step 4. Return $(\mathbf{U}_{\text{liq}}, \mathbf{U}_{\text{vap}}, s)$, where

$$\begin{aligned} \varepsilon_2 &:= \varepsilon(\tau_2, T_2), & \varepsilon_3 &:= \varepsilon(\tau_3, T_3), \\ \mathbf{v}_{\text{liq}} &:= v_2 \mathbf{n} + \sum_{k=1}^{d-1} (\mathbf{u}_2)_k \mathbf{t}_k, & \mathbf{v}_{\text{vap}} &:= v_3 \mathbf{n} + \sum_{k=1}^{d-1} (\mathbf{u}_3)_k \mathbf{t}_k \\ \mathbf{U}_{\text{liq}} &:= \frac{1}{\tau_2} \left(1, \mathbf{v}_{\text{liq}}, \varepsilon_2 + \frac{1}{2} |\mathbf{v}_{\text{liq}}|^2 \right), & \mathbf{U}_{\text{vap}} &:= \frac{1}{\tau_3} \left(1, \mathbf{v}_{\text{vap}}, \varepsilon_3 + \frac{1}{2} |\mathbf{v}_{\text{vap}}|^2 \right). \end{aligned}$$

Theorem 10.13 states, that a \mathbb{k} -micro solution is found, if the root-finding algorithm converges. Conditions, upon which unique solutions of the target function exist, are not part of this work.

Remark 10.16 (Applying different sharp interface models).

The approach is quite flexible concerning kinetic relations and jump conditions for the energy. Almost any kind of residual can be stated for r_7 and r_8 in Step 7 of Algorithm 10.12. Thus, the microsolver is easily applicable to other sharp interface models.

We consider in the following the kinetic relations \mathbb{k}_1 , \mathbb{k}_2 and \mathbb{k}_3 as in (10.19) with associated functions

$$g_1(j) = 0, \quad g_2(j) = k^* j, \quad g_3(j) = k^* \text{sign}(j) j^2,$$

respectively. Note that they correspond to K_1 , K_2 and K_3 in Table 6.1. For $T_{\text{liq}} = T_{\text{vap}} = T_{\text{ref}}$ they are equivalent. Corresponding relations to K_4 , K_6 and K_7 are just not implemented. Applying a kinetic relation like K_5 leads to discontinuous target functions. This is delicate for the root-finding algorithm, even if a unique solution exists. The target function for kinetic relation $\mathbb{k}_8(\mathbf{U}_{\text{liq}}, \mathbf{U}_{\text{vap}}, j) := j$ is overdetermined, since always $j = 0$ holds. As in the previous chapters, we write \mathbb{k}_n -micro solution, \mathbb{k}_n -microsolver and $\tilde{M}_{\mathbb{k}_n}$ if the demanded kinetic relation is \mathbb{k}_n and $n \in \{1, 2, 3\}$.

10.2.3 \mathbb{k} -micro solutions and influence of parameters

The following examples illustrate the non-isothermal \mathbb{k} -micro solutions in one spatial dimension. We compute Riemann solutions with the solver of the previous subsection for different kinetic relations and reference temperatures. Note that for a single application of $\tilde{M}_{\mathbb{k}}$, reference temperature T_{ref} and surface tension term ζ are constant.

Example 10.17 (Influence of entropy production coefficient k^*).

The first example addresses the influence of the entropy production coefficient k^* onto the \mathbb{k}_2 -micro solution. We consider an n-dodecane fluid with initial conditions, such that

$$(p, v, T) = \begin{cases} (1.39 \text{ bar}, 0, 500 \text{ K})^\top & \text{for } x \leq 0, \\ (0.4 \text{ bar}, 0, 500 \text{ K})^\top & \text{for } x > 0 \end{cases}$$

holds. The liquid phase is on the left hand side, the surface tension term is $\zeta = 0$ bar and the reference temperature $T_{\text{ref}} = 500$ K corresponds to $L(T_{\text{ref}}) = 249410 \text{ J/kg}$.

The \mathbb{k}_2 -micro solution is shown in Figure 10.4. For the parameter $k^* = 0 \text{ m}^3/\text{kg s}$, it consists of a left shock wave followed by an evaporation wave of speed $s = -0.94 \text{ m/s}$, the

	T_{ref}	$L(T_{\text{ref}})$	ζ	s
(a)	500 K	249410 J/kg	0 bar	-0.28 m/s
(b)	504 K	246784 J/kg	0 bar	-0.33 m/s
(c)	508 K	244115 J/kg	0 bar	-0.37 m/s
(d)	504 K	246784 J/kg	-0.1 bar	-0.36 m/s
(e)	504 K	246784 J/kg	0.1 bar	-0.30 m/s

Table 10.1: Parameters for Example 10.18. The last column displays the propagation speed of the \mathbb{k}_2 -micro solutions.

contact wave and a right shock wave. Note that the contact wave is visible only in the temperature distribution.

The solution for $k^* = 50 \text{ m}^3/\text{kg s}$ and $k^* = 100 \text{ m}^3/\text{kg s}$ is composed of a left rarefaction wave, an evaporation wave, the contact wave and a right shock wave. Note that the slope of the rarefaction wave is quite strong in the chosen spatial scaling. The results indicate how the variation in k^* influences the predicted mass flux rates and the interface speed. In fact, the speed of the evaporation wave is $s = -0.28 \text{ m/s}$ for $k^* = 50 \text{ m}^3/\text{kg s}$ and $s = -0.1 \text{ m/s}$ for $k^* = 100 \text{ m}^3/\text{kg s}$. Here, the liquid pressure is below the saturation pressure of 1.39 bar and the state $(\tau_{\text{liq}}, \eta_{\text{liq}})$ is metastable.

Figure 10.4 shows also the isothermal micro-solution for the same setting. The solutions are very similar, except for the propagation speeds in the liquid bulk phase and the temperature distribution.

Example 10.18 (Influence of reference temperature and surface tension term).

The second example addresses the effect of the choice of the reference temperature and the surface tension to a single \mathbb{k}_2 -micro solution. Consider n-dodecane with initial states such that

$$(p, v, T) = \begin{cases} (1.39 \text{ bar}, 0 \text{ m/s}, 500 \text{ K})^\top & \text{for } x \leq 0, \\ (0.4 \text{ bar}, 0 \text{ m/s}, 508 \text{ K})^\top & \text{for } x > 0 \end{cases}$$

holds and $k^* = 50 \text{ m}^3/\text{kg s}$. Reference temperature and surface tensions are given in Table 10.1. At 500 K the liquid pressure of 1.39 bar corresponds to the saturation pressure. Figure 10.5 shows the \mathbb{k}_2 -micro solutions. The solutions have the same wave pattern as in the previous example.

Differences in the reference temperature result only in slightly different solutions. The structure of the solution is quite the same, but the values of the constant states are different. The speed of the evaporation wave can be found in Table 10.1.

The dashed lines in Figure 10.5 correspond to solutions with surface tension. Capillarity forces affect in particular the pressure distribution. Temperature and fluid velocity coincide with the solution of the planar case. The amount of surface tension in case (d) corresponds to a 3-dimensional droplet of 0.0035 mm diameter ($\zeta^* = 0.0089 \text{ N/m}$ at $T = 503 \text{ K}$). Test case (e) corresponds to a bubble with the same diameter as only the sign alters.

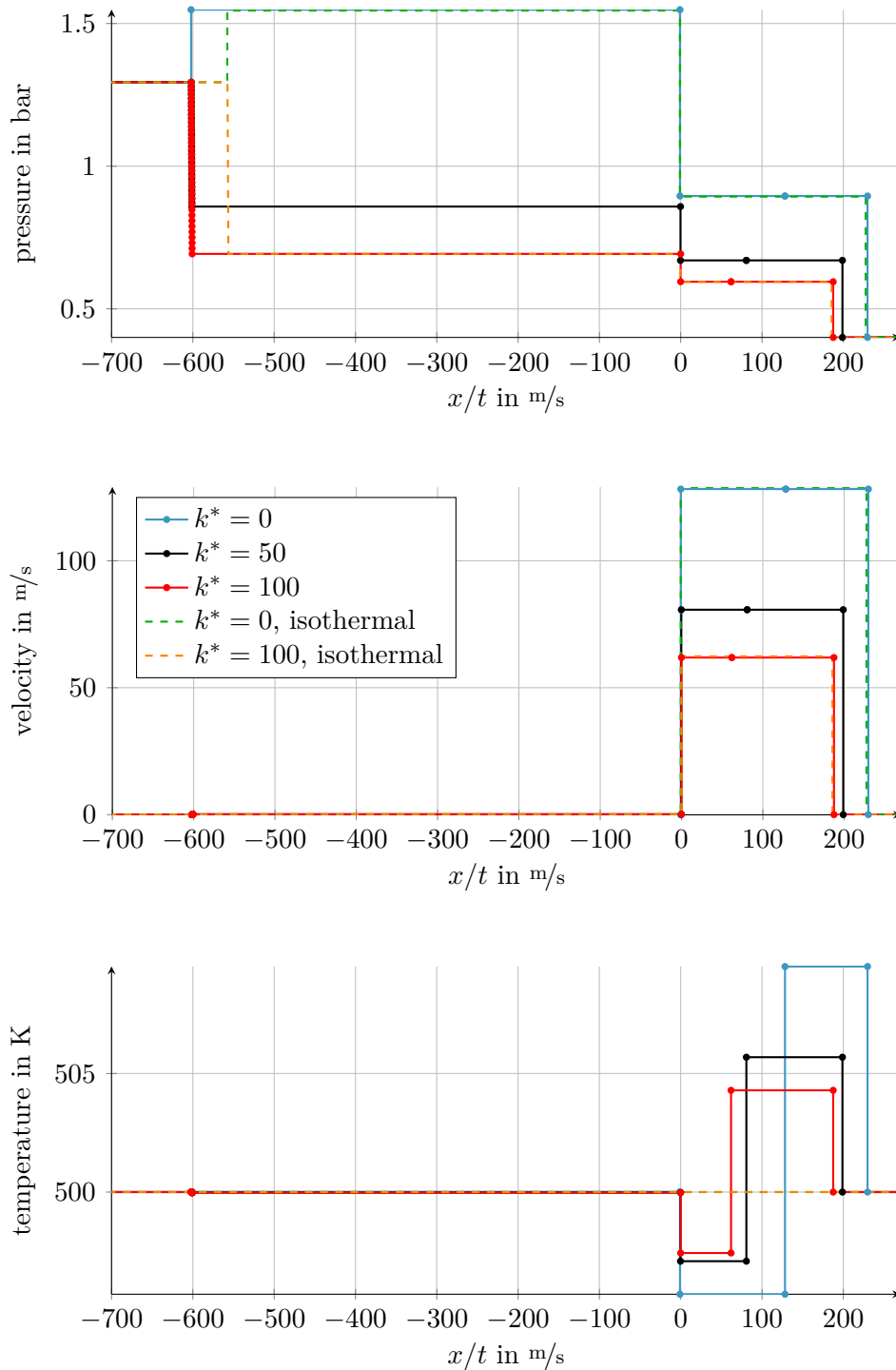


Figure 10.4: \mathbb{k}_2 -micro solutions of Example 10.17 with different entropy dissipation rates. All figures correspond to the same legend.

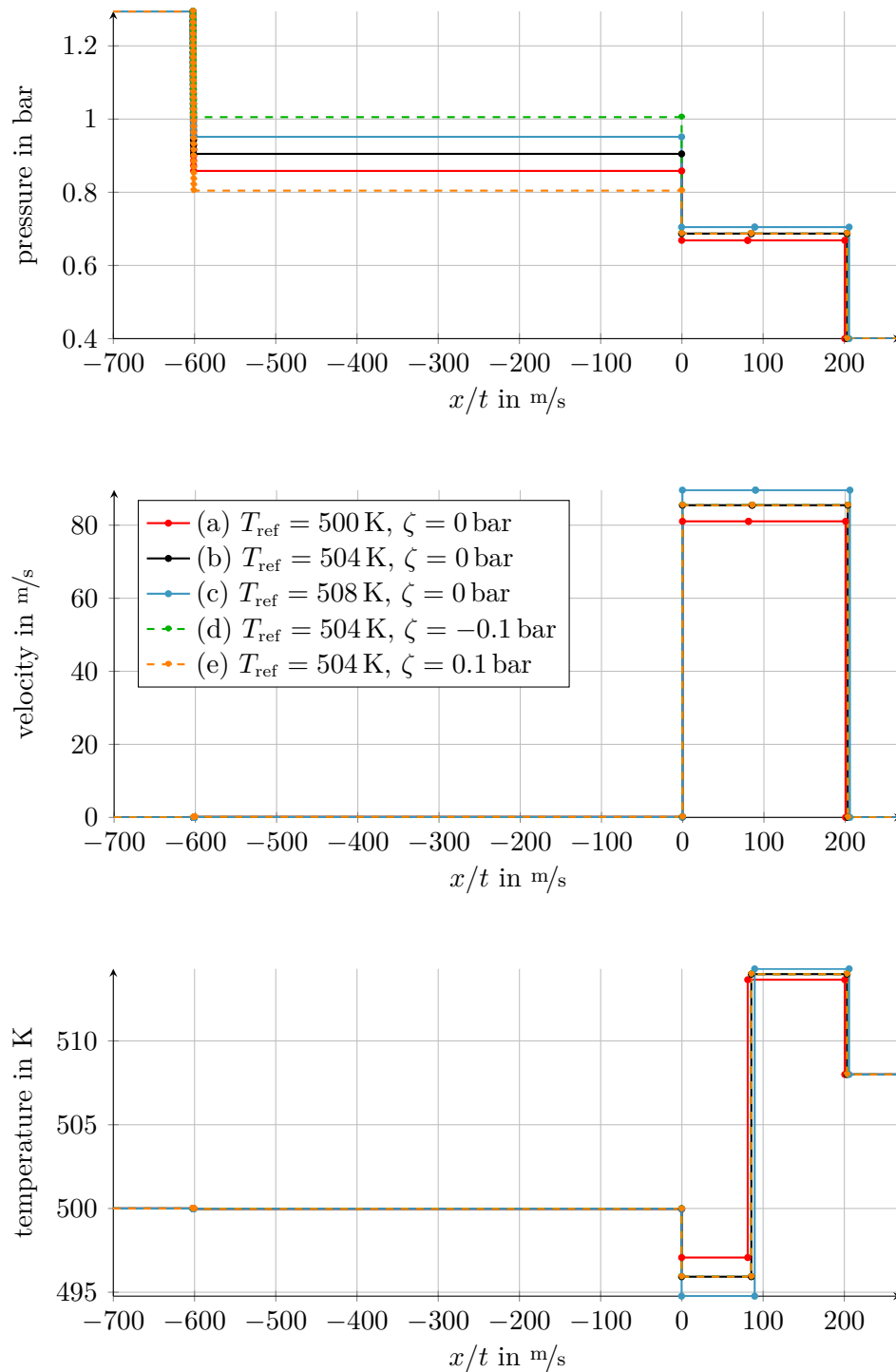


Figure 10.5: k_2 -micro solutions of Example 10.18 and parameters in Table 10.1. All figures correspond to the same legend.

	p_L	p_R	v_L	v_R	T_L	T_R	\mathring{T}_∞	\mathbb{k}	k^*
(f)	1.39 bar	0.4 bar	0 m/s	0 m/s	230 °C	230 °C	230 °C	\mathbb{k}_2	50 m ³ /kg s
(g)	1.39 bar	1.0 bar	0 m/s	0 m/s	230 °C	230 °C	230 °C	\mathbb{k}_2	50 m ³ /kg s
(h)	1.39 bar	0.4 bar	0 m/s	0 m/s	500 K	504 K	508 K	\mathbb{k}_2	50 m ³ /kg s

Table 10.2: Initial conditions for n-dodecane test examples.

10.3 Numerical and thermodynamic verification

This section addresses the verification of the complete non-isothermal method, i.e. the combination of \mathbb{k} -microsolver and the bulk solver of Chapter 8. We analyze the convergence of numerical approximations in Subsection 10.3.1. Thermodynamic consistency is verified in Subsection 10.3.2. But let us first explain the modification of the bulk solver, in order to approximate the full Euler system (10.12).

We apply the bulk solver with front tracking for one-dimensional solutions of Chapter 8. The moving mesh scheme of Algorithm 8.2 is applicable to the inviscid Euler system using $\mathbf{W} = \mathbf{W}(x, t) = (\varrho(x, t), m(x, t), E(x, t))^T$ with $E = \varrho e$ and the flux function $\mathbf{F}(\mathbf{W}) = (m, m^2/\varrho + p, (E + p)m/\varrho)^T$.

10.3.1 Experimental order of convergence

We examine grid convergence in one spatial dimension. The verification for radially symmetric solutions is omitted, because we expect the same results as in Example 9.6. The focus lies on the new microsolver and not on the bulk solver. As in Section 9.1, we compare numerical approximations against exact Riemann solutions. The exact solution is given via the \mathbb{k}_2 -micro solution for fixed reference temperature \mathring{T}_∞ and shall be denoted by $\hat{\mathbf{W}} = (\hat{\varrho}, \hat{m}, \hat{E})^T$. Initial states

$$\mathbf{W}(x, 0) = \begin{cases} \mathbf{W}_L & : 0 \text{ m} \leq x < 0.7 \text{ m} \\ \mathbf{W}_R & : 0.7 \text{ m} \leq x \leq 1 \text{ m}. \end{cases}$$

are determined such that the values in Table 10.2 hold. Domain and simulation end time $\theta = 0.8 \text{ ms}$ are chosen such that the waves do not reach the boundary. Furthermore, we use the boundary condition $\mathbf{W}(0, t) = \mathbf{W}_L$, $\mathbf{W}(1, t) = \mathbf{W}_R$, for $t \in (0, \theta)$.

The *relative error* is given by

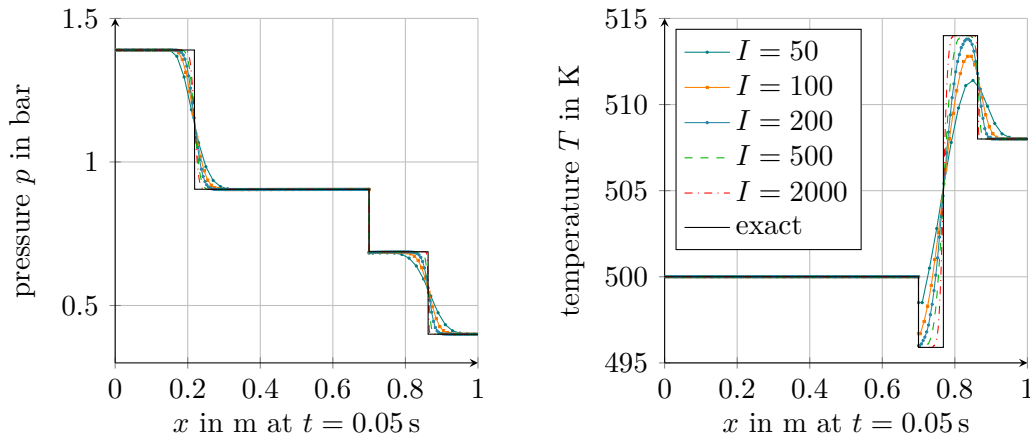
$$e_I = \int_0^\theta \int_{R_{\min}}^{R_{\max}} A_d(r) \left(\frac{|\varrho_I - \hat{\varrho}|}{1 + |\hat{\varrho}|} + \frac{|m_I - \hat{m}|}{1 + |\hat{m}|} + \frac{|E_I - \hat{E}|}{1 + |\hat{E}|} \right) dr dt,$$

where (ϱ_I, m_I, E_I) is the numerical solution on a grid with $I \in \mathbb{N}$ cells. For a sequence of grids with $I_l \in \mathbb{N}$, for $l \in \mathbb{N}$, cells and corresponding relative errors e_{I_l} we compute the *experimental order of convergence*

$$\text{eoc}_l := \frac{\ln(e_{I_l}/e_{I_{l-1}})}{\ln(I_{l-1}/I_l)}.$$

I	Test (f) with $\tilde{M}_{\mathbb{k}_2}$		Test (g) with $\tilde{M}_{\mathbb{k}_2}$		Test (h) with $\tilde{M}_{\mathbb{k}_2}$	
	e_I	eoc	e_I	eoc	e_I	eoc
500	6.4e-04		3.5e-04		6.4e-04	
1000	4.0e-04	0.67	2.4e-04	0.56	4.0e-04	0.67
2000	2.7e-04	0.60	1.6e-04	0.56	2.6e-04	0.60
4000	1.6e-04	0.70	1.1e-04	0.55	1.6e-04	0.72
8000	1.0e-04	0.71	7.5e-05	0.53	9.9e-05	0.71

Table 10.3: Error analysis for initial conditions of Table 10.2.

Figure 10.6: Pressure (left) and temperature distribution (right) of the one-dimensional test case (h) on different grids and the \mathbb{k}_2 -micro solution. Both figure correspond to the same legend.

Note that the number I is the degree of freedom in Algorithm 8.2. The optimal order that can be achieved in view of the first-order scheme and solutions, that contain discontinuities is between 0.5 and 1, cf. [52].

Example 10.19 (Error analysis applying the \mathbb{k} -microsolver).

The tests are performed with a time step restriction that corresponds to (8.6) and $\text{CFL} = 0.9$ and the equations of state for n-dodecane. Table 10.3 demonstrates that the convergence order is in the expected optimal range. The numerical solution for test case (h) at the final time is displayed in Figure 10.6. It shows the numerical approximation for a sequence of refined grids and the (exact) \mathbb{k}_2 -micro solution over the Eulerian space variable. The solution consists of a 1-rarefaction wave, followed by an evaporation wave, a 2-contact wave and a 3-shock wave. Note that all waves are well resolved. With decreasing grid size, \mathbf{W}_I tends to the reference solution.

Note that, on every grid resolution, the phase transition wave remains sharp and it is located at the correct position. This demonstrates that the moving mesh algorithm resolves the phase transition very well with the information of the microsolver, here $\tilde{M}_{\mathbb{k}_2}$.

10.3.2 Global entropy release and steady state solutions

A transient solution should reach its steady state for $t \rightarrow \infty$, at the same time, the total mathematical entropy should be minimized. The mathematical entropy is the (physical)

entropy with a negative sign. In order to apply the model assumptions, we rewrite the total entropy balance equation (2.5) of Section 2.2. Applying the divergence theorem gives

$$\frac{d}{dt} \int_{\Omega_{\text{liq}} \cup \Omega_{\text{vap}}} \varrho \eta \, dv - \int_{\Omega_{\text{liq}} \cup \Omega_{\text{vap}}} \boldsymbol{\varphi} \, dv + \int_{\Gamma} \llbracket \boldsymbol{\varphi} \cdot \mathbf{n} \rrbracket \, da - \int_{\Omega_{\text{liq}} \cup \Omega_{\text{vap}}} \eta_{\Omega} \, dv - \int_{\Gamma} \eta_{\Gamma} \, da = 0.$$

The entropy flux $\boldsymbol{\varphi}$ is neglected in the bulk phases, the second term is therefore zero. The third term is replaced by the latent heat assumption $L(T_{\text{ref}}) = -T_{\text{ref}} \llbracket \boldsymbol{\varphi} \cdot \mathbf{n} \rrbracket / j$. Furthermore, we skip the entropy production terms η_{Ω} and η_{Γ} and integrate the equation over time. This leads to the definition of the total entropy at time $\theta > 0$

$$\begin{aligned} \mathcal{E}(\varrho(\cdot, \theta), \mathbf{m}(\cdot, \theta), e(\cdot, \theta)) := \\ \int_{\Omega_{\text{liq}} \cup \Omega_{\text{vap}}} \varrho \eta \left(\varrho, e - \frac{|\mathbf{m}|^2}{2\varrho} \right) \, dv - \int_0^{\theta} \int_{\Gamma} j \left(\eta_{\text{vap}}^{\text{sat}}(T_{\text{ref}}) - \eta_{\text{liq}}^{\text{sat}}(T_{\text{ref}}) \right) \, da \, dt. \end{aligned}$$

Note that \mathcal{E} increases in time, since production terms are neglected.

We study the time evolution of \mathcal{E} for radially symmetric solutions in \mathbb{R}^3 . The moving mesh scheme of Algorithm 8.2 is applicable using $\mathbf{W} = \mathbf{W}(r, t) = (\varrho(r, t), m(r, t), E(r, t))^{\top}$ with

$$\varrho(\mathbf{x}, t) = \varrho(r, t), \quad \mathbf{m}(\mathbf{x}, t) = \frac{\mathbf{x}}{r} m(r, t) \quad (\varrho e)(\mathbf{x}, t) = E(r, t), \quad |\mathbf{x}| = r$$

instead of (8.1) and the following flux function and (geometric) source term

$$\mathbf{F}(\mathbf{W}) = \left(m, \frac{m^2}{\varrho} + p, \frac{(E + p)m}{\varrho} \right)^{\top}, \quad \mathbf{Q}(\mathbf{W}) = (0, p, 0)^{\top}.$$

Remark 10.20 (Conservation properties and preserving of isolated phase boundaries). The scheme conserves total mass and total energy for $d \in \{1, 2, 3\}$. The proof of energy conservation is analog to the proof mass conservation in Lemma 8.3. For momentum conservation we refer to Remark 8.4.

Furthermore, isolated phase boundaries are preserved in the sense of Lemma 8.5.

Example 10.21 (Entropy evolution of the complete method).

We want to study the time evolution of the total entropy and the influence of different choices of the reference temperature \dot{T} in (10.23). We apply equations of state for n-dodecane, initial conditions that satisfy

$$(p, v, T)(r, 0) = \begin{cases} (1.4 \text{ bar}, 0 \text{ m/s}, 230 \text{ }^{\circ}\text{C})^{\top} & \text{for } 0.1 \text{ m} \leq r \leq 0.4 \text{ m}, \\ (0.8 \text{ bar}, 0 \text{ m/s}, 230 \text{ }^{\circ}\text{C})^{\top} & \text{for } 0.4 \text{ m} < r \leq 1.0 \text{ m}, \end{cases}$$

kinetic relation \mathbb{k}_2 with $k^* = 30 \text{ m}^4/\text{kg s}$ and $\zeta^* = 2000 \text{ N/m}$. The problem is considered in \mathbb{R}^3 such that one may think of an (artificial) large n-dodecane droplet with artificial high surface tension. The time step is restricted with $\text{CFL} = 0.5$. We apply reflecting boundary conditions (10.13), such that there is neither mass nor energy exchange through the outer boundary.

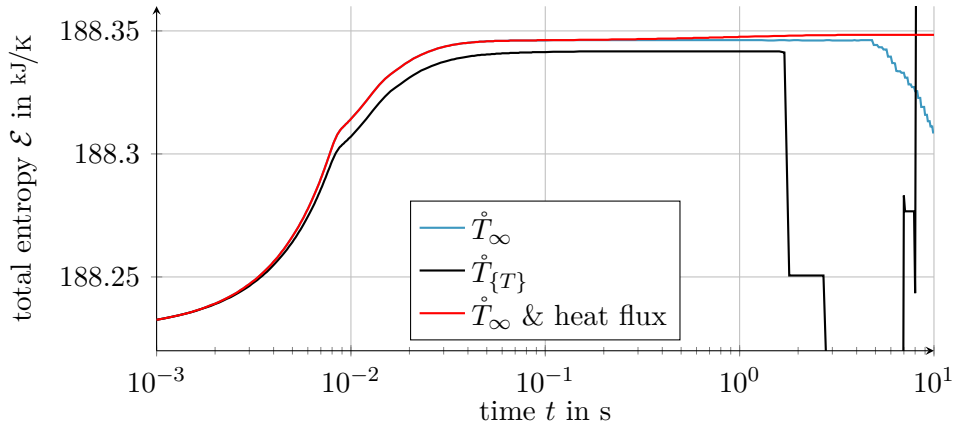


Figure 10.7: Time evolution of the total entropy for different choices of the reference temperature. The red line refers to a solution of the modified numerical model of Definition 10.22.

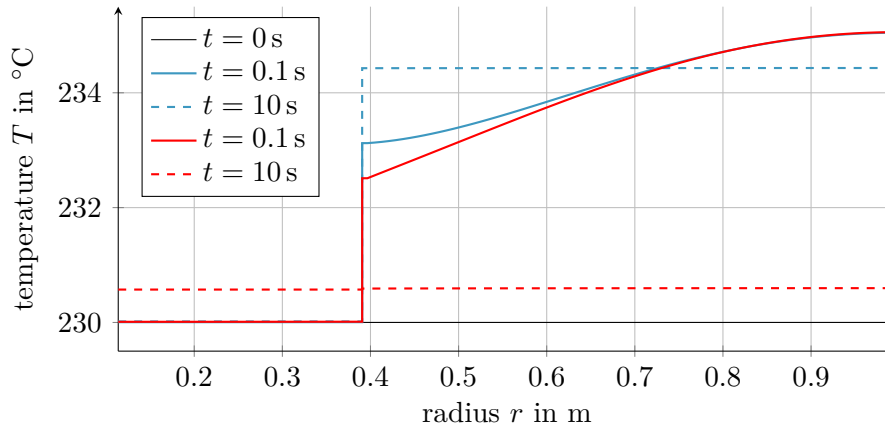


Figure 10.8: Temperature distribution at different time steps. The blue lines refer to the solution of the non-isothermal model of Definition 10.8 and the red lines to the modified numerical model of Definition 10.22.

Two configurations for the reference temperature are compared: a constant value $T_{\text{ref}} = \dot{T}_{\infty} = 230^{\circ}\text{C}$ ($L(\dot{T}_{\infty}) = 247345 \text{ J/kg}$) over time and adaptation at every evaluation of \dot{M}_{k_2} by the mean value of the input states $T_{\text{ref}} = \dot{T}_{\{T\}}$, see (10.23). Note that the latter choice changes the entropy contribution, since $L(\dot{T}_{\{T\}})$ is not constant.

Figure 10.7 shows the evolution of the total entropy $t \rightarrow \mathcal{E}(\rho, \mathbf{m}, e)$ for $I = 100$ cells. The total entropy increases in time and reaches a local maximum for $t = 1$ s. The numerical solution is almost static, but there remains a difference in the temperature of 4.4°C at the phase boundary, see Figure 10.8. This was expected, since static solutions are not necessarily in thermodynamic equilibrium, see Lemma 10.10.

For $t > 1$ s, the numerical solution behaves unstable. The total entropy in Figure 10.7 decreases (case \dot{T}_{∞}) or jumps (case $\dot{T}_{\{T\}}$). Note that there is no unique static solution, see Lemma 10.10. In case of $\dot{T}_{\{T\}}$, the k-microsolver stopped without reaching the tolerance.

We have seen in the last example and Lemma 10.10, that the non-isothermal model provides no unique static solution. Figure 10.8 shows, that the temperature is discontinuities at the interface. We assume, that this is caused by the lack of thermal diffusion

and propose a modification of the numerical non-isothermal model. The modification is motivated by Fourier's law (10.7) and compensates thermal differences. In order to compare with Example 10.21, the modification applies only the flux across the phase boundary. We adopt the notation of Chapter 8.

Definition 10.22 (Numerical model with interfacial heat flux).

Let $\{\mathbf{W}_i^n \mid n \in \mathbb{N}, 0 \leq i \leq I\}$ be a family of states at time t^n and let a numerical approximation $q^{diff} = q^{diff}(\mathbf{W}_{i-1}^n, \mathbf{W}_i^n)$ of the heat flux (10.7) be given.

Replace the flux (8.5) in Chapter 8 by

$$\mathbf{F}_{i,-/+}^n = \begin{cases} \mathbf{F}_{num}(\mathbf{W}_{i-1}^n, \mathbf{W}_i^n) & \text{for } i \neq i_\gamma^n, \\ \mathbf{F}(\mathbf{W}_{-/+}^n) - s^n \mathbf{W}_{-/+}^n + (0, 0, q^{diff}(\mathbf{W}_{i-1}^n, \mathbf{W}_i^n))^\top & \text{for } i = i_\gamma^n, \end{cases}$$

where i_γ^n is the index of the phase boundary edge.

Example 10.23 (Entropy evolution with interfacial heat flux).

Consider the setting of Example 10.21. We apply the modification of Definition 10.22 with $\alpha = 100 \text{ W/m K}$.

The entropy evolution for $t < 1 \text{ s}$ is the same as in Example 10.21, see Figure 10.7. The dynamics is here governed by mechanical forces, e.g., the numerical solution shows pressure differences and we observe bulk waves.

For $t > 1 \text{ s}$, temperature differences across the interface are compensated (Figure 10.8 red lines) by the heat flux. The total entropy raises to a higher level (Figure 10.7), where the numerical solution remains static with states in the global thermodynamic equilibrium.

The examples show that the total entropy of (stable) numerical solutions increases in time. Adding heat flux as in Definition 10.22 leads to stable transient solutions, that are in thermodynamic equilibrium. Furthermore, the total entropy reaches a high level.

10.4 Validation with shock tube experiments

This section addresses the validation of the \mathbb{k} -micro solutions and the complete method against shock tube experiments. We compare with published data for explosive evaporation/boiling for the fluids n-dodecane, butane and propane. The fluids belong to the class of alkanes and we assume that the kinetic relation K_2 , adapted as in Example 6.13 with parameters k^* from density functional theory, provides good approximations.

In the first subsection, we consider pure \mathbb{k} -micro solutions. In the second subsection, the combination of bulk solver and \mathbb{k} -microsolvers is validated with the experimental data.

10.4.1 Validation of \mathbb{k} -micro solutions

We consider propagation speeds of pure Riemann solutions. In the first example the temperature is kept constant and we compare a series of different vapor pressure values. In the second example, also the temperature difference in the initial states varies.

Example 10.24 (Dodecane shock tube experiments).

We consider again the shock tube experiment described in Section 6.3. Liquid n-dodecane

at saturation condition is expanded into a low pressure vapor reservoir. The initial temperature in both phases is $T = 230^\circ\text{C}$, but now, the temperature distribution of the \mathbb{k} -micro solutions may vary.

The propagation speeds of evaporation waves for different kinetic relations and the measured values are depicted in Figure 10.9. We are particularly interested in the pressure range from almost vacuum to $p_R = 0.7$ bar, where Simoes-Moreira and Shepherd [68] observed stable evaporation fronts. The propagation speed from almost vacuum to $p_R = 0.4$ bar is nearly constant and tends to zero in $p_R = 0.7$ bar.

The propagation speed in \mathbb{k}_1 -micro solutions is overestimated opposed to the measurements. The values are the same as in the isothermal Example 6.17, except for low pressure values. At the lowest value $p_R = 0.01$ bar the speed is even negative. We believe that the lack of heat conduction is the reason for this behavior, see Subsection 10.4.2 below.

We apply K_{dtf} from Example 6.13, that is nothing but K_2 with $k^* = 28 \text{ m}^2/\text{kg s}$, and K_3 with $k^* = 0.1 \text{ m}^6/\text{kg}^2$. The computed propagation speeds match the experimental measurements for $0.1 \text{ bar} \leq p_R \leq 0.5 \text{ bar}$, see Figure 10.9. Note that both kinetic relations lead to almost the same result in terms of evaporation speeds. For higher pressure values $p_R > 0.6$ bar, we observe a linear decrease of the evaporation front speed. This should be due to the assumed micro-scale model, because static phase boundaries under non-saturated conditions would require a different kinetic relation, cf. Remark 6.8.

Example 10.25 (Butane and propane evaporation experiments).

Reinke and Yadigaroglu [65] investigated the explosive boiling of various liquids and developed a correlation for the evaporation front speed s (U_{fr} in [65]) based on their experiments. They expanded experimentally a saturated liquid at superheated temperatures to a state at ambient conditions. Based on the experimental data they correlated the front speed using the nominal superheat $\Delta T_{\text{nom}} := T_L - T^{\text{sat}}(1 \text{ bar})$ as dependent variable. For butane one finds $T^{\text{sat}}(1 \text{ bar}) = 272.3 \text{ K}$ and for propane $T^{\text{sat}}(1 \text{ bar}) = 230.74 \text{ K}$.

We compare the evaporation front speeds for butane and propane during the expansion process for various initial superheats. More precisely, the initial conditions are such that the liquid is on the left hand side and

$$(p, v, T)(x, 0) = \begin{cases} (p^{\text{sat}}(T_L), 0 \text{ m/s}, T_L)^{\top} & \text{for } x \leq 0, \\ (1 \text{ bar}, 0 \text{ m/s}, T^{\text{sat}}(1 \text{ bar}))^{\top} & \text{for } x > 0 \end{cases}$$

holds, for the temperature values $T_L > T^{\text{sat}}(1 \text{ bar})$ in Figure 10.10. Note that, except of the phase boundary, both phases are initially in thermodynamic equilibrium. The temperature dependent values for the entropy production coefficient k^* in K_2 are determined as in Example 6.13, with respect to the reduced temperature corresponding to T_L .

The numerical results are plotted in Figure 10.10 together with the experimental measurements of Reinke and Yadigaroglu [65] and their linear regression line. The \mathbb{k}_{dtf} -micro solutions show increasing temperature differences $T_{\text{liq}} - T_{\text{vap}}$ up to 10 K at the phase boundary for rising the liquid initial temperature T_L . We applied two different values for the reference temperature: $T_{\text{ref}}^1 := \{T\}$ and T_{ref}^2 with higher weights for the temperature T_L .

The results with T_{ref}^2 and $T_L > 310 \text{ K}$ for butane, $T_L > 265 \text{ K}$ for propane are within the 80% confidence limits of the experiments. The trend of the increasing front speeds for increasing superheats is covered by the Riemann solutions.

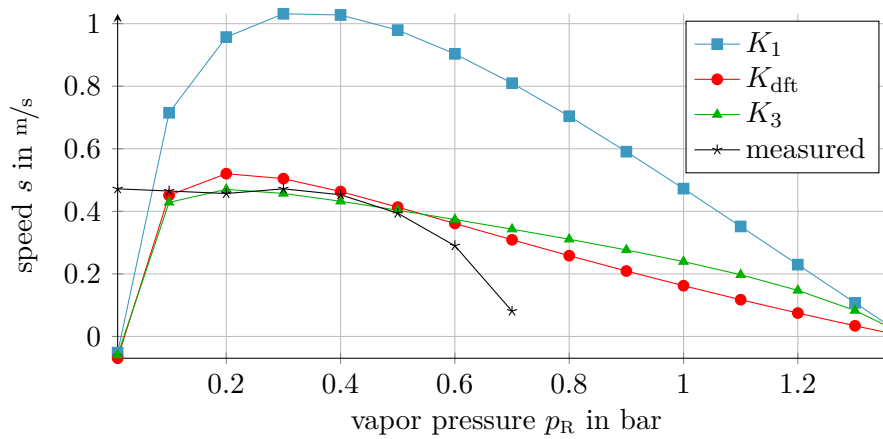


Figure 10.9: Comparison of evaporation front speeds for n-dodecane and for different initial vapor pressure values p_R . In black, the measured values from [68]. The colored lines refer to interface speeds of \mathbb{k}_i -micro solutions with $i \in \{1, 2, 3\}$.

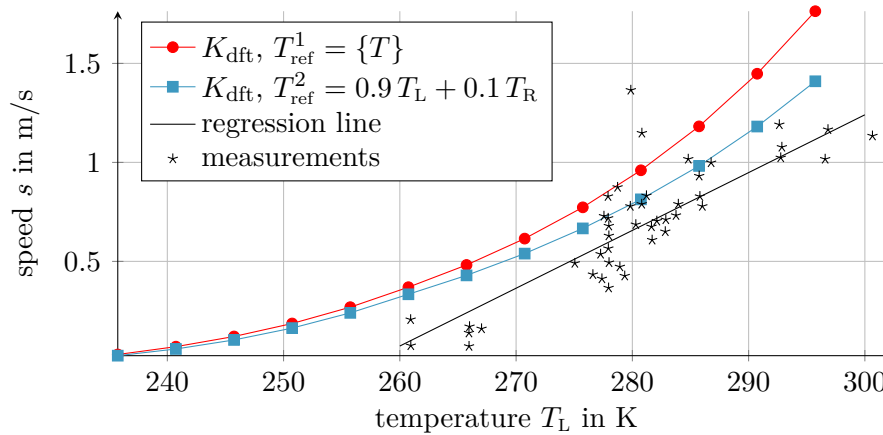
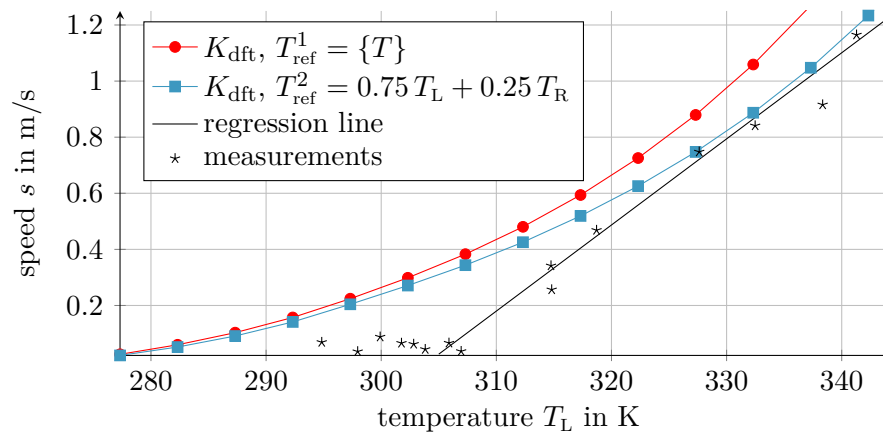


Figure 10.10: Speed of the boiling front for butane (top) and propane (bottom). In black, measured values and line of best fit from [65]. In red the interface speed of the \mathbb{k}_{dft} -micro solutions.

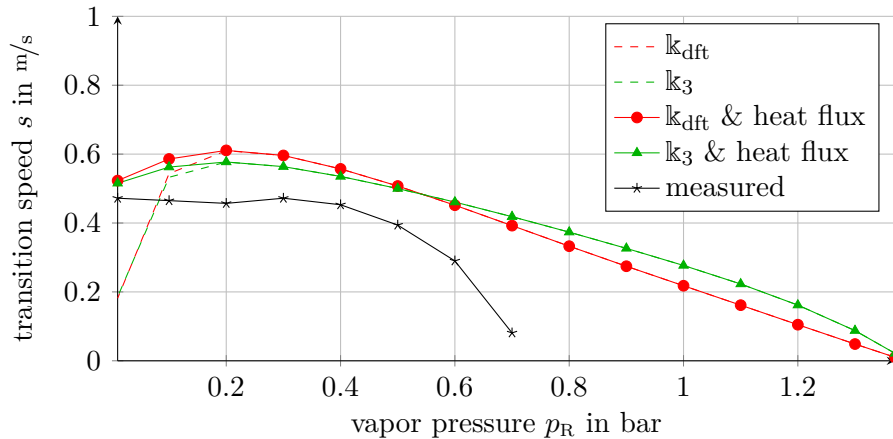


Figure 10.11: Comparison of evaporation front speeds for n-dodecane and for different initial vapor pressure values p_R . In black, the measured values from [68]. The dashed lines refer to the complete method without heat flux and the colored solid lines to modified numerical model of Definition 10.22.

As in the n-dodecane examples, static phase boundaries occurred under non-saturated conditions. That explains the overestimated front speeds at low temperature differences. To summarize, the results are very convincing, in particular, in view of the highly temperature driven experimental setting.

10.4.2 Validation of the complete method

We proceed with the validation of the complete method and, in partially, answering the question if the loss of speed for low pressure values p_R in Example 10.24 stems from the lack of heat conduction. Thus, we consider again the n-dodecane experiments, described in Section 6.3.

Example 10.26 (Dodecane shock tube experiments).

We use initial conditions as in Example 10.24, i.e. saturated liquid on the left hand side and the vapor pressure values p_R in Figure 10.11 on the right hand side. The reference temperature (10.23) is chosen to be the initial temperature: $\bar{T}_\infty = 230^\circ\text{C}$. At the left end of the domain we use reflecting boundary conditions (10.13). At the right boundary, where in the experimental facility the low pressure chamber was mounted, we apply the outflow condition $\mathbf{F}_{I+1,-}^n = \mathbf{F}(\mathbf{W}_I^n)$. The one-dimensional computational domain has the length of 1 m and is decomposed in $I = 100$ cells. The phase boundary is initially places at the center of the domain and we compare the results after 0.1 s. The time step is restricted with $\text{CFL} = 0.9$.

Figure 10.11 shows the propagation speed of the numerical solution (actually the arithmetic mean within the last 0.02s) and the measured front speed of the experiment. The numerical solution is computed with the complete method and the microsolvors $\tilde{M}_{k_{\text{dft}}}$ (red dashed line) and \tilde{M}_{k_3} with $k^* = 0.1 \text{ m}^6/\text{kg}^2$ (green dashed line). As in Example 10.24, the evaporation speed strongly reduces for p_R towards zero. The evaporation speeds for $0.1 \text{ bar} \leq p_R \leq 0.6 \text{ bar}$ are slightly overestimated. This was also observed in the isothermal setting of Example 9.11.

We apply now the modification of Definition 10.22 to relax temperature difference at the phase boundary. The results for $\alpha = 300 \text{ W/m K}$ are depicted in Figure 10.11 (colored solid lines). The front speed values are unchanged for $p_R \geq 0.2$, here temperature differences are negligible. More important, we find non-decreasing speed values, which fit much better to the experimental measurements near the vacuum state.

This demonstrates the reliability of the non-isothermal model and the corresponding microsolvors as long as low temperature difference occur. On the other hand, the model may predict nonphysical high temperature jumps at the phase boundary.

10.5 Shock-droplet interaction

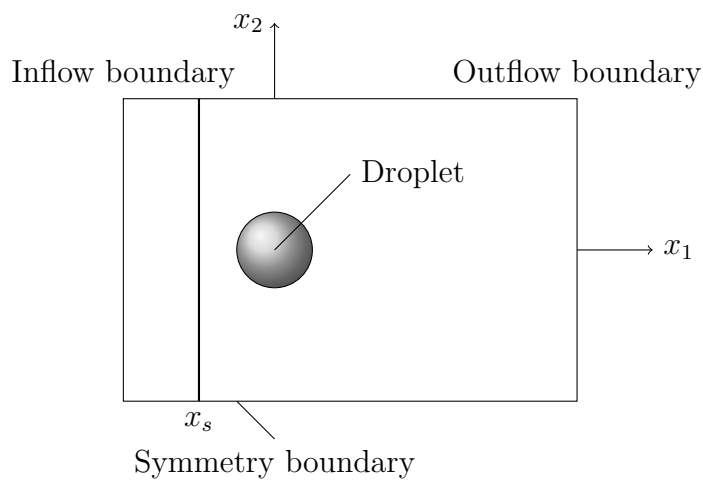
Many microsolvors have been presented in this work. They are tested and successfully validated with the bulk solver for radially symmetric solutions of Chapter 8. However, the actual purpose of these microsolvors is the application in really multidimensional schemes. This was not part of this work but we want to show one of these applications.

In the joint work [30], we apply the non-isothermal k-microsolver of Algorithm 10.12 within the framework of a two-dimensional *discontinuous Galerkin scheme with sub-cell resolution*. The scheme was developed by Stefan Fechter and applies a ghost fluid technique [31] to couple microsolver and bulk solver. Here we quote the last example of the joint publication [30].

[...] This test case is used to validate of correct wave propagation at the interface in a compressible flow field. A shock wave of Mach number 1.2 is impinging onto a n-dodecane droplet at rest. The impinging shock wave is partially reflected on the droplet surface and is partially transmitted into the droplet. Inside the droplet the shock wave travels at a higher speed due to the higher sound velocity in the liquid phase. Due to the post-shock momentum of the flow, the droplet gets deformed.

The initial conditions and the computational domain used for the simulation are defined as in Figure 10.12. Initially the shock is placed at $x_s = -1.5 \text{ mm}$ within the computational domain of $[-2.5, -5] \times [7.5, 5] \text{ mm}$. The shock-droplet interaction is calculated as two-dimensional test case with 240 DOF in each direction. The initial conditions are chosen so that the droplet evaporates at the pre-shock conditions.

Figure 10.13 provides an explanation of the shock structures that are visible in the shock-droplet interaction. The results at different time instances plotted in Figures 10.14 and 10.15 reproduce the characteristics of shock-droplet interactions without resolved phase transition effects. Due to the resolved phase transition effects an additional shock wave can be seen in the solution. This wave is due to the initial evaporation of the droplet in the pre-shock state. The numerical approach detects the evaporation and condensation regimes accordingly on the droplet surface. Due to the impinging shock wave, the surrounding gas conditions are changed so that condensation instead of evaporation takes place. Note that evaporation and condensation may occur at the same time at different locations on the droplet surface. [...]



Initial conditions:

Vapor:

$$(\rho, \mathbf{v}, p) = \begin{cases} (6.272 \text{ kg/m}^3, (47.85, 0, 0)^\top \text{ m/s}, 1.45 \text{ bar}) & \text{if } x_1 \leq x_s \\ (4.383 \text{ kg/m}^3, (0, 0, 0)^\top \text{ m/s}, 1.0 \text{ bar}) & \text{else.} \end{cases}$$

Liquid:

$$(\rho, \mathbf{v}, p) = (584.01 \text{ kg/m}^3, (0, 0, 0)^\top \text{ m/s}, 1.3 \text{ bar})$$

Figure 10.12: Initial setting for the shock-droplet interaction test case for a n-dodecane droplet interacting with a Mach 1.2 shock wave. The initial shock position is $x_s = -0.15$ mm.

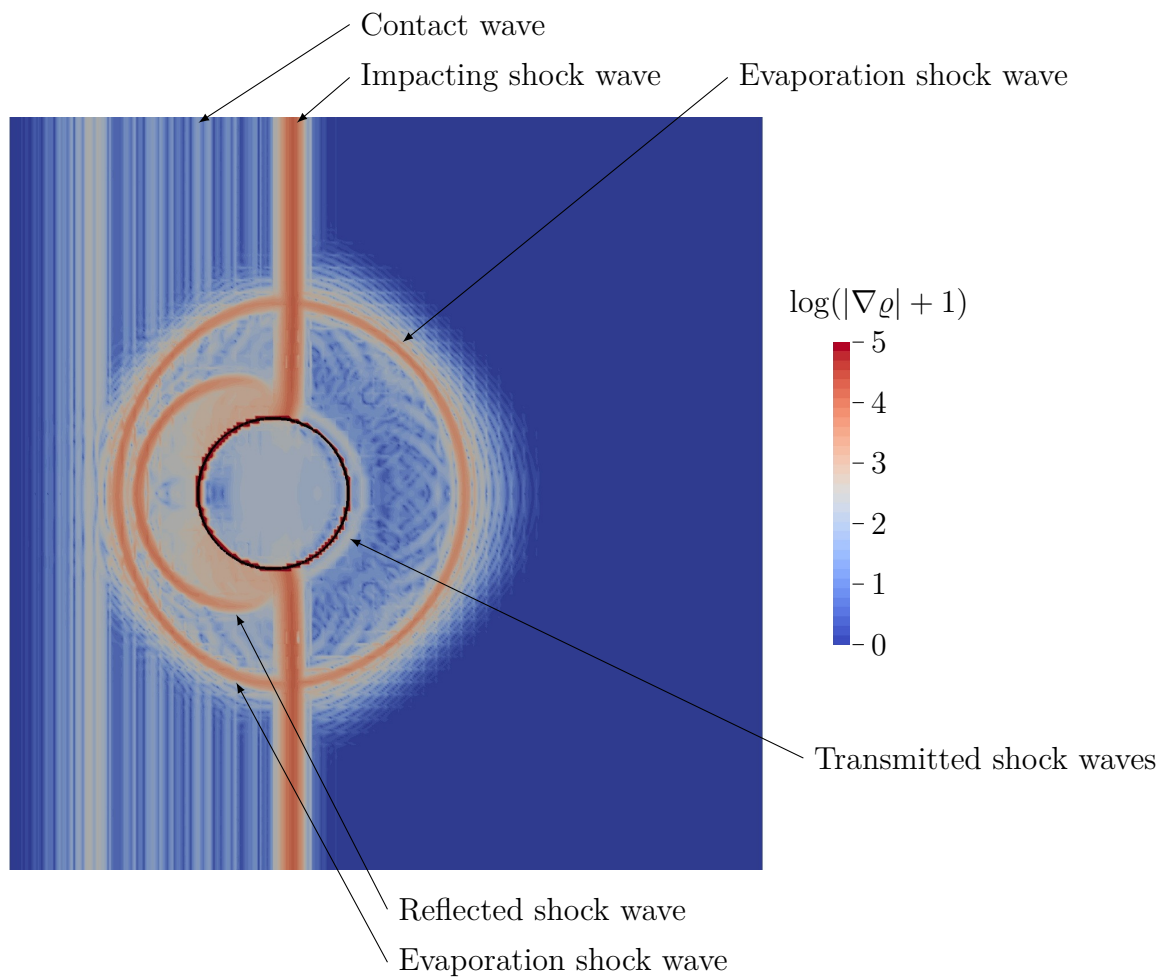


Figure 10.13: Illustration of the wave structure for the shock-droplet interaction test case with evaporation at $t = 0.1$ ms. The black line shows the position of the phase interface.

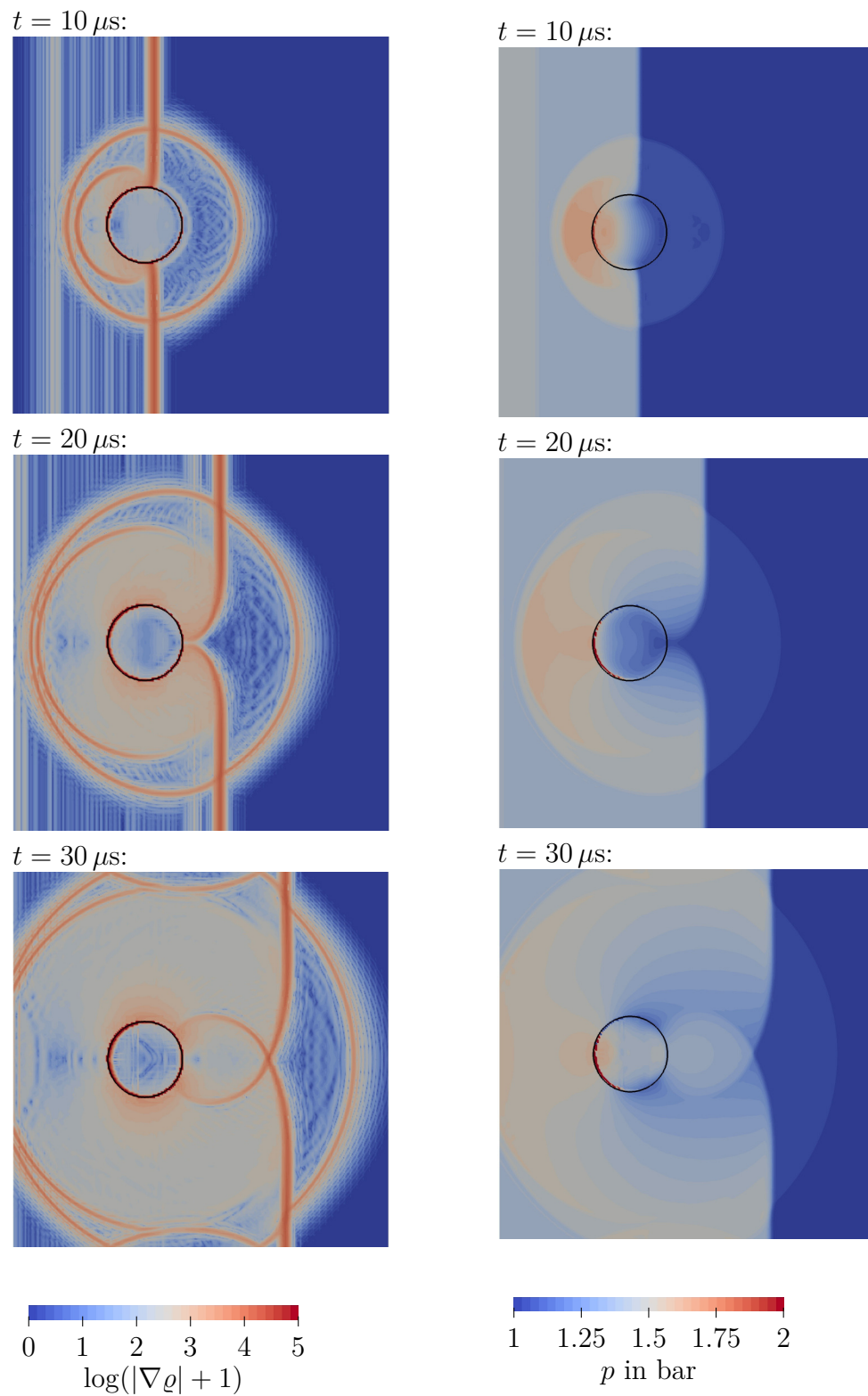


Figure 10.14: The shock-droplet interaction for different times. The black solid line indicates the interface position as determined by the level-set method. Left: Logarithmic density gradient visualization. Right: Pressure visualization.

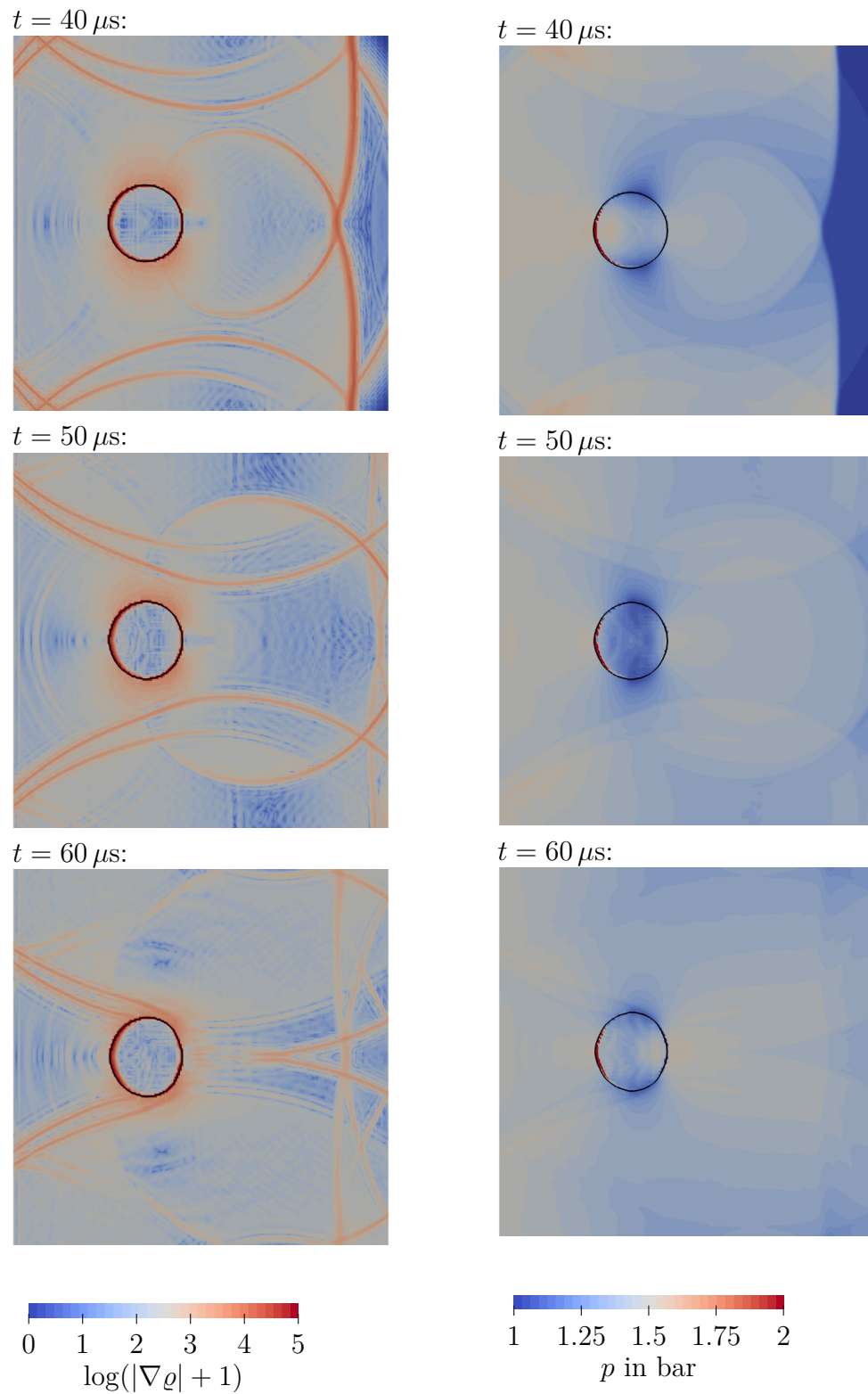


Figure 10.15: The shock-droplet interaction for different times. The black solid line indicates the interface position as determined by the level-set method. Left: Logarithmic density gradient visualization. Right: Pressure visualization.

10.6 Conclusion on the non-isothermal method

Let us first note that the presented compressible and temperature dependent two-phase model of Definition 10.8 is a novelty on its own. It regards latent heat and permits thermodynamically consistent static solutions. Although the selected constitutive assumption for absorption and release of latent heat is rather simple, the numerical solutions are in good agreement to real world experiments.

Riemann solvers for compressible and temperature dependent two-phase flows are new. The presented solver works properly even for equations of state of real fluids. The algorithm of the \mathbb{k} -microsolver is extreme flexible concerning different constitutive laws for latent heat or kinetic relations and equations of state. In particular, interface conditions, that prevent static solutions with temperature jump, would be an interesting enhancement.

The complete method was numerically validated in Example 10.19. The order of convergence was in the expected optimal range. The global physical entropy increases in time, as long as numerical solutions are stable, see Example 10.21. Numerical solution may develop instabilities, since static solutions are not unique, see Lemma 10.10. Furthermore, the model admits temperature jumps at the interface, that seem to be nonphysical. However, for solutions with low temperature differences at the phase boundary, the measured data of the shock tube experiments in Subsection 10.4 are met very well. The discrepancy for high temperature differences are not surprisingly, since heat conduction was generally neglected.

We introduced in Definition 10.22 a modification of the numerical model, that relaxes temperature differences at the phase boundary. In Example 10.23, this modification led to numerical results with global entropy production towards stable static solutions in thermodynamic equilibrium. Furthermore, this combination leads to better agreements with shock tube experiments, as shown in Example 10.26.

Most notably, we can answer the question of kinetic relations in nature, for the case of fast evaporating alkanes. Section 10.4 demonstrated that the numerical solution with kinetic relations predicted by density functional theory (cf. Example 6.13) match with the experiments. This is, without doubt, the correct kinetic relation and moreover confirms the high quality of the presented sharp interface model for the dynamics of liquid vapor flows. But note that the corresponding kinetic functions are non-decreasing, such that the theory from the literature does not apply here.

Chapter 11

Conclusion and outlook

We developed microsolvers and analyzed interface models for liquid vapor flows with phase transitions under the presence of capillary forces. The presented models and solvers are numerically verified, thermodynamically consistent and successfully validated against real world measurements.

We generally demonstrated that the sharp interface approach with the proposed macro and micro-scale coupling and the surface tension treatment is successful. Regarding curvature effects exclusively in the (formally one-dimensional) microsolvers is an appropriate way to take capillary forces into account. That holds also for the fully multidimensional case. It was not shown here, but in several joint works [27, 30, 40] (see also [26, Chapter 7]), with different multidimensional bulk solvers developed by our colleagues. The reason for the limitation to moderate amounts of surface tension is the lack of adequate equations of state, as they are fitted to measurements regardless of surface tension, see Remark 2.7. Higher amounts of surface tension would require enhanced pressure laws or an approach that does not rely on equations of state. Note that, the restriction does not apply to the microsolvers itself. The same holds for the complete method, as long as curvature is measurable on the macro-scale.

Well-posedness results for the isothermal micro solutions were presented. These tasks are missing in the non-isothermal case. The development for the temperature dependent case is just at its beginnings. We introduced an adapted two-phase Euler model in order to satisfy thermodynamic consistency requirements. The numerical results are in agreement with experiments, but theoretical results are fully missing.

An open question was the physically correct kinetic relation. The comparison with evaporation experiments showed great correspondence for numerical solutions of two-phase models with non-decreasing kinetic functions. Classical well-posedness analysis [47] for mixed hyperbolic-elliptic problems assumes that kinetic functions are monotone decreasing. Theory and microsolvers for more general kinetic relations are necessary. Due to Remark 6.14 that should be possible without losing the monotonicity property of the generalized Lax curves.

Bibliography

- [1] R. Abeyaratne and J. K. Knowles. *Evolution of phase transitions: a continuum theory*. Cambridge University Press, 2006.
- [2] R. Abeyaratne and J. K. Knowles. “On the driving traction acting on a surface of strain discontinuity in a continuum”. *Journal of the Mechanics and Physics of Solids* 38.3 (1990), pp. 345–360.
- [3] D. M. Anderson, G. B. McFadden, and A. A. Wheeler. “Diffuse-interface methods in fluid mechanics”. *Annual Review of Fluid Mechanics* 30.1 (1998), pp. 139–165.
- [4] T. Aslam. “A level set algorithm for tracking discontinuities in hyperbolic conservation laws II: systems of equations”. *Journal of Scientific Computing* 19.1-3 (2003), pp. 37–62.
- [5] E. Axdaahl (en>User:Axda0002). *Cavitation damage evident on the propeller of a personal watercraft*. Creative Commons Attribution-Share Alike License v. 2.5. Wikimedia Commons. URL: https://commons.wikimedia.org/wiki/File:Cavitation_Propeller_Damage.JPG (visited on 07/19/2015).
- [6] I. H. Bell, J. Wronski, S. Quoilin, and V. Lemort. “Pure and Pseudo-pure Fluid Thermophysical Property Evaluation and the Open-Source Thermophysical Property Library CoolProp”. *Industrial & Engineering Chemistry Research* 53.6 (2014), pp. 2498–2508.
- [7] S. Benzoni-Gavage and H. Freistühler. “Effects of surface tension on the stability of dynamical liquid-vapor interfaces”. *Archive for Rational Mechanics and Analysis* 174.1 (2004), pp. 111–150.
- [8] B. Boutin and C. Chalons. “Convergent and conservative schemes for nonclassical solutions based on kinetic relations. I”. *Interfaces and Free Boundaries* 10 (2008), pp. 399–421.
- [9] J. U. Brackbill, D. Kothe, and C. Zemach. “A continuum method for modeling surface tension”. *Journal of Computational Physics* 100.2 (1992), pp. 335–354.
- [10] C. E. Brennen. *Cavitation and bubble dynamics*. Oxford University Press, 1995.
- [11] F. Caro, F. Coquel, D. Jamet, and S. Kokh. “A simple finite-volume method for compressible isothermal two-phase flows simulation”. *International Journal on Finite Volumes* 3 (2006), pp. 1–37.
- [12] C. Chalons, F. Coquel, P. Engel, and C. Rohde. “Fast Relaxation Solvers for Hyperbolic-Elliptic Phase Transition Problems”. *SIAM Journal on Scientific Computing* 34.3 (2012), pp. A1753–A1776.

- [13] C. Chalons, P. Engel, and C. Rohde. “A Conservative and Convergent Scheme for Undercompressive Shock Waves”. *SIAM Journal on Numerical Analysis* 52.1 (2014), pp. 554–579.
- [14] C. Chalons. “Transport-equilibrium schemes for computing nonclassical shocks. Scalar conservation laws”. *Numerical Methods for Partial Differential Equations* 24.4 (2008), pp. 1127–1147.
- [15] C. Chalons, F. Coquel, and C. Marmignon. “Well-balanced time implicit formulation of relaxation schemes for the Euler equations”. *SIAM Journal on Scientific Computing* 30.1 (2008), pp. 394–415.
- [16] C. Chalons and P. G. LeFloch. “Computing undercompressive waves with the random choice scheme. Nonclassical shock waves”. *Interfaces and Free Boundaries* 5.2 (2003), pp. 129–158.
- [17] C. Chen and H. Hattori. “Exact Riemann solvers for conservation laws with phase change”. *Applied Numerical Mathematics* 94 (2015), pp. 222–240.
- [18] I.-L. Chern, J. Glimm, O. McBryan, B. Plohr, and S. Yaniv. “Front tracking for gas dynamics”. *Journal of Computational Physics* 62.1 (1986), pp. 83–110.
- [19] R. M. Colombo and F. S. Priuli. “Characterization of Riemann Solvers for the Two Phase p-System”. *Communications in Partial Differential Equations* 28.7-8 (2003), pp. 1371–1389.
- [20] C. M. Dafermos. *Hyperbolic conservation laws in continuum physics*. 3rd ed. Springer, 2010.
- [21] C. M. Dafermos. “The entropy rate admissibility criterion for solutions of hyperbolic conservation laws”. *Journal of Differential Equations* 14.2 (1973), pp. 202–212.
- [22] Davidhv22. *Cavitation generated by a water propeller*. Creative Commons Attribution-Share Alike License v. 4.0. Wikimedia Commons. URL: <https://commons.wikimedia.org/wiki/File:Cavitacion.jpg> (visited on 03/11/2016).
- [23] J.-M. Delhayé, M. Giot, and M. L. Riethmüller. *Thermohydraulics of two-phase systems for industrial design and nuclear engineering*. Ed. by J.-M. Delhayé. Hemisphere Publishing Corporation, 1981.
- [24] A. Dressel and C. Rohde. “A finite-volume approach to liquid-vapour fluids with phase transition”. In: *Finite volumes for complex applications V*. ISTE, London, 2008, pp. 53–68.
- [25] J. Dunning-Davies. *Concise Thermodynamics: Principles and Applications in Physical Science and Engineering*. Horwood, 2007.
- [26] P. Engel. “Numerical methods for sharp-interface dynamics of phase boundaries”. PhD thesis. Universität Stuttgart, Nov. 2012.
- [27] S. Fechter, F. Jaegle, M. Boger, C. Zeiler, C.-D. Munz, and C. Rohde. “A discontinuous Galerkin based multiscale method for compressible multiphase flow”. In: *Seventh International Conference on Computational Fluid Dynamics (ICCFD7)*. Big Island, Hawaii, 2012.

- [28] S. Fechter, F. Jaegle, and V. Schleper. “Exact and approximate Riemann solvers at phase boundaries”. *Computers & Fluids* 75 (2013), pp. 112–126.
- [29] S. Fechter and C.-D. Munz. “A discontinuous Galerkin-based sharp-interface method to simulate three-dimensional compressible two-phase flow”. *International Journal for Numerical Methods in Fluids* 78.7 (2015), pp. 413–435.
- [30] S. Fechter, C.-D. Munz, C. Rohde, and C. Zeiler. “A sharp interface method for compressible liquid-vapor flow with phase transition and surface tension”. Submitted to *Journal of Computational Physics*.
- [31] R. P. Fedkiw, T. Aslam, B. Merriman, and S. Osher. “A non-oscillatory Eulerian approach to interfaces in multimaterial flows (the ghost fluid method)”. *Journal of Computational Physics* 152.2 (1999), pp. 457–492.
- [32] E. Godlewski and P.-A. Raviart. *Numerical approximation of hyperbolic systems of conservation laws*. Springer, 1996.
- [33] E. Godlewski and N. Seguin. “The Riemann problem for a simple model of phase transition”. *Communications in Mathematical Sciences* 4.1 (2006), pp. 227–247.
- [34] M. E. Gurtin. “On a theory of phase transitions with interfacial energy”. *Archive for Rational Mechanics and Analysis* 87.3 (1985), pp. 187–212.
- [35] M. Hantke, W. Dreyer, and G. Warnecke. “Exact solutions to the Riemann problem for compressible isothermal Euler equations for two-phase flows with and without phase transition”. *Quarterly of Applied Mathematics* 71 (2013), pp. 509–540.
- [36] H. Hattori. “The Riemann problem for a van der Waals fluid with entropy rate admissibility criterion—isothermal case”. *Archive for Rational Mechanics and Analysis* 92.3 (1986), pp. 247–263.
- [37] H. Hattori. “The Riemann problem for thermoelastic materials with phase change”. *Journal of Differential Equations* 205.1 (2004), pp. 229–252.
- [38] C. B. Herbert. *Thermodynamics and an Introduction to Thermostatistics*. Wiley, 1985.
- [39] C. W. Hirt and B. D. Nichols. “Volume of fluid (VOF) method for the dynamics of free boundaries”. *Journal of Computational Physics* 39.1 (1981), pp. 201–225.
- [40] F. Jaegle, C. Rohde, and C. Zeiler. “A multiscale method for compressible liquid-vapor flow with surface tension”. *ESAIM: Proceedings* 38 (2012), pp. 387–408.
- [41] K. Jittorntrum. “An implicit function theorem”. *Journal of Optimization Theory and Applications* 25.4 (1978), pp. 575–577.
- [42] E. Johannessen, J. Gross, and D. Bedeaux. “Nonequilibrium thermodynamics of interfaces using classical density functional theory”. *The Journal of Chemical Physics* 129.18, 184703 (2008).
- [43] D. D. Joseph and Y. Y. Renardy. *Fundamentals of two-fluid dynamics. Part I: Mathematical theory and applications*. Vol. 3. 1993.
- [44] B. Kabil. “Analysis of Liquid-Vapor Interfaces and Periodic Waves in Dynamical Lattice Systems”. PhD thesis. Universität Stuttgart. Submitted.

- [45] B. Kabil and C. Rohde. “The Influence Of Surface Tension And Configurational Forces On The Stability Of Liquid-Vapor Interfaces”. *Nonlinear Analysis: Theory, Methods & Applications* 107 (2014), pp. 63–75.
- [46] L. D. Landau and E. M. Lifšic. *Hydrodynamik*. 5th ed. Harri Deutsch, 2007.
- [47] P. G. LeFloch. *Hyperbolic systems of conservation laws*. Lectures in Mathematics ETH Zürich. The theory of classical and nonclassical shock waves. Birkhäuser Verlag, 2002.
- [48] P. G. LeFloch and M. D. Thanh. “Non-classical Riemann solvers and kinetic relations. II. An hyperbolic-elliptic model of phase-transition dynamics”. *Proceedings of the Royal Society of Edinburgh: Section A Mathematics* 132.01 (2002), pp. 181–219.
- [49] P. G. LeFloch and M. D. Thanh. “Properties of Rankine-Hugoniot curves for van der Waals fluids”. *Japan Journal of Industrial and Applied Mathematics* 20.2 (2003), pp. 211–238.
- [50] E. W. Lemmon and M. L. Huber. “Thermodynamic properties of n-dodecane”. *Energy & Fuels* 18.4 (2004), pp. 960–967.
- [51] R. J. LeVeque. *Finite volume methods for hyperbolic problems*. Cambridge University Press, 2007.
- [52] R. J. LeVeque. *Numerical methods for conservation laws*. 2nd ed. Birkhäuser, 1992.
- [53] S. Levy. *Two-phase flow in complex systems*. Wiley, 1999.
- [54] S. Li. “WENO Schemes for Cylindrical and Spherical Grid”. In: *Proceedings of the 2006 International Conference on Scientific Computing (CSC’06)*. Ed. by H. R. Arabnia. Las Vegas, USA: CSREA Press, 2006, pp. 177–183.
- [55] T.-P. Liu. “The Riemann problem for general 2×2 conservation laws”. *Transactions of the American Mathematical Society* 199 (1974), pp. 89–112.
- [56] T.-P. Liu. “The Riemann problem for general systems of conservation laws”. *Journal of Differential Equations* 18.1 (1975), pp. 218–234.
- [57] R. Menikoff and B. J. Plohr. “The Riemann problem for fluid flow of real materials”. *Reviews of Modern Physics* 61.1 (1989), pp. 75–130.
- [58] C. Merkle and C. Rohde. “The sharp-interface approach for fluids with phase change: Riemann problems and ghost fluid techniques”. *ESAIM: Mathematical Modelling and Numerical Analysis* 41.06 (2007), pp. 1089–1123.
- [59] I. Müller. *Grundzüge der Thermodynamik: mit historischen Anmerkungen*. 3rd ed. Springer, 2001.
- [60] I. Müller. *Thermodynamics*. Pitman, 1985.
- [61] I. Müller and W. Weiss. *Entropy and Energy: A Universal Competition*. Berlin, Heidelberg: Springer Berlin Heidelberg, 2005.
- [62] S. Müller and A. Voß. “The Riemann problem for the Euler equations with nonconvex and nonsmooth equation of state: construction of wave curves”. *SIAM Journal on Scientific Computing* 28.2 (2006), pp. 651–681.

- [63] S.-C. Ngan and L. Truskinovsky. “Thermal trapping and kinetics of martensitic phase boundaries”. *Journal of the Mechanics and Physics of Solids* 47.1 (1998), pp. 141–172.
- [64] S. Osher and R. Fedkiw. *Level set methods and dynamic implicit surfaces*. Vol. 153. Springer Science & Business Media, 2003.
- [65] P. Reinke and G. Yadigaroglu. “Explosive vaporization of superheated liquids by boiling fronts”. *International Journal of Multiphase Flow* 27.9 (2001), pp. 1487–1516.
- [66] C. Rohde. “On local and non-local Navier-Stokes-Korteweg systems for liquid-vapour phase transitions”. *Zeitschrift für Angewandte Mathematik und Mechanik* 85.12 (2005), pp. 839–857.
- [67] C. Rohde and C. Zeiler. “A relaxation Riemann solver for compressible two-phase flow with phase transition and surface tension”. *Applied Numerical Mathematics* 95 (2015), pp. 267–279.
- [68] J. R. Simões-Moreira and J. E. Shepherd. “Evaporation waves in superheated dodecane”. *Journal of Fluid Mechanics* 382 (1999), pp. 63–86.
- [69] I. Suliciu. “On the thermodynamics of rate-type fluids and phase transitions. I. Rate-type fluids”. *International Journal of Engineering Science* 36.9 (1998), pp. 921–947.
- [70] L. Truskinovsky. “Kinks versus Shocks”. In: *Shock induced transitions and phase structures in general media*. Springer, 1993, pp. 185–229.
- [71] S. O. Unverdi and G. Tryggvason. “A front-tracking method for viscous, incompressible, multi-fluid flows”. *Journal of Computational Physics* 100.1 (1992), pp. 25–37.
- [72] W. Wagner and A. Pruß. “The IAPWS formulation 1995 for the thermodynamic properties of ordinary water substance for general and scientific use”. *Journal of Physical and Chemical Reference Data* 31.2 (2002), pp. 387–535.
- [73] C. Waibel. “Berechnung von Transportwiderstandskoeffizienten an Phasengrenzflächen mit der klassischen Dichtefunktionaltheorie”. Master’s thesis. Universität Stuttgart, 2013.
- [74] E. Weinan, B. Engquist, X. Li, W. Ren, and E. Vanden-Eijnden. “Heterogeneous multiscale methods: a review”. *Journal of Computational Physics* 2.3 (2007), pp. 367–450.
- [75] X. Zhong, T. Y. Hou, and P. G. LeFloch. “Computational methods for propagating phase boundaries”. *Journal of Computational Physics* 124.1 (1996), pp. 192–216.

Index

- Assumptions
 - isothermal pressure, 11
- Bulk solver, 19
- CFL condition, 85
- CoolProp, 15
- Critical
 - point, 106
 - temperature, 12
- Density, 9
- Driving force, 58
- Entropy
 - flux, 10
 - mathematical, 17, 112
 - production, 10
 - solution, *see* Solution
 - specific, 10
 - total, 10
- Entropy criterion
 - kinetic function, 46
 - kinetic relation, 57
 - Lax, 27
 - Liu, 34
- Equal area rule,
 - see* Maxwell construction,
- Equation of state, 10
 - isentropic, 107
 - isothermal, 10
 - mixture, 32
 - non-isothermal, 106
- Equilibrium
 - chemical, 13
 - mechanical, 13
 - thermal, 13
 - thermodynamic, global, 13
 - thermodynamic, local
 - bulk, 106
 - interface, 13, 107
- Gibbs free energy
 - isothermal, 11
 - mixture, 32
 - non-isothermal, 106
- Heat flux, 9
- Helmholtz free energy
 - isothermal, 11
 - mixture, 32
 - non-isothermal, 106
- Interface, *see* Sharp interface
- Internal energy, 9
 - non-isothermal, 106
- Isothermal process, 10
- Kinetic energy, 9
- Kinetic function
 - mon. decreasing, 46
 - kinetic functions, 58
 - Kinetic relation, 57, 112
- Latent heat, 110
- Mass flux, 16, 108
- Maxwell construction, 14
- Mean curvature, 8
- Micro solution, *see also* Solution, 21
 - for kinetic functions, 47
 - for kinetic relations, 63
 - Liu micro solution, 33
 - non-isothermal, 115
 - relaxation approximation, 76
- Microsolver, 21

- Eulerian coord., 23
- for kinetic functions, 54
- for kinetic relations, 63
- Lagrangian coord., 25
- Liu microsolver, 40
- relaxation, 76, 79
- Model
 - isothermal, 15
 - macro-scale, 19
 - micro-scale, 19
 - Eulerian coord., 23
 - Lagrangian coord., 24
 - non-isothermal, 114
 - mixed hyperbolic-elliptic, 17
 - non-isothermal, 110
 - two-phase Euler, 108
 - two-phase Euler Fourier, 108
- Momentum, 9
- Order of convergence
 - experimental, 91, 123
- Phase, *see also* State or region
 - admissible set, 10
 - liquid, 10
 - vapor, 10
- Phase boundary, 7
- Pressure, 9
 - isothermal, 11, 16
 - mixture, 32
 - non-isothermal, 106
 - van der Waals, 12
- Relative error, 90, 123
- Saturation curve, 107
- Saturation state, 11, 107
- Sharp interface, 8
 - computational, 20
- Solution
 - entropy solution
 - Eulerian coord., 18, 23
 - Lagrangian coord., 25
 - non-isothermal, 112
 - macro solution, 19
 - micro solution, 21
 - reference, 91
 - thermodynamic equilibrium, 26, 113
- Sound speed, 11
 - Lagrangian coord., 25
 - non-isothermal, 106
- State or region
 - elliptic, 12
 - metastable, 15, 107
 - mixture, 14
 - spinodal, 12, 107
 - stable, 15
 - unstable, 12
- Surface tension, 9
- Target function, 116
- Temperature
 - critical, 12
 - isothermal, 10
 - non-isothermal, 106
- Total energy, 9
 - specific, 108
- Velocity, 9
- Volume
 - specific, 10
- Wave
 - characteristic, 29
 - condensation, 28
 - discontinuous, 27
 - elementary, 27
 - evaporation, 28
 - Lax shock, 27
 - metastable, 29
 - phase transition, 28
 - admissible, 46
 - relaxation, 76
 - rarefaction, 26
 - sonic, 29
 - stable, 29
 - subsonic, 28, 112
 - supersonic, 29
- Young-Laplace law, 14